

**Nature and characteristics of metasedimentary rock hosted gold
and base metal mineralization in the Workamba area, central
Tigray, northern Ethiopia**

**A Thesis submitted to the Faculty of Geosciences at Ludwig-
Maximilians University, Munich in partial fulfillment of the
requirements for the Ph.D. degree**

Solomon Gebresilassie Gebremariam

June 2009

Evaluators: Prof. Dr. Robert Marschik

Dr. Albert Hans Gilg

Date of Defence: 26.11.2009

Contents

1 Introduction.....	1
1.1 Problem statement.....	2
1.2 Geography of Tigray and study area.....	2
1.3 Mineral potential of Ethiopia.....	3
2 Geologic context.....	6
2.1 Geodynamic evolution of the East African Orogen.....	6
2.1.1 Geology of the Arabian-Nubian Shield.....	7
2.1.2 Geology of the Ethiopian basement rocks.....	9
2.1.3 Geology of Tigray basement rocks.....	11
2.1.3.1 Stratigraphic classification.....	11
2.1.3.2 Regional tectonic structure.....	16
2.2 Geology of the study area.....	17
2.2.1 Tsaliet Group.....	19
2.2.1.1 Metavolcanic rock.....	19
2.2.1.2 Quartz-sericite rock.....	19
2.2.2 Tambien Group.....	19
2.2.2.1 Sericite-chlorite schist.....	19
2.2.2.2 Slate and phyllite.....	20
2.2.3 Intrusive rocks.....	21
2.2.3.1 Monzogranite.....	21
2.2.3.1 Lamprophyre.....	21
2.2.4 Structural elements of the study area.....	23
2.2.4.1 Foliation.....	24
2.2.4.2 Shear zones.....	25
2.2.4.3 Folds.....	26
2.2.4.4 Faults.....	27
2.2.4.5 Joints, lineations and fractures.....	27
2.2.5 Quartz veins.....	28
2.2.6 Geology of the mineralized (drilled) zone.....	30
2.2.7 Down-hole geology.....	30
3 Geochemistry.....	32
3.1 Analytical method.....	32

3.2 Major and trace element abundance in metasedimentary rocks.....	32
3.3 Element mobility in metasedimentary rocks.....	32
3.4 Trace element patterns of metasedimentary rocks.....	38
3.5 Major, trace, and rare earth element abundance in intrusive rocks.....	40
3.5.1 Element abundance.....	40
3.5.2 Element mobility of the Workamba intrusive rocks.....	41
3.5.3 Trace and rare earth element patterns of intrusive rocks.....	45
4 Hydrothermal alteration and mineralization.....	48
4.1 Hydrothermal alteration.....	48
4.2 Mineralization.....	51
4.3 Paragenetic sequence.....	54
4.4 Geochemistry of mineralized rocks.....	56
4.5 Sulfide mineral chemistry.....	57
5 Microthermometry.....	59
5.1 Sampling and petrography.....	59
5.1.1 Liquid-only fluid inclusions (Type I).....	59
5.1.2 Liquid-rich two phase fluid inclusions (Type II).....	59
5.1.3 Vapor-rich two phase fluid inclusions (Type III).....	60
5.2 Nature of fluid inclusions.....	62
5.3 Microthermometric measurements.....	62
5.3.1 Type I fluid inclusions.....	62
5.3.2 Type II fluid inclusions.....	63
5.3.3 Type IIIA and B fluid inclusions.....	64
5.4 Interpretation of the fluid inclusion data.....	64
6 Isotope geochemistry.....	67
6.1 Sulfur isotope analysis and result.....	67
6.2 Carbon and oxygen isotope analysis and result.....	69
6.3 Lead isotope analysis and result.....	71

7 Discussion.....	77
8 Conclusion and recommendation.....	89
References.....	91
Annexes.....	102

List of figures

Fig. 1.1 Location and access map.....	1
Fig. 1.2 Mineral occurrences in Ethiopia.....	4
Fig. 2.1 Rock distribution in the Arabian-Nubian Shield.....	6
Fig. 2.2 Tectonic evolution of the East African Orogen.....	7
Fig. 2.3 Gondwana Supercontinent in early Mesozoic.....	8
Fig. 2.4 Distribution of basement rocks in Ethiopia.....	10
Fig. 2.5 Distribution of Tsaliyet and Tambien Groups in Tigray.....	12
Fig. 2.6 Stratigraphic section showing the Lower Tsaliyet and Upper Tambien Groups.....	13
Fig. 2.7 Major tectonic structures existing in Tigray.....	17
Fig. 2.8 Geological map of the study area.....	18
Fig. 2.9 Examples of exposed rock outcrops in the study area.....	20
Fig. 2.10 Photomicrographs showing identified minerals in thin section.....	22
Fig. 2.11 QAP classification diagram of the intrusive rocks.....	23
Fig. 2.12 Structural map of the study area.....	24
Fig. 2.13 Diagram showing relationships between S1 foliation, weakly developed second shear deformation, mylonitization, and later brittle fault.....	24
Fig. 2.14 Photograph showing closely spaced quartz veins in a shear zone.....	25
Fig. 2.15 Diagram displaying NE oriented brittle-ductile and NNE oriented ductile shear zones.....	26
Fig. 2.16 Photographs showing D1 and D2 folds.....	27
Fig. 2.17 Photograph showing E-W trending joints and fractures.....	28
Fig. 2.18 Photographs displaying second generation quartz veins occurring parallel to or cutting the foliation.....	28
Fig. 2.19 Geological map of the mineralized zone.....	29
Fig. 2.20 Showing types of exposed rocks and exploration structures in the mineralized zone.....	30
Fig. 2.21 Geological borehole sections displaying down-hole geology.....	31

Fig. 3.1 Isocon diagrams demonstrating element mobility in metasedimentary rocks.....	33
Fig. 3.2 Trace element patterns of metasedimentary rocks of the study area along with that of nearby metavolcanic and metasedimentary rocks.....	39
Fig. 3.3 Isocon diagrams displaying element mobility in intrusive rocks.....	42
Fig. 3.4 Major element discrimination diagrams for the intrusive rocks.....	44
Fig. 3.5 Trace element patterns of intrusive rocks.....	45
Fig. 3.6 Rare earth element patterns of intrusive rocks.....	46
Fig. 3.7 Trace element discrimination diagrams of intrusive rocks.....	47
Fig. 4.1 Geology and alteration map of the study area.....	48
Fig. 4.2 Photograph showing propylitic alteration occurrence in the study area.....	49
Fig. 4.3 Photographs showing different alteration types that affected the rocks.....	50
Fig. 4.4 Photomicrographs showing identified sulfides in the study area.....	52
Fig. 4.5 Boreholes sections indicating the distribution of base metal sulfides in the rocks.....	53
Fig. 4.6 Malachite occurrence on the cleavage planes of the metavolcanic rocks.....	54
Fig. 4.7 Photomicrographs displaying paragenetic relationships between the sulfides.....	55
Fig. 4.8 Paragenetic sequence of the sulfides and coexisting gangue and alteration minerals.....	56
Fig. 5.1 Showing the type of fluid inclusions occurring in the mineralized and unmineralized quartz or quartz-calcite veins of the study area.....	60
Fig. 5.2 Photomicrographs displaying the types of recognized fluid inclusions.....	61
Fig. 5.3 Histograms displaying the ranges of ice melting temperature, salinity and homogenization temperature of the heated/freeze inclusions.....	63
Fig. 5.4 Photomicrograph showing coexisting liquid- and vapour-rich two phase fluid inclusions in calcite.....	65
Fig. 5.5 Homogenization temperature versus salinity diagrams of the different types of heated/freeze fluid inclusions.....	66

Fig. 6.1 Diagram showing the position of sulfur isotope composition of Workamba sulfides relative to that of sediment-hosted orogenic gold deposits elsewhere.....	68
Fig. 6.2 Diagram displaying plot of carbon and oxygen isotope composition of Workamba hydrothermal calcites together with that of nearby Tambien Group rocks.....	70
Fig. 6.3 Lead isotope data plot of sulfides, feldspars and whole rock samples relative to the growth curves and fields of Zartman and Doe (1981).....	74
Fig. 6.4 Lead isotope composition of sulfides from Workamba plotted relative to the discrimination diagrams of Stacey et al.(1980).....	76
Fig. 7.1 Compilation of major geologic and tectonic events occurred in the study area and Tigray region.....	79
Fig. 7.2 Showing the crustal continuum model of orogenic gold deposits and the position of Workamba gold and base metal mineralization with respect to it.....	83
Fig. 7.3 A summary of the ore forming processes and inferred depth of formation of the mineralization at Workamba	84

List of tables

Table 2.1 Geochronological data of intrusive rocks in Tigray.....	15
Table 3.1 Whole rock geochemistry data of Workamba metasedimentary rocks.....	34
Table 3.2 Selected major and trace element concentrations of Workamba and nearby metasedimentary rocks used for estimation of element mobility.....	37
Table 3.3 Trace element ratios of the Workamba metasedimentary rocks along with those of reference nearby metasedimentary rocks.....	38
Table 3.4 Whole rock geochemistry data of Workamba intrusive rocks.....	43
Table 4.1 Whole rock geochemistry data showing concentrations of gold and base metals in mineralized rocks.....	57
Table 4.2 Representative electronprobe analysis results of pyrite, sphalerite and galena from Workamba.....	58
Table 6.1 Result of sulfur isotope analysis.....	67
Table 6.2 Result of carbon and oxygen isotope analysis.....	69
Table 6.3 Result of lead isotope analysis of sulfides.....	73
Table 6.3 Result of lead isotope analysis of whole rock samples.....	73
Table 7.1 Comparison of the Workamba gold and base metal mineralization with the characteristics of orogenic gold deposits elsewhere.....	85

Acknowledgement

I would like to thank very much Deutscher Akademische Austausch Dienst (DAAD) for granting me a scholarship. The scholarship enabled me to study and live in Germany with my family for the last four years. I would also like to acknowledge DAAD for covering the expenses of my fieldwork. Generally, I run out of words to express the extraordinary financial help I received from DAAD so that I finish my studies successfully.

I am very grateful of Prof. Dr. Robert Marschik, my supervisor, for the continuous and extraordinary help, follow up, and guidance that he dedicated to me from the beginning to the end of my studies. This work could not have been materialized without his significant input, constructive criticisms, and fruitful discussions.

I would also like to thank very much the Department of Earth and Environmental Sciences of Ludwig-Maximilians University for allowing me to have full access to various facilities, such as laboratories, library, internet, printer and photocopy.

A lot of thank goes to Dr. Albert Hans Gilg for his incredible help and guidance especially during the laboratory works of fluid inclusions. I am very thankful of the constructive discussions I had had with him regarding interpretations of fluid inclusion data.

I am highly indebted to Dr. Frank Söllner for his guidance and unreserved help during the energy dispersive spectrometry (EDS) analysis.

I would like to highly acknowledge Prof. Dr. Karl Thomas Fehr and Ms. Saskia Bernstein for helping me during the electronprobe microanalysis.

My heartfelt acknowledgments go to Prof. Dr. Stefan Hölzl and my friends, Tobias Bauer and Susanne Rummel, for their unreserved help and guidance during the lead isotope analysis.

I would like to thank very much Dr. Christoph Mayer (Geo-Bio-Center) for doing the carbon and oxygen isotope analysis.

Ms. Madlen Fischer is highly acknowledged for preparing the thin and polished sections as well as double polished sections for fluid inclusion studies.

I am greatly indebted to the National Mining Corporation and its staff members, especially Mr. Senbeto Chewaka, Kibret Sifeta, and Muluwork Ambaye for allowing me to work in their project site and providing logistical support during the fieldwork. I would also like to thank very much Mekelle University (my base University) for providing me a vehicle during the field work.

I am very grateful of my friend, Dr. Dirk Küster (who was a staff member of Mekelle University) for initiating the idea of doing Ph.D. in Germany and for all his helps and advises.

Abstract

Exploration activities outlined a shear zone-hosted gold and base metal occurrence in low-grade metasedimentary rocks near the town of Workamba, Tigray State, northern Ethiopia. Gold resources are estimated at ~2 t Au with concentrations reaching up to 8 g/t Au in the ore. The geology of the study area is dominated by foliated or sheared, lower greenschist facies metavolcanic and metasedimentary rocks, which are correlated to the lower island-arc metavolcanic rocks of the ~860 to 750 Ma Tsaliyet Group and upper carbonate and metasedimentary rocks of the ~740 Ma Tambien Group, respectively. The Tsaliyet and Tambien groups represent the southern parts of the Arabian-Nubian Shield. The Tsaliyet Group, which is exposed in the north-western parts of the study area, consists mainly of metavolcaniclastic rocks. The overlying slate, phyllite, sericite-chlorite schists and marbles of the Tambien Group occupy the south-eastern part of the area. A steeply dipping NE trending ductile shear zone occurs in the metasediments along the contact with the Tsaliyet Group. It is intruded by monzogranite and lamprophyre dikes or sills. The shear zone is correlated with an early regional deformation event (D1), which also caused NE foliations and ENE trending folds. A second regional deformation phase (D2) resulted in NNE oriented weakly developed dextral shear bands and N-S trending parasitic folds. NW striking brittle faults postdate D1 and D2 ductile structures.

Trace element patterns of the metasedimentary rocks support findings of previously published works suggesting that they are derived from the rocks of the Tsaliyet Group. Major, trace, and rare earth element characteristics of the monzogranite dikes/sills permit the conclusion that they are related to the ~620 to 520 Ma post-tectonic magmatism in the Tigray region. The post-tectonic granitoids are resulted from mantle-derived magmas, which are modified by fluid components of the subducted slab or involvement of continental crust. Petrographic and geochemical results of the lamprophyres show that they are calc-alkaline in nature. The monzogranite dikes/sills have $^{208}\text{Pb}/^{204}\text{Pb}$, $^{207}\text{Pb}/^{204}\text{Pb}$, and $^{206}\text{Pb}/^{204}\text{Pb}$ values between 37.176 to 37.310, 15.508 to 15.525, and 17.799 to 18.310, respectively. These lead isotope ratios are compatible with a significant mantle component in these rocks. Lead isotope ratios of the metasedimentary and metavolcanic rocks at Workamba are heterogeneous, suggesting that not all samples did retain their original Pb isotope signatures. However, the original Pb isotope composition of these rocks tends to be less radiogenic as those of the post-tectonic dikes/sills.

Field and petrographic observations show that the metavolcanic rocks are locally affected by propylitic alteration and sericitization. The metasedimentary rocks suffered from pervasive silicification, sericitization, and carbonatization. The monzogranite and lamprophyre dikes/sills locally experienced pervasive sericitization, carbonatization, epidotization, and chloritization. Two generations of quartz veins occur cutting and/or parallel to D1 foliation on the Tsaliet and Tambien groups. The first generation quartz veins are folded and less abundant as compared to the unfolded second generations. The metasedimentary rocks and the dikes/sills are also cut by calcite \pm quartz veinlets in the mineralized zone. Mass balance calculations of the metasedimentary rocks suggest that Na₂O, and Sr are removed by hydrothermal fluids from the original composition of the rocks. K₂O, MnO, CaO, Ba, and Pb are variably added or removed. The dikes/sills retained near original geochemical composition.

The shear zone hosted metallic mineralization occurs within the metasedimentary rocks, in close spatial proximity to the dikes/sills. It took place under brittle conditions. Pyrite, sphalerite, galena, and chalcopyrite are the main sulfide phases, whereas pyrrhotite, arsenopyrite, and chalcocite are minor components. Gold is invisible and was only detected in geochemical analysis. Gangues include calcite, sericite, and quartz. The mineralized rocks are enriched in Au, As, Sb, and Ag. The Au/Ag ratio of all analyzed samples is less than 10. The paragenetic relationships show that pervasive sericitization and chlorite-epidote (propylitic) alteration occurred before an early quartz and/or calcite \pm quartz veining event. The mineralization occurred roughly concomitant with carbonatization and calcite \pm quartz veining, after the intrusion of the monzogranite and lamprophyre dikes/sills.

Sulfur isotope signature of sulfides ($\delta^{34}\text{S}_{(\text{VCDT})} = 1.8$ to 9.1 ‰) is compatible with the hypothesis that S is derived from the country rocks through leaching by hydrothermal fluids. The carbon isotope signature of hydrothermal calcite ($\delta^{13}\text{C}_{(\text{VPDB})} = -5.6$ to $+1.8$ ‰) and that of a fluid in equilibrium with this calcite ($\delta^{13}\text{C}_{(\text{VPDB})} = -3.7$ to $+3.7$ ‰) are similar to those of Tambien Group carbonate rocks ($\delta^{13}\text{C}_{(\text{VPDB})} = -4.5$ to 7 ‰). Therefore, the C is dominantly derived from the Tambien Group. The calculated oxygen isotope signature ($\delta^{18}\text{O}_{(\text{VSMOW})}$ values between 5.1 to 8.7 ‰) of a hydrothermal fluid in equilibrium with calcite is compatible with a fluid of magmatic or metamorphic origin. The $^{208}\text{Pb}/^{204}\text{Pb}$, $^{207}\text{Pb}/^{204}\text{Pb}$, and $^{206}\text{Pb}/^{204}\text{Pb}$ values of sulfides, which range between 36.94 to 36.99 , 15.47 to 15.49 , and 17.36 to 17.38 respectively, differ markedly from those of monzogranite dikes/sills. The data implies that the

mineralization is unrelated to post-orogenic magmatism and that the Pb isotope signature of the sulfides represents the original Pb isotope signature of the metasedimentary and metavolcanic rocks. Overall evaluation of S, C, and Pb isotopic data permits to conclude that metals, sulfur, and other ore components are derived from the country rocks through leaching by metamorphic fluids.

Petrographic studies of fluid inclusions show the presence of coexisting liquid-only, liquid-rich and vapour-rich two phase fluids. The fluid inclusions are predominantly secondary or pseudo-secondary in nature. Microthermometric measurements show that all fluid inclusions are of low-salinity (~1 to 8 wt. % NaCl_{equiv.}) aqueous types. Average homogenization temperatures of fluid inclusions in calcite are around 300°C, i.e. close to temperatures found in orogenic gold systems.

The mineralization at Workamba was likely generated by devolatilization and dehydration processes during metamorphism of the Tsaliet and Tambien Group rocks. The major collision orogeny which waned in Tigray at ~630 Ma might have caused eviction of the mineralizing fluids from deep regions. These mineralizing fluids were then channeled in the shear zone. Gold was presumably transported as Au(HS)₂⁻ complexes at intermediate oxidation states by near-neutral fluids, and sulfidation of host rocks is proposed as the likely gold deposition mechanism. The sub- to greenschist facies metamorphism of the Tambien and Tsaliet Group rocks, the enrichment in Sb, and As, the brittle-ductile shearing experienced by the rocks, and the mineralization under brittle conditions suggest a depth of formation between 4 to 6 km.

Generally, the findings of this study suggest that the genesis of metallic mineralization at Workamba is of orogenic gold type and unrelated to post-orogenic magmatism in the area, although a close spatial proximity to post-orogenic dikes/sills exists. The age of the mineralization is estimated to be late Neoproterozoic.

1. Introduction

Ongoing exploration activities being conducted by the National Mining Corporation (NMiC) outlined a gold and base metal occurrence with estimated resource of 2 t Au at a grade of 8 g/t Au near the town of Workamba, northern Ethiopia (NMiC 2006, personal communication; Fig. 1.1a and b). The mineralized zone is hosted in sheared Neoproterozoic greenschist metamorphosed sedimentary rocks adjacent to monzogranite and lamprophyre dikes/sills. It was defined by stream sediment sampling, a geophysical survey, trenching and drilling. The prospect area is located about 900 km north of Addis Ababa and lies between UTM 500 000 to 508 000 east and 1517 000 to 1521 800 north. It covers ~25 km². The region suffered civil war from 1974 to 1991, leaving only few geological information available on it for a long time. More recently, several regional scale geological studies or studies on specific aspects were conducted (e.g. Alene 1998; Alene et al. 2000, 2006; Asrat 2002; Tadesse 1996; Tadesse et al. 1999, 2000; Miller et al. 2003; Stern et al. 2005).

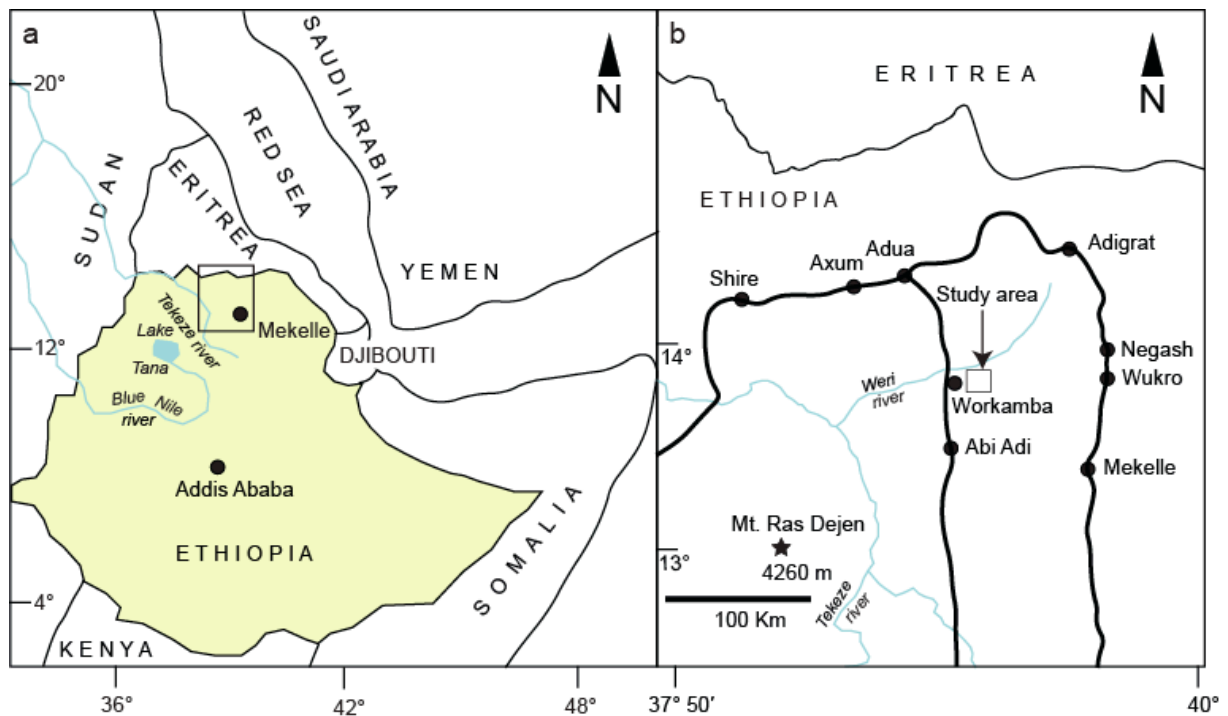


Fig. 1.1. Map of Ethiopia, and northeast Africa and Arabia showing, a) position of Ethiopia with respect to East Africa and Arabia, and portions of northern Ethiopia and south Eritrea (inset rectangle), b) enlarged map of the inset rectangle showing the location and accessibility of the study area and different towns of the region.

1.1 Problem statement

The nature of the gold and base metal mineralization in the study area is unknown. The geotectonic and structural setting, host rock types and alteration, and ore mineralogy is compatible with an orogenic gold-type mineralization (e.g. Groves et al. 1998; Goldfarb et al. 2001, Klein et al. 2005). However, taking into account a close spatial relationship between the monzogranite and lamprophyre dikes/sills and the mineralized zone, the mineralization could be related to a porphyry copper type at depth or represent skarn-type deposit (e.g. Ray 1998). The objectives of this study are to determine rock and alteration types and their distribution, the ore mineralogy and a paragenetic sequence, the source of metals and sulfur, characteristics and source of aqueous fluids involved in the ore formation, and controls on the mineralization. The final goal is to present a model for the gold and base metal mineralization at Workamba, and relate it to the geologic evolution of the region. These problems were addressed by employing different techniques, such as field mapping, drill core logging, transmitted and reflected light microscopy, microthermometry on fluid inclusions, electronmicroprobe analysis on selected sulfide minerals, whole rock geochemistry, and stable and radiogenic isotope geochemistry studies. This research is conducted with the logistical support of the National Mining Corporation.

1.2 Geography of Tigray and the study area

Tigray is the northern province of Ethiopia and one of the historical regions of the country where ancient cities like Axum are found. Mekelle, the capital city of Tigray, can be reached using daily flight from Addis Ababa or via the main highway. Climate conditions of Tigray region vary from arid to semi-arid with average annual rainfall of 600-800 mm and annual average temperature of 25°C (Garland 1980). The Triassic to Jurassic Adigrat Sandstone (e.g. Bosellini et al. 1997) unconformably lies on the basement rocks. This unit is one of the important water reservoirs of the region. The Adigrat sandstone is also widely used as a dimension stone. The study area is located 100 km northwest of Mekelle (Fig. 1.1b). From Mekelle, it is accessible by gravel roads. Generally, the area is characterized by rugged and dissected topography. The drainage pattern of the study area is mainly accomplished by the perennial Weri river, which is used by the local people for domestic purposes and to pan placer gold. Other intermittent small-scale rivers feed the Weri river. The study area is sparsely vegetated by cactus. The means of living of the inhabitants of the area is dominantly agriculture (farming and livestock production).

1.3 Mineral potential of Ethiopia

Ethiopia is endowed with substantial amounts of metallic and non-metallic mineral resources and has a long history of mining (e.g. Assefa 1985; Tadesse et al. 2003). It was suggested that gold was under mining since the 6th century (e.g. Walsh 1981; Assefa 1985). However, the country gains marginal economic benefits from these resources, since the mining sector only accounts for 1% of the GDP (International Monetary Fund 2005a). One reason is the lack of basic geological information and skills, particularly related to mineral exploration techniques.

Modern exploration and mining activities targeted on diverse metallic (gold, platinum, tantalum, iron, copper, manganese, molybdenum, lead, zinc, nickel, cobalt and chromium) and industrial minerals (potash, sulfur, bentonite, lignite, soda ash, salt and diatomite). They have been conducted since 1941 by the ministry of Mines and Energy and Geological Survey of Ethiopia in collaboration with various foreign companies (Walsh 1981). Most of the explorations activities were carried out on the basement rocks as they contain majority of the mineral resources of the country (Tadesse et al. 2003). The location of the most relevant metallic mineral deposits and occurrences is given in Fig. 1.2. The majority of them are concentrated in southern, southwestern, western, eastern, and northern Ethiopia. Gold is the dominant mineral commodity and occurs mainly in the form of secondary placer deposits. Primary gold is currently mined at the Lega Dembi deposit in southern Ethiopia, which has a resource of ~60 t Au with an average 6 g/t of Au (Billay et al. 1997; Tadesse et al. 2003). It is hosted in Neoproterozoic greenstone rocks and shear-zone controlled. Gold occurs mainly as native Au or electrum in quartz veins, stringers, and to some extent in selvages of altered wall rocks (Billay et al. 1997; Tadesse et al. 2003; Tadesse 2004). Pyrite, galena, pyrrhotite and sphalerite are sulfide gangue. Rb-Sr dating of sericite yielded an estimated age of about 545 Ma for the mineralization (Billay et al. 1997). Near to the Lega Dembi gold mine, the Kenticha Ta deposit produces 80 t of Ta concentrate (~55 wt. % Ta₂O₅, Küster et al. 2007) annually. Its estimated resources are 500-2500 t Ta₂O₅ (Tadesse et al. 2003). The deposit is in pegmatites, which are emplaced along a N-S trending fault system. The ore is associated with rare elements such as Nb, Li, Rb, and Cs and silicates like lepidolite, spodumene, and beryl. U-Pb dating of tantalite suggests an age of about 530 Ma for the deposit (Küster et al. 2007).

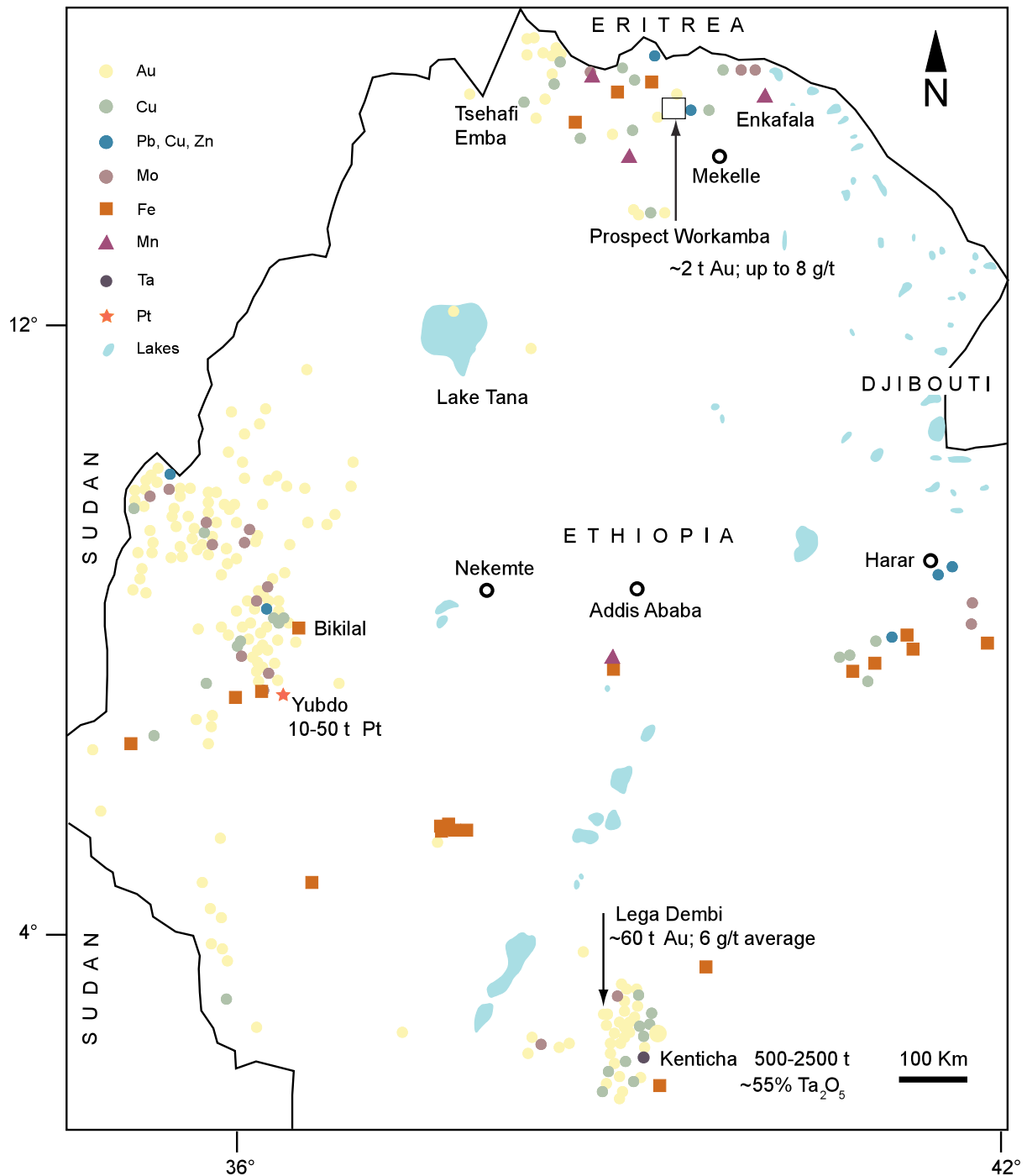


Fig. 1.2. Distribution of metallic mineral deposits and occurrences in Ethiopia (modified after Tadesse et al. 2003). Locations of major cities are indicated (open circle). The mineral deposits are mainly concentrated within the basement rocks. The majority of the mineral occurrences are of placer gold type. The only deposits mined at industrial scale are the Lega Demi gold deposit and the Kenticha Ta deposit.

There are also Ni ores in the Kenticha area. They were formed by weathering of serpentinites (e.g. Clark 1978, Gebresilassie et al. 2003). The Ni deposit has an estimated resource of 0.02-0.2 Mt Ni with Co and Cr as possible by products (Tadesse et al. 2003). A platinum deposit is present in the Yubdo area (western Ethiopia), which is hosted in laterites and resulted from insitu weathering of serpentinitized dunite (de Wit and Berg 1981). Resources range from 10 to 50 t Pt (Tadesse et al. 2003). Mogessie et al. (2000) and Belete (2000) have also reported enrichment of sulfur poor PGE mineralization in chromite-bearing mafic-ultramafic intrusions. Copper (and/or lead, zinc), iron, and molybdenum occurrences are also widely reported in many localities of the country, although their reserve is not well constrained. Among these, the Bikilal iron deposit is the largest with estimated resource of 10-100 Mt of iron (Tadesse et al. 2003). Manganese occurrences are rare, and mainly found in northern Ethiopia (e.g. Enkafala, Tigray). Few reconnaissance surveys conducted in the 1970s and 80s, show that the presence of some prospects for gold and base metal mineralization hosted in Tigray basement rocks (e.g. Beyth 1972; de Wit 1981). They were classified as massive sulfide deposits and ores consist of pyrite, with copper, zinc, and lead sulfides (de Wit 1981). Copper mineralization in metagabbro was identified in western Tigray (Tsehafi Emba, Morton 1981).

Industrial minerals including salt, clay, diatomite, bentonite, feldspars, mica, soda ash, potash, and rocks like gypsum, anhydrite, limestone, dolomite, marble, sandstone, pumice, granite as well as gemstones are also widely reported throughout Ethiopia (Assefa 1985; Tadesse et al. 2003).

2. Geologic context

2.1. Geodynamic evolution of the East African Orogen

The basement rocks in the Workamba area belong to the Arabian-Nubian Shield (ANS), which stretches from the Arabian Peninsula over Egypt, Sudan, Somalia, into Ethiopia (Fig. 2.1, Berhe 1990). The ANS is interpreted to consist of accreted terranes and represents the northern part of the East African Orogen (Vail 1983; Vail 1985; Stern 1994). The East African Orogen developed due to the collision of East and West Gondwana (Fig. 2.2) during the late Proterozoic, which finally formed the Gondwana Supercontinent (Fig. 2.3; de Wit and Chewaka 1981; Stern 1994; Stern 2002; Stern et al. 2005). The East African Orogen also represents one of Earth's greatest collision zones. This orogen is about 6000 Km long and evolved over a time period of about 350 Ma (Stern 2002).

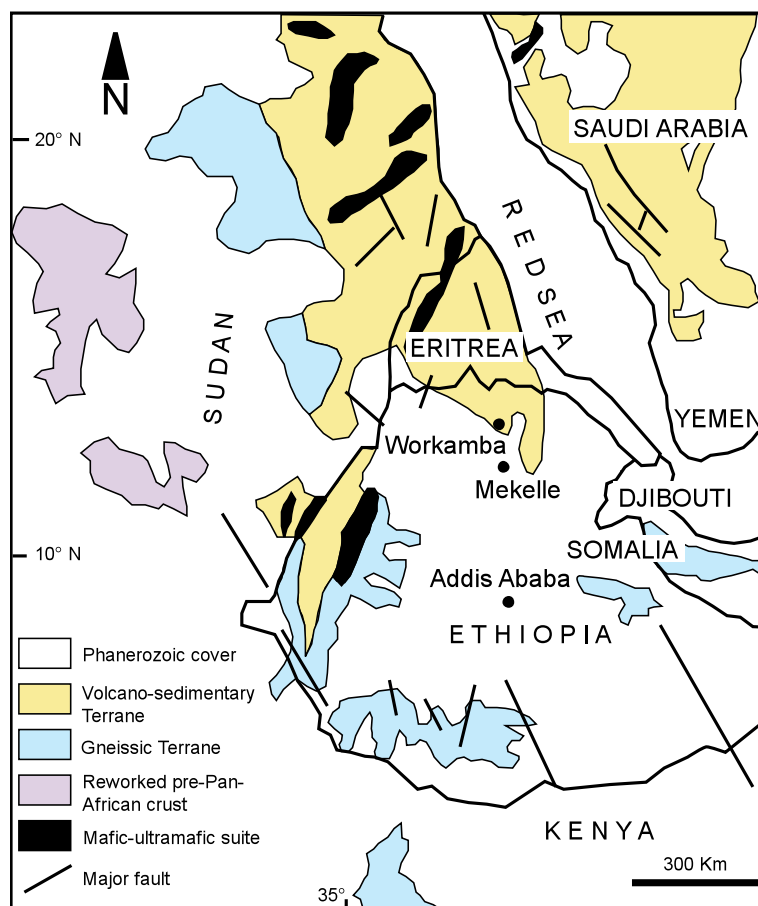


Fig. 2.1. Distribution of rocks of the Arabian-Nubian Shield, which form the basement rocks Arabian Peninsula, northeast Africa (Egypt and Sudan), and Ethiopia (modified from Ayalew et al. 1990; Berhe 1990; Asrat et al. 2001).

The tectonic evolution of the East African Orogen are: (1) Rodinia rifting and break-up at ~900-850 Ma; (2) seafloor spreading, arc and back-arc basin formation, and terrane accretion from 870 to 690 Ma; (3) continent-continent collision from 630 to 600 Ma, and (4) further crustal shortening, orogenic collapse and extension leading to the break-up of Gondwana during 600 to 540 Ma (de Wit and Chewaka 1981; Stern 1994; Stern et al. 2006). The southern part of the East African Orogen is represented by the Mozambique Belt, which is formed by Himalayan-type collision. The Mozambique Belt comprises high-grade gneisses, migmatites and schists (Asrat et al. 2001). This belt can be traced in southern, western, and eastern Ethiopia (Berhe 1990; Asrat et al. 2001).

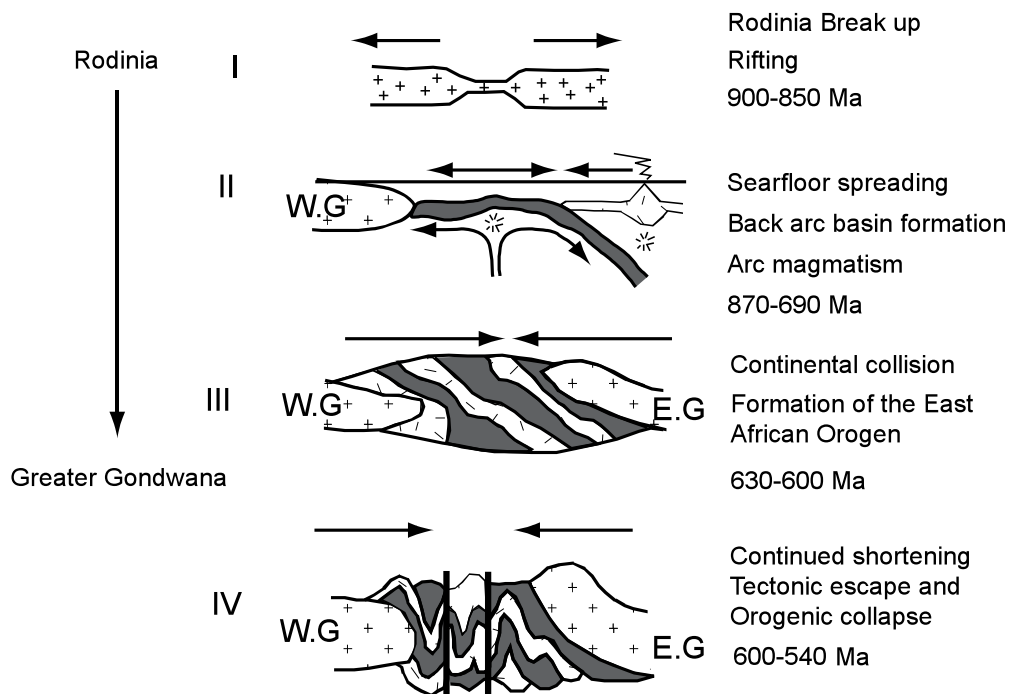


Fig.2.2. Tectonic evolution of the East African Orogen that resulted in the greater Gondwana Supercontinent (modified from Stern et al. 2006). W.G = West Gondwana and E.G = East Gondwana.

2.1.1 Geology of the Arabian-Nubian Shield

Johnson and Woldehaimanot (2003) summarized and interpreted available data on the ANS. They suggested that it is a collage of terranes. Accretion took place from ~780 to 550 Ma between different terranes of the ANS. The ANS consists of three principal units (Fig. 2.1): (1) gneissic terranes dominated by quartzofeldspathic gneisses, migmatites, and metasediments of amphibolite to granulite facies, which are found in the western part of the Nubian shield (e.g. Halfa and Bayuda terranes, Sudan), eastern Arabian shield (Afif and Al Rayn terranes,

Saudi Arabia), and in some regions of the central part of the shield such as the Barka and Ghedem Terrans of Eritrea, Red Sea Hills of Sudan, and Aswan region of Egypt (Vail 1985; Johnson and Woldehaimanot 2003; Sultan et al. 2004; Stacey and Hedge 1984).

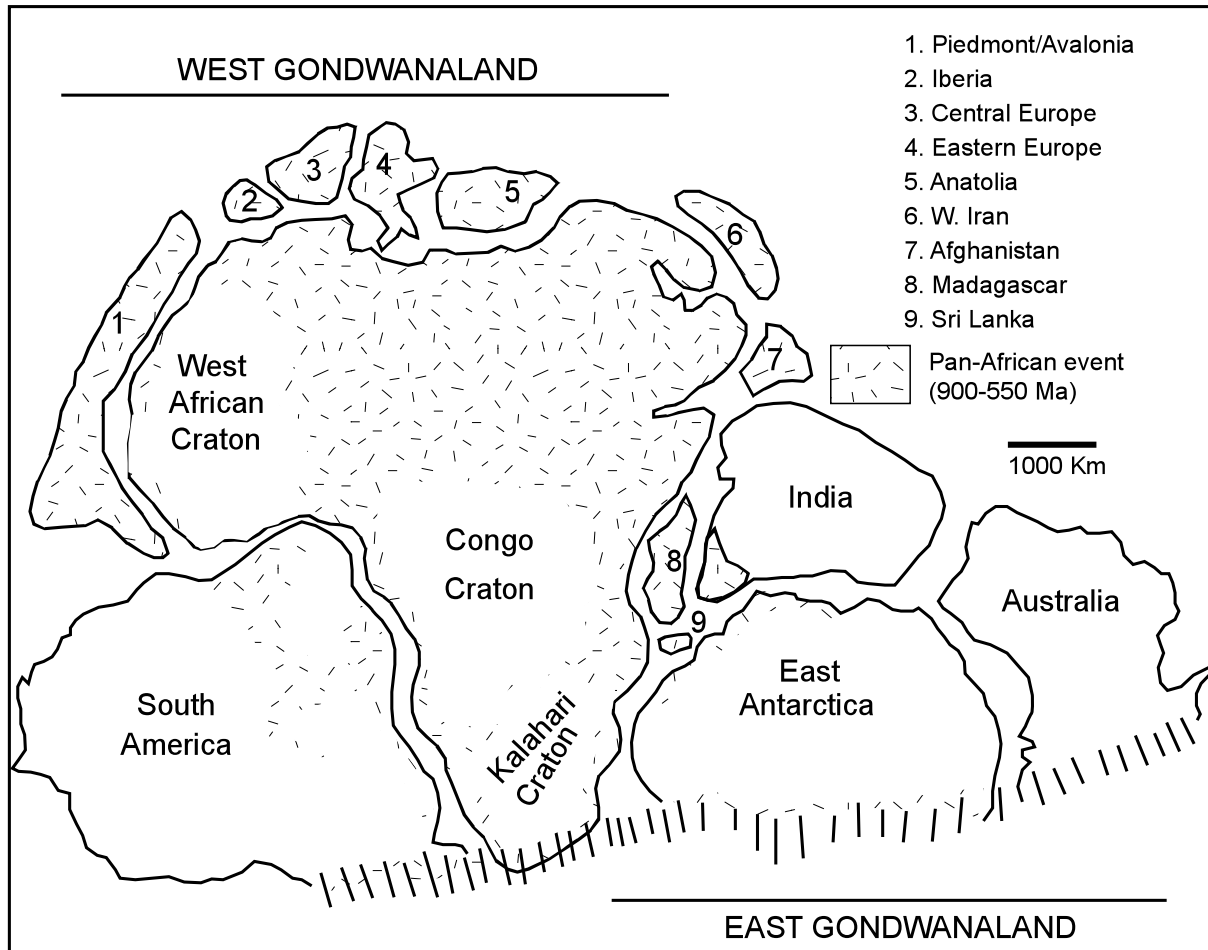


Fig. 2.3. Gondwana Supercontinent formed by collision of east and west Gondwana from 630-600 Ma and showing the position of the continents in early Mesozoic, which were about 25% larger at the end of Precambrian mostly on the Australian, Indian, Arabian, and NE African margins. Bottom vertical to sub-vertical solid lines represent early Paleozoic passive margin, modified from de Wit and Chewaka (1981), Stern (1994), and Stern et al. (2005).

These high grade rocks were derived from continental crust recycled during the East African Orogen; (2) greenschist to lower amphibolite metamorphosed volcano-sedimentary terranes including calc-alkaline basaltic and andestic lavas, tuffs, pyroclastics, and rhyolites, which are intruded by various pre-, syn-, and post-tectonic granitoids and occurring between the western and eastern gneissic terrain (Vail 1985). Geochemical and Nd, Sr, and Pb isotope characteristics of the rocks of this terrane indicate that they resulted from accretion of intra-oceanic island arcs composed of juvenile Neoproterozoic crust, which is mainly derived from

a depleted mantle source (e.g. Kröner et al. 1991; Stern 1994; Stern 2002; Kröner et al. 1991; Beyth et al. 1997; Stern and Abdelsalam 1998, Tadesse et al. 1999, 2000; Teklay et al. 2002, Andersson et al. 2006). There is evidence for input of older crustal components into this juvenile Neoproterozoic crust. Examples include the 1125 ± 2.5 and 1656.8 ± 1.4 Ma zircon xenocrysts in the 604.7 ± 1.4 Ma metarhyolite of eastern Ethiopia (Teklay et al. 1998); 1729 ± 4 to 1822 ± 5 Ma or 987 Ma zircon xenocrysts hosted in 814 ± 7 Ma diorite or 626 ± 11 Ma granodiorite intrusions of Somalia, respectively (Kröner and Passi 1996; Lenoir et al. 1994), and 2.1 to 1.9 Ga inherited zircon in a ca. 689 Ma anorthosite of Gebel El Asir area, Egypt (Sultan et al. 1994). Teklay et al. (2002) have suggested the presence of plume-related magmatism that enriched the source of metavolcanic rocks from northern Eritrea prior to the onset of generation of subduction-related magmas; (3) mafic-ultramafic suites comprising ophiolite assemblages, narrow discontinuous belts of dismembered serpentinites, gabbros, sheeted dikes, pillow lavas, and ultramafic rocks. These mafic-ultramafic suites are interpreted to represent suture zones between intraoceanic plates or continent-island arc margins (Kröner 1985; Vail 1985; Berhe 1990).

Abdelsalam and Stern (1996) recognized two deformation belts in the ANS: (1) Related to arc-arc and arc-continent collision, which are both associated with sutures. The arc-arc deformation belts are manifested by the occurrence of E-W and N-S verging ophiolities in the northern and southern parts of the ANS respectively. The E-W verging ophiolities are steepened by upright folds, whereas those of N-S vergence are deformed by up-right folds and strike slip faults related to oblique collision of the terranes at about 800-700 Ma. The arc-continent deformation belts are related to the collision of East and West Gondwana. (2) Post-accretionary structures (~650-550 Ma) resulted from continuous shortening of the ANS and developed NW trending strike slip faults and shear zones during the waning stages of ANS formation.

2.1.2 Geology of the Ethiopian basement rocks

The Ethiopian basement rocks are exposed in eastern, western, northern, and southern parts of the country (Fig. 2.4). They have been studied for the last three decades by researchers such as Kazmin (1971, 1975), Kazmin et al. (1978), Beyth (1972), de Wit and Chewaka (1981), Ayalew et al. (1990), Alemu (1998), Tadesse (1996), Tadesse et al. (1997, 1999, 2000), Alene et al. (2000, 2006), and Asrat et al. (2001).

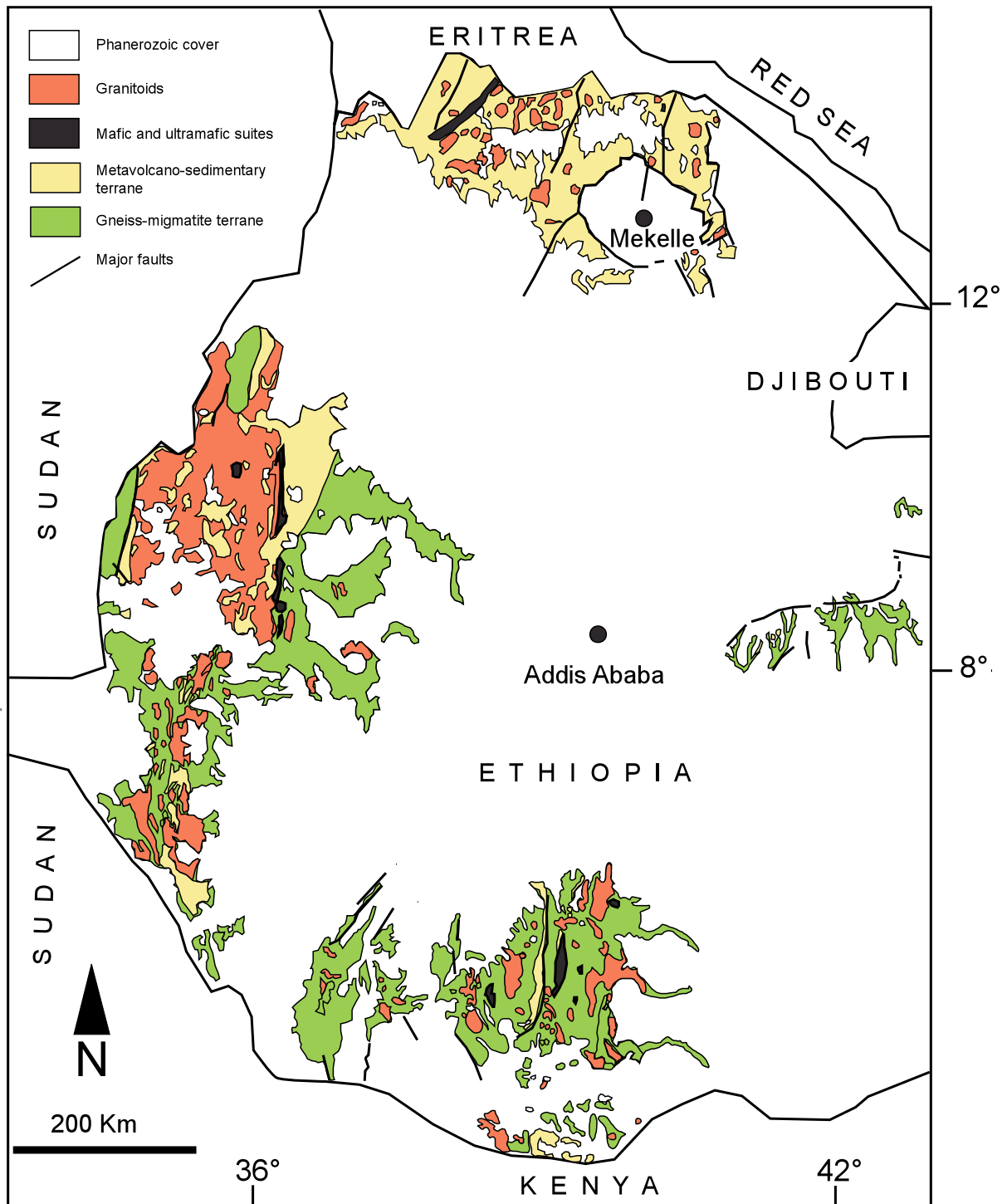


Fig. 2.4. Distribution of the low-grade volcano-sedimentary sequences of the ANS and high-grade gneisses and migmatites of the Mozambique Belt in Ethiopia (modified from Asrat et al. 2001).

Kazmin (1971, 1975), who explored the basement rocks for the first time subdivided them into Lower, Middle, and Upper Complexes based on compositional, deformational and metamorphic grade variations. Recently, this subdivision has been revised as the rocks of Lower Complex, which were thought to be Archean in age, turned out to be Late Proterozoic

in age (e.g. Ayalew et al. 1990; Teklay et al. 1998). According to the new subdivision, the Ethiopian basement is composed of two major blocks: (i) a gneissic and migmatic terrain, which essentially consists of the Lower and Middle Complex (Kazmin 1971, 1975), and correlated with the Mozambique Belt; (ii) a low-grade volcano-sedimentary terrain, which comprises all the rocks of the Upper Complex and is correlated with the ANS (Fig. 2.4). Pre-, syn-, and post-tectonic granitoids intruded the Ethiopian basement rocks (Asrat et al. 2001).

2. 1.3 Geology of Tigray basement rocks

The basement rocks of the Tigray region represent an accretion of compositionally different (immature to evolved) intra-oceanic island arcs (Tadesse et al. 1999). Sm-Nd isotope data of the syn-tectonic granitoids of Axum area (Tadesse et al. 2000) and the late- to post-tectonic granitoid of Negash (Asrat 2002), which intruded the metavolcano-sedimentary rocks, suggest predominantly a depleted mantle source. This signature is similar as those of the Eritrean Neoproterozoic crust (Beyth et al. 1997; Teklay et al. 2002; Andersson et al. 2006) and the ANS rocks elsewhere (e.g. Sudan, Stern and Abdelsalam 1998; Kröner et al. 1991).

2.1.3.1 Stratigraphic subdivisions

Beyth (1972) broadly subdivided the basement rocks of the ANS in the Tigray region into two groups based on stratigraphical relationships: (i) the Tsaliet Group, and (ii) the Tambien Group. The Tsaliet Group covers most of the area of the region occupied by basement rocks (Fig. 2.5a). It consists of arc-related metavolcano-sedimentary rocks (Fig 2.6) including metavolcanic/volcanoclastic rocks, sericite-chlorite schist, slate, greywacke, impure marble, calcareous siltstone, well bedded, intermediate to acidic welded tuffs, lappili tuff, and agglomerates (Beyth 1972; Beyth et al. 2003, Tadesse et al. 1999; Alene et al. 2000). The thickness is unknown. Beyth (1972) estimated more than 1500 m. Chlorite thermometry conducted on mineral assemblages of the metavolcanic rocks shows peak regional metamorphism at ~245-375°C (pumpellite-actinolite to lower greenschist facies, Alene 1998). NE-SW trending shear zones with a sinistral-strike slip sense of movement affect the rocks of this group (Tadesse et al. 1999). The age of the Tsaliet Group is not well constrained. However, based on lithologic similarities, these rocks are correlated with the metavolcanic rocks of the Ghedem terrane in Eritrea (Alene et al. 2006), which were dated $\sim 854 \pm 3$ Ma using the Pb/Pb single-zircon evaporation method (Teklay 1997).

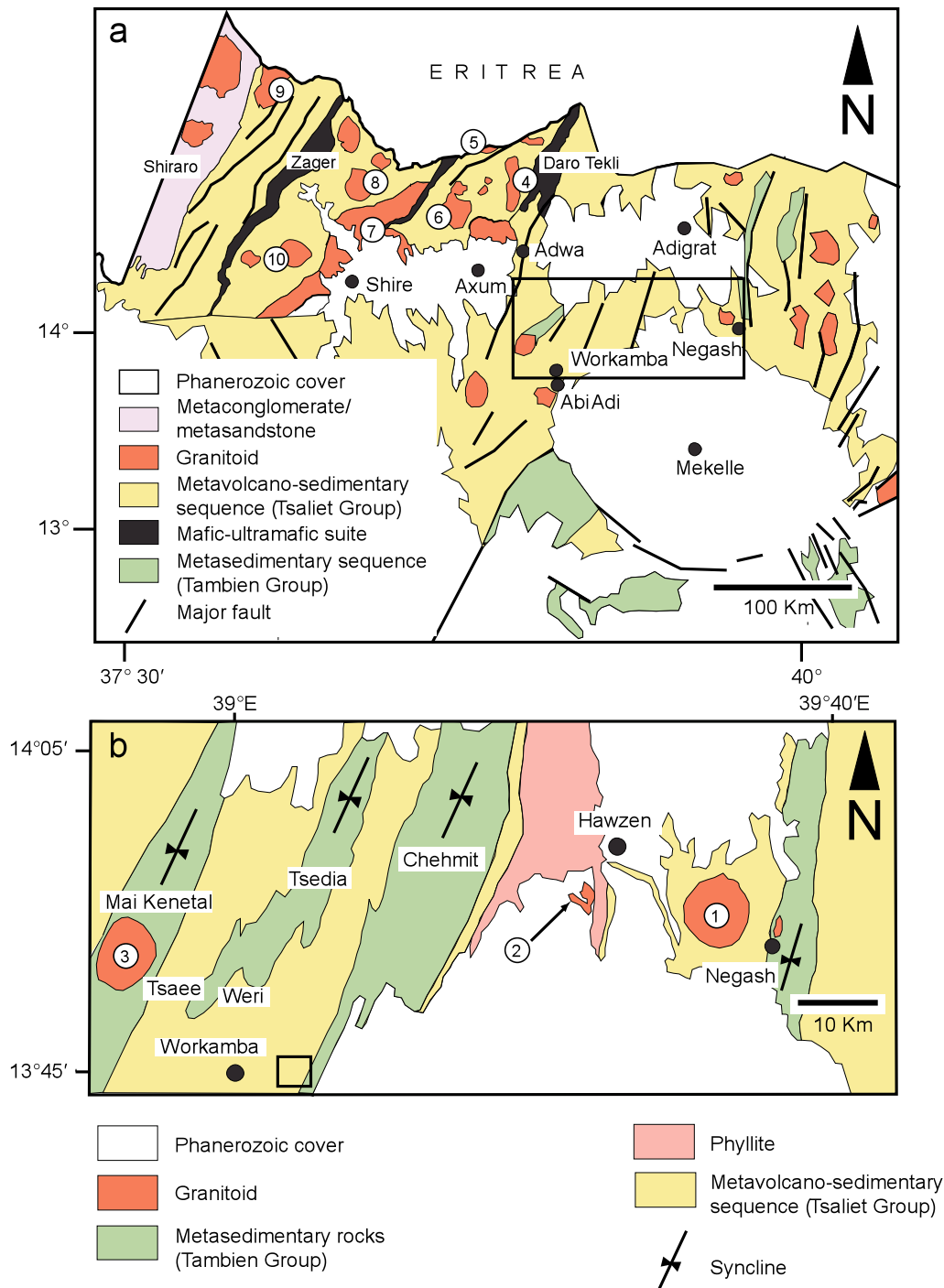


Fig. 2.5. a) Distribution of the Tsaliet and Tambien groups in the Tigray region, northern Ethiopia. The inset rectangle shows the region near the study area where the Tambien Group is exposed; b) Close-up of the area between Workamba and Negash. The Tambien Group occurs in four synclinoria inliers (modified from Tadesse et al. 2000; Asrat et al. 2001; Alene et al. 2006). The location of the study area is indicated. The circles with number represent the location of dated granitoids in the region, which are both syn- and post-tectonic in origin (1 = Negash, 2 = Hawzen, 3 = Mai Kenetal, 4 = Rama, 5 = Mereb, 6 = Chila, 7 = Shire, 8 = Deset, 9 = Azeho, and 10 = Sibta granitoids). Their ages are given in Table 2.1.

A greenish fine-grained sill intruding Tsaliet Group rocks in the Negash area yield a SHRIMP U-Pb zircon age of 774.7 ± 5.7 Ma (Avigad et al. 2007). The sill is interpreted to represent the youngest part of Tsaliet Group igneous activity (Avigad et al. 2007). The environment of deposition of the Tsaliet Group is shallow marine (Beyth 1972).

Various mafic- and ultramafic suites (e.g. the Zager and Daro Tekli belts) interpreted as supra-subduction zone ophiolites (Fig. 2.5a, Tadesse et al. 1999) and younger metaconglomerate/sandstone (Shiraro molasses, Tadesse et al. 1999, Fig. 2.5a) also occur associated with the Tsaliet Group rocks. Avigad et al. (2007) estimated the age of these younger metasedimentary rocks to be ~ 740 Ma from U-Pb dating of detrital zircons and suggested that they are preferentially derived from western Eritrea basement rocks.

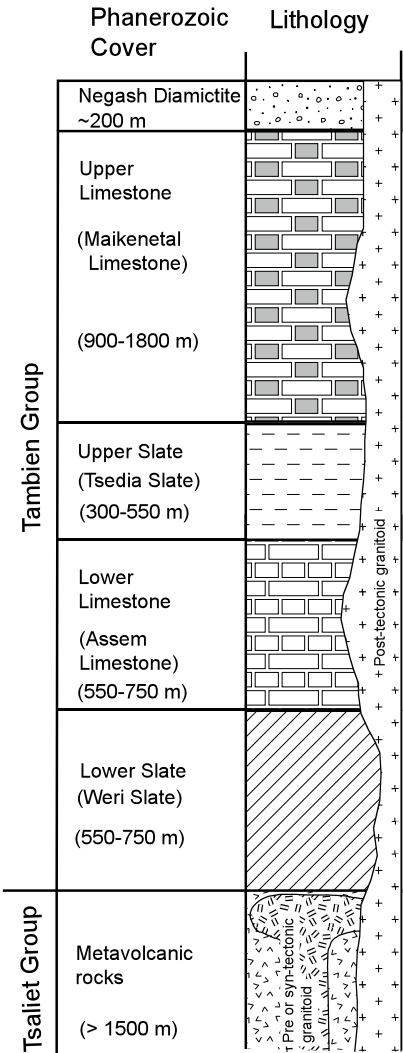


Fig. 2.6. Stratigraphic section of Tigray basement rocks showing relationship between the Tsaliet and Tambien group rocks. The pre- or syn-tectonic granitoids intruded the Tsaliet Group at about ~ 800 to 735 Ma, whereas the post-tectonic granitoids intruded both the Tambien and Tsaliet groups as well as the diamictites between ~ 620 and ~ 520 Ma (modified from Beyth 1972; Alene et al. 2006, Avigad et al. 2007). The names of the units of the Tambien Group are adapted from Beyth (1972).

The Tambien Group was deposited in a shallow marine environment during a period of regional arc-magmatic lull (Avigad et al. 2007). It is mainly exposed in a series of synclinal inliers surrounded by the Tsaliet Group rocks. These synclinoria are from west to east: Mai Kenetal, Tsedia, Chehmit, and Negash inliers (Beyth 1972; Alene et al. 2006, Fig. 2.5b). Based on tectonic reconstructions, Alene et al. (2006) estimate a thickness of ~2 to 3 km for the Tambien Group. The Mai Kenetal synclinorium contains the most complete sequence of the Tambien Group rocks, which are from bottom to top (Fig. 2.6): (a) the Lower Slate (Weri Slate), which mainly consists of black to blue-greenish, well laminated and foliated slate, greenish calcareous slate, and black silty greywacke. Locally, this unit contains phyllite or graphite schist (Beyth 1972); (b) the Lower Limestone (Assem Limestone) comprising mainly black to brown-greenish limestone (~90 wt. % calcite) with stromatolitic lamination and dark stylolites (Alene et al. 2006); (c) the Upper Slate on top of the Lower Limestone consisting of purple silty non-calcareous slate, greenish grey feldspathic slate, greenish grey vitreous slate, and greenish grey slaty marl (Beyth 1972); (d) the Upper Limestone, which is exposed at the core of the Mai Kenetal synclinorium. The Upper Limestone is black in color and composed of up to 95 wt. % calcite with minor amounts of detrital quartz, and albite (Alene et al. 2006). It may also contain detrital pyrite. Alene et al. (2006) estimate the age of the Tambien Group between 800 and 735 Ma based on $\delta^{13}\text{C}$ and $\delta^{18}\text{O}$ and $^{87}\text{Sr}/^{86}\text{Sr}$ characteristics.

In the Negash area, a dark grey to grayish-green pebbly slate, which could represent a lower glacial diamictite overlies the Upper Limestone (Miller et al. 2003). However, Avigad et al. (2007) suggested that it is not of glacial origin. They pointed out that the clasts in the diamictites are derived from proximal sources, i.e., the Tsaliet metavolcanics and related granitoids based on field characteristics and U-Pb dating of detrital zircons separated from the clasts and matrix. They also proposed that the Negash diamictite is younger than ~750 Ma and deposited at about the same time as the Shiraro molasses. This pebbly slate does not occur in the other inliers. Generally, the diamictites and Tambien Group rocks are weakly metamorphosed (Alene et al. 2006; Avigad et al. 2007). Peak of metamorphic temperatures in Tambien Group rocks are lower (i.e. at assumed temperatures of around 250°C) than those that experienced the Tsaliet Group rocks (Alene et al. 2006). The nature of the contact between the Tsaliet and Tambien groups is controversial. Beyth (1972) recognized an unconformable contact, whereas Alene et al. (1998) describe a conformable, gradational contact.

The Tigray basement rocks are intruded by I-type pre or syn- and post-tectonic granitoids (Tadesse et al. 1997; 1999, 2000; Alene et al. 2000, 2006; Asrat 2002, Avigad et al. 2007).

Table 2.1. Geochronological data of post- and pre- or syn-tectonic granitoids intruding the basement rocks of Tigray.

Locality Name	Sample No.	Granitoid type	Location	Method	Age (Ma)	Error (Ma)	Dated mineral	Source/ Remark
South Adigrat	TG32	Red granite		Ar-Ar	663.3	± 14.0	Muscovite	a
				Ar-Ar	565.2	± 10.0	Biotite	
				Ar-Ar	564.8	± 10.1	K-feldspar	
	TG22	Tonalite		Ar-Ar	665.8	± 13.0	Biotite	
	TG5	Tonalite		Ar-Ar	647.2	± 13.0	Biotite	
Negash		Granite		Pb-Pb	606	± 0.9	Zircon	b
	N914	Monzogranite		U-Pb	608	± 7	Zircon	c, l-p
	T3-11-10	Greenish volcanic rock sill	N13.94560°, E39.61816°	U-Pb	774.7	± 5.7	Zircon	J
Hauzien		Granite		K-Ar	583	± 16	Muscovite	d
		Granite		K-Ar	621	± 27	Biotite	
		Granite		Pb-Pb	613.4	± 0.9	Zircon	b
Mai Kenetal		Granite		K-Ar	~650		Muscovite	e J, p
				U-Pb	612.3	± 5.4	Zircon	
Adigrat		Granodiorite		K-Ar	582	± 22	Biotite	d
Axum-Adigrat Road	EE28	Red granite directly overlain by Jurassic sediment	N14° 16' 27.5" E39° 06' 15.2" 1964 m	Ar-Ar	600.3	± 10.7	Muscovite	a
				Ar-Ar	565.2	± 10.0	Biotite	
				Ar-Ar	564.8	± 10.1	K-feldspar	
North Axum	EE26	Granodiorite Leocogneisse lenses in to darker gneiss	N14° 20' 36.4" E38° 48' 36.2" 1522 m	K-Ar	570	± 31	Muscovite	a
				Ar-Ar	374.4	± 34.9	Biotite	
				Ar-Ar	742.8	± 12.8	K-feldspar	
North Axum	EE27	Metagranodiorite crosscutting the leoco gneiss lenses (EE26)	N14° 20' 36.4" E38° 48' 36.2" 1522 m	Ar-Ar	736.6	± 12.8	Biotite	a, s
				Ar-Ar	734.7	± 12.1	K-feldspar	
Mereb		Granodiorite Granite		K-Ar	690	± 4	Biotite	f, p
				Th-U-total Pb	524	± 14	Zircon	g, p
					Rb-Sr	633	± 62	WR
Rama	TT900	Granodiorite		Ar-Ar	745.3	± 4.1	Biotite	h, s
		Granitoid		Sm-Nd	793	± 51	WR; Pl, Bt + hbl	i, s
Chila	TT570	Granitoid		Th-U-Pb	806	± 21	Zircon	i, s
		Granodiorite		Ar-Ar	792	± 7.2	Hbl	h, s
Deset	KK1399	Granitoid		Th-U-Pb	757	± 30	Zircon	i, s
Shire	AG1117	Granite		Rb-Sr	559	± 22	WR	i, p
Sibta	TT950	Granite		Rb-Sr	550	± 35	WR	i, p
Azeho	GS1957	Granitoid		Sm-Nd	756	± 33	WR	i, s
	T4-7-1	Aplite microgranite	N13.89018° E39.41531°	U-Pb	784	± 14	WR	j, s

a = Mock et al. (1999), b = Miller et al. (2003), c = Asrat (2002), d = Garland (1980), e = Beyth (1972), f = Miller et al. (1967), g = Tadesse et al. (1997), h = Alemu (1998), i = Tadesse et al. (2000), j = Avigad et al. 2007, p = post-tectonic, l-p = late- to post-tectonic, s = pre- or syn-tectonic, hbl = hornblende, bt = biotite, WR = whole rock, and pl = plagioclase.

The deformation of the pre- or syn-tectonic granitoids is manifested by mylonitic fabrics (Tadesse et al. 2000). The pre- or syn-tectonic granitoids were mainly emplaced into the Tsaliyet Group, whereas post-tectonic granitoids intruded all the basement rocks (Fig 2.6). The geochronological data on intrusive rocks in the region are listed in Table 2.1. The ages of the pre- or syn-tectonic granitoids range from 800 to ~735 Ma, whereas that of post-tectonic plutons varies from ~620 to 520 Ma. The 690 ± 4 Ma K-Ar biotite age of Mereb post-tectonic granitoid (Miller et al. 1967) is not considered reliable and needs to be confirmed.

The ages of the pre- or syn-tectonic granitoids in Tigray are similar to those dated elsewhere in the ANS (e.g. 728.6 ± 0.6 Ma Konso charnockitic gneiss, southern Ethiopia, Teklay et al. 1998; 795 ± 14 Ma metagranitoid rocks of Ghedem sub-domain, Eritrea, Andersson et al. 2006; 763 ± 4 Ma Bagarah gneiss of Asir terrane, Saudi Arabia, Cooper et al. 1979; 653 ± 78 Ma granite gneiss of northeast Sudan, Stern and Kröner 1993; 634 ± 4 Ma granite gneiss of Aswan city, Sultan et al. 1994; 718 ± 9 to 808 ± 8 biotite to sillimanite bearing ortho- and para-gneisses of Somalia, Kröner and Passi 1996). Similarly, the age range of the post-tectonic granitoids overlaps with that of post-tectonic granitoids elsewhere in the ANS (e.g. the $541^{+10/-16}$ and 552 ± 49 Ma late-tectonic granites of western Ethiopia, Ayalew et al. 1990; 574 ± 12 to 613 ± 13 Ma post-tectonic granitoids of Red Sea Hills, northeast Sudan, Vail and Hughes 1977; 580 ± 24 Ma post-tectonic composite pluton of northeast Sudan, Stern and Kröner 1993; 652 ± 14 Ma post-tectonic pink granite of Jabal Um Achabe of Sudan, Kröner et al. 1991). These ages suggest contemporaneous arc-magmatism and crustal growth in the ANS (Tadesse et al. 2000).

2.1.3.2 Regional tectonic structure

The tectonic structures recorded by the Tsaliyet and Tambien group rocks are related to the collisional stress that resulted in the amalgamation of the ANS in Tigray. Generally, two phases of deformation (D1 and D2) are recognized (Alene et al. 2006). Deformation D1 is caused by N-S compression and resulted in tight minor folds with a wavelength of several mm to dm, elongation lineation and pervasive regional foliation (Alene et al. 2006). D2 deformation resulted from E-W directed compression at the waning stage of the collision between East and West Gondwana and yielded long wave length (about 8 km), upright, open parallel folds without a significant cleavage, thrust, and strike slip faulting (Fig. 2.7, Alene et al. 2006). The distribution of major structures in Tigray is shown in Fig. 2.7b. In western Tigray, NE to SW trending thrust faults and shear zones are identified within the low-grade

metavolcano-sedimentary sequences (Tadesse 1996; Tadesse et al. 1999). Major NE-SW oriented synclinoria such as the Mai Kenetal, Tsedia, Chehmit and Negash, which folded the Tambien Group rocks are present in central Tigray (Beyth 1972; Alene et al. 2006). NNE striking faults are also common in the Tsaliet and Tambien group rocks.

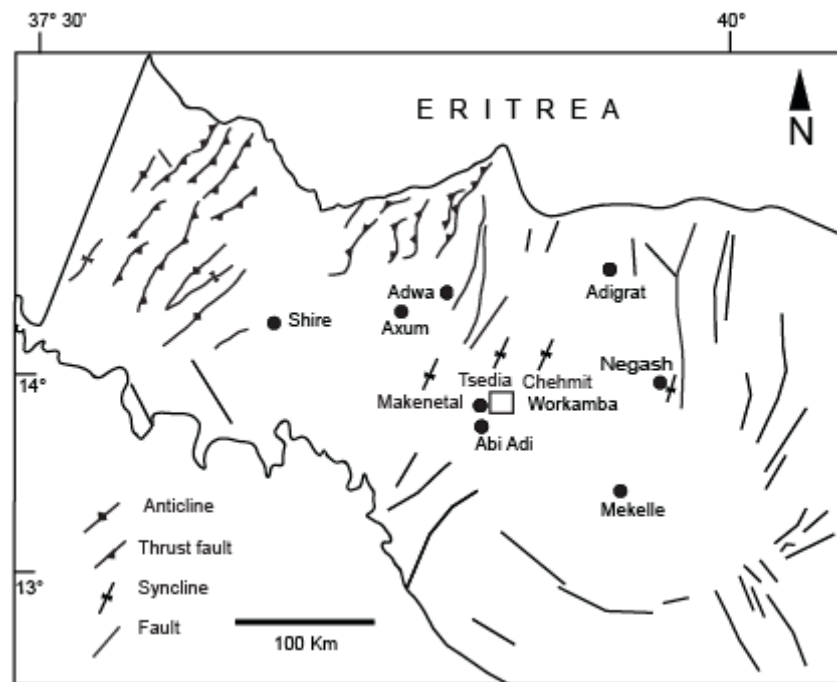


Fig. 2.7. Distribution of major tectonic structures in Tigray (modified after Tadesse et al 1996, 1999; Asrat et al. 2001). Inset square represents the study area.

2.2 Geology of the study area

The study area is part of the Chemit Inlier (Fig. 2.5 and 2.7), and rocks of both, the Tsaliet and Tambien groups are exposed (Fig. 2.8). The Tsaliet Group is represented by metavolcanic and volcanoclastic rocks as well as relatively massive quartz-sericite rock, which occupy the northwestern part of the area (Fig. 2.8). These are overlain by metasediments of the Tambien Group in the south east. Most of these rocks are sheared, foliated, and contain 1-2 m thick quartz veins, which are parallel to or cutting the foliation. Intrusive rocks in the study area are sills or dikes. They are emplaced roughly parallel to or cutting the foliation. They do not show evidence of deformation suggesting that they are related to post-tectonic magmatism. The list of samples collected, measured orientation data of different structures, the geographic location of the boreholes, drill core logging, and transmitted light microscope studies data are reported in Annexes 1.1 to 1.4.

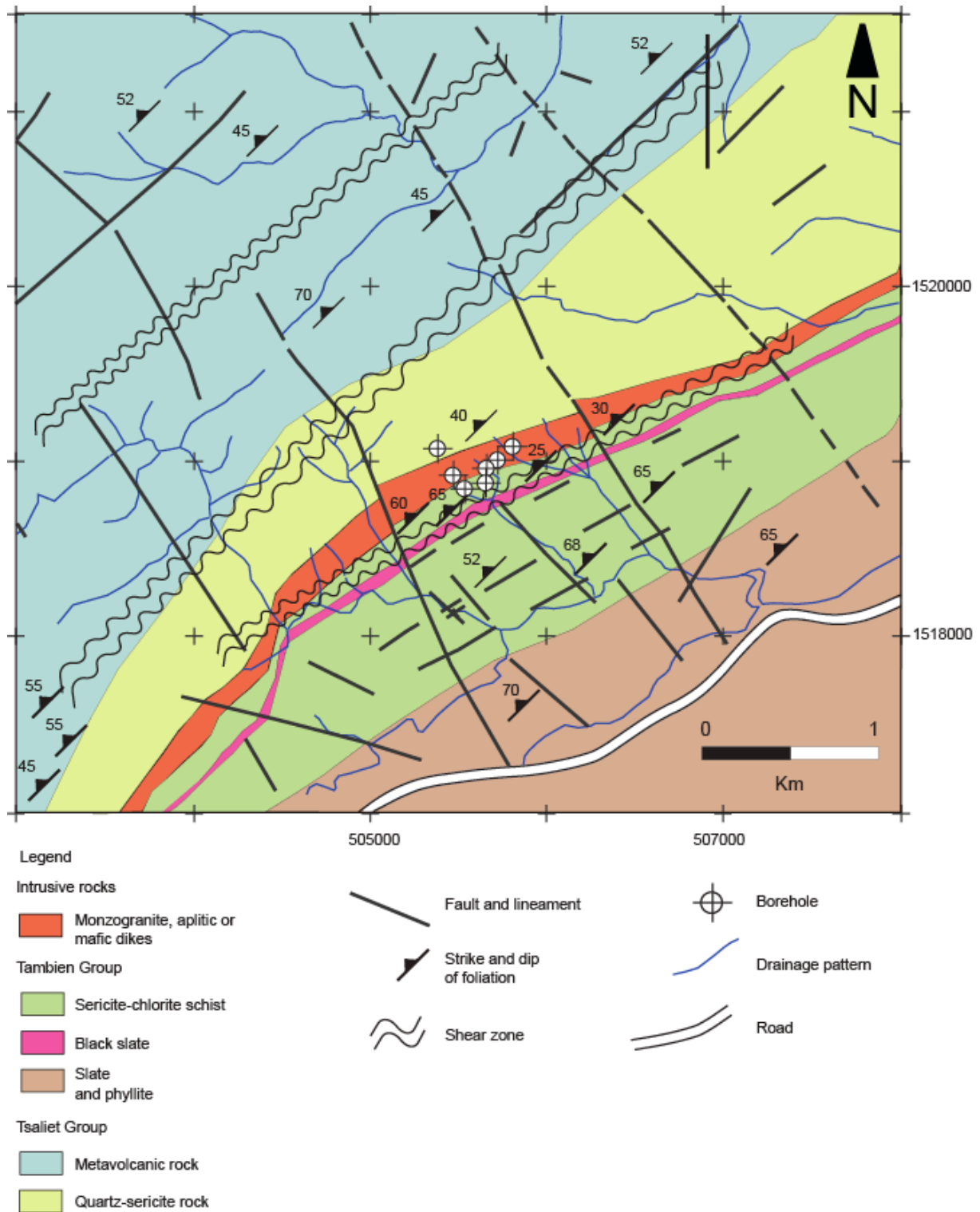


Fig. 2.8. Geological map of the study area (inset square in Fig. 2.5b). Mafic to intermediate metavolcanic rocks of the Tsaliyet Group crop out in the northwestern part, and massive quartz-sericite rock occur in a NE trending belt. Monzogranite dikes intruded the metasedimentary rocks near the contact between the Tsaliyet and Tambien groups. Thin layers of black slate (Tambien Group), quartz bearing sericite-chlorite schist; and alternations of slate and phyllite of the Tambien Group are exposed in the southeastern part of the area.

2.2.1 Tsaliet Group

2.2.1.1 Metavolcanic rock

Fine-to medium-grained metavolcanic rocks of the Tsaliet Group are exposed in the northwestern part of the study area (Fig. 2.8). Their colour varies from greenish to whitish grey. They are mainly composed of plagioclase, chlorite, epidote and quartz suggesting that they are metamorphosed products of mafic to intermediate volcanic rocks. In places, rounded to angular, 1-5 cm in size clasts of mafic to intermediate composition are found engulfed within the metavolcanic rocks (Fig. 2.9a). Thin layers of slate and phyllite occur as intercalations. The metavolcanic rocks have a gradational contact with the adjacent quartz-sericite rock.

2.2.1.2 Quartz-sericite rock

The quartz-sericite rock crops out east of the metavolcanic rock (Fig. 2.8). It is fine-grained, whitish-pink, and generally massive. A slight foliation is notable in the mineralized area. Thin (up to 5 cm) intercalated layers of chert are common. Numerous mm- to cm size quartz veins occur in it. The rock is composed of subhedral quartz (~50 vol. %), sericite (~45 vol. %), hematite (~3 vol. %), and biotite (~2 vol. %). It is a product of hydrothermal alteration. Textural characteristics and spatial relationships suggest that this rock represents a felsic volcanic rock of the Tsaliet Group. The quartz-sericite rock displays sharp contacts with the monzogranite dike located immediately east of it.

2.2.2 Tambien Group

2.2.2.1 Sericite-chlorite schist

Sericite-chlorite schists are exposed in the eastern central part of the study area (Fig. 2.8). They are greenish and have a fine- to medium-grained texture. Based on their mineralogical composition as estimated from thin section studies, they are categorized into two: (i) sericite-quartz-chlorite schist, which mainly comprises sericite (~50 vol. %, Fig. 2.10a), euhedral to subhedral quartz (~25 vol. %); anhedral biotite (~10 vol. %), chlorite (~15 vol. %), pyrite (~3 vol. %), and hematite (~2 vol. %, Fig. 2.10b). Locally, biotite and sericite form composite layers in alternating bands in sericite-quartz-chlorite schist (Fig. 2.10c). (ii) chlorite-quartz schist, which consists of chlorite (~50 vol. %, Fig. 2.10d); subhedral quartz (~30 vol. %); sericite (~10 vol. %); anhedral biotite (~5 vol. %), and opaques (hematite and pyrite, ~5 vol. %). The sericite-chlorite schists are foliated, sheared, and occur commonly intercalated with a less foliated or compact black slate layer (up to 30 m thick; Fig. 2.8), and thin (~20 cm thick)

layers of graphite schist. They also contain few lens-shaped of impure marble and vuggy talcose domains (Fig. 2.19b). The contact between these rocks and stratigraphically overlying slate and phyllite dominated unit is gradational.

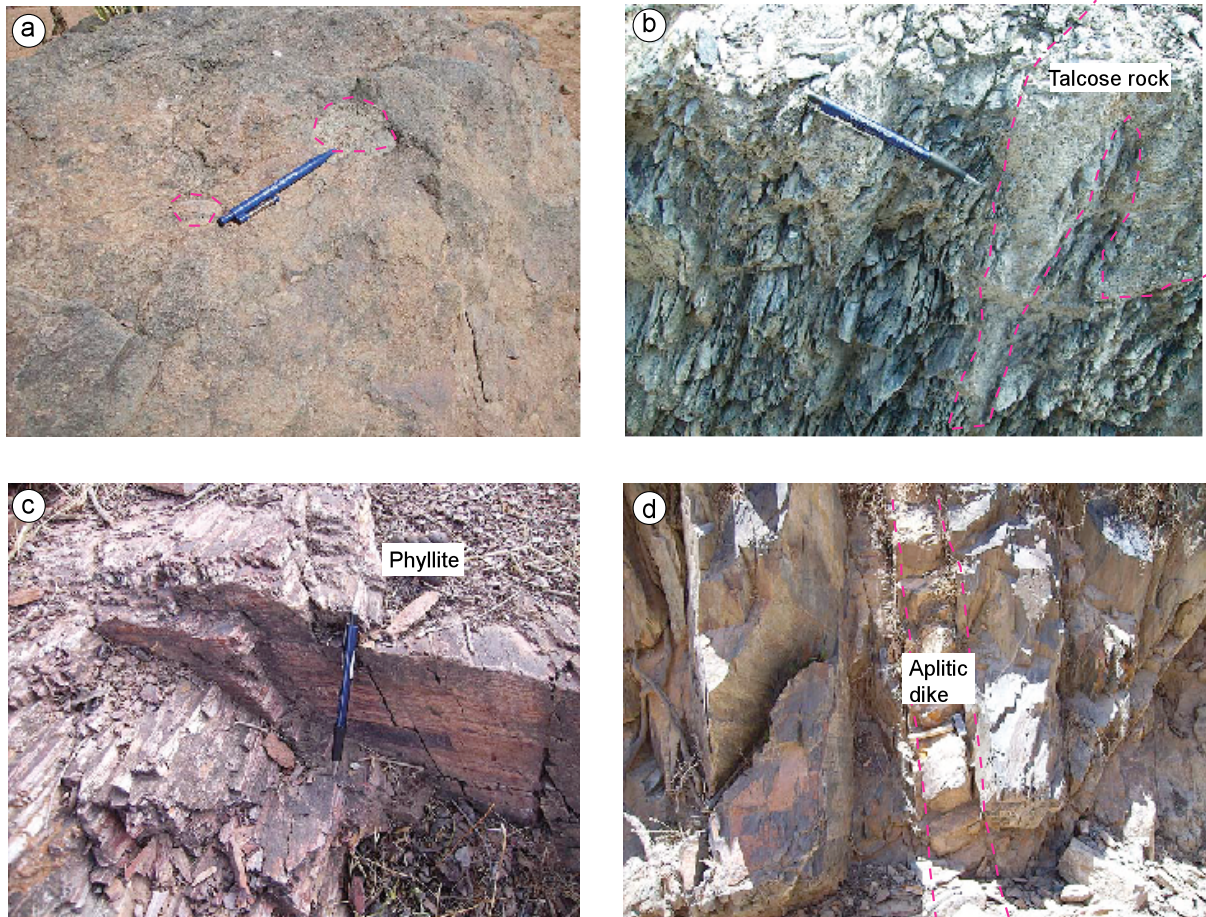


Fig. 2.9. a) North view on intermediate metavolcanic rocks with rounded (e.g. dashed circles) to angular clasts of 1-5 cm in size; b) Northeast view on whitish and vuggy talcose rocks intercalated in sheared sericite-chlorite schist. The vesicles in these rocks are mostly filled with Fe oxides (oxidized pyrite); c) Northeast view on pinkish and foliated phyllite showing horizontally laminated layers towards right (pen used as a scale); d) view towards northeast, outcrop in a stream bed of less foliated and compact black grey slate intruded by ~0.5 m thick vertical to sub vertical parallel aplitic dike (see hammer for scale).

2.2.2.2 Slate and phyllite

An alternating slate and phyllite sequence is exposed in the southeastern part of the study area (Fig. 2.8). The phyllite is pinkish, strongly foliated, feasible (Fig. 2.9c), and locally hematized with lustrous sheen, whereas the slate is greyish black and moderately foliated (Fig. 2.9d). Graphite schist, thin chert, and carbonate layers as well as sericite-chlorite schist are encountered as intercalations in this unit. The black grey colour and compact nature of the

slate are similar to that of Weri Slate (Tambien Group, Beyth 1972). Based on similar lithological characteristics and spatial relationships, it is correlated to the Weri Slate.

2.2.3 Intrusive rocks

Felsic and mafic intrusive rocks are observed in the study area. Felsic dikes/sills are of monzogranitic composition, whereas mafic intrusive rocks are classified as lamprophyres.

2.2.3.1 Monzogranite

Monzogranite dikes/sills intrude the basement rocks of the Tambien Group near its lower contact. They show medium to coarse-grained or fine-grained textures. A prominent coarse-grained, pinkish, and up to 100 m thick monzogranite dike/sill occurs in the stratigraphic footwall of the mineralized rocks (Fig. 2.8). It is mainly composed of euhedral to subhedral and coarse-grained K-feldspar (~30 vol. %), subhedral to anhedral, coarse- to medium-grained quartz (~25 vol. %), which is interstitial to K-feldspar, euhedral, up to 2 mm long coarse-grained plagioclase (~20 vol. %); subhedral biotite (~20 vol. %), and sericite (~4 vol. %). At least parts of the sericite are of hydrothermal origin as are other minor components such as calcite and hematite, which make up around 1 vol. %; Figs. 2.10e; 2.11). Fine-grained monzogranite dikes/sills are light coloured or whitish in colour. They may attain apparent thicknesses of up to 20 m in drill holes. Fine-grained monzogranite dikes/sills commonly contain no or minor biotite. However, there are exceptions. The fine-grained monzogranite bodies usually suffered more intense hydrothermal alteration than the coarse-grained monzogranite rocks, and therefore, contain variable quantities of e.g. sericite, calcite, chlorite, and also biotite. Locally, trace disseminated pyrite have been observed (e.g. sample J4-28). The fine-grained monzogranite dikes/sills are referred to as aplites in this work, though they do not strictly comply with the aplite definition (e.g. Fig. 2.9d).

2.2.3.2 Lamprophyre

Biotite-rich mafic dikes in the study area are classified as lamprophyres. They are only encountered in drill cores, where they reach an apparent thickness of about 3 m. The lamprophyres are composed of coarse- to medium-grained (up to 2 mm), euhedral to subhedral biotite phenocrysts (~55 vol. %, e.g. Fig. 2.10f) in a fine-grained groundmass. The groundmass mainly consists of K-feldspar (~30 vol. %), chlorite (~7 vol. %), calcite (~1 to 2 vol. %), quartz (~2 to 3 vol. %), epidote (~1 vol. %), and minor constituents such as hematite, and pyrite (~1 vol. %).

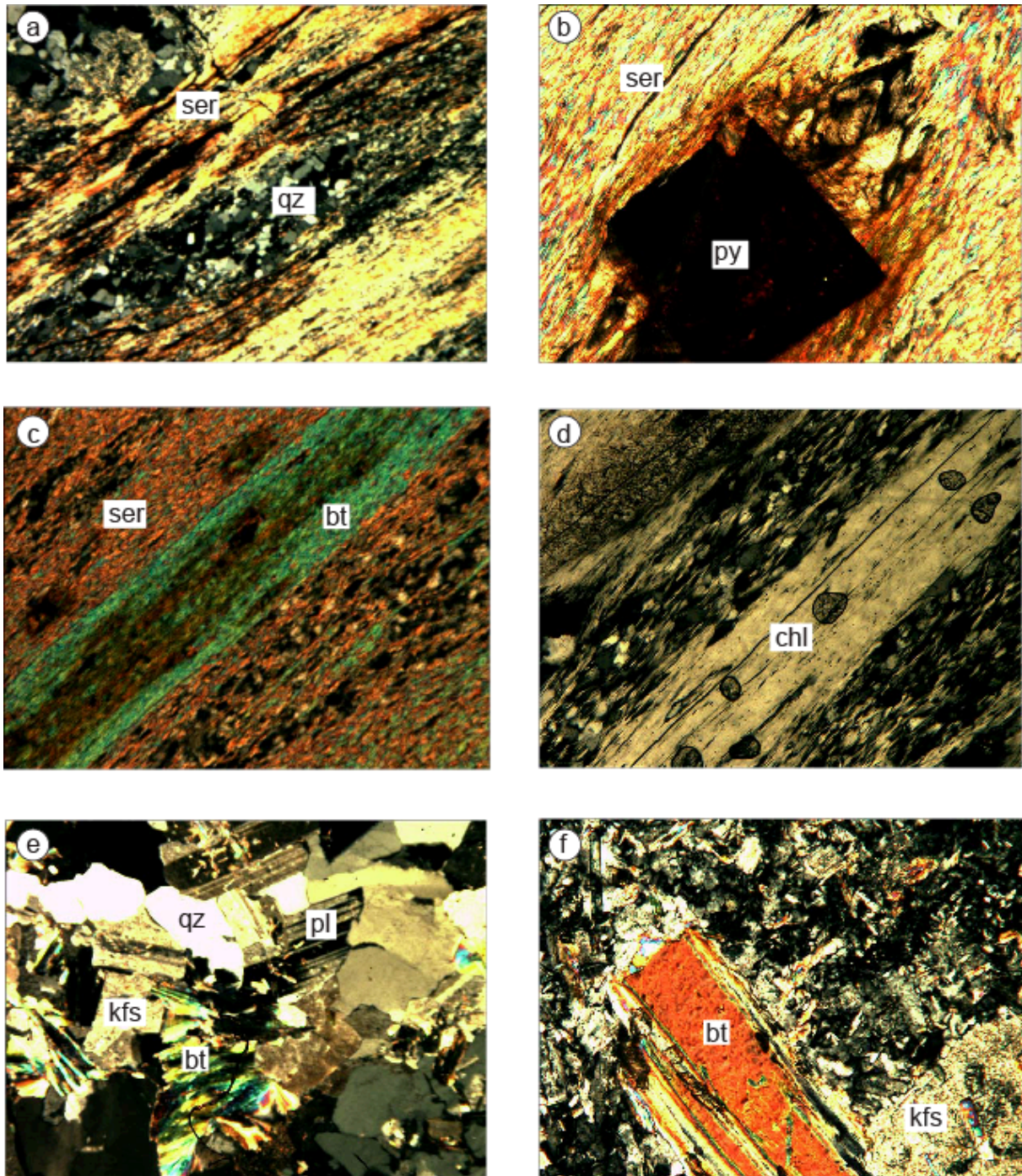


Fig. 2.10. Photo micrographs under crossed nicols. a) sericite-quartz-chlorite schist composed of sericite defining foliation planes, and aligned quartz; b) hematized pyrite within sericite-quartz-chlorite schist; c) sericite and biotite layers in sericite-quartz-chlorite schist; d) aligned coarse-grained chlorite defines the foliation of the chlorite-quartz schist; e) monzogranite, consisting of K-feldspar, plagioclase, subhedral biotite, and interstitial quartz; f) lamprophyre with biotite phenocrysts in a groundmass of mainly feldspar, biotite, muscovite, and quartz. Field of view for all micrographs is 0.6 mm. Abbreviations: chl = chlorite, pl = plagioclase, kfs = k-feldspar, ser = sericite, bt = biotite, py = pyrite, and qz = quartz.

Calcite is unevenly distributed in the rock. It occurs in clusters (e.g. sample GBH10-67) or as veinlets (sample J2-30, J5-13), and is of hydrothermal origin, as is pyrite. Hematite is interpreted as a supergene oxidation product of pyrite. The mineralogical composition of the lamprophyres is similar to that of calc-alkaline kersantites type lamprophyres (e.g. Rock 1990; Nockolds et al. 1978).

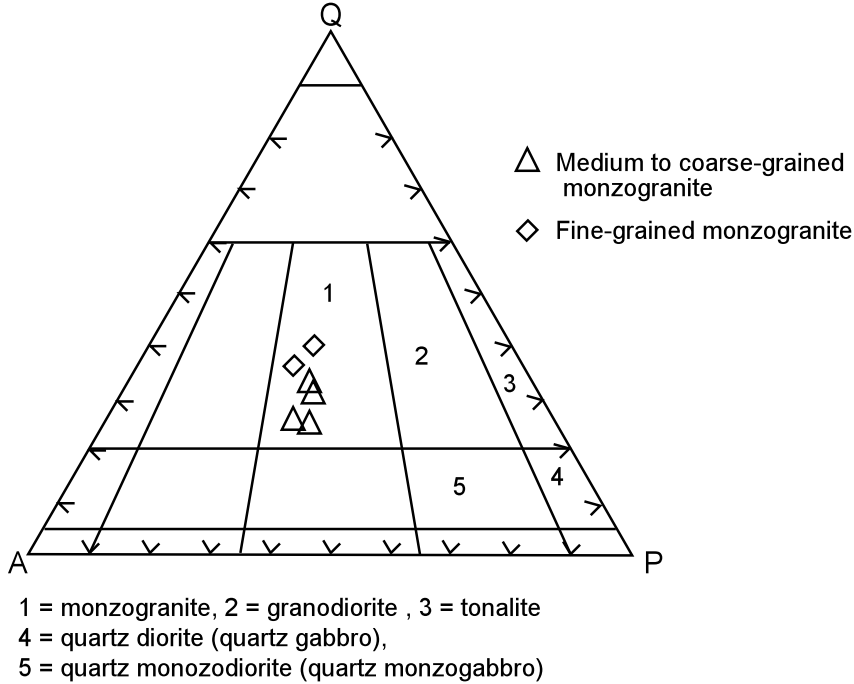


Fig. 2.11. QAP classification diagram of Streckeisen (1976), showing the monzogranitic composition of the monzogranite dikes/sills in the study area.

2.2.4 Structural elements in the study area

Both, ductile and brittle tectonic structures are present in the region. The structural pattern of the study area is dominated by: (i) regional scale, N40°E striking foliation, (ii) NE striking shear zones, and (iii) NW striking brittle faults (Fig. 2.12). In addition, other types of structures, such as slickensides, folds, joints and fractures, and small shear zones were observed in different localities of the study area.

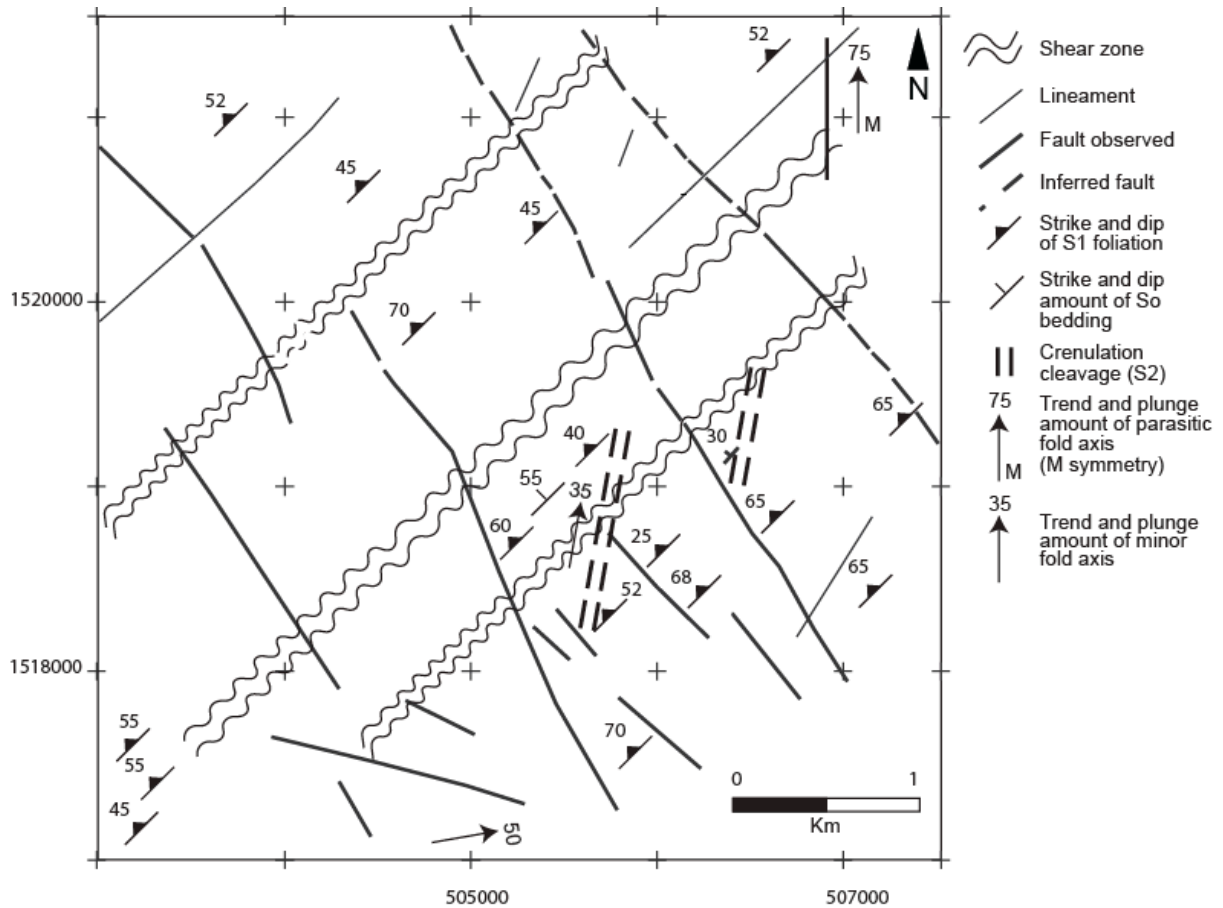


Fig. 2.12. Map showing the various brittle and ductile structures in the study area.

2.2.4.1. Foliation

The Tambien and Tsaliet Group rocks of the study area are affected by well developed penetrative foliation. This foliation commonly strikes N40°E with a dip of about 25 to 80°W.

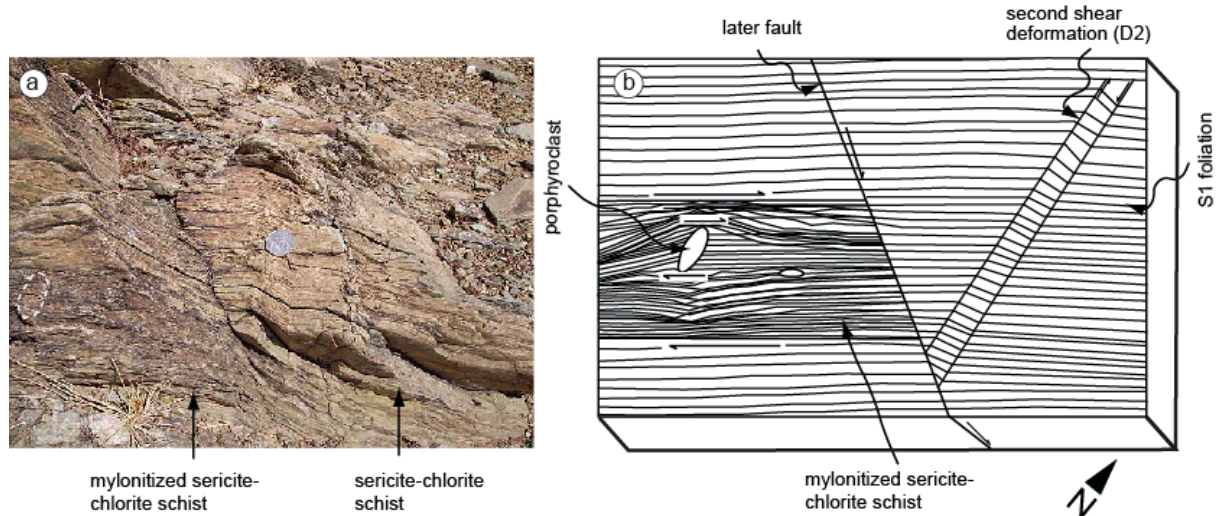


Fig. 2.13. a) Plan view on a rock domain showing relationships between S1 foliation, weakly developed second shear deformation, mylonitization, and later brittle fault in the sericite-chlorite schist. White dashed circle show feldspar porphyroclast used as a kinematic indicator; b) hand sketch (not to scale) interpretation of the relationship between the different generations of structures shown in Fig. 2.13 a).

It is defined by the alignment of micas in the Tambien Group metasedimentary rocks, and chlorite and feldspar in the Tsaliet Group metavolcanic rocks (Fig. 2.13a and b). The foliation is correlated with the regional D1 deformation, which was caused as a result of N-S compression (Alene et al. 2006).

2.2.4.2. Shear zones

Shear zones are defined by up to 200 m wide zones of increasing density of foliation planes within the foliated country rocks (Fig. 2.13). Mylonitic domains are observed in some places (e.g. Fig. 2.13) within the shear zones. The shear zones commonly contain closely spaced quartz veins, which are parallel to the NE strike of the shear zones (Fig. 2.14). They locally host en-echelon tension gashes with sinistral sense of shear, which are commonly interpreted to represent brittle-ductile deformation (e.g. McClay 1987; Twiss and Moores 1973). The tips of en-echelon tension gashes provide constraints on the stress pattern as the minimum compressive stress (σ_3) is perpendicular to any unrotated part of the gash fractures (Twiss and Moores 1973; Fig. 2.15). Based on this, the direction of maximum principal compression stress (σ_1) in the study area is N-S. This is similar to the orientation of regional compressive stress, which resulted in D1 deformation (e.g. Alene et al. 2006). Therefore, the NE oriented brittle-ductile shear zones are correlated to D1 deformation. Manifestations of a weakly developed, second shear deformation phase are observed at various places (Fig. 2.12).



Fig. 2.14. Major NE trending shear zone containing closely spaced quartz veins (view towards N).

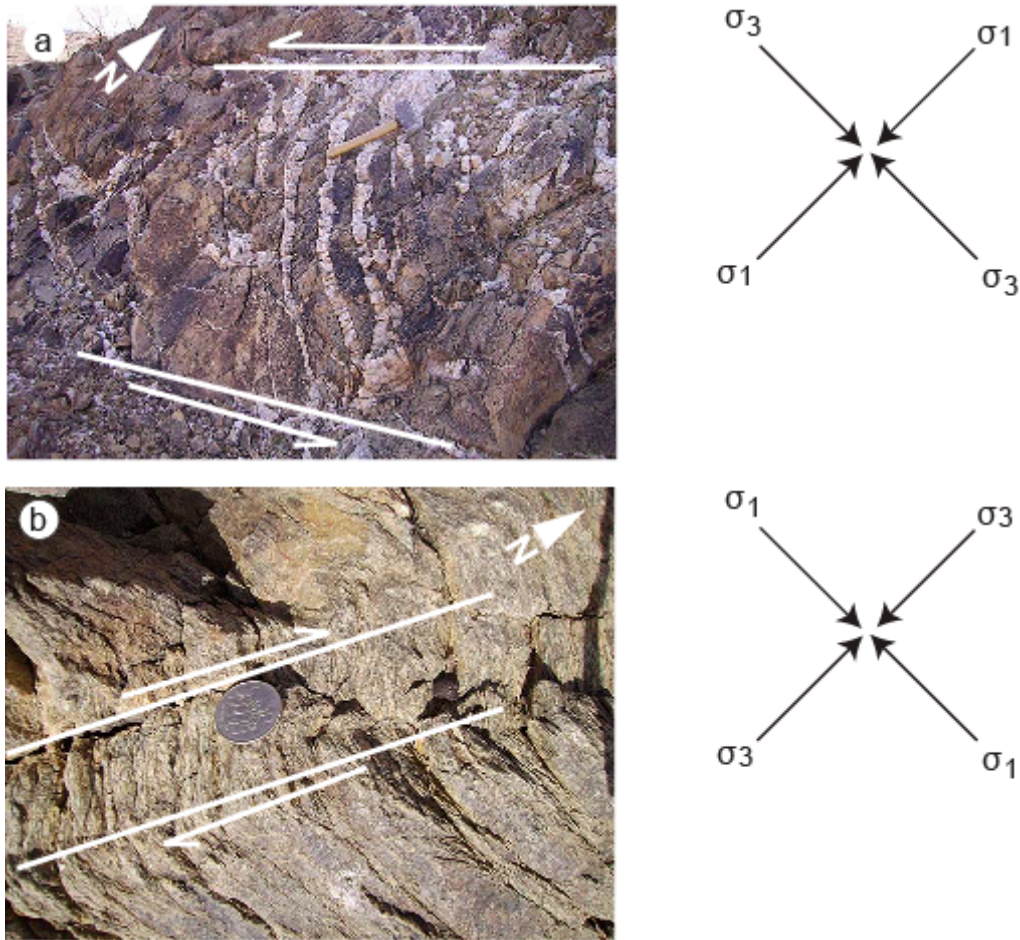


Fig. 2.15. a) View towards N, showing NE oriented sinistral brittle-ductile shear zone, which is manifested by quartz filled tension gashes and correlated with D1 deformation; b) view on a small scale NNE trending dextral ductile shear correlated with D2 deformation.

These are relatively small (up to 5 cm), well defined NNE elongated zones, in which the foliation is locally rotated clockwise by about 45° relative to the strike of the major shear zone and regional foliation trend (Fig. 2.15). These NNE oriented shearing, therefore, has a dextral sense of shear (Fig. 2.15a) and is correlated with the D2 deformation of Alene et al. (2006) caused by E-W compression.

2.2.4.3 Folds

Two types of folds occur in the study area. A fold with a fold axis plunging 50° ENE has been observed in the Tambien Group rocks exposed in the southern part of the study area (e.g. Fig. 2.16a). The orientation of the fold is compatible with N-S oriented D1 shortening (Alene et al. 2006). The other folds are parasitic folds with a fold axis plunging 75° N (e.g. Fig. 2.16b).

The orientation of the fold axes of these parasitic folds suggests that they are related D2 deformation due to E-W shortening (Alene et al. 2006).

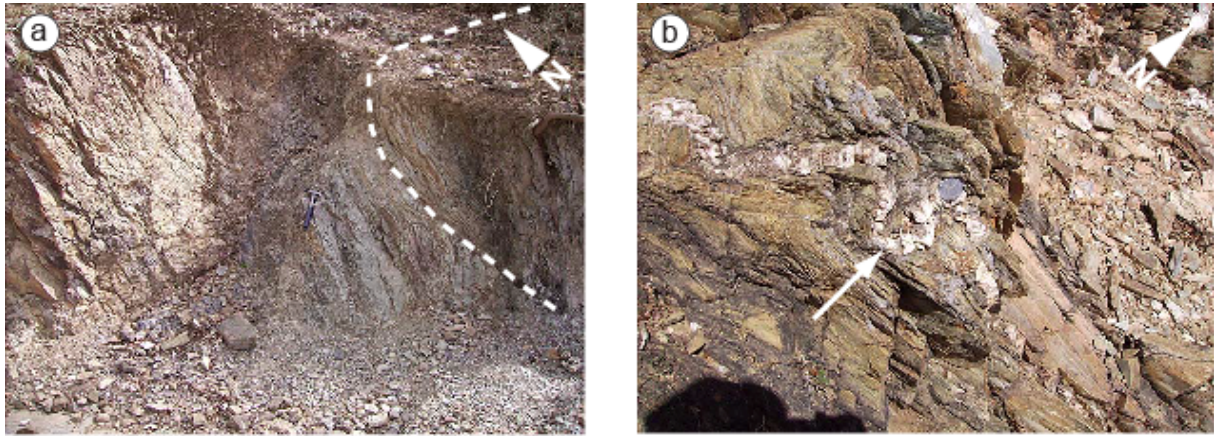


Fig. 2.16. a) View to the SE on a NWW-SEE trending fold which folded the layers of the slate and phyllite unit (Tambien Group) and is correlated with D1 deformation; b) view to the N showing parasitic fold (folded quartz vein, white arrow) with N-S trending fold axis, which are related to D2 deformation.

2.2.4.4 Faults

Northwest trending brittle faults cut the rocks of the Tsaliet and Tambien Groups and the dikes/sills (Figs. 2.12, and 2.13). They post-date D1 and D2 deformations, quartz-calcite veins, and mineralization. The fault planes strike approximately N30-60°W and dip 30 to 60 E (e.g. Fig. 2.13). The lateral component of displacement (ΔL) in the mineralized zone is sinistral and in the order of 25 to 45 m.

2.2.4.5 Joints, fractures and lineations

East to west trending vertical to subvertical joints and fractures cut the Tsaliet and Tambien Group rocks (e.g. Fig. 2.17). They are dense and closely spaced in the sheared rocks near to the mineralized zone and sparse outside of it. Some of the joints and fractures are filled by quartz or quartz-calcite veins. Northeast trending lineations, quartz boudins, NNE-SSW trending slickenlines, and elongated pebbles/clasts also occur in the study area. The quartz boudins are found within the sheared sericite-chlorite schist. The elongated pebbles/clasts and slickenlines have been observed mainly in the metavolcanic rocks. The orientation of the lineations is subparallel to the S1 foliation suggesting that these lineations are formed by D1 deformation.



Fig. 2.17. An example of E-W trending joints and fractures cutting phyllite (view towards W).

2.2.5 Quartz veins

Two generations of quartz veins were observed. The first generation are thin (~1-5cm thick), and folded occurring in the northern and southern parts of the study area mainly within the quartz-sericite rock and sericite-chlorite schist (Fig. 2.16b).

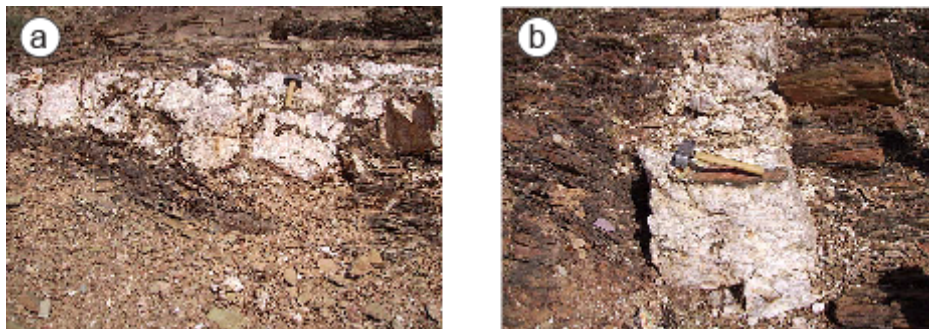


Fig. 2.18. Showing examples of the second generation quartz veins found in the study area, which are up to 2 m thick a) occurring parallel to the foliation; b) cutting the foliation. The rock which is affected by the veins is phyllite. Hammer is used as scale.

The second generation quartz veins are abundant throughout the study area and occur in the form of vein swarms with higher density in the shear zones. Their thickness ranges from 0.5-2 m. They occur parallel to (Fig. 2.18a) and/or cut the foliation (Fig. 2.18b) as well as D2 folds at an angle of ~30-60°. Some of the concordant quartz veins tend to develop boudins (Fig. 2.18a).

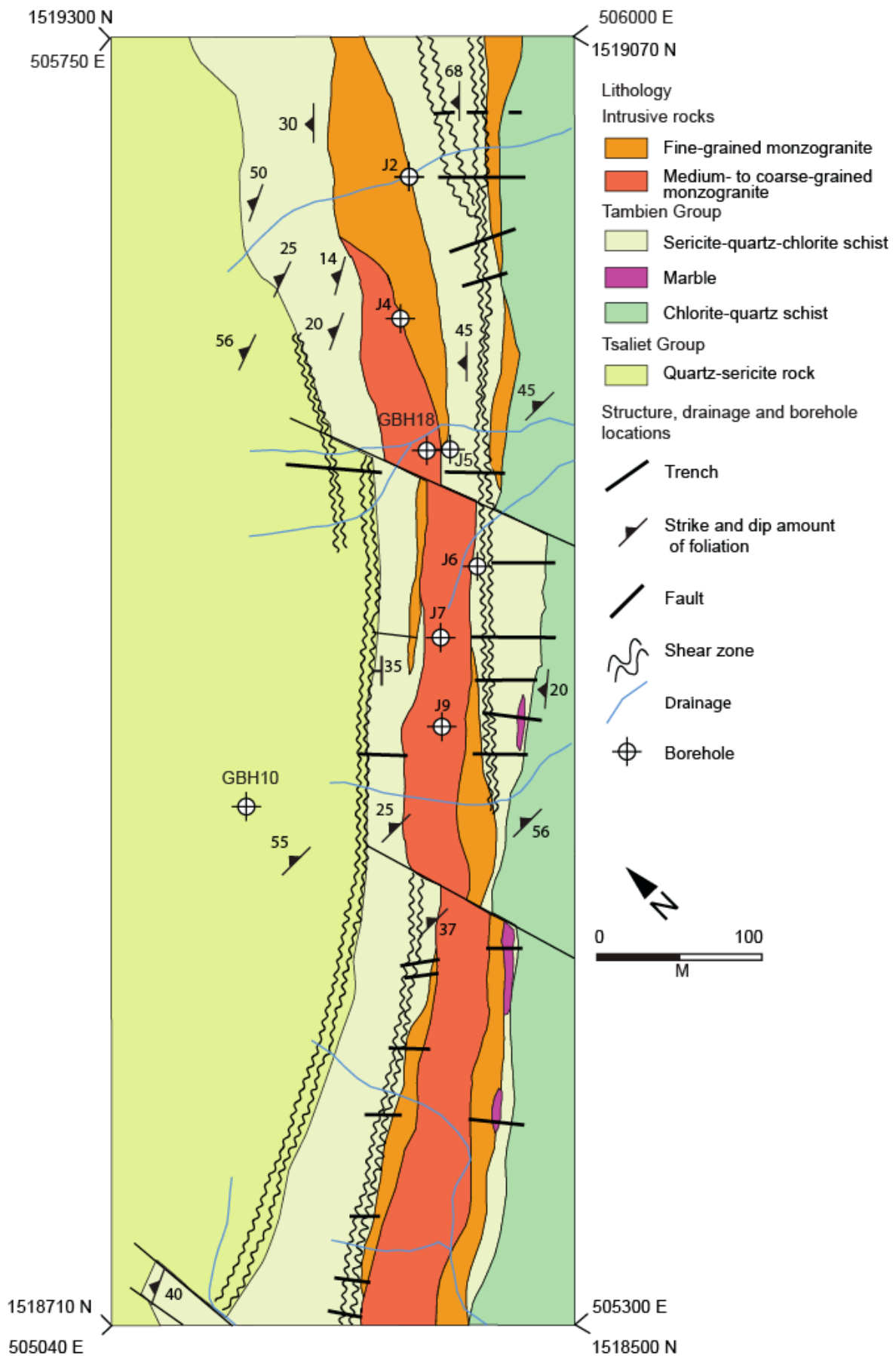


Fig. 2.19. Geological map of the mineralized zone together with the location of trenches and boreholes drilled by the exploration company (based on a map by the National Mining Corporation 2006).

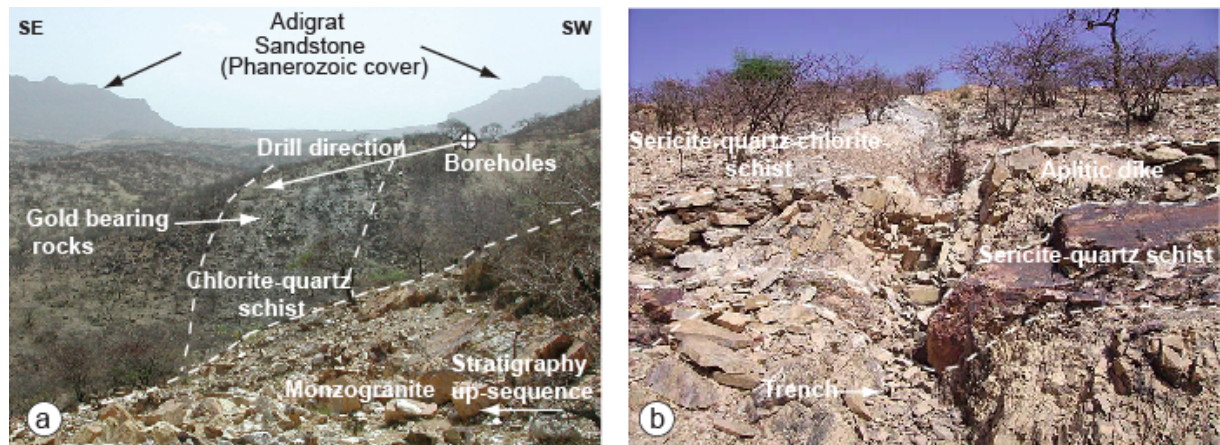


Fig. 2.20. a) Southwest view on the mineralized zone showing the gold-bearing low-grade metasedimentary rocks of the Tambien Group. The apparent thickness of the chlorite-quartz schist is ~50 m. Cliffs of the Mesozoic Adigrat Sandstone are shown in the background. The strata dip towards the NW. Stratigraphic relationships are youngest rock at the left-hand side of the image; b) West view of one of the exploration trenches cutting the sericite-quartz-chlorite schist (with apparent thickness of ~100 m). These silicified metasedimentary rocks are intruded by a fine-grained monzogranite (aplite).

2.2.6 Geology of the mineralized zone

The geology of the mineralized (drilled) zone is shown in Fig. 2.19 and 2.20. In the west, the quartz-sericite rock (Tsaliet Group) is exposed. The sericite-quartz-chlorite schist (Tambien Group), which is intruded by monzogranite dikes/sills, occupies the central part of the mapped area. The contact between the Tsaliet Group (quartz-sericite rock) and the Tambien Group (sericite-quartz-chlorite schist) is obscured as it is tectonically disturbed by the NE trending shear zone. The chlorite-quartz schist crops out in the eastern part of the mineralized zone. The sericite-quartz-chlorite and chlorite-quartz schists are stratigraphically equivalent to the Lower Slate or Weri Slate (Fig 2.6, Beyth 1972). Marble lenses locally occur dispersed in the sericite-quartz-chlorite schist or at the contact between the schist and fine-grained monzogranite (Fig. 2.19).

2.2.7 Down-hole geology

The down-hole geology of the mineralized zone is illustrated by the borehole logs shown in Fig. 2.21. Data on the drillholes are given in Annex 1.3. The stratigraphic sequence is inverted with older rocks at shallow levels younging down-hole. The quartz-sericite rock represents the oldest rock in the stratigraphic sequence. It is overlain by alternating sericite-quartz-chlorite and chlorite-quartz schists. The monzogranite dikes/sills are encountered at variable

depths. Lamprophyres apparent thicknesses between 1 to 3 m have been penetrated by three holes in the northeastern part of the drilled area.

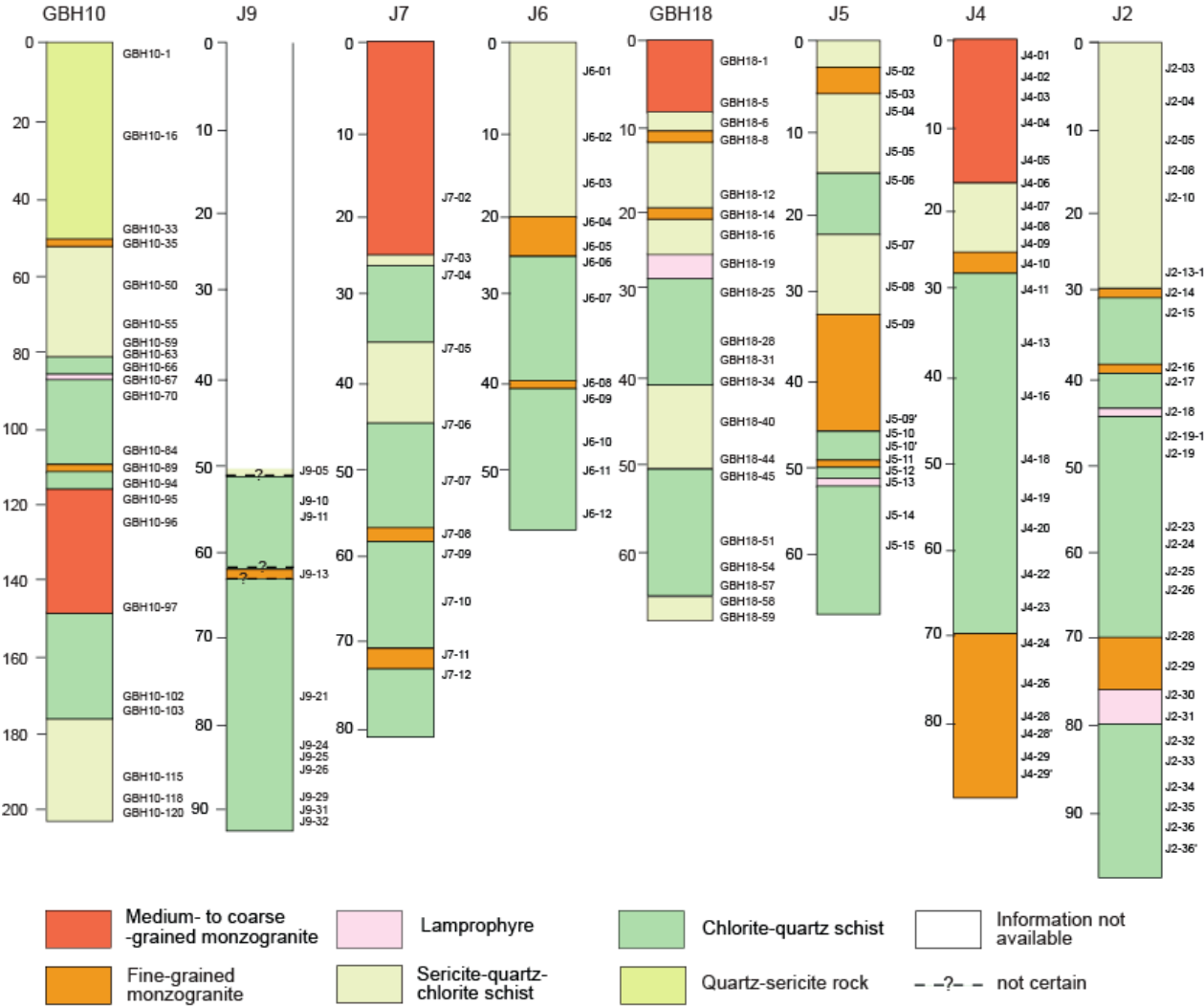


Fig. 2.21. Drillcore logs showing the down-hole geology of the prospect area (note that borehole sections are inverse to stratigraphy). The numbers at the left side of the sections indicate the depth in meter and sample numbers are listed at the right side. The log of borehole J9 is unavailable. Rocks units shown are based on drill core samples provided by the National Mining Corporation.

3. Geochemistry

3.1 Analytical methods

Twenty surface and core samples (barren and mineralized) have been analysed for their chemical composition. The surface samples include three samples from the monzogranite dikes/sills, and a sample from each of the black slate, a mafic metavolcanic rock, and a sericite-chlorite schist. Ten core samples are from metasedimentary rocks (sericite-quartz-chlorite schist, chlorite-quartz schist and carbonatized chlorite-quartz schist), two from aplite dikes/sills and two from lamprophyric dikes. The analysis for major and trace elements was carried out in Activation Laboratories (ACTLABS), Canada, using a combination of fusion ICP-MS and INAA. The precision of the geochemical data is equal to or better than 0.07 %. The results are listed in Tables 3.1 and 3.4, respectively. Whole rock geochemistry data of intrusive and metasedimentary rocks of Tigray region, which are compiled from previous works for comparison with this study are reported in Annexes 2.1 to 2.7.

3.2 Major and trace element abundance in metasedimentary rocks

The major element composition of the metasedimentary rocks of the study area are similar to those of Weri metasedimentary rocks (e.g. Weri2 metasediments of Sifeta 2003; Tables 3.1), except a sample showing anomalous high SiO₂ value of 85.98 wt. % (sample J2-023) and a sample with a CaO concentration of ~43 wt. % (sample J2-034), which are due to silicification and carbonatization, respectively. The trace element concentrations in the sericite-quartz-chlorite and chlorite-quartz schists of the study area are inhomogeneous (Table 3.1). The carbonatized chlorite-quartz schist, black slate, and mafic metavolcanic rock have Rb, Ba, Th, Nb, and Zr contents, which are lower than the sericite-quartz-chlorite and chlorite-quartz schists (Table 3.1).

3.3 Element mobility in Workamba metasedimentary rocks

Mass balance calculations of the metasedimentary rocks of the study area were conducted based on the isocon method to assess the mobility of elements during the hydrothermal event(s) and to determine which elements are suitable for petrogenetic interpretation (Gresens 1967; Grant 1986). The slope of the isocon is obtained by dividing the mass of an unaltered rock sample (M^i) to the mass after alteration (M^f), i.e., (M^i / M^f). The median

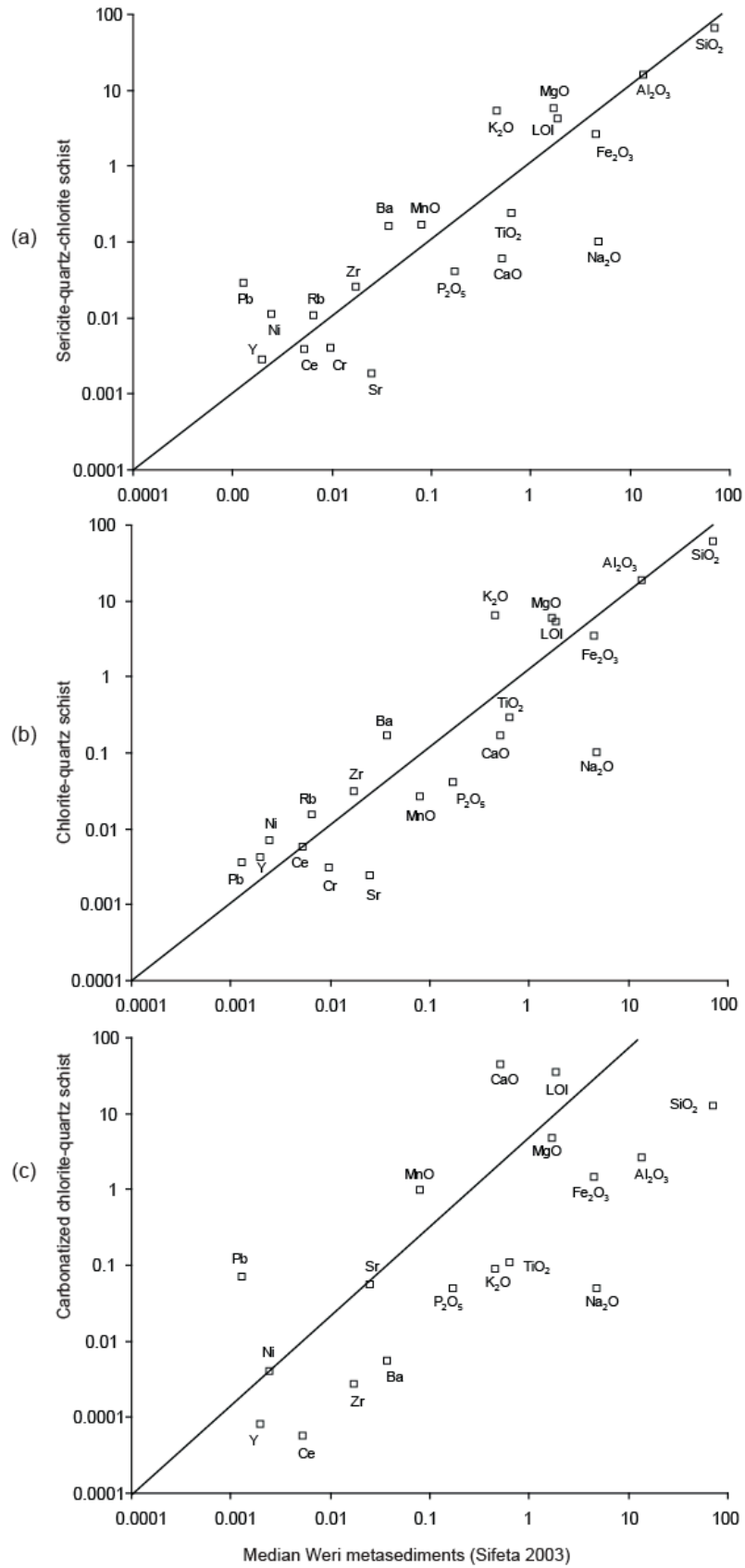


Fig. 3.1a-c. Isocon diagrams showing element contents of metasedimentary rocks of the study area vs. median composition of Werri metasedimentary rocks of Sifeta (2003). A deviation from the isocon suggests an increase or depletion of a particular element relative to the reference rocks, which is taken to assess a measure of element mobility.

Table 3.1. Major (wt. %) and trace element (ppm) compositions of the metasedimentary rocks at Workamba. Abbreviations: carb = carbonatized; chl = chlorite; ser = sericite; qtz = quartz; MV = metavolcanic; b.d. = below detection limit; n.d. = not determined

Rock type	Chl-qtz schist			Ser-qtz- chl schist	Carb chl- qtz schist	Ser-chl schist	Black slate	Mafic MV	Detection limit
Sample No.	J2-15	J2-19	J2-23	J2-05	J2-34	TG06015	TG06034	TG06007	
SiO ₂	56.18	59.71	85.98	66.30	12.63	n.d.	n.d.	n.d.	0.01
Al ₂ O ₃	14.24	18.75	5.44	15.70	2.59	n.d.	n.d.	n.d.	0.01
Fe ₂ O ₃ (T)	2.61	3.37	1.04	2.64	1.45	n.d.	n.d.	n.d.	0.01
MnO	0.10	0.03	0.10	0.17	0.99	n.d.	n.d.	n.d.	0.001
MgO	17.80	5.98	2.94	5.61	4.63	n.d.	n.d.	n.d.	0.01
CaO	0.09	0.17	0.05	0.06	43.05	n.d.	n.d.	n.d.	0.01
Na ₂ O	0.04	0.10	0.06	0.10	0.05	n.d.	n.d.	n.d.	0.01
K ₂ O	1.49	6.51	1.53	5.23	0.09	n.d.	n.d.	n.d.	0.01
TiO ₂	0.21	0.29	0.08	0.23	0.11	n.d.	n.d.	n.d.	0.001
P ₂ O ₅	0.03	0.04	0.03	0.04	0.05	n.d.	n.d.	n.d.	0.01
LOI	7.54	5.28	2.24	4.21	34.33	n.d.	n.d.	n.d.	
Total	100.30	100.20	99.50	100.20	99.98	n.d.	n.d.	n.d.	
Trace and rare earth elements									
Ba	377	1639	668	1581	55	222	69.2	33.1	3
Rb	38	167	44	136	b.d.	3.7	2.1	0.9	2
Th	8.2	9.6	2.6	7.7	0.7	1.5	2.2	0.5	0.1
U	2	6.8	0.9	0.9	0.8	0.1	0.1	b.d.	0.1
Nb	7	9	2	7	1	b.d.	b.d.	b.d.	1
Ta	0.6	0.8	0.2	0.6	b.d.	b.d.	b.d.	b.d.	0.1
Sr	10	24	7	18	546	71.7	14.8	73.4	2
Zr	245	309	85	249	27	1.8	5.6	0.8	4
Hf	6.8	8.7	2.3	6.6	0.8	b.d.	0.1	b.d.	0.1
Y	32	42	15	28	8	4.13	6.31	5.01	2
V	b.d.	6	6	b.d.	13	7	28	77	5
Cr	20	30	190	40	b.d.	2.8	57.3	16.7	20
Co	b.d.	1	2	b.d.	b.d.	5.5	16.5	32.2	1
Ni	50	70	480	110	40	5.4	31.1	18.6	20
Pb	15	36	1130	288	700	3.62	0.29	0.92	5
Cs	0.8	3.3	0.9	2.5	b.d.	0.1	0.2	b.d.	0.5
Sc	4	5	1	5	2	0.7	5.1	5.1	0.1
La	21.4	25.1	6.1	19.3	3.1	10.3	13.4	3.3	0.1
Ce	42.9	57.3	14.9	38	5.7	18.8	32.3	8.41	0.1
Pr	5.81	7.24	1.87	4.69	0.7	2.4	3.8	1.1	0.05
Nd	23	28.4	7.8	17.6	2.9	8.1	14.7	4.67	0.1
Sm	5.4	6.7	1.8	3.8	0.7	1.3	3.1	1.1	0.1
Eu	0.82	1.42	0.33	0.5	0.43	0.3	0.9	0.3	0.05
Gd	5.3	6.7	2.3	3.4	0.8	1.1	2.6	1	0.1
Tb	0.9	1.2	0.4	0.7	0.1	0.1	0.3	0.2	0.1
Dy	5.6	7.3	2.5	5.2	1	0.8	1.6	1	0.1
Ho	1.2	1.5	0.5	1.1	0.2	0.2	0.3	0.2	0.1
Er	3.8	4.8	1.6	3.6	0.8	0.4	0.6	0.6	0.1
Tm	0.63	0.77	0.26	0.59	0.13	0.1	0.1	0.1	0.05
Yb	4.2	5.2	1.7	4	1	0.2	0.4	0.5	0.1
Lu	0.65	0.81	0.25	0.62	0.17	b.d.	b.d.	b.d.	0.04
Eu/Eu*	0.4	0.65	0.5	0.43	1.78	0.76	0.97	0.89	
(La/Yb)N	3.41	3.23	2.4	3.2	2.07	34.44	22.4	4.4	
ΣREE	121.61	154.44	42.31	103.1	17.73	44.1	74.1	22.48	n.d.

Table 3.1. Continued.....

Rock type	Chl-qtz schist			Ser-qtz- chl schist	Car. chl- qtz schist	Ser-chl schist	Black slate	Mafic MV
Sample No.	J2-15	J2-19	J2-23	J2-05	J2-34	TG06015	TG06034	TG06007
Th/Sc	2.05	1.92	2.6	1.54	0.35	2.14	0.43	0.1
Zr/Sc	61.25	61.8	85	49.8	13.5	2.57	1.1	0.12
Ti/Zr	4.9	5.4	5.5	5.4	23.01	n.d.	n.d.	n.d.
La/Sc	5.4	5.02	6.1	3.86	1.55	14.7	2.6	0.65
Zr/TiO ₂	0.12	0.11	0.1	0.11	0.02	n.d.	n.d.	n.d.
Nb/Y	0.22	0.2	0.13	0.25	0.13	n.d.	n.d.	n.d.
La/Th	2.61	2.6	2.3	2.5	4.4	6.9	6.1	6.6
Th/U	4.1	1.41	2.9	8.6	0.88	15	22	n.d.
Zr/Th	29.9	32.2	32.7	32.3	38.6	1.2	2.5	1.6

value of the geochemical data of Sifeta (2003) from the nearby metasedimentary rocks was plotted on the x-axis representing less altered rocks (Table 3.2), whereas the values of the metasedimentary rocks from the study area are plotted on the y-axis (Fig. 3.1).

In the diagram of Fig. 3.1a, Al₂O₃ defines the isocon for the sericite-quartz-chlorite schist. Its slope (M^i / M^f) is 0.93, which is equivalent to $M^f / M^i = 1.07$ and thus with a mass increase of 7 %. Cerium defines the isocon for the chlorite-quartz schist (Fig. 3.1b). The slope of this isocon is 1.07, i.e. an M^f / M^i value of 0.93 %, which is equivalent to a net mass decrease of 7 %. For the carbonatized chlorite-quartz schist (Fig. 3.1c), the only M^i / M^f (slope) value close to 1 is obtained from that of Ni, which is 1.63 leading to a net mass decrease of 37 % due to carbonatization. The strong alteration of this rock is also illustrated by a high L.O.I. value (34.33%, Table 3.2).

The major and trace element contents in the sericite-quartz-chlorite schist are fairly similar as those of the Weri metasediments (Sifeta 2003). However, some major and trace element contents show deviations from the median values of the Weri metasediments (Table 3.2, Fig. 3.1a). The Na₂O concentration of 0.1 wt. % is ~27 times lower but still close to the lowest Na₂O content reported for the Weri metasediments, which is 0.15 wt. % (Sifeta 2003; Table 3.2). The CaO content is over 20 times lower, and Pb concentration is over 14 times higher than the corresponding reported minimum or maximum values in the Weri metasediments, respectively. The Sr content is lower than the medium Sr content of the Weri metasediments. It also is slightly lower than the lowest reported Sr value of these latter rocks. Therefore, the original CaO, Pb, and Sr contents are modified and these element contents cannot be used for petrogenetic interpretations.

The major and trace element contents of two of the analyzed samples from chlorite-quartz schists (J2-15 and J2-19) are also similar to those of Weri metasediments (Table 3.2, Fig. 3.1b). However, one of the samples (J2-23) shows evidence of silicification, which influenced the absolute concentrations of most major and trace elements (Table 3.2). Element contents of sample J2-19 are plotted against the median element concentration of the Weri metasediments of Sifeta (2003) for mass balance calculation (Fig 3.1b). The Na₂O value of the sample is the same as in the sericite-quartz-chlorite schist (see above). The Pb concentration is ~3 times higher than the Pb median value of Weri metasediments and also higher than the reported maximum value of the latter sediments. Also in this rock, the original Pb concentration has been modified. Strontium in the chlorite-quartz schist is depleted in relation to the median Sr value and also relative to the reported minimum Sr concentrations in the reference rocks (Table 3.2).

The geochemical composition of the carbonatized chlorite-quartz schist is significantly different from the Weri metasediments (Fig. 3.1c, Table 3.2). The Na₂O concentration is ~50 times lower than the median value of Weri metasediments. The CaO and MnO concentrations are ~90 and 100 times higher than that of median value of the reference metasediments due to carbonatization, respectively. The L.O.I content is also ~12 times higher than the median value of Weri metasediments. The Pb content is ~35 times higher than the highest reported Pb value of the Weri metasediments, due to the presence of hydrothermal galena. The Sr concentration is ~ 2 times higher than the median concentrations of Weri metasediments and higher than the maximum concentration of these metasediments. In contrast, Ce, Zr, and Ba are ~6 to 7 times lower in concentration as compared to the median reference value (Fig 3.1c, Table 3.2). These elements are also lower than the minimum value reported for the Weri metasediments. The mass balance calculation of the carbonatized chlorite-quartz schist suggests that CaO, MnO, Sr, and Pb were added to the rock, whereas Na₂O, Ce, Zr, and Ba were removed.

Table 3.2. Major (wt. %) and trace element concentrations (ppm) in selected Tambien Group metasedimentary rocks from the Workamba and surrounding areas used to calculate metasomatic effects (Sifeta 2003).

Sample no.	Weri metasedimentary rocks (Sifeta 2003)							Workamba metasedimentary rocks, this study				
	WS134	WS135	WS136	WS137	WS138	WS139	Median	J2-05	J2-15	J2-19	J2-23	J2-34
SiO ₂	81.50	63.04	73.07	61.02	72.18	70.93	71.56	66.26	56.18	59.71	85.98	12.63
Al ₂ O ₃	11.51	15.03	12.95	17.56	13.80	13.67	13.74	15.66	14.24	18.75	5.44	2.59
Fe ₂ O ₃ (T)	0.67	7.04	4.46	8.52	4.54	4.71	4.63	2.64	2.61	3.37	1.04	1.45
MnO	0.01	0.10	0.08	0.12	0.08	0.08	0.08	0.166	0.105	0.02	0.101	0.988
MgO	0.45	5.04	1.72	3.63	1.58	1.86	1.72	5.61	17.8	5.98	2.94	4.63
CaO	0.13	1.27	0.49	0.63	0.34	0.72	0.53	0.06	0.09	0.17	0.05	43.05
Na ₂ O	0.30	0.15	4.37	1.04	5.06	4.56	2.70	0.1	0.04	0.1	0.06	0.05
K ₂ O	2.43	2.23	0.51	2.82	0.30	0.62	1.67	5.23	1.49	6.51	1.53	0.09
TiO ₂	0.44	0.92	0.51	0.85	0.59	0.72	0.68	0.234	0.212	0.292	0.082	0.109
P ₂ O ₅	0.01	0.26	0.13	0.19	0.16	0.19	0.16	0.04	0.03	0.04	0.03	0.05
LOI	2.10	4.85	1.94	3.82	1.72	2.03	2.88	4.21	7.54	5.28	2.24	34.33
Total	99.55	99.93	100.23	100.20	100.35	100.09	100.35	100.21	100.337	100.228	99.493	99.967
Ba	740	686	670	658	550	211	380.5	1581	377	1639	668	55
Ce	18	19	50	67	64	43	53.5	38	42.9	57.3	14.9	5,7
Cr	107	200	91	79	35	163	99	40	20	30	190	
Ni	4	80	54	58	20	29	24.5	110	50	70	480	40
Pb	3	3	7	3	20	6	13	288	15	36	1130	700
Rb	90	60	71	95	112	19	65.5	106	46	155	42	
Sr	109	69	129	26	350	154	252	18	10	24	7	546
Y	7	22	21	31	22	18	20	28	32	42	15	8
Zr	126	191	157	200	190	160	175	249	245	309	85	27

Table 3.3. Trace element ratios of the metasedimentary rocks of the study area along with those of reference Weri metasediments of Sifeta (2003).

Sample no.	WS 134	WS 135	WS 136	WS 137	WS 138	WS 139	Median	J2-05	J2-15	J2-19	J2-34	J2 - 23
Th/Sc	0.55	0.55	0.13	0.17	0.16	0.16	0.16	1.54	2.05	1.92	0.35	2.60
Zr/Sc	16.80	16.80	10.62	6.40	9.30	14.50	11.90	49.8	61.30	61.80	13.50	85.00
Ti/Zr	19.90	27.40	28.20	30.86	26.70	25.70	26.20	5.4	4.90	5.40	23.00	5.50
La/Sc	0.98		1.20		0.97	0.67	0.82	3.86	5.40	5.02	1.55	6.10
Zr/TiO ₂	0.03	0.02	0.02	0.02	0.02	0.02	0.02	0.11	0.12	0.11	0.02	0.10
Nb/Y	20.00	0.60	0.50	0.50	0.40	0.56	0.50	0.25	0.22	0.21	0.13	0.13
La/Th	1.80		9.10		5.99	4.10	50.00	2.51	2.61	2.60	4.43	2.30
Th/U								8.56	4.10	1.41	0.88	2.90
Zr/Th	30.70	34.70	79.20	38.30	57.30	88.90	73.10	32.34	29.88	32.20	38.60	32.70

Generally, the major and trace element mass balance calculations suggest that Na₂O, and Sr were removed from the Workamba metasedimentary rocks by the hydrothermal fluids, whereas Pb was added. K₂O, MnO, CaO, and Ba were mobile and variably added or removed. Therefore, the original composition of the Workamba metasedimentary rocks has been modified.

3.4 Trace element patterns of metasedimentary rocks

Chondrite-normalized multi-(trace) element patterns of the Weri metasediments of Sifeta (2003) are shown together with patterns of Weri metavolcanic rocks (Sifeta 2003), mafic to intermediate and felsic metavolcanic rocks (Alene et al. 2000) in Fig. 3.2a (chondrite of Sun and McDonough 1989). The majority of Weri metasediment patterns mirror those of Weri metavolcanic rocks (Sifeta 2003) and mafic to intermediate and felsic metavolcanic rocks (Alene et al. 2000). The similar trace element patterns of the equivalent metasedimentary rocks at Workamba are shown in Fig. 3.2b and c. The chlorite-quartz and sericite-quartz-chlorite schists at Workamba show enrichments in Rb, Ba, Th, U, and negative Nb anomalies similar as the metavolcanic rocks of the region (Alene et al. 2000; Sifeta 2003; Fig. 3.2a). However, Sr is depleted in the chlorite-quartz and sericite-quartz-chlorite schists as compared to the metavolcanic rocks of the region and Weri metasediments. Lead, Hf, and Zr are relatively enriched in the sericite-quartz-chlorite schist and on the chlorite-quartz schists (Fig. 3.2b). The black slate, mafic metavolcanic rock, sericite-chlorite schist, and carbonatized chlorite-quartz schist show significant deviations in some elements from the patterns of the regionally exposed metavolcanic rocks (Alene et al. 2000; Sifeta 2003; Fig. 3.2b). Most significant variations are a positive Pb anomaly of the carbonatized chlorite-quartz schist and

Zr depletion in the mafic metavolcanic rock, black slate, and sericite-chlorite schist (Fig. 3.2b). The latter is also depleted in Pb, Sr, and Hf.

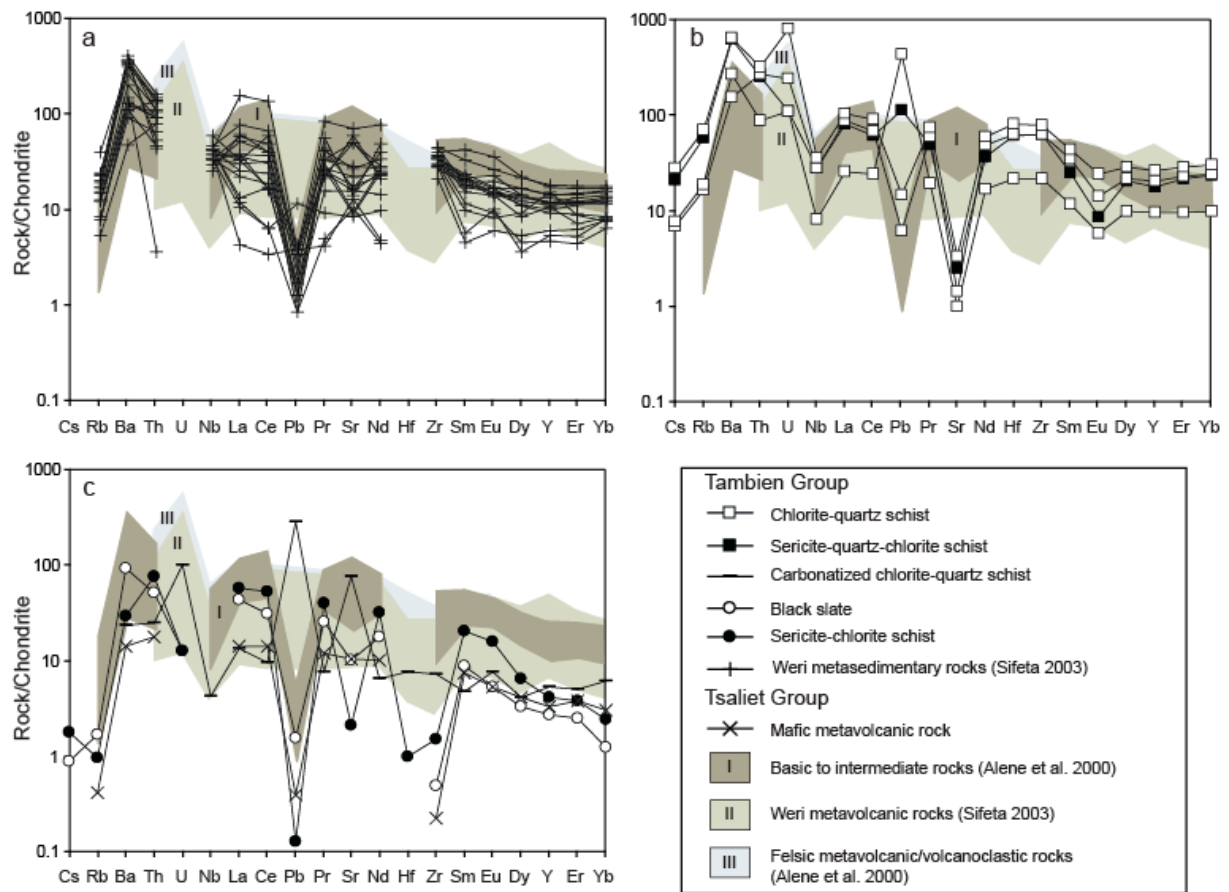


Fig. 3.2. Chondrite-normalized trace element patterns of a) Weru metasedimentary rocks; b) chlorite-quartz schist, and sericite-quartz-chlorite schists; c) carbonated chlorite-quartz schist, black slate, sericite-chlorite schist, and mafic metavolcanic rock. Background trace element patterns represent that of Weru metavolcanic rocks (Sifeta, 2003) and Mai Kenetal-Hawzen mafic to felsic metavolcanic/volcanoclastic rocks (Alene et al. 2000), which are plotted for comparison. Generally, enrichment in Ba, Th, and U and negative Nb anomalies are common characteristics of all the rocks. Normalizing values are from Sun and McDonough (1989).

The sericite-quartz-chlorite schists, chlorite-quartz schists, and the metavolcanic rocks of the region display enrichments in Rb, Ba, Th, and U as well as negative Nb anomalies compared to chondrite values, which is characteristic of island arc basalts and andesites (Wilson 1989). This suggests that the sericite-quartz-chlorite and chlorite-quartz schists inherited the Rb, Ba, Th, U, and Nb compositions of the metavolcanic rocks. The slight enrichment in Hf, Zr, and negative Eu anomaly displayed by the sericite-chlorite quartz schist and chlorite-quartz schists as compared to the metavolcanic rocks could be related to sediment mixing from different parent rocks, which have variable compositions of these elements. The anomalous

Pb values in the chlorite-quartz schists of Workamba metasedimentary rocks are due to presence of hydrothermal galena, which is part of the gold and base metal mineralization. The low Sr concentrations are due to Sr-leaching by hydrothermal fluids as indicated in the mass balance calculations. The negative Pb anomaly in the metavolcanic rocks, and sericite-quartz-chlorite and chlorite-quartz schists is related to high normalizing value ($Pb = 2.47$ ppm for chondrite as compared to 0.185 for primitive mantle, Sun and McDonough 1989). The scattered pattern shown by the black slate, mafic metavolcanic rock, and sericite-chlorite schist suggests that the chemical composition of these rocks is modified by hydrothermal alteration or weathering processes.

Trace elements ratios can be used to infer the provenance and tectonic setting of the rocks (e.g. Bhatia 1983; Bhatia 1985; Bhatia and Crook 1986). Trace element ratios of the Workamba metasedimentary rocks, which are used in some standard plots, are compared with those of the reference Weri metasediments to assess effects of hydrothermal alteration (Table 3.3). Th/Sc, Zr/Sc, La/Sc, and Zr/TiO₂ ratios obtained from Workamba metasedimentary rocks, except the values for carbonatized chlorite-quartz schist, are ~3 to 10 times higher than the median and lowest or highest values of Weri metasediments (Table 3.3). In contrast, the Ti/Zr, Nb/Y, La/Th, and Zr/Th ratios in these rocks are ~2 to 5 times lower than the reference metasediments. These results show that the original trace element ratios have been modified presumably by hydrothermal alteration. Therefore, these trace element ratios do not provide information about the source and tectonic setting of the Workamba metasedimentary rocks. However, the enrichment in Rb, Ba, Th, and U, and negative Nb anomalies of the Workamba metasedimentary rocks are compatible with the hypothesis that the Tambien Group metasedimentary rocks are dominantly derived from the island-arc metavolcanic rocks of the Tsaliel Group (Sifeta 2003; Fig. 2.5b).

3.6. Major, trace, and rare-earth element distribution in intrusive rocks

3.6.1 Element abundance

The monzogranite dikes/sills have SiO₂ contents ranging from 68.43 to 69.45 wt. %, and K₂O, Na₂O, and CaO contents from 3.63 to 4.81 wt. %, 2.89 to 4.84 wt. %, and 0.45 to 2.09 wt. %, respectively (Table 3.4). These major element contents are similar to those of post-tectonic granitoids in Tigray (e.g. Negash, Asrat 2002; Axum, Tadesse et al. 2000). The K₂O and Na₂O contents of the monzogranite dikes/sills are a reflection of alkali feldspar component in these rocks, whereas relatively high CaO contents of 2 wt. % are caused by carbonatization.

The SiO₂ contents of the lamprophyre dikes are around 50 wt. %. Their K₂O and Na₂O contents are lower, whereas CaO, MgO, Fe₂O₃ concentrations and loss on ignition (L.O.I.) are significantly higher than those of monzogranite dikes/sills (Table 3.1). The CaO, MgO, Fe₂O₃ and L.O.I. values can be attributed to the abundant calcite and biotite in these rocks.

The monzogranite dikes/sills have Rb 85 to 131 ppm, Ba 1463 to 1886 ppm, Th 6.2 to 7.1, and U 2.3 to 3 ppm. The lamprophyres contain slightly lower amounts of these elements than the monzogranite dikes/sills (Table 3.4). The value of Nb for the monzogranite and aplitic dikes/sills is 2 ppm, whereas those of lamprophyres vary from 12 to 15 ppm. Zr in lamprophyres is higher than those of monzogranite dikes/sills and calc-alkaline lamprophyres elsewhere (e.g. Rock 1990, Table 3.1). The Cr, Co, V, and Σ REE contents of the monzogranite dikes/sills are lower than the concentrations of these elements in the lamprophyres (Table 3.4). However, Ni concentrations are similar for all intrusive rocks except for the sample J2-14, which has low Ni value (Table 3.4). The higher Cr, Co, and V contents of the lamprophyres over the monzogranite dikes/sills are mainly due to the abundance of these elements in biotite (e.g. Yang and Rivers 2000). The enrichment in Rb, Ba, and Th of the monzogranite dikes/sills than the lamprophyres might be attributed to the presence of these elements in the crystal lattices of feldspars (e.g. Ribbe et al. 1972).

3.6.2 Element mobility of the Workamba intrusive rocks

The average major and trace element values of the three analyzed medium- to coarse-grained monzogranites are plotted against a monzogranite sample (N9-14) from Negash granitoid of Asrat (2002) with a similar SiO₂ content to estimate element mobility and possible metasomatic affects (Fig. 3.3). The fine-grained monzogranites (aplites) are plotted in the same way (Figs. 3.3b and c). In Fig. 3.3a, Al₂O₃ defines the isocon for the medium- to coarse-grained monzogranite with a slope of (M^i / M^f) 1.01, which is equivalent to $M^f / M^i = 0.99$ and thus a mass decrease of 1 %. The isocon of the sample J2-10 (fine-grained aplitic monzogranite) is defined by K₂O having a slope of 1.01% (Fig. 3.2b). This implies an M^f / M^i value of 0.99 %, which is equivalent to a net mass decrease of 1 %. The isocon of the sample J2-14 (another fine-grained monzogranite) is defined by Al₂O₃ with a slope of 1.01 (Fig. 3.3c). This slope value is equivalent to an M^f / M^i value of 0.99 % and a net mass decrease of 1 %.

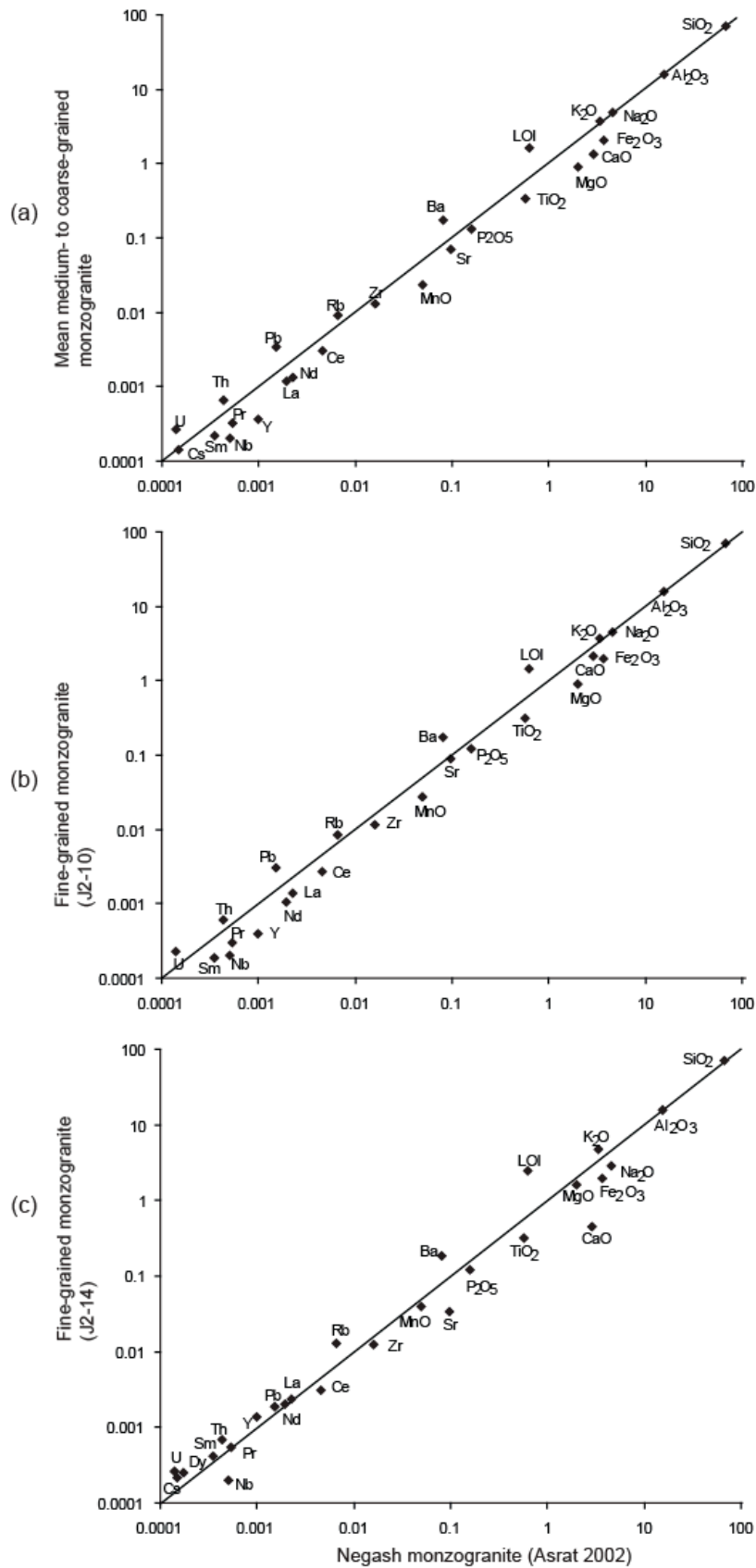


Fig. 3.3a-c. Isocon diagrams showing element contents of monzogranite dikes/sills of the study area vs. monzogranite mean composition of Negash granitoid (Asrat 2002). The major and trace element values are plotted close to the slope of the isocon suggesting that there is no significant mass increase or decrease as compared to the reference monzogranite rock.

Table 3.4. Major (wt. %) and trace (ppm) element compositions of intrusive rocks of the study area along with the average values for calc-alkaline lamprophyres from Rock (1990), which are used as a reference. Abbreviations: n.d. = not determined.

Rock type	Medium- to coarse-grained monzogranite			Fine-grained monzogranite		Lamprophyre			Detection limit
	Sample No.	TG06037	TG06043	TG06051	J4-10	J2-14	J2-18	J2-30	
SiO ₂	69.54	69.45	68.43	69.05	69.40	50.30	50.02	51	0.01
Al ₂ O ₃	15.69	15.98	16.01	15.56	15.76	12.19	12.66	14	0.01
Fe ₂ O ₃ (T)	1.96	2.08	2.11	1.99	1.92	6.92	8.08	8.2	0.01
MnO	0.02	0.03	0.03	0.03	0.04	0.10	0.10	0.13	0.001
MgO	0.76	0.95	1.04	0.91	1.61	7.38	7.58	7	0.01
CaO	0.78	1.29	1.93	2.09	0.45	7.24	5.43	7	0.01
Na ₂ O	4.84	4.77	4.74	4.53	2.89	2.40	3.35	2.70	0.01
K ₂ O	3.68	3.65	3.59	3.63	4.81	2.94	2.81	3.10	0.01
TiO ₂	0.23	0.34	0.40	0.30	0.30	1.50	1.70	1.10	0.001
P ₂ O ₅	0.12	0.13	0.14	0.12	0.12	1.43	0.84	0.60	0.01
LOI	1.47	1.63	1.74	1.46	2.48	7.05	7.70	4.40	n.d.
Total	99.17	100.30	100.10	99.66	99.80	99.50	100.20		
Trace and rare earth elements									
Ba	1463	1810	1886	1707	1873	1580	1467	1050	3
Rb	97	88	87	85	131	58	76	70	2
Th	7.1	6.3	6.4	6.2	7	5.3	4.4	9	0.1
U	2.9	2.2	3	2.3	2.6	2.2	2.2	3	0.1
Nb	2	2	2	2	2	12	15	13	1
Ta	0.2	0.2	0.2	0.2	0.2	0.7	1.2	0.9	0.1
Sr	552	673	886	877	345	816	1000	715	2
Zr	121	127	135	115	126	588	284	190	4
Hf	3.3	3.4	3.5	3.2	3.5	14.8	7.6	5.2	0.1
Y	4	3	4	4	14	22	13	23	2
V	39	45	51	44	45	174	176	170	5
Cr	110	90	80	120	40	280	250	370	20
Co	6	5	4	5	4	27	32	36	1
Ni	270	240	200	330	70	270	260	150	20
Pb	35	33	34	31	19	25	13	13	5
Cs	1.3	1.3	1.6	0.9	2.2	0.7	2.8	3	0.5
Sc	4	4	5	4	4	20	13	20	0.1
La	12.9	10.3	16.7	13.7	23.6	36	28.7	53	0.1
Ce	26.2	32.4	32	26.8	31.4	85.8	66.3	110	0.1
Pr	3	2.94	3.87	3.04	5.47	11.7	8.57	11	0.05
Nd	10.7	11.2	13.6	10.5	20.2	48.5	34.3	56	0.1
Sm	1.9	2.2	2.5	1.9	4.2	10.3	6.6	10.5	0.1
Eu	0.53	0.65	0.75	0.59	1.23	3.4	1.97	3.1	0.05
Gd	1.4	1.6	1.7	1.4	3.5	8.1	5.1	11	0.1
Tb	0.2	0.2	0.2	0.2	0.5	1	0.7	1.1	0.1
Dy	0.9	0.9	1	0.8	2.5	4.9	3.2	3.7	0.1
Ho	0.2	0.2	0.2	0.1	0.4	0.8	0.5	0.9	0.1
Er	0.4	0.5	0.5	0.4	1.1	2.1	1.3	1.6	0.1
Tm	0.06	0.06	0.07	b.d	0.14	0.29	0.17	0.24	0.05
Yb	0.4	0.4	0.4	0.3	0.8	1.8	1	1.8	0.1
Lu	0.06	0.06	0.06	0.06	0.11	0.26	0.14	0.26	0.04
Eu/Eu*	1.0	1.0	1.1	1.13	1.0	1.1	1.04		
(La/Yb) _N	21.6	17.2	27.92	30.5	19.7	13.4	19.2		
ΣREE	58.85	63.61	73.55	59.79	95.15	214.95	158.55		
Rb/Sr	0.2	0.1	0.1	0.1	0.4	0.01	0.08		
Rb/Ba	0.1	0.05	0.05	0.05	0.1	0.04	0.05		
Zr/Sc	30.25	31.75	27	28.75	31.5	29.4	21.85		
Ti/Zr	14.09	15.04	15.16	15.32	14.43	14.97	33.18		
La/Sc	3.23	2.56	3.34	3.43	5.9	1.8	2.21		
Nb/Y	0.5	0.67	0.5	0.5	0.43	0.43	1.15		

Major and trace element contents of all the monzogranite dikes/sills are fairly similar to the reference Negash monzogranite (Table 3.4; Annex 2.1; Fig. 3.2a-c). Yttrium, Nb, Zr, and TiO_2 concentrations in the monzogranite dikes/sills are lower than in the Negash monzogranite, whereas Ba and Ni concentrations are higher in the latter. Sample J2-14 has CaO, Na_2O , Rb, Zr, Sr, Y, Cr, Ni and some REE (e.g. La and Ce) contents, which are significantly different from the other monzogranite rocks at Workamba and the reference Negash pluton (Table 3.4; Fig. 3.2c). The CaO content in this sample is ~6 and 4 times lower, whereas L.O.I. is 4 times higher than the corresponding values of Negash monzogranite. Niobium and Sr are ~2 to 3 times lower than in the latter. Barium concentration in J2-14 is ~2 times higher than the concentration of Negash monzogranite. However, trace element ratios, such as Zr/TiO_2 (~0.04, monzogranite dikes/sills and ~0.03, Negash monzogranite) and Nb/Y (~0.5, monzogranite dikes/sills and ~0.52, Negash monzogranite) are similar. In general, the original magmatic geochemical composition of the monzogranite dikes/sills (except of sample J2-14) and lamprophyres has not been significantly changed by post-magmatic processes.

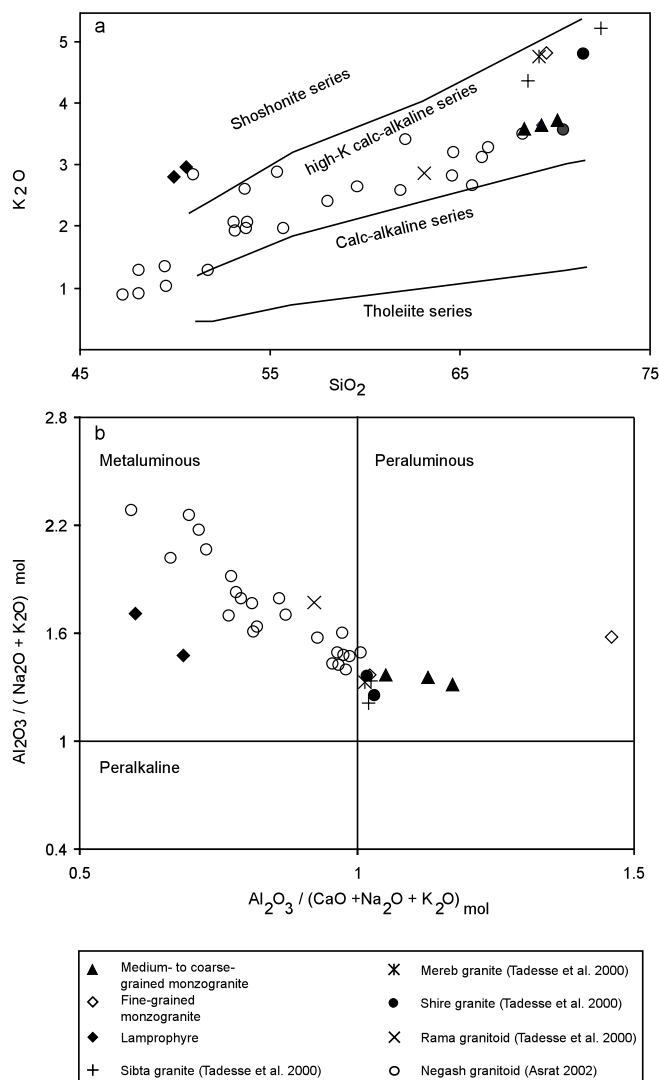


Fig. 3.4. Discrimination diagrams a) showing the calc-alkaline nature of monzogranite dikes/sills and regional post-tectonic granitoids (boundary lines after Peccerillo and Taylor 1976); b) Alumina Index diagram suggesting that the monzogranite dikes/sills are peraluminous, whereas the lamprophyres are metaluminous. The regional post-tectonic granitoids vary from metaluminous to peraluminous.

3.6.3 Trace and rare earth element patterns of intrusive rocks

The SiO₂ and K₂O analytical data of dikes/sills of the study area are plotted on standard diagrams (e.g. Peccerillo and Taylor 1976) together with equivalent data from post-tectonic plutons of Tigray (Fig. 3.4). The monzogranite dikes/sills and regional intrusive rocks occupy the field of granitoids with calc-alkaline affinity (Fig. 3.4a). The lamprophyres plot in the shoshonitic field. Similarly, in alumina index diagram, the monzogranite dikes/sills are peraluminous whereas, the lamprophyres are metaluminous (Fig. 3.4b). The regional post-tectonic granitoids vary from metaluminous to peraluminous.

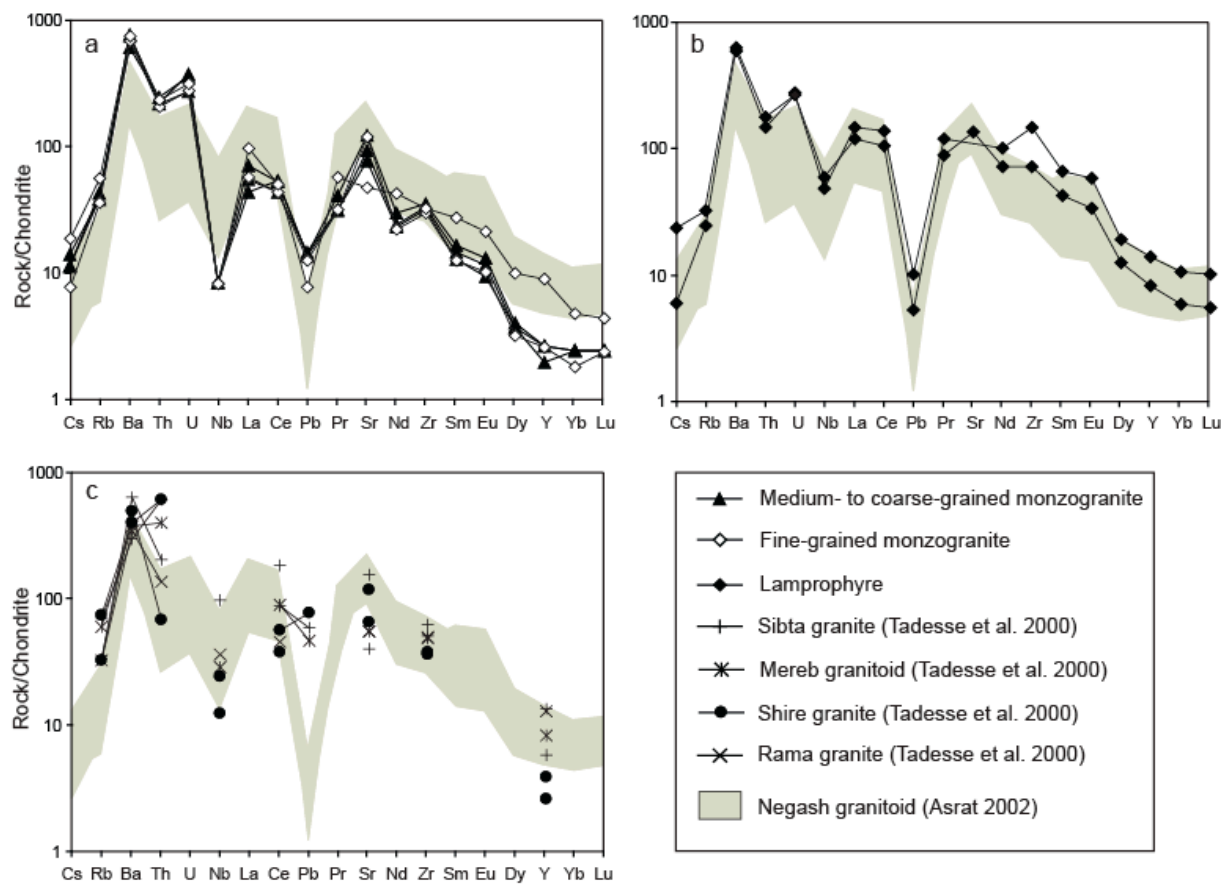


Fig. 3.5. Chondrite-normalized trace element patterns of a) monzogranite dikes/sills; b) lamprophyres; and c) nearby post-tectonic granitoids (Tadesse et al. 2000). The background trace element pattern represents that of Negash post-tectonic granitoid (Asrat 2002). The Workamba monzogranite dikes/sills and lamprophyres show similar trace element patterns with the Negash granitoid as well as the nearby post-tectonic granitoids. Normalizing values are from Sun and McDonough (1989).

The chondrite-normalized trace element patterns of the monzogranite dikes/sills, lamprophyres, and post-tectonic plutons in the region are shown in Fig. 3.5 (chondrite from Sun and McDonough 1989). They mirror the pattern of Negash granitoid (Fig. 3.5a). The monzogranite dikes/sills (Fig. 3.5a) and lamprophyres (Fig. 3.5b) are enriched in Ba, Th, U, Rb, and Ce as compared to Y and Yb. They also show negative Nb and Pb anomalies. These characteristics are also shared by I-type post-tectonic granitoids of Sibta, Mereb, Shire, and Rama (Tadesse et al. 2000; Fig. 3.5c).

Chondrite-normalized rare earth element pattern of the monzogranite dikes/sills and lamprophyres are essentially the same as those of the post-tectonic Negash granitoids (chondrite from Sun and McDonough 1989; Fig. 3.6). However, REE concentrations in the lamprophyres are higher as those in the monzogranite.

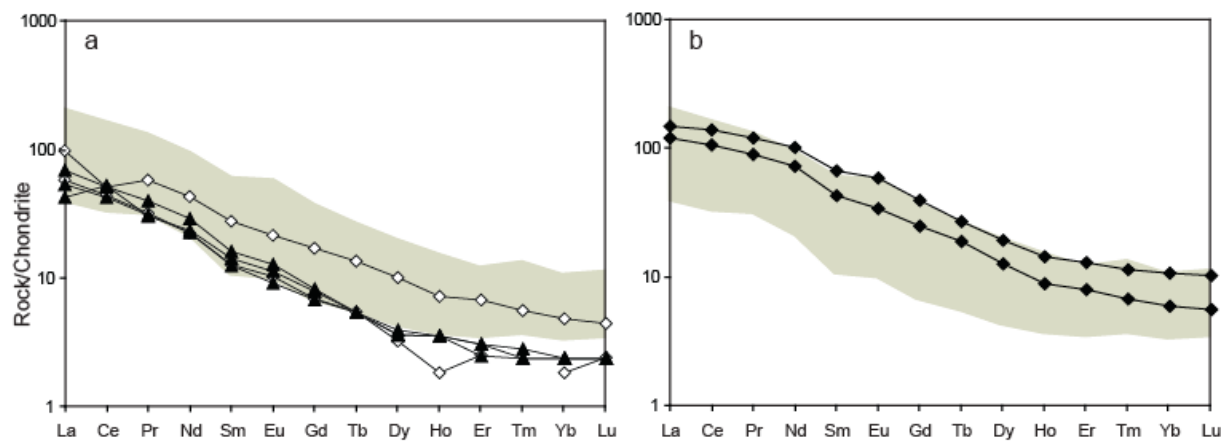


Fig. 3.6. Chondrite-normalized rare earth element patterns of a) monzogranite dikes/sills; and b) lamprophyres showing similar REE pattern with the Negash granitoid. Normalizing values are from Sun and McDonough (1989). The legend is the same as that in Fig. 3.3.

Trace element data of Workamba dikes/sills and those of the nearby post-tectonic granitoids (Tadesse et al. 2000; Asrat 2002) of the ANS in the Tigray province are plotted in discrimination diagrams for granites of Pearce et al. (1984; Fig. 3.7 a and b). The trace element characteristics of these rocks are consistent with a volcanic arc setting as previously suggest by Tadesse et al. (2000). Exceptions are an aplite sample in the Negash pluton and one sample from the Shire post-tectonic granite, which are plotted within the syn-collision granite field (Fig. 3.7).

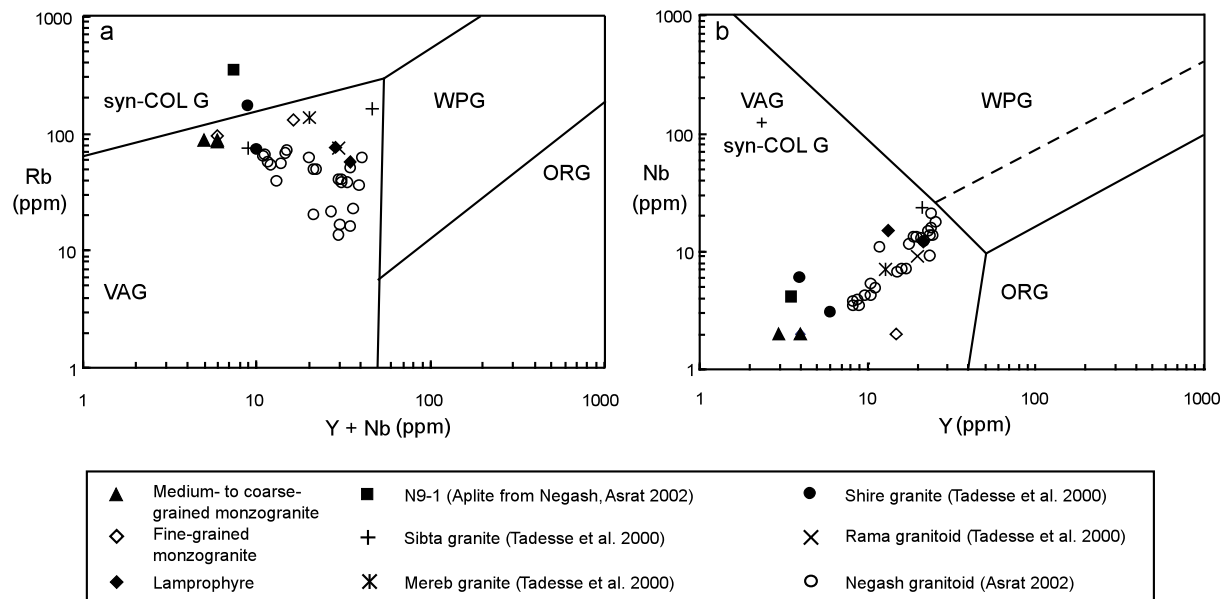


Fig. 3.7. a) Rb-Y+Nb, and b) Nb-Y discrimination diagrams of Pearce et al. (1984) showing volcanic-arc setting of the Workamba monzogranite dikes/sills and post-tectonic granitoids of the region.

The thin section data on the dikes/sills of Workamba shows evidences of alteration such as carbonatization, epidotization, chloritization, and sericitization. However, mass balance calculations suggest that they retained their near original geochemical composition. The major, trace, and rare earth element contents of these dikes/sills are similar to those of nearby post-tectonic granitoids of the ANS in the Tigray province (e.g. Negash, Asrat 2002; Sibta, Mereb, Shire, and Rama, Tadesse et al. 2000; Fig. 2.5 and Table 2.1). The Workamba dikes/sills post-date regional shear deformation suggesting that they are post tectonic. Therefore, the monzogranite dikes/sills and lamprophyres belong to the calc-alkaline, Pan-African, and post-tectonic volcanic-arc granitoids of Tigray region (e.g. Tadesse et al. 2000; Asrat 2002). The latter are derived from I-type magmas formed by partial melting of mantle and modified by the fluid component of the subducted slab or involvement of continental crust (e.g. Tadesse et al. 2000; Asrat 2002).

4. Hydrothermal alteration and mineralization

4.1 Hydrothermal alteration

The rocks in the study area locally suffered pervasive sericitization, silicification, carbonatization or propylitic (epidote) alteration (Fig. 4.1a and b). Quartz and/or calcite occur also as continuous and discontinuous veins or veinlets.

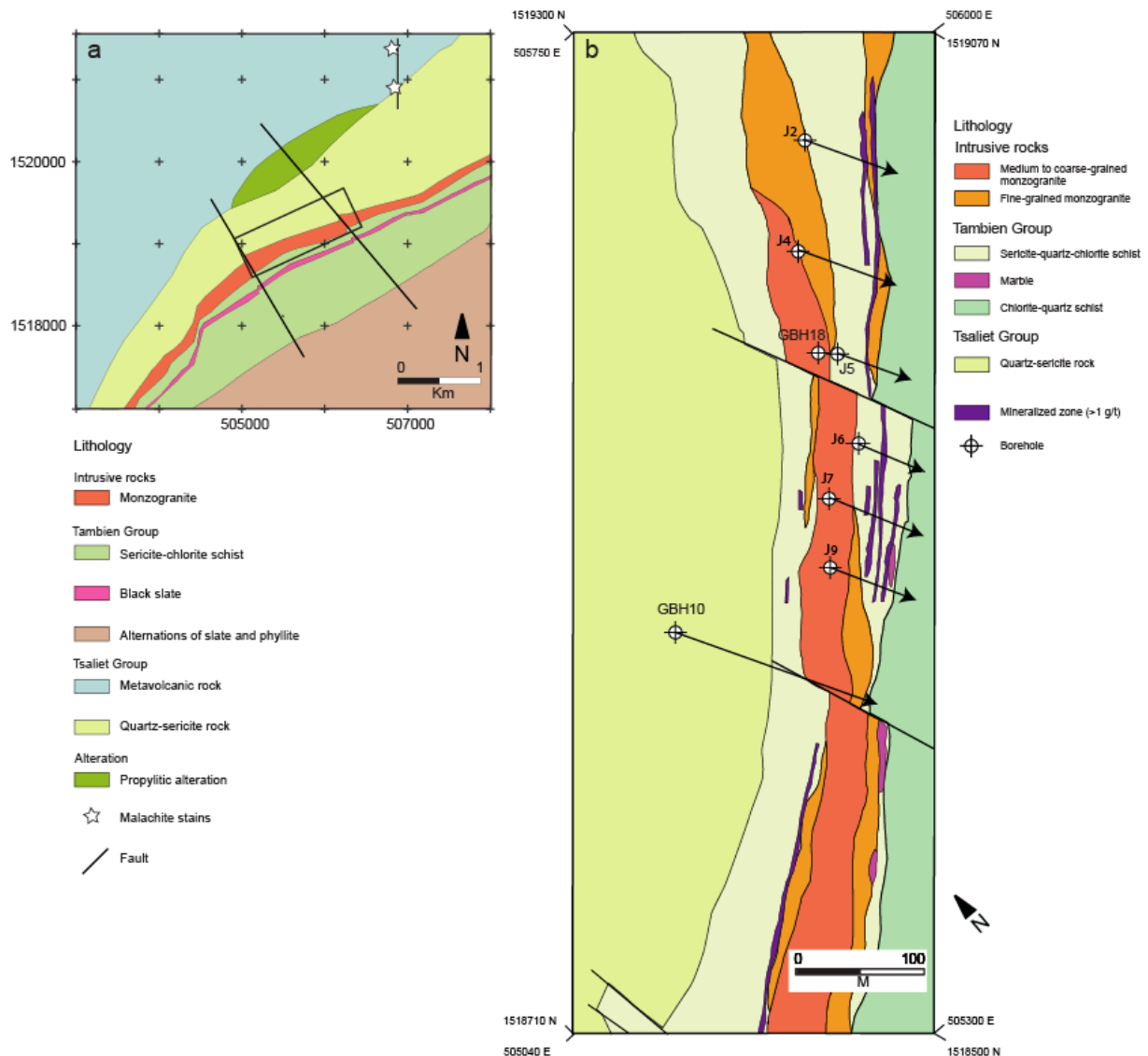


Fig. 4.1. (a) Geological and alteration overview map. Inset rectangle represents the location of the drilled area; b) geological and alteration map of the drilled area (modified after National Mining Corporation 2006). Arrows on the drill hole symbols indicate the azimuth of drilling.

Propylitic (epidote) alteration, characterized mainly by patchy occurrence of epidote (Fig. 4.2), affects the metavolcanic rocks along the contact with the quartz-sericite rock to the northwest of the mineralized (drilled) area (Fig. 4.1a and 4.2). Propylitic alteration has also been observed in places in the monzogranite dikes/sills and lamprophyres (Fig. 4.3a and b). This alteration type has not been detected in the metasedimentary rocks of the Tambien Group.

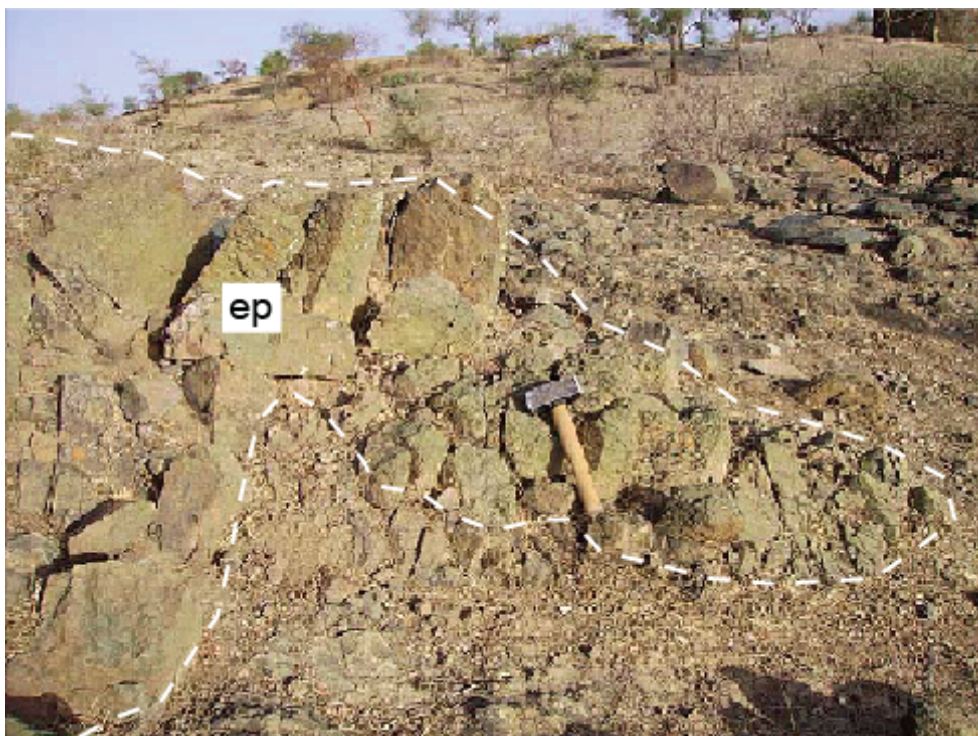


Fig. 4.2. An example of patchy propylitic (epidote) alteration occurrence marked by seams of yellowish-green epidote (ep), which overprints the fabric of the metavolcanic rocks.

Pervasive sericite-quartz alteration affects the uppermost part of the volcanic rocks of the Tsaliet Group and the lower part of the Tambien Group (e.g. Fig. 4.1a and b). Hydrothermal sericite-quartz is also common in the monzogranite dikes/sills and lamprophyres. Sericite and quartz with minor amounts of hematite, and pyrite are the mineral assemblages recognized in this alteration. Assessment of structural and textural data suggests the presence of at least two phases of sericite-quartz alteration in the study area. The first phase is characterized by the occurrence of aligned sericite and quartz crystals suggesting that this sericite alteration phase is related to hydrothermal fluid movements during D1 shear deformation (Fig. 4.3c). Since the monzogranite dikes/sills and lamprophyres post-date deformation, the sericite alteration therein (Fig. 4.3d) is interpreted to have occurred later.

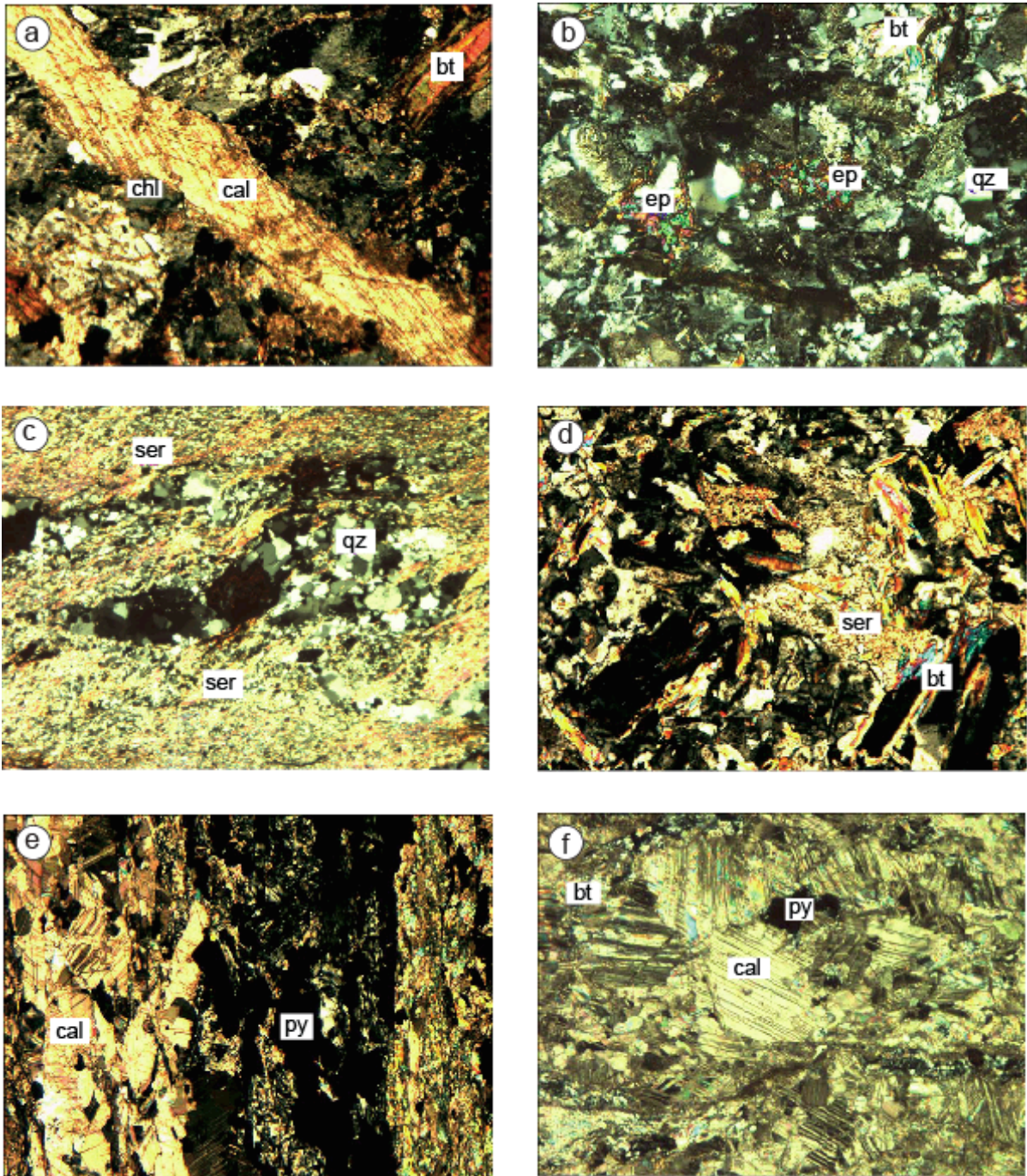


Fig. 4.3. Thin section micrographs showing the different alteration types that affected the rocks. Crossed nicols. a) Calcite vein cutting hydrothermal chlorite in monzogranite dikes/sills; b) propylitic (epidote) alteration observed in the dikes/sills; c) showing pervasive first phase sericite-quartz alteration affecting the metasedimentary rocks in the study area; d) second phase of sericitization affecting the dikes/sills in the mineralized zone; e) subparallel bands of calcite and sulfide veinlets cutting the foliation of the chlorite-quartz schist; f) carbonatization of chlorite-quartz schist in the mineralized zone. Field of view for all micrographs is 0.6 mm. Abbreviations: ep = epidote, bt = biotite, cal = calcite, py = pyrite, chl = chlorite, qz = quartz, and ser = sericite.

Sericite-quartz alteration modified the original geochemical composition of the metasedimentary rocks in the mineralized zone (chapter 3).

Carbonate-quartz alteration affected the chlorite-quartz schist and, locally, dikes/sills in the mineralized zone. Mineral associations in this alteration are calcite, quartz, and sulfides. In the chlorite-quartz schist, it is commonly manifested by subparallel calcite veinlets and sulfide veinlets, which cut the foliation (e.g. Fig. 4.3e), and/or by pervasive carbonatization (e.g. Fig. 4.3f), whereas in the intrusive rocks, calcite veinlets and calcite disseminations are commonly present (Fig. 4.3a). Carbonate-quartz alteration is interpreted to be the youngest alteration phase as it post-dates the sericite-quartz and propylitic alterations.

4.2 Mineralization

Pyrite, sphalerite, galena, and chalcopyrite are the main sulfide phases, whereas pyrrhotite, arsenopyrite and chalcocite are minor components. A list of sulfides is given in annex 1.5.

Pyrite is the most abundant sulfide ore mineral and present in grains up to 1 mm in size, which tend to form euhedral crystal shape. Pyrite grains occur in cluster (Fig. 4.4a), or disseminated in the silicate or carbonate gangue. Pyrite also exists in monomineralic veinlets, which are 0.1mm to 1 cm thick. Galena (Fig. 4.4b), pyrrhotite (Fig. 4.4c), chalcopyrite, and/or sphalerite inclusions are commonly observed within pyrite.

Sphalerite is second dominant sulfide phase. Most of the grains are coarse (up to 3 mm), and display subhedral to irregularly shaped crystal form (Fig. 4.4d). Sphalerite occurs in the form of up to 0.5 cm wide continuous to discontinuous monomineralic veinlets, or as isolated grains in quartz or calcite veins. It may contain abundant chalcopyrite blebs (e.g. Fig. 4.4e) and/or inclusions of pyrite, or galena. The chalcopyrite blebs are interpreted to represent exsolution products (chalcopyrite disease, see e.g. Ramdohr 1969). Sphalerite displays zigzag grain boundary with the gangue.

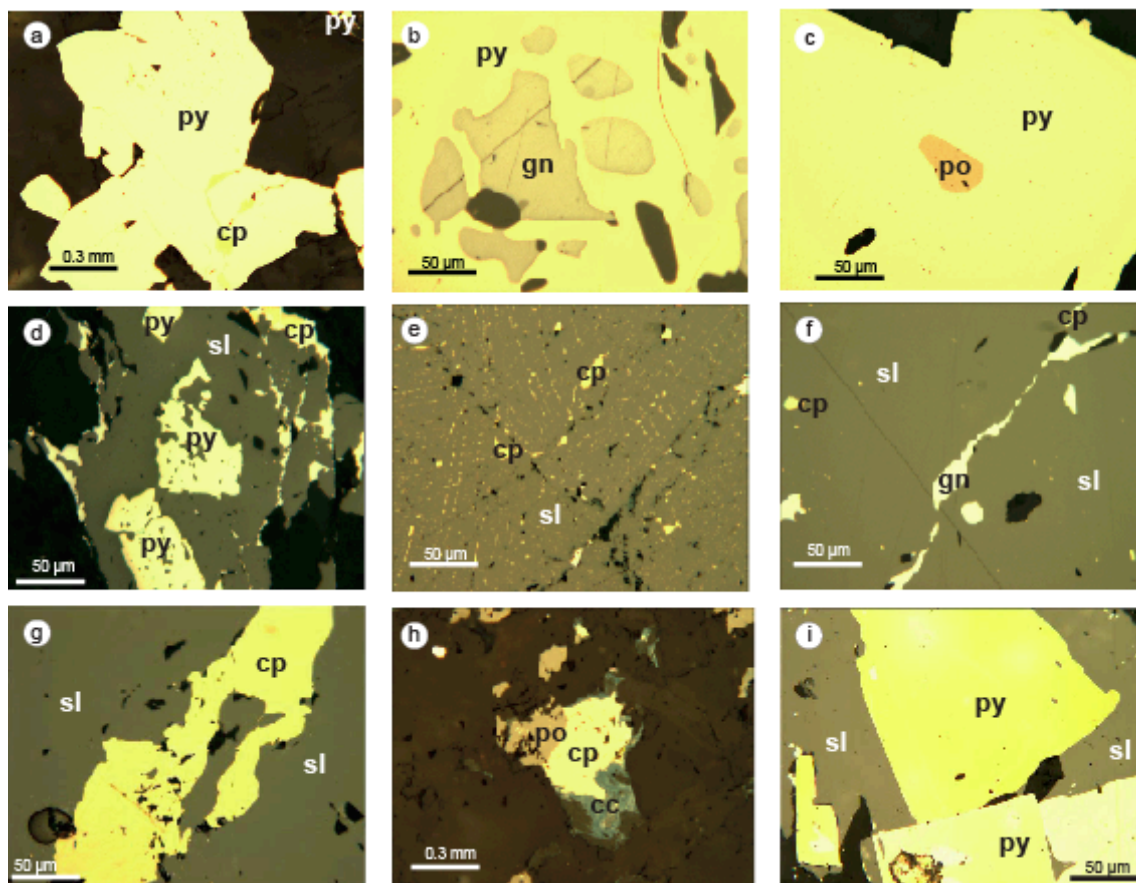


Fig. 4.4a-i. Reflected-light photomicrographs showing relationships between opaque minerals. a) cluster of pyrite grains with chalcopyrite postdating pyrite; b) galena inclusions in pyrite; c) pyrrhotite inclusion in pyrite; d) pyrite overgrown by sphalerite; e) chalcopyrite blebs inside sphalerite (chalcopyrite disease); f) galena veinlet cutting sphalerite; g) chalcopyrite veinlet cutting sphalerite; h) chalcopyrite replaces pyrrhotite and is in turn replaced by chalcocite; i) sphalerite interstitial to pyrite. Abbreviations: py = pyrite, cp = chalcopyrite, cc = chalcocite, po = pyrrhotite, sl = sphalerite, cal = calcite, bt = biotite, and gn = galena.

Galena is up to 0.2 mm in size, and occurs as veinlets cutting sphalerite (Fig. 4.4f) and anhedral grains. Galena as inclusions in sphalerite is common. The contact between galena and sphalerite as well as the gangue varies from irregular to straight.

Chalcopyrite grains are mainly around 50 μm in diameter. However, individual chalcopyrite grains are rare. Chalcopyrite is mainly present in the form of inclusions, and tiny veinlets cutting pyrite, and sphalerite (e.g. Fig. 4.4m).

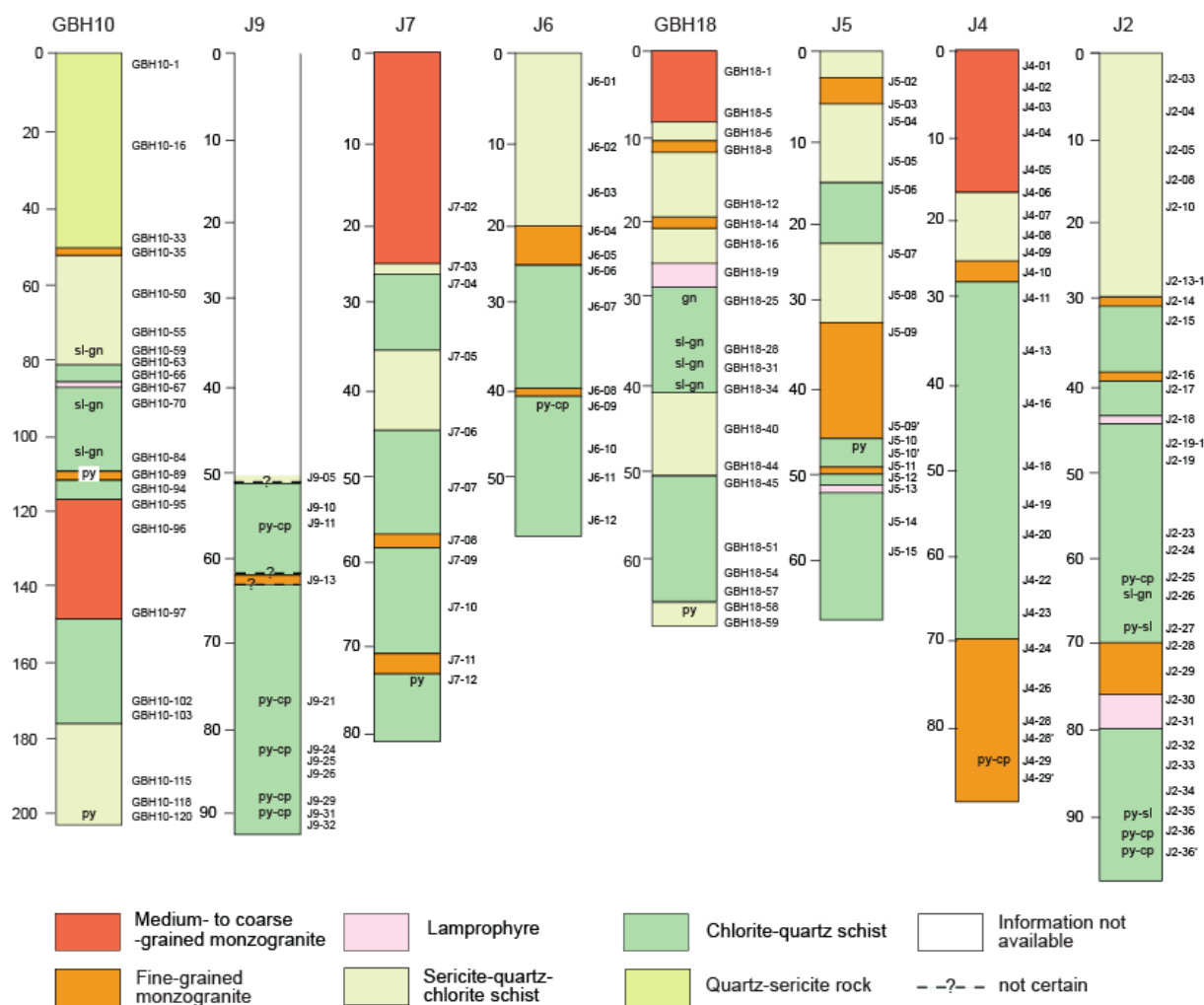


Fig. 4.5. Borehole logs showing the various rock types in the mineralized area. Sulfides mostly occur in the chlorite-quartz and sericite-quartz-chlorite schists. The quartz-sericite rock and dike/sills are barren or locally contain trace quantities of pyrite. Abbreviations: py = pyrite, sl = sphalerite, cp = chalcopyrite, and gn = galena.

Pyrrhotite commonly occurs as rounded to sub-rounded inclusions in pyrite (e.g. Fig. 4.4e). Chalcocite replaces chalcopyrite (Fig. 4.4n). Arsenopyrite is rare and is present in the form of few inclusions within pyrite.

The sulfide mineralization mainly occurred in the chlorite-quartz and sericite-chlorite quartz schists. The quartz-sericite rock and monzogranite dikes/sills are barren. The dikes/sills may contain sulfides in trace quantities. The distribution of sulfides in the boreholes is illustrated in Fig. 4.5.

In addition to the sulfide mineralization in the shear zone, malachite showings on cleavage planes in Tsaliet Group metavolcanic rocks observed at two locations in the northern part of the study area suggest the presence of hypogene Cu mineralization at depth (Fig. 4.6). The malachite showings are located along a N-S trending brittle fault (Fig. 4.1a). Copper mineralization in the metavolcanic rocks is also reported from several localities nearby (e.g. Beyth 1972).



Fig. 4.6. Malachite staining on cleavage planes of the metavolcanic rocks suggest potential for a hypogene Cu mineralization at depth.

4.3 Paragenetic sequence

A paragenetic scheme is shown in Fig. 4.8. Pervasive sericitization and chlorite-epidote (propylitic) alteration occurred before an early quartz and/or calcite veining event. The metallic mineralization commenced with the formation of pyrrhotite. Pyrrhotite occurs as inclusions in pyrite (Fig. 4.4c). Two generation (I and II) of chalcopyrite, sphalerite, galena, and pyrite have been identified. Chalcopyrite I replaced pyrrhotite (Fig. 4.4h), and is in turn replaced by pyrite I (Fig. 4.7a).

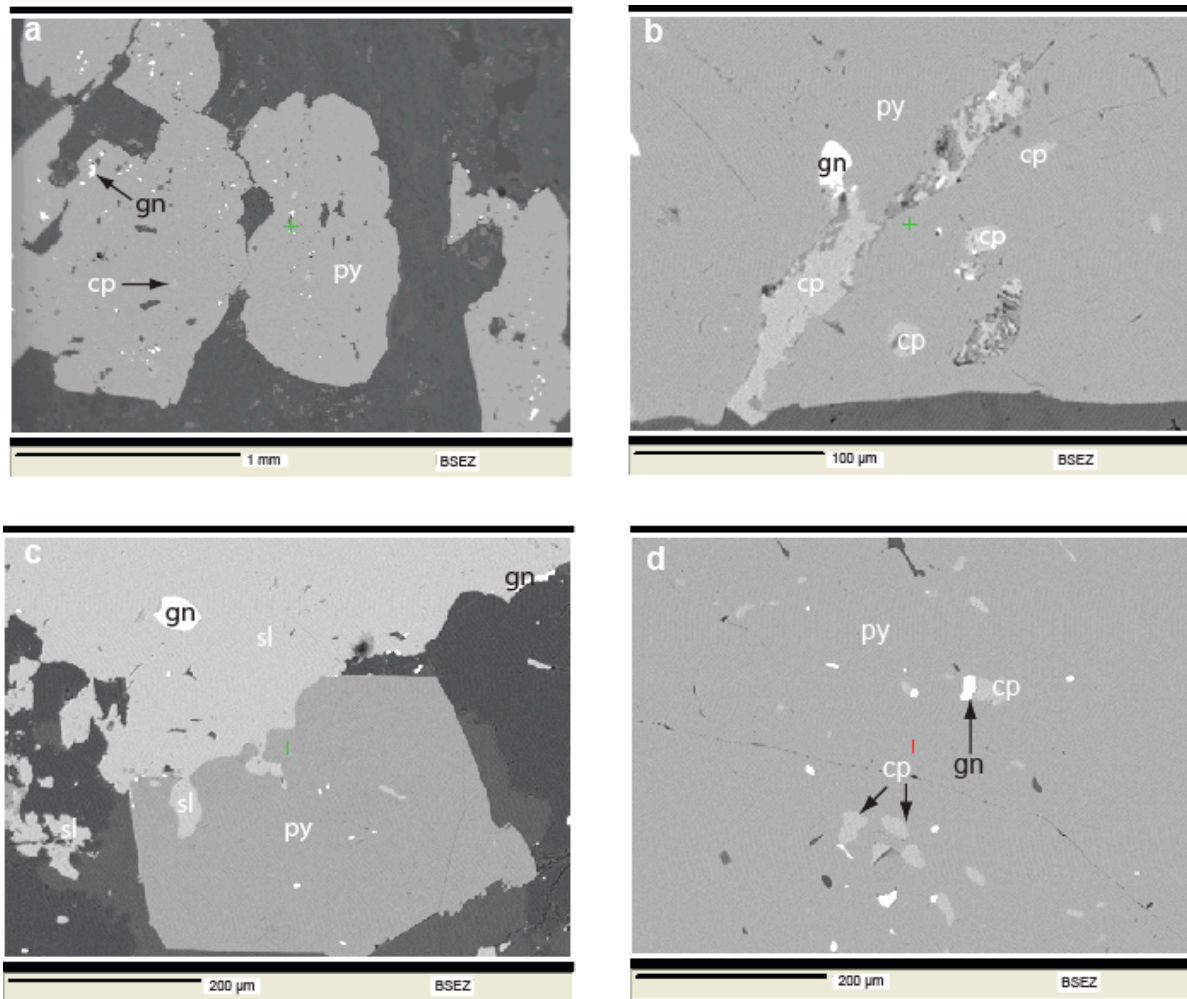


Fig. 4.7. Scanning electron micrographs (back scattered electron image) illustrating paragenetic relationships among sulfides a) clustered pyrite grains with galena I and chalcopyrite I inclusions; b) galena I and chalcopyrite I inclusions in pyrite I and chalcopyrite II filling fractures in pyrite I; c) pyrite II replaces sphalerite II; d) chalcopyrite I and galena I inclusions in pyrite I; galena I in contact with chalcopyrite I. Mineral abbreviations are the same as in Fig. 4.4.

Pyrite I hosts inclusions of chalcopyrite I and galena I (Fig. 4.4b; 4.7a). Sphalerite II contains inclusions of galena I and is cut by galena II veinlets (Fig. 4.4f; 4.7c). It overgrew pyrite I (Fig. 4.4d). Sphalerite II was replaced later by pyrite II (Fig. 4.7c). Chalcopyrite II filled fractures in pyrite I (Fig. 4.4a and Fig. 4.7b) and sphalerite II (Fig. 4.4g). The temporal relationship between galena I and chalcopyrite I is not clear. They may share common contacts (e.g. Fig. 4.7d). Cross-cutting relationships are not observed. Late stage calcite veinlet cut sphalerite II. Chalcopyrite may be partially converted into chalcocite (Fig. 4.4h), which is interpreted as a supergene alteration.

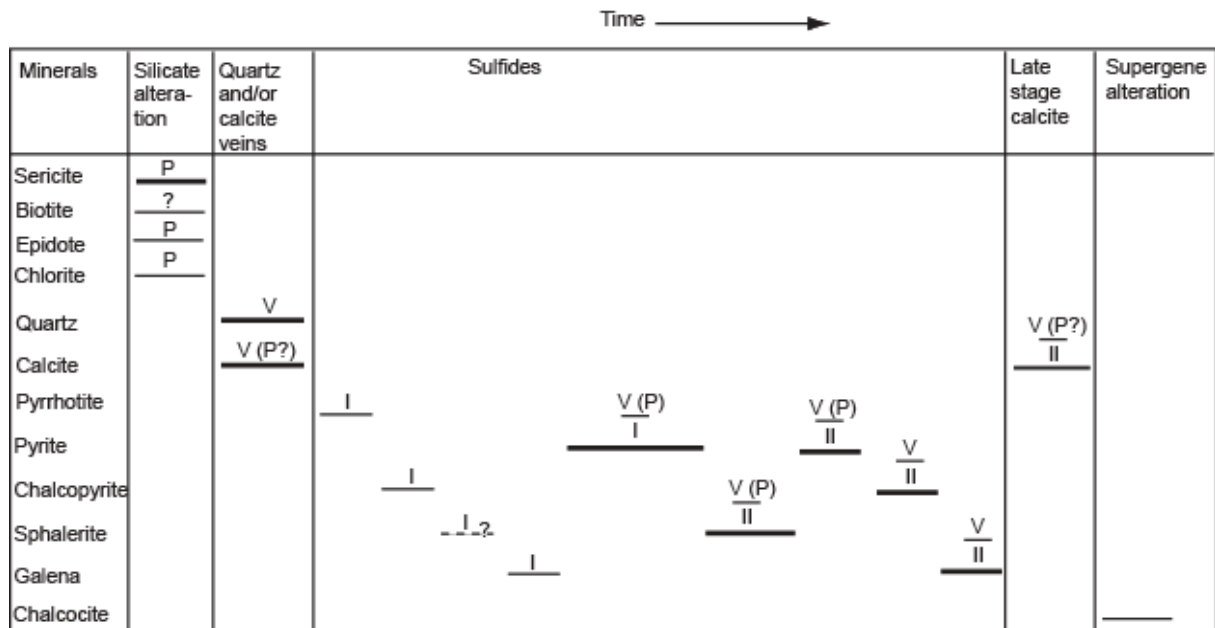


Fig. 4.8. Paragenetic scheme showing the relative temporal relationships of alteration and ore minerals. Abundance of the sulfides decreases from heavy to light lines. V = veinlet, P = pervasive, and dashed line and ? = uncertain. Roman numbers indicate the different generations of sulfides.

4.4 Geochemistry of mineralized rocks

Assaying of composite samples by the mining company revealed gold concentrations in the range of 0.02 to 7.7 ppm in the cores of the holes J2, J4, J5, J6, J7, and J9 (NMIc 2007, written communication; Fig. 4.1 and 4.5). A similar range of Au contents (4 to ~8 ppm) has been detected using whole rock geochemistry on drill core samples (i.e. handspecimen, this study, Table 4.1). The Au concentrations in the metasedimentary rocks are variable. Highest values were detected in the carbonatized chlorite-quartz schist (Table 4.1). Gold contents in the dikes/sills are low. Lamprophyres (e.g. J2-18) locally contain up to 122 ppb Au. Silver contents reach up to 76 ppm in the metasedimentary rocks and are below detection limits in the dikes/sills. In the mineralized area, Zn concentrations are up to 4220 ppm, Pb up to 1630 ppm, and Cu up to 176 ppm. There is no clear relationship that exists between Au and the base metals except that samples with highest gold values tend to have low copper values and vice versa (Table 4.1). Lead and Zn values tend to be high in the Au-rich metasedimentary samples. Cu contents are relatively high in the dikes/sills, and may be also elevated in the sediments in close proximity to the intrusive rocks.

Table 4.1. Gold (ppb) and base metal (ppm) content of drill core composite samples from Workamba area (average continental crust values of Taylor and McLennan 1985; Rudnick and Fountain 1995).

Rock type/description	Element	Au	Ag	As	Cu	Sb	Zn	Pb	Hg	Bi	Mo	Au/ Ag
	Unit	ppb	ppm	ppm	ppm	ppm	ppm	ppm	ppm	ppm	ppm	
	Detection limit	2	0.3	0.5	1	0.1	1	3	1	2	1	
Continental crust composition		3	0.08	1	24	0.2	80	8	<1	<2	1	0.04
Monzogranite	TG 06037	4	<0.3	2.7	1350	0.4	<1	35	<1	<2	<1	
Monzogranite	TG 06043	<2	<0.3	10.3	1350	1.8	40	33	<1	<2	<1	
Monzogranite	TG 06051	<2	<0.3	4.5	1700	1.5	40	34	<1	<2	<1	
Fine-grained monzogranite	J4-10	20	<0.3	2.3	1550	0.6	30	31	<1	<2	<1	
Fine-grained monzogranite	J2-14	7	<0.3	36.3	1600	1.9	<1	19	<1	<2	<1	
Lamprophyre	J2-18	122	<0.3	109	1650	2.4	<1	25	<1	<2	<1	
Lamprophyre	J2-30	<2	<0.3	4.3	1500	2.3	<1	13	<1	<2	3	
Sericite-quartz-chlorite schist	J2-05	<2	<0.3	9.4	1500	1.1	400	288	<1	<2	<1	
Chlorite-quartz schist	J2-15	6	<0.3	34.3	430	1.8	50	15	<1	<2	<1	
Chlorite-quartz schist	J2-19	41	<0.3	433	1750	13.9	50	36	<1	<2	10	
Carbonatized chlorite-quartz schist	J2-34	61	17	30.2	<1	11.8	1350	700	<1	<2	3	3.90
Chlorite-quartz schist	J2-23	20	<0.3	17.3	620	1.2	3240	1130	<1	<2	4	
Carbonatized chlorite-quartz schist	J7-12	8120	28.1	18.1	95	81.5	4220	1630	<1	<2	61	0.29
Carbonatized chlorite-quartz schist	J9-10	1790	5	115	124	5.1	2900	865	<1	<2	35	0.36
Carbonatized chlorite-quartz schist	J9-24	2210	75.5	853	176	37.9	685	239	<1	<2	73	0.03
Carbonatized chlorite-quartz schist	J9-28	1530	3	911	68	<0.1	142	92	<1	<2	3	0.51
Carbonatized chlorite-quartz schist	J9-32	7620	6.7	54.2	36	0.8	149	65	<1	<2	<1	1.14

Arsenic and Sb values are high (up to 911 ppm and 82 ppm respectively). Mercury and Bi concentrations are below detection limits in all rock types. Molybdenum contents are variable with highest values of 73 ppm in the metasedimentary rocks.

4.5. Sulfide mineral chemistry

Microprobe analysis was conducted on pyrite, sphalerite, and galena to determine their trace element contents and mineral inclusions. The analysis was done on Cameca SX100 microprobe at the Mineralogy section of the Department of Earth and Environmental Sciences. Selected results of the electronprobe micro analyses are presented in Table 4.2. Analytical conditions, machine settings, and results are given in Annexes 3.1 and 3.2.

Natural pyrite may contain minor to trace amounts of e.g. Ni, Co, As, Cu, Zn, and/or Ag (Schröcke and Weiner 1981). Pyrite at Workamba has Ni contents of less than 0.1 wt. %, and

As up to 0.1 wt. %. Cobalt was not detected (Table 4.2). The Fe content in natural sphalerite is highly variable, reaching up to 18 wt. % (Schröcke and Weiner 1981). According to Schröcke and Weiner (1981), this mineral phase may also contain trace quantities of Cd and/or Mn (up to 1.6%). Sphalerite from the study area is characterized by moderate to low amounts of Fe (up to 10 wt. % with a median of 2.6 wt. %) and trace quantities of Cd and Mn (Table 4.2). Silver production from galena-rich ores is common since this mineral may be host to recoverable concentrations of Ag (up to 1 wt. %, Schröcke and Weiner 1981). Galena from Workamba, however, contains low quantities of Ag (up to 0.07%). No free gold was detected within or between grain boundaries of the sulfides during the back-scattered electron image scanning.

Table 4.2. Representative microprobe analysis results of sulfides from the study area. All results are in wt. %, n.d. = not determined.

Pyrite						Sphalerite						Galena			
S	54.60	54.70	54.80	54.70	54.30	32.09	32.44	36.42	35	39.60	32.40	13.25	13.10	13.40	13.50
Fe	43.10	43.40	43.40	43.40	43.80	1.92	1.69	10.16	5.31	7.21	1.69	0.02	0.00	0.09	0.00
Mn	n.d.	n.d.	n.d.	n.d.	n.d.	0.06	0.06	0.15	0.23	0.21	0.06	0.01	0.02	0.00	0.00
Co	0.00	0.00	0.00	0.00	0.00	n.d.	n.d.	n.d.	n.d.	n.d.	n.d.	n.d.	n.d.	n.d.	n.d.
Ni	0.09	0.03	0.04	0.00	0.03	n.d.	n.d.	n.d.	n.d.	n.d.	n.d.	n.d.	n.d.	n.d.	n.d.
Cu	0.06	0.07	0.00	0.00	0.00	0.08	0.00	0.46	0.38	0.08	0.00	0.02	0.00	0.02	0.03
Zn	0.20	0.07	0.01	0.00	0.00	60.14	66.36	53.26	58.50	50.90	66.40	0.01	0.07	0.02	0.00
As	0.09	0.02	0.11	0.07	0.01	n.d.	n.d.	n.d.	n.d.	n.d.	n.d.	n.d.	n.d.	n.d.	n.d.
Ag	0.00	0.00	0.00	0.00	0.00	0.00	n.d.	n.d.	n.d.	n.d.	n.d.	0.07	0.00	0.03	0.01
Pb	n.d.	n.d.	n.d.	n.d.	n.d.	0.00	0.00	0.00	0.00	0.00	0.00	86.64	86.60	86	86
Cd	n.d.	n.d.	n.d.	n.d.	n.d.	0.23	0.11	0.17	0.22	0.13	0.11	n.d.	n.d.	n.d.	n.d.
Total	98.10	98.3	98.30	98.10	98.20	100.50	100.70	100.60	99.70	98.10	101	100.10	100	99.60	99.60

5. Microthermometry

5.1 Sampling and petrography

Two carbonatization or calcite \pm quartz veining events bracket mineralization at Workamba (see paragenetic sequence, Chapter 4). This relationship suggests that primary fluid inclusions in quartz-calcite veins provide the closest information on the nature of the mineralising hydrothermal fluids at Workamba. Unmineralized, monomineralic quartz, or mineralized quartz-calcite veins were sampled for fluid inclusion studies. The samples of the unmineralized quartz veins were taken about 100 m away from the mineralized zone, whereas the samples of the mineralized quartz-calcite veins were selected from drill cores.

Petrographic studies were conducted on eight double polished 100 μ m thick slabs to determine the nature (primary, pseudosecondary, or secondary) and type of fluid inclusions (liquid or vapour dominated, number of phases present at room temperature, etc.) present, degree of filling, and behavior during freezing and heating. The quartz of the monomineralic veins contains relatively abundant fluid inclusions as compared to that of the quartz-calcite veins. In the quartz-calcite veins, the fluid inclusions hosted in the quartz are more abundant and larger compared to those in the calcite. Generally, three types of fluid inclusions are distinguished (Fig. 5.1) in both the unmineralized, monomineralic quartz, and mineralized quartz-calcite veins: liquid-only (type I), liquid-rich two-phase (Type II), and vapour-rich two-phase (Type IIIA and IIIB).

5.1.1 Liquid-only fluid inclusions (Type I)

Liquid-only fluid inclusions are small, commonly less than 2 μ m. They occur as intergranular planar trails or isolated inclusions. Those occurring in planar trails are abundant. Liquid-only fluid inclusions coexist with the liquid- and vapour-rich fluid inclusions. They display circular to polygonal shape (Fig. 5.1).

5.1.2 Liquid-rich two-phase fluid inclusions (Type II)

Liquid-rich two-phase fluid inclusions are the predominant inclusion type in unmineralized quartz and mineralized quartz-calcite veins. Their size varies from 2 to 16 μ m (Fig. 5.1). The relatively big (\sim 16 μ m) inclusions are common in the unmineralized quartz veins. Liquid-rich two-phase fluid inclusions commonly show a uniform liquid/vapour ratio, with \sim 80% of liquid filling at room temperature. In general, they occur in inter to intra-granular fracture

healings (e.g. Fig. 5.2a), as clustered fluid inclusions (Fig. 5.2b) or as isolated inclusions (Fig. 5.2c, bottom right). Type II fluid inclusions commonly display rounded to polygonal shapes. Inclusions with irregular form are also observed (e.g. Fig. 5.2d).

5.1.3 Vapour-rich two-phase fluid inclusions (Type III)

Vapour-rich two fluid inclusions are found commonly coexisting with liquid-rich two-phase and liquid-only fluid inclusions in both the mineralized quartz and unmineralized quartz-calcite veins (Fig. 5.2a, b, c, and d).

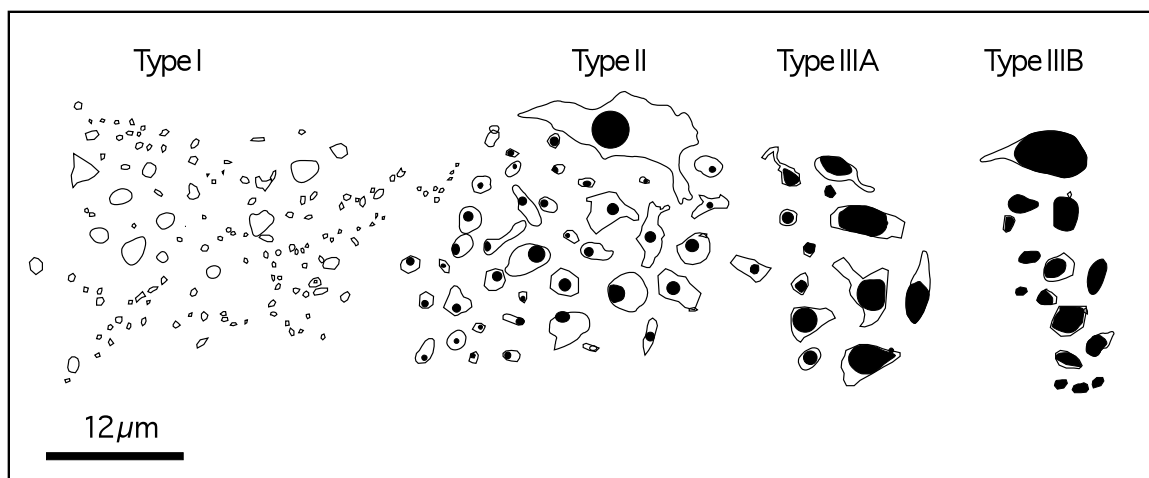


Fig. 5.1. Sketch of fluid inclusions types in the unmineralized quartz and mineralized quartz-calcite veins at Workamba.

Their size varies from 4 to 10 μm . Type III inclusions are subdivided in to two groups (Type IIIA and Type IIIB) based on their liquid and vapour volume percentages (Fig. 5.1). Type IIIA has between 60 to 80% of vapour in volume, and Type IIIB > 80% (vapour-dominated with or without small amount of liquid). Type III fluid inclusions have similar mode of occurrence, but are less abundant as compared to the liquid-rich two-phase fluid inclusions. They display rounded, polygonal, and irregular shape.

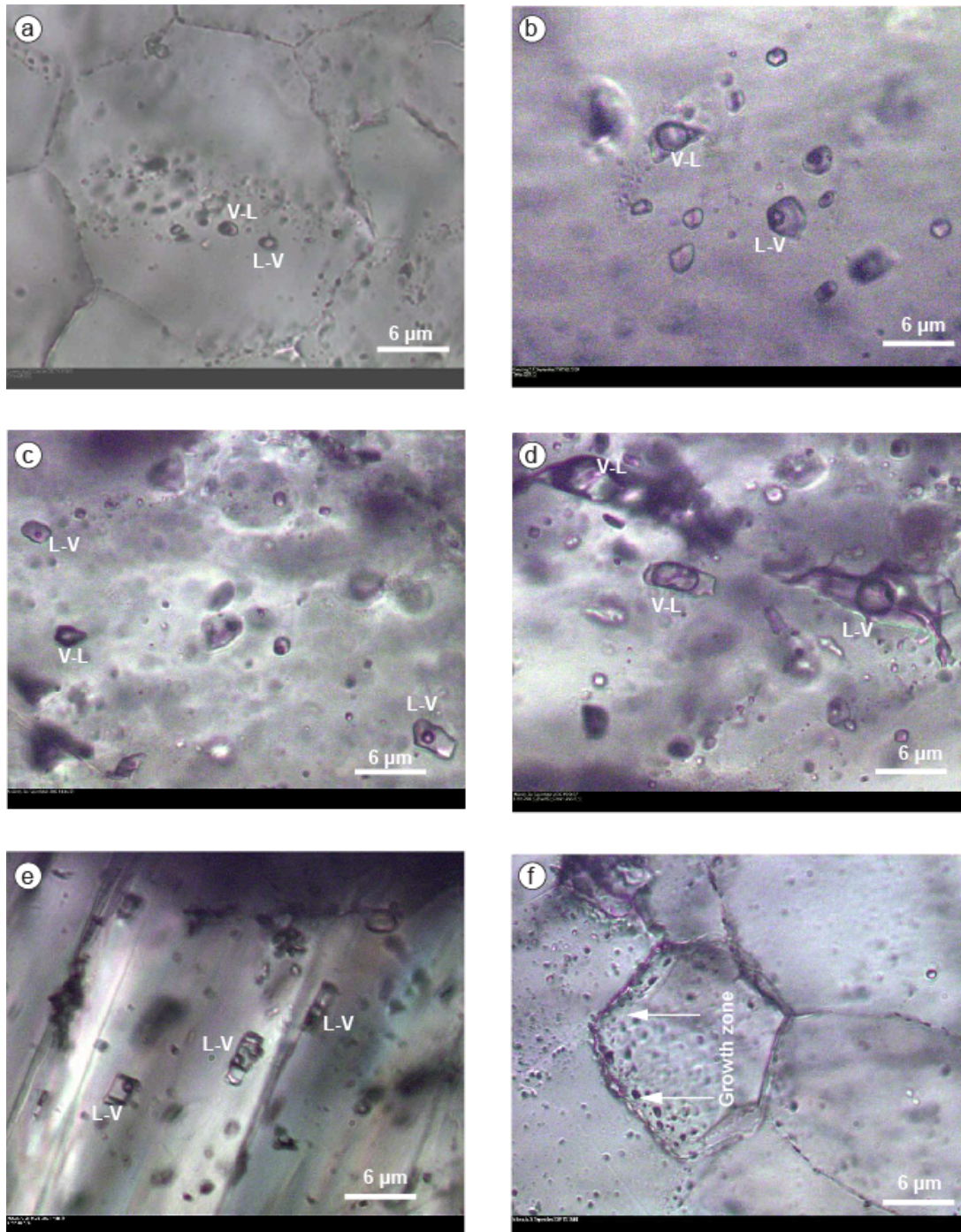


Fig. 5.2. a) Secondary to pseudo-secondary fluid inclusions crossing or terminating at the grain boundaries; b) example of cluster of liquid-only, liquid-rich, and vapour-rich two phase fluid inclusions present in a quartz grain; c) occurrence of isolated liquid-only, liquid- and vapour-rich two phase fluid inclusions in quartz; d) irregularly shaped two phase liquid- and vapour-rich fluid inclusions coexisting in quartz veins; e) isolated liquid-rich two-phase fluid inclusions with negative crystal shapes in calcite; f) possibly primary fluid inclusions in weakly developed growth zone in quartz (center left of image). Abbreviations: V = vapour and L= liquid.

5.2 Nature of fluid inclusions

According to Roedder (1984) and Goldstein and Reynolds (1994), primary fluid inclusions are trapped by mechanisms such as cavities formed at the center of the crystal faces due to lack of sufficient nutrients as compared to the crystal edges, which are closed by later crystal growth; voids resulting from rapid crystal growth that are filled later by the fluid flowing over the crystal; disturbance of growth of a crystal, e.g. by formation of cracks, or creating reentrants that are later sealed, among others. No strongly developed growth zones that could suggest the existence of primary fluid inclusions have been recognized. The predominant occurrence of the fluid inclusions in fracture healings and the termination of some of the planar trails at the grain boundary suggest that they are either secondary or pseudo-secondary, respectively. However, the existence of some isolated, negative crystal shape, and intragranular liquid-rich two phase fluid inclusions in calcite (Fig. 5.2e) and quartz may suggest that such inclusions are primary. Primary fluid inclusions might have also trapped in some weakly developed growth zones (e.g. Fig. 5.2f)

5.3 Microthermometric measurements

Microthermometric measurements of the fluid inclusions described above were performed using a Linkam TMS 94 microthermometer connected to a THMGS 600 heating-freezing stage mounted on a modified Leitz Laborlux 12 POL microscope. The heating-freezing stage is calibrated with synthetic standards. Heating-freezing procedures according to Roedder (1984) and Goldstein and Reynolds (1994) were applied for the measurements. The final melting temperature of ice was obtained using cycling methods of Goldstein and Reynolds (1994). The fluid salinity was determined from the Freezing Point Depression (FPD) table of Bodnar (1992a), which was calculated from Bodnar (1992a) equation of state for the H₂O-NaCl system by relating final ice melting temperature to salinity. The accuracy of ice melting temperature measurements is $\pm 0.5^{\circ}\text{C}$ and that of homogenization temperature is $\pm 1^{\circ}\text{C}$. The microthermometric data is presented in Annex 4.1.

5.3.1 Type I fluid inclusions

Many Type I inclusion did not show any phase change at all upon cooling over a temperature range from 0 to -120°C . The group of inclusions showing phase changes did so over a relatively wide temperature range. During freezing, ice crystals formed in some Type I fluid inclusions below -26°C . Initial ice melting occurred around -14°C . The final melting temperature between -1 to -5°C was determined on four inclusions. The calculated fluid

salinities are between 1.74 to 7.86 wt. % $\text{NaCl}_{\text{equiv}}$.

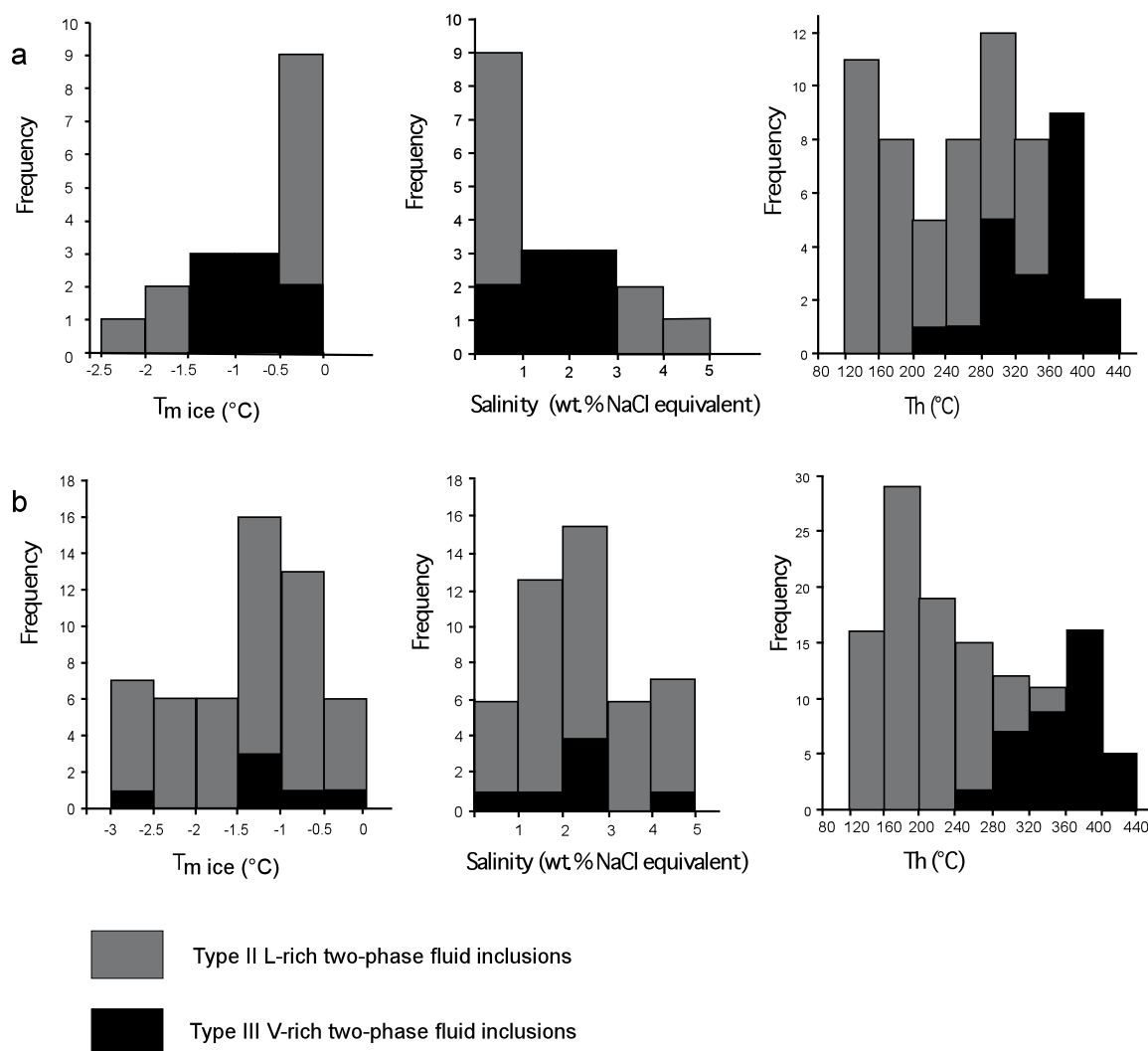


Fig. 5.3. Histograms showing the ranges of ice melting temperature, salinity and homogenization temperatures of fluid inclusions in mineralized quartz-calcite veins (Fig. 5.3a) and unmineralized quartz veins (Fig. 5.3b).

5.3.2 Type II fluid inclusions

Heating-cooling experiments were performed on Type II fluid inclusions from both unmineralized quartz and mineralized quartz-calcite veins. These Type II inclusions showed some differences in their physical behavior upon freezing regardless of the type of host mineral. In some inclusions, the gas bubble disappeared at -31°C due to ice expansion, whereas in most of the remaining the vapour bubble existed as low as -150°C , although its overall size decreased. Ice melting temperatures for the fluid inclusions hosted in mineralized quartz-calcite veins vary from -0.5 to -2.5°C with estimated salinities of 1 to 4 wt. % $\text{NaCl}_{\text{equiv}}$. (Fig. 5.3a). Upon heating, the fluid inclusion homogenizes into a liquid phase at

temperatures ranging from 160 to 387°C (Fig. 5.3a). Type II fluid inclusions in unmineralized quartz veins have similar ice melting temperatures and salinities ranging from -0.5 to -3°C or 1 to 5 wt.% NaCl_{equiv} respectively (Fig. 5.3b). They homogenize into a vapour phase at temperatures between 120 and 320 °C (Fig. 5.3b).

5.3.3 Type IIIA and B fluid inclusions

Microthermometric measurements on Type IIIA fluid inclusions yielded ice melting temperature that range from -0.5 to -1.5 °C and calculated salinities between 1 to 3 wt. % NaCl_{equiv}. for the mineralized quartz-calcite veins (Fig. 5.3a), and -0.5 to -3°C with salinities from 1 to 5 wt. % NaCl_{equiv}. for the unmineralized quartz veins (Fig. 5.3b). The final ice melting temperature for the vapour-rich Type IIIB inclusions could not be determined. The homogenization temperatures of Type IIIA and B fluid inclusions are similar ranging from 256 to 405 °C (Fig. 5.3a and b) and are higher than that of Type II. Type IIIA fluid inclusions homogenize to a liquid, whereas Type IIIB to a vapour phase.

5.4 Interpretation of the fluid inclusion data

The microthermometric measurements suggest that all fluid inclusions are of low salinity aqueous types. The presence of co-existing liquid- and vapour-rich two phase fluid inclusions may be explained by heterogeneous entrapment of these phases during boiling or necking down of homogenous fluid after entrapment and phase changes by cooling (Goldstein and Reynolds 1994; Loucks 2000). Evidences that suggest boiling during entrapment include similar homogenization temperatures of the vapour- and liquid-rich fluid inclusion assemblages, presence of individual growth zones that suggest both (vapour- and liquid-rich) fluid inclusion types are contemporaneous, and lower salinity of the vapour-rich inclusions as compared to the liquid-rich once. The occurrences of only vapour-rich fluid inclusions along healed fractures could also imply boiling prior to entrapment (Bodnar et al. 1985). Boiling of a homogenous fluid also occurs at shallow depths (~1 km deep) under hydrostatic pressure or a pressure that exceeds hydrostatic but less than lithostatic (Reed and Spycher 2000). On the other hand, the criteria suggesting necking down, in addition to the presence of vapour- and liquid-rich fluid inclusions, are variable salinities and homogenization temperatures of the fluid inclusion assemblages, irregular shapes of the fluid inclusions, and the occurrence of closed off necks between adjacent fluid inclusions (Goldstein and Reynolds 1994). The presence of one-phase liquid-filled inclusions and different L/V ratios among the liquid-rich fluid inclusions could also indicate necking down (Bodnar et al. 1985).

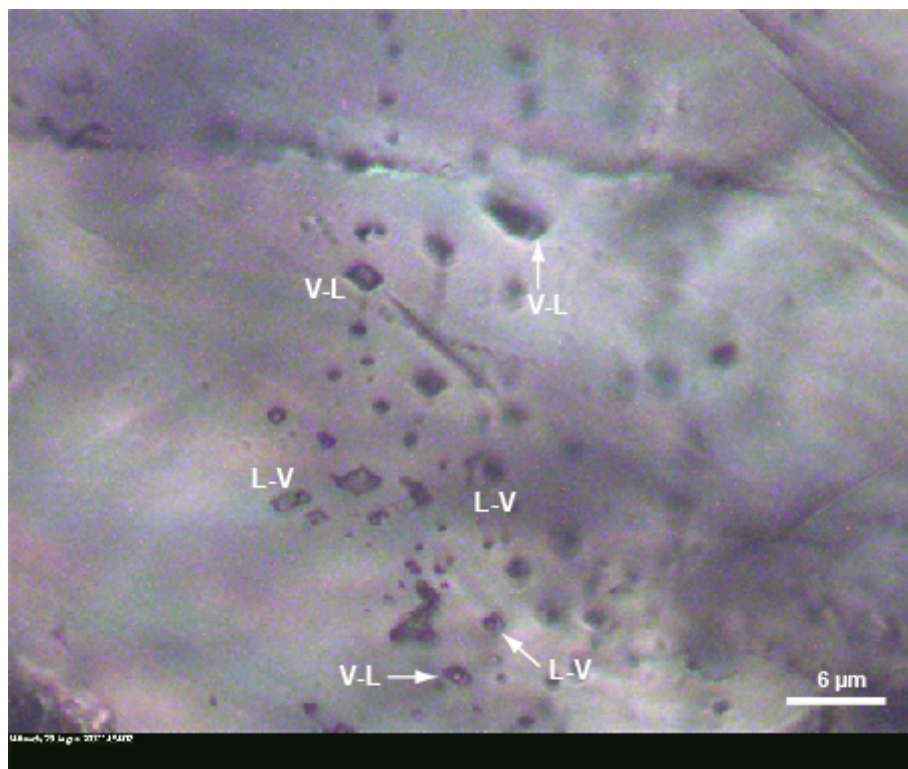


Fig. 5.4. Photomicrograph showing co-existing liquid- and vapour-rich two-phase fluid inclusions in calcite with similar homogenization temperatures as described in the text. This could suggest the fluid inclusions are entrapped during boiling.

The coexisting Type I, II, and III fluid inclusions may also be simply formed by different aqueous fluids. The fact that the mineralized quartz-calcite and unmineralized quartz veins contain essentially the same types of fluid inclusions is consistent with such a hypothesis.

The homogenization temperature of the coexisting liquid-rich and vapour-rich fluid inclusion assemblages (types II and III) along healed fractures in the quartz and quartz-calcite veins are different suggesting that the inclusions are not of same origin (i.e.. they were not formed by boiling). Healed fractures hosting solely vapour-only fluid inclusions, which could imply boiling at a deeper level and before entrapment, are not recognized in the studied samples. However, some fluid inclusion assemblages of these type II and III, with similar homogenization temperatures between the vapour-and liquid-rich fluids are recognized in calcite (e.g. Fig. 5.4). Six liquid-rich fluid inclusions in a sample shown in Fig. 5.4 homogenize between 270 to 305°C to a liquid, and three vapour-rich fluids homogenize between 291 to 341°C to a vapour phase. However, there are no well developed growth zones in calcites or quartz that could indicate that the co-existing vapour- and liquid-rich fluid inclusions are contemporaneous.

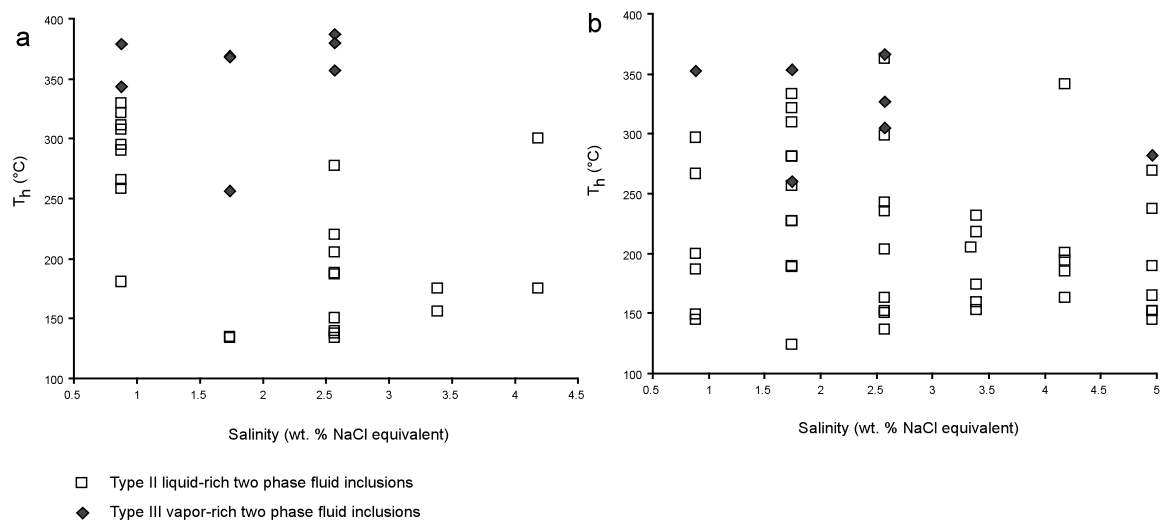


Fig. 5.5. Homogenization temperature (T_h) versus salinity diagrams a) for mineralized quartz-calcite veins; and b) for unmineralized quartz veins. Generally, the homogenization temperature and salinities of the fluid inclusions are variable, which could suggest necking down of the inclusions after entrapment.

The coexistence of liquid-only, liquid-dominated and vapour-rich fluid inclusion assemblages, variable homogenization temperatures and salinities of the fluid inclusions (Fig. 5.5), and irregular shapes of some of the fluid inclusion assemblage suggest that the inclusions experienced necking down (e.g. Fig. 5.2d). However, there are liquid-rich two-phase fluid inclusions (Type II) with homogenous liquid to vapour ratios in negative crystal shape. They occur isolated or in fracture healings in both quartz and calcite grains and do not show evidence of closed off necks between adjacent inclusions (Fig. 5.2e). Thus, this type of liquid-rich two-phase fluid inclusions might be resulted from natural cooling of a trapped homogeneous fluid and the measured phase changes are useful for geological interpretations (Roedder 1984; Goldstein and Reynolds 1994).

6. Isotope geochemistry

6.1. Sulfur isotope analysis and result

Ten sulfide samples (5 pyrite; 3 sphalerite; 2 galena) from drill cores were prepared for sulfur isotope analysis. The sulfides were collected from chlorite-quartz or carbonatized-chlorite-quartz schists (Table 6.1). Pyrites are extracted from continuous to discontinuous veinlets coexisting with calcite (samples J2-35; J2-36) or that cut the foliation (samples J5-10; J9-31; GBH18-58). Two of the sphalerite samples are taken from discontinuous veinlets and disseminated grains (samples GBH18-28; GBH10-84). One sphalerite sample is collected from a veinlet, which later have been reopened and re-used by later calcite (sample GBH10-59). The galena samples are prepared from veinlets, one (sample GBH18-25) of which is cutting a quartz veinlet.

Sulfur isotope analysis was performed in the stable isotope laboratory of the Institute of Mineralogy at the TU Bergakademie Freiberg, Germany. Analytical method and errors are given in the annex 5.1. The $\delta^{34}\text{S}$ are reported relative to the Vienna Canyon Diablo Troilite standard (VCDT). The sulfur isotope ratios of pyrite and/or chalcopryrite, sphalerite and galena range from 1.8 to 9.1 ‰ with an average value of ~ 6.4 ‰ (Table 6.1). No significant variations in the $\delta^{34}\text{S}$ values between the different sulfide species are observed.

Table 6.1 Results of sulfur isotope analysis.

Sample	Description	$\delta^{34}\text{S}(\text{‰})\text{VCDT}$
J2-26	Galena veinlet cutting carbonatized chlorite-quartz schist	6.6
J2-35	Pyrite veinlets cutting the foliation and coexisting with calcite	6.3
J2-36	Pyrite veinlets associated with calcite	3.7
J5-10	Pyrite veinlets cutting the foliation	2.3
J9-31	Pyrite with minor galena, sphalerite, pyrrhotite, and chalcopryrite	6.4
GBH18-25	Galena vein cutting quartz veinlet	4.3
GBH18-28	Sphalerite disseminations in carbonatized chlorite-quartz schist	7.7
GBH18-58	Pyrite with minor chalcopryrite and galena inclusions	1.8
GBH10-59	Sphalerite veinlet re-opened by calcite veinlet	7.8
GBH10-84	Sphalerite veinlets and disseminated grains in carbonatized chlorite-quartz schist	9.1

The range sulfur isotope ratios ($\delta^{34}\text{S}$ from 1.8 to 9 ‰) from the study area exceed the range commonly accepted for sulfur of magmatic origin. However, a magmatic sulfur input can not be excluded because a similar sulfur isotope signature may be resulted through direct reduction of magmatic SO_2 (e.g. Ohmoto and Rye 1979). Chang et al. (2008) discussed sulfur isotope signatures of sulfides of sediment-hosted orogenic gold deposits (Fig. 6.1). The sulfur isotope composition of sulfides from these deposits of various ages show a pattern generally parallel to the seawater sulfate curve through geologic time, suggesting that the sulfur in these deposits originated from the reduction of seawater sulfate.

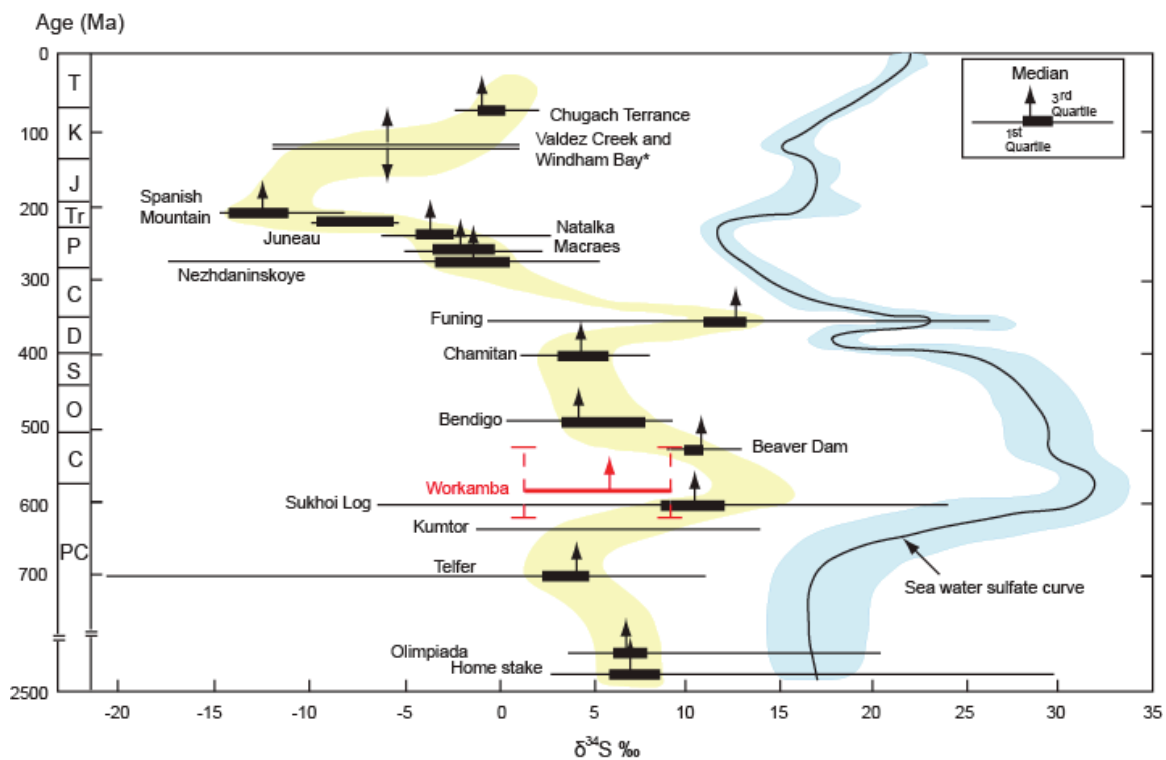


Fig. 6.1. Sulfur isotope compositional range of sulfides of sediment-hosted orogenic gold deposits through time and seawater sulfate curve, after Chang et al. (2008). The range of sulfur isotope ratios of sulfides from Workamba are shown for comparison. Assuming a mineralization age at Workamba from 620 to 520 Ma, the sulfur isotope composition could fit the $\delta^{34}\text{S}$ trend defined by the sediment-hosted orogenic gold deposits.

The age of mineralization at Workamba most likely occurred within or shortly after 620 to 520 Ma (see discussion below). Depending on the exact mineralization age, the sulfur isotope data presented here could fit the curve defined by the sulfur isotope composition of orogenic gold deposits of Chang et al. (2008; Fig. 6.1).

However, the probability that the sulfur is originated from seawater is low. There is no sedimentary record in the area between 620 to 520 Ma and shortly thereafter indicating the presence of marine conditions in the region. Tectonic deformation possibly accompanied by uplift took place before the intrusion of 620 to 520 Ma post-tectonic granites, which would favour continental conditions and erosion. The $\delta^{34}\text{S}$ value of Workamba sulfides are within the range of those of island arc volcanic rocks (-0.2 to +20.7 ‰, Rollinson 1993). Therefore, the sulfur of the sulfides at Workamba may be dominantly derived from the country rocks (Tsaliet and Tambien Group rocks) through leaching by hydrothermal fluids.

6.2 Carbon and oxygen isotope analyses

Five samples of calcite were taken from hydrothermal calcite \pm quartz veinlets that cut the metasedimentary rocks or dikes/sills for carbon and oxygen isotope analyses. The analytical work was performed in the stable isotope laboratory of the GeoBioCenter, Munich, Germany. The analytical method is detailed in annex 5.2.

Table 6.2. Results of carbon and oxygen isotope analysis.

Sample	Description	$\delta^{13}\text{C}(\text{‰})$	$\delta^{18}\text{O}(\text{‰})$	$\delta^{18}\text{O}(\text{‰})$
		VPDB	VPDB	VSMOW
J4-28-1	Calcite veinlet cutting dikes/sills	-2.9	-16.9	13.4
J4-29-1	Calcite vein cutting dikes/sills	-3.2	-18.9	11.4
J5-14	Calcite veinlet cutting chlorite-quartz schist	-5.6	-15.5	14.9
J6-07	Calcite veinlet cutting chlorite-quartz schist	1.8	-19.1	11.2
J6-12	Calcite veinlet coexisting with sulfides in chlorite-quartz schist	1.1	-19.1	11.3

The isotope ratios are stated relative to Vienna PDB (Peedee Belemnite; $\delta^{13}\text{C}_{(\text{VPDB})}$ or $\delta^{18}\text{O}_{(\text{VPDB})}$) or Vienna Standard Mean Ocean Water; $\delta^{18}\text{O}_{(\text{VSMOW})}$). Results are given in Table 6.2. $\delta^{13}\text{C}_{(\text{VPDB})}$ or $\delta^{18}\text{O}_{(\text{VPDB})}$ values of nearby Tambien Group rocks are reported in annex 5.3. The $\delta^{13}\text{C}_{(\text{VPDB})}$ values of the calcite vary from -5.6 to +1.8 ‰ (Table 6.2).

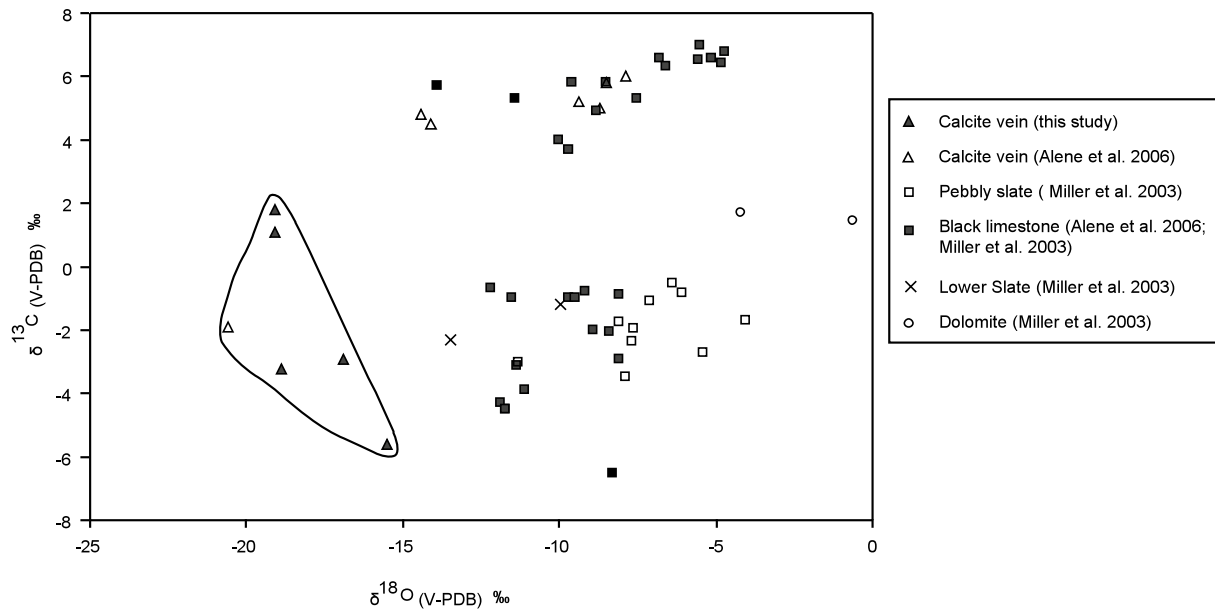


Fig. 6.2. $\delta^{13}\text{C}$ relative to $\delta^{18}\text{O}$ plot of the Workamba hydrothermal calcite veins (closed line) together with data of nearby carbonates and metasedimentary rocks from Alene et al. (2006) and Miller et al. (2003). $\delta^{13}\text{C}$ isotope of the hydrothermal calcite veins of this study show similar range with the nearby carbonates and metasedimentary rocks suggesting the carbon is dominantly derived from Tambien Group rocks. Calculated $\delta^{13}\text{C}$ signature of a fluid in equilibrium with calcite is consistent with derivation of C from carbonate rocks.

The oxygen isotope values range from -19.1 to -15.5 ‰ $\delta^{18}\text{O}_{(\text{VPDB})}$, or $\delta^{18}\text{O}_{(\text{VSMOW})}$ from 11.2 to 14.9 ‰, respectively. The $\delta^{13}\text{C}_{(\text{VPDB})}$ signature of calcites from Workamba (-5.6 to 1.8 ‰) is similar to that of limestones of Rollinson (1993), with $\delta^{13}\text{C}_{(\text{VPDB})}$ between ~ -12 to 3 ‰. It overlaps with that of Tambien Group limestones, and epiclastic metasedimentary rocks, and hydrothermal calcite veinlets in Tambien Group black limestone ($\delta^{13}\text{C}_{(\text{VPDB})}$ from -4.5 to 7 ‰; Alene et al. 2006; Miller et al. 2003; Fig. 6.2; Annex 5.2). However, the $\delta^{18}\text{O}_{(\text{VPDB})}$ values of Workamba calcite (-15.5 to -19.1 ‰, Table 6.2) are significantly lower than the nearby Tambien Group limestones, and epiclastic metasedimentary rocks ($\delta^{18}\text{O}_{(\text{VPDB})} = -4.7$ to -13.9 ‰; Alene et al. 2006; Miller et al. 2003; annex 5.3). They lie within the range of values of the vein carbonates ($\delta^{18}\text{O}_{(\text{VPDB})} = -7.9$ to -20 ‰) analyzed by Alene et al. (2006). Alene et al. (2006) suggest that the carbon source of the vein carbonates could be the regionally exposed limestones as they have similar $\delta^{13}\text{C}$ compositions. They also proposed that the lower $\delta^{18}\text{O}$ values of some of the carbonate rock samples could be due to interactions with low $\delta^{18}\text{O}$ bearing meteoric or metamorphic fluids that formed the vein carbonates.

The $\delta^{18}\text{O}$ and $\delta^{13}\text{C}$ isotope compositions of an aqueous fluid in equilibrium with the hydrothermal calcite can be calculated if the calcite formation temperature is known. The temperature of formation can be obtained from microthermometric measurement of primary fluid inclusions in the calcite. Although, the majority of the fluid inclusions are secondary or pseudo-secondary in origin, some liquid-rich two phase fluid inclusions with negative crystal shapes in calcite have been observed. They are interpreted as of primary origin. Nine of these primary fluid inclusions homogenized between 220 to 340°C with an average of 293°C. If this average homogenization temperature is used as a proxy for the calcite formation temperature, a fluid in equilibrium would have calculated $\delta^{18}\text{O}_{(\text{VPDB})}$ values between -24.9 and -21.3 ‰ or $\delta^{18}\text{O}_{(\text{VSMOW})}$ values between 5.1 to 8.7 ‰. Calculated $\delta^{13}\text{C}_{(\text{VPDB})}$ values for the fluid are between -3.7 and +3.7 ‰ (fractionation factors for calcite- H_2O from Friedman and O'Neil 1977 and for calcite- CO_2 from Ohmoto and Rye 1979). The calculated oxygen isotope signature of the hydrothermal fluid is compatible with magmatic or metamorphic fluid origin (e.g. Rollinson 1993). The similarities between the $\delta^{13}\text{C}_{(\text{VPDB})}$ signature of hydrothermal calcite of this study and the calculated $\delta^{13}\text{C}_{(\text{VPDB})}$ values of a hydrothermal fluid in equilibrium with the nearby carbonate and metasedimentary rocks supports the conclusions of Alene et al. (2006), i.e., most of the carbon is originated from these Tambien Group rocks.

6.3 Lead isotope analysis and result

Eleven sulfide (pyrite, galena, and sphalerite), five whole-rock samples, and three feldspar separates were prepared for lead isotope analysis (Table 6.3 and 6.4). Lead isotope analysis was carried out at the laboratory for radiogenic isotopes of Bayerische Staatssammlung für Paläontologie und Geologie, Munich. The detailed information on sample location, description and analytical method is reported in Annexes 5.4 and 5.5. Initial lead ratios were determined for the whole-rock samples to remove radiogenic Pb based on the measured lead isotope ratios, current concentrations of U and Th, and ages of the intrusive, metavolcanic, and metasedimentary rocks. The measured and corrected Pb isotope ratios are provided in Table 6.3 and 6.4. The $^{208}\text{Pb}/^{204}\text{Pb}$, $^{207}\text{Pb}/^{204}\text{Pb}$, and $^{206}\text{Pb}/^{204}\text{Pb}$ values of sulfides from the study area, which range between 36.94 to 36.99, 15.47 to 15.49, and 17.36 to 17.38 respectively, are generally low as compared to the values for the feldspars and whole-rock sample of the fine-grained monzogranite dike/sill but are similar to those of metasedimentary and metavolcanic rocks. They are also characterized by uniform values indicating that they are derived from homogeneous source (e.g. Tosdal et al. 1999). Figure 6.3 a and b shows the Pb isotope data of rocks and sulfides relative to the mantle, upper crust, lower crust, and

orogene version II growth curves of Zartman and Doe (1981). Lead isotope ratios of sulfides plot close together with a quartz-sericite-chlorite schist host rocks (J2-015; Tambien Group) and a metavolcanic rock (Tsaliet Group). The intrusive rocks define a separate field due to higher $^{208}\text{Pb}/^{204}\text{Pb}$, $^{207}\text{Pb}/^{204}\text{Pb}$ and $^{206}\text{Pb}/^{204}\text{Pb}$ values. In the $^{207}\text{Pb}/^{204}\text{Pb}$ versus $^{206}\text{Pb}/^{204}\text{Pb}$ diagram, all of these sample data lie between the mantle and orogene growth curves (Fig 6.3b). A black slate (Tambien Group) is shown in the $^{207}\text{Pb}/^{204}\text{Pb}$ and $^{206}\text{Pb}/^{204}\text{Pb}$ diagram (Fig 6.3b). However, due to a relatively low $^{208}\text{Pb}/^{204}\text{Pb}$ value (19.711, Table 6.3), its data point lies outside the plotted area shown in Fig. 6.3a. Another quartz-sericite-chlorite schist (TG06015, sampled outside the mineralized zone) also shows anomalous Pb isotope ratios and plots far to the right of the fields of intrusive rocks (Fig. 6.3a and b). The calculated low $^{208}\text{Pb}/^{204}\text{Pb}$ initial value of the black slate (TG06034) and high $^{208}\text{Pb}/^{204}\text{Pb}$ initial value of the quartz-sericite-chlorite schist (TG06015) suggest that the measured lead isotope ratios of these two rocks are dominated by radiogenic Pb. Both samples (TG06015 and TG06034), therefore, did not retain their original Pb isotope signatures and are excluded from the petrogenetic discussion. The lead isotope ratios of metasedimentary, metavolcanic, and intrusive rocks, which plot between the mantle and orogene curves suggests a significant mantle component in these rocks (Fig. 6.3). The Pb isotope signature of the intrusive rocks is similar to MORB or primitive arc igneous rocks as indicated by the discrimination diagrams of Zartman and Doe (1981; Fig. 6.3c, and d). The low $^{208}\text{Pb}/^{204}\text{Pb}$ and $^{207}\text{Pb}/^{204}\text{Pb}$ values of the metasedimentary and metavolcanic rock suggest that they are more primitive as the post-tectonic dikes/sills, which is compatible with the geochemical data (chapter 3).

The ANS in Eritrea and Tigray predominantly represent juvenile crust derived from a depleted mantle source (e.g. Vail 1983, 1986; Kröner et al. 1991; Tadesse et al 1999, 2000; Stern and Abdelsalam 1998; Teklay et al. 2002; Andersson et al. 2006). The Tsaliet Group shows MORB characteristics at Axum, mixed MORB island ocean basalt to immature island arc tholeiite geochemical characteristics in the Adi Hageray and Adi Nebrid blocks, and a more evolved calc-alkaline, island arc-like geochemistry in the Adwa block, to the north of the study area (e.g. Tadesse et al. 2000). Post-tectonic granitoids are interpreted to be related to crustal thickening and collision. Their magmas were generated by remelting of previous lower crust (e.g. Andersson et al. 2006).

Table 6.3. Result of lead isotope analysis of sulfides.

Sample	Description	$^{208}\text{Pb}/^{204}\text{Pb}$	$^{207}\text{Pb}/^{204}\text{Pb}$	$^{206}\text{Pb}/^{204}\text{Pb}$	$^{208}\text{Pb}/^{207}\text{Pb}$	$^{206}\text{Pb}/^{207}\text{Pb}$
		m	m	m	m	m
J2-26	Galena	36.943	15.471	17.365	2.388	1.122
J2-36	Pyrite with galena inclusions	36.953	15.473	17.412	2.388	1.125
J9-24	Pyrite and chalcopyrite with galena inclusion	36.982	15.475	17.467	2.390	1.129
J9-31	Pyrite and chalcopyrite with galena inclusion	36.971	15.481	17.484	2.388	1.129
18-25	Galena	36.947	15.472	17.368	2.388	1.123
18-28	Sphalerite	36.978	15.482	17.374	2.388	1.122
18-31	Sphalerite	36.993	15.486	17.381	2.389	1.122
18-34	Sphalerite	36.935	15.470	17.364	2.387	1.122
18-58	Pyrite and chalcopyrite with galena inclusion	36.953	15.474	17.381	2.388	1.123
10-59	Sphalerite with minor gn, py, and cpy	36.990	15.483	17.382	2.389	1.123
10-84	Sphalerite	36.958	15.474	17.367	2.388	1.122

Table 6.4. Result of lead isotope analysis of feldspars and whole rock samples. Lead, U, and Th values are in ppm.

Sample	Description	$^{208}\text{Pb}/^{204}\text{Pb}$	$^{207}\text{Pb}/^{204}\text{Pb}$	$^{206}\text{Pb}/^{204}\text{Pb}$	$^{208}\text{Pb}/^{207}\text{Pb}$	$^{206}\text{Pb}/^{207}\text{Pb}$	Pb	U	Th	Age (Ma)	$^{208}\text{Pb}/^{204}\text{Pb}$	$^{207}\text{Pb}/^{204}\text{Pb}$	$^{206}\text{Pb}/^{204}\text{Pb}$
		m	m	m	m	m					i	i	i
TG06037	Monzogranite dike/sill (feldspars)	37.757	15.542	18.587	2.429	1.196	20.3	0.9	4.7	608	37.297	15.525	18.310
TG06049	Monzogranite dike/sill (feldspars)	37.480	15.513	18.215	2.416	1.174	24.2	0.3	2.6	608	37.268	15.508	18.139
TG06052	Monzogranite dike/sill (feldspars)	37.567	15.521	18.265	2.420	1.177	22.3	0.4	2.9	608	37.310	15.514	18.154
J4-010	Fine-grained monzogranite (whole rock)	37.612	15.536	18.244	2.421	1.174	16.7	1.2	3.7	608	37.176	15.509	17.799
TG06034	Black slate (whole rock)	41.389	15.747	21.127	2.628	1.342	0.29	0.1	2.2	800	19.711	15.541	18.006
J2-015	Quartz-sericite-chlorite schist (rock powder)	38.198	15.538	18.462	2.458	1.188	15.0	2.0	8.2	800	36.755	15.465	17.348
TG06007	Mafic metavolcanic rock (whole rock)	37.314	15.489	17.731	2.409	1.145	0.92	<0.1	0.5	854	35.816	15.456	17.256
TG06015	Quartz-sericite-chlorite schist (whole rock)	40.144	15.722	21.445	2.553	1.364	3.62	0.1	1.5	800	38.974	15.706	21.198

m = measured

i = initial

When element concentrations are below detection limit (e.g. U of sample TG06007), half of the concentration of the detection limit was used for calculation of initial lead isotope ratios

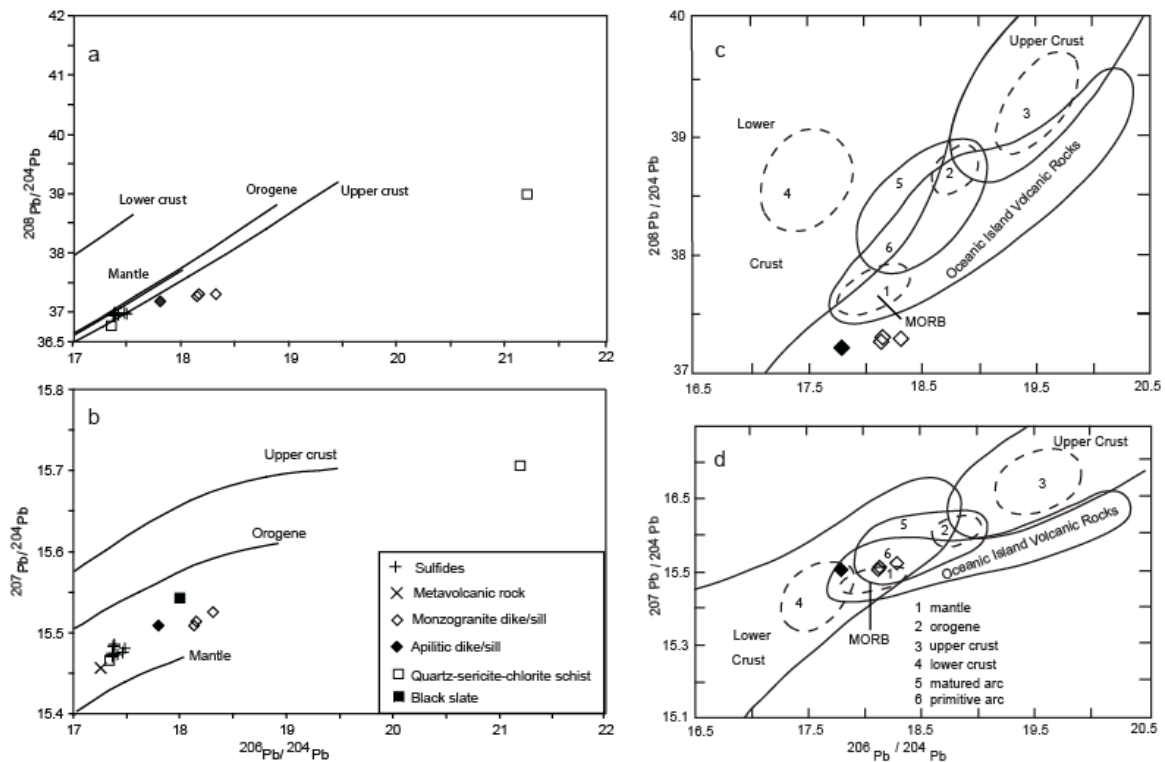


Fig. 6.3. Lead isotope data plot of sulfides, feldspars and whole rock samples relative to the growth curves and fields of Zartman and Doe (1981). Fig. 6.3a and b are constructed based on version II growth curve values, whereas Fig. 6.3c and d are drawn based on values for version I growth curves. Solid lines in Fig. 6.3c and d enclose 80% of all data points for each field and dashed lines enclose probable average values for mantle, orogene, upper crust, and lower crust. Generally, the lead isotope data suggest significant mantle component for the sulfides, feldspars, and sericite-chlorite schists (Fig. 6.3a and b) and the primitive arc setting of the intrusive rocks (Fig. 6.3c and d).

The field relationships and geochemical characteristics suggest that the dikes/sills in the study area are related to post-tectonic magmatism (Chapter 3). They are calc-alkaline island arc granitoids which are resulted from magmas derived by partial melting of mantle modified by the fluid component of the subducted slab or involvement of continental crust. The lead isotope signature of the intrusive rocks is consistent with whole rock geochemical data (Fig. 6.3). The distribution of immobile trace elements in the metasedimentary Tambien Group rocks from the study area indicate that they are dominantly derived from the island arc Tsaliet Group metavolcanic rocks (Chapter 3). Therefore, they should have inherited the juvenile signature of the parent rocks.

The similarity of the lead isotope ratios of the sulfides with that of metasedimentary and metavolcanic rocks suggests similar or common Pb sources, respectively. Since most of the

samples are taken from the mineralized or altered host rocks, the Pb in these rocks could be introduced by the ore-forming hydrothermal fluids.

The samples of the dikes were also collected in the prospect area, which raises the question whether the original Pb isotopic signature could be modified by the ore forming fluids. First thing to note is that the Pb isotope signature of the dikes is different as that of the sulfides and host rocks. If Pb would have been contributed entirely by the hydrothermal system, the Pb isotope composition of the dikes/sills should be the same as the sulfides.

Dike/sill emplacement post-dating the mineralization would exclude changes in the isotopic composition by the hydrothermal fluids. However, the timing of dike emplacement relative to the mineralization is not known. There is evidence that the dikes experienced hydrothermal alteration. This is also documented by the geochemical data on the dikes. However, the element distribution in the dikes/sills is essentially the same as those of the post-tectonic plutons, which indicates that the geochemistry of the dikes is not significantly affected by post-magmatic (hydrothermal) modifications (Figure 3.3a-c). Furthermore, the Pb isotope analysis was carried out on separates of fresh magmatic feldspars that contain the Pb in their crystal lattice. Therefore, the Pb isotopic composition of the dikes/sills should represent their original Pb isotope signature.

Metals in orogenic gold and VHMS type deposits are derived from the surrounding rock sequences at a regional scale through leaching by hydrothermal fluids (e.g. Schmidt-Mumm 2000; Huston 2000). A Pb isotope study on galenas from these deposits was conducted in the northern part of ANS, in western Saudi Arabia (e.g. Stacey et al. 1980). Generally, two distinct Pb isotope signatures of galenas (Group I and II) were distinguished (Fig. 6.4). The Group I galenas have low lead isotope ratio values. They are derived from an oceanic crust or depleted mantle source. Group II galenas are characterized by high Pb isotope ratio values, which are originated from ANS continental crust. Lead isotope ratios of the sulfides from the study area plot in the field defined by Group I galenas (Fig. 6.4a and b), which is consistent with Pb derived rocks with a primitive oceanic crust signature as those of the Tsaliyet and Tambien Group rocks in Tigray. This result supports the hypothesis that Pb and by inference other metals at Workamba are derived from the country rocks.

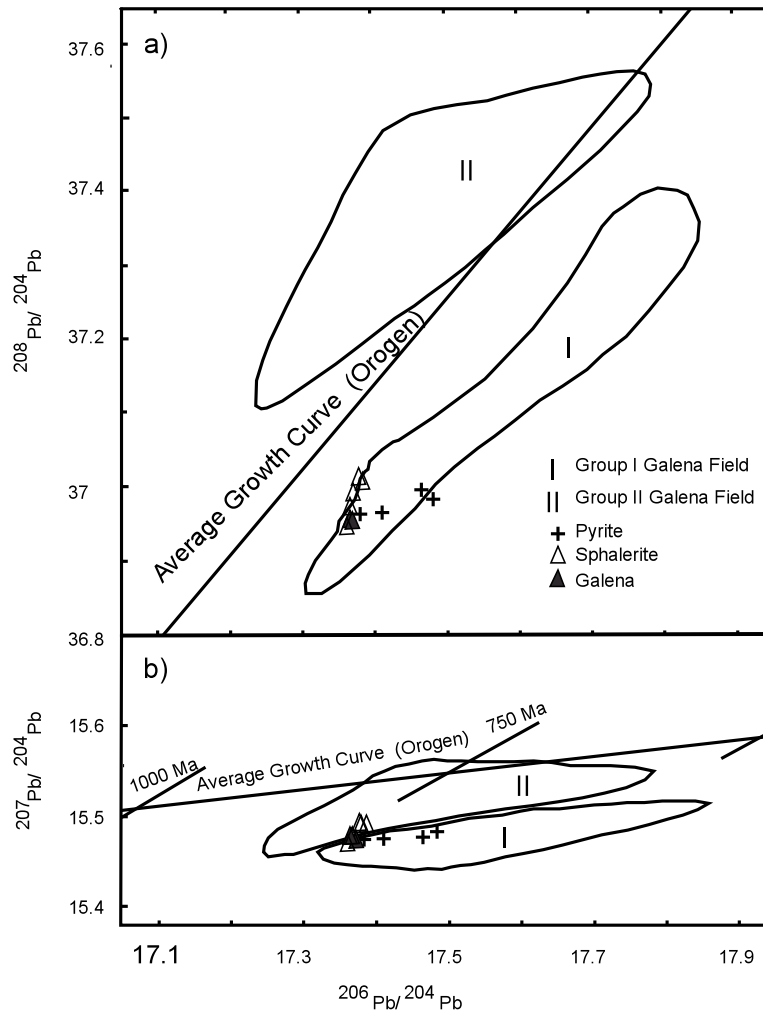


Fig. 6.4. a) $^{208}\text{Pb}/^{204}\text{Pb}$ and $^{206}\text{Pb}/^{204}\text{Pb}$; b) $^{207}\text{Pb}/^{204}\text{Pb}$ and $^{206}\text{Pb}/^{204}\text{Pb}$ binary diagrams of sulfides from Workamba gold and base metal mineralization plotted relative to the fields of Group I and II galenas from the Arabian shield, which indicate the derivation of Pb from oceanic (depleted mantle) and continental crust respectively. The plot of the sulfides from the study area in the Group I galena field suggest that they are derived from an oceanic crust. Group I and II galena fields are taken from Stacey et al. (1980). Average growth lines are from Stacey and Kramers (1975).

7. Discussion

In recent years, there have been several important publications on the ANS, which significantly improved the understanding of the geological evolution of northern Tigray. However, the geological record is incomplete, and there are a number of controversial statements so that many open questions remain. The evolution of the area is discussed based on the review of the recently published data and own observations in order to relate the mineralization at Workamba to its regional geological framework (geotectonic and structural setting; nature and timing of mineralization).

Island-arc magmatism produced the volcanic-volcaniclastic rocks of the Tsaliet Group (Alene et al. 2000, Tadesse et al. 1999). This volcanism most likely started at around ~ 860 Ma based on the age of metavolcanic rocks in Eritrea dated at 854 ± 3 Ma that are correlated with the Tsaliet Group rocks in Tigray (Teklay et al. 1997, 2002; Fig. 7.1). Detrital zircons and zircons separated from volcanic rock clasts in the Negash and Shiraro diamictites (Avigad et al. 2007) with an age of 745 Ma, and ~800 to 735 Ma pre- or syn-tectonic I-type volcanic-arc plutons suggest that arc-magmatism took place during the first half of the Cryogeryan (Neoproterozoic; Fig 7.1). The Tambien Group overlies the Tsaliet Group. The timing of the deposition of the sediments of the Tambien Group is a controversy. Alene et al. (2006) estimate the age of the Tambien Group between 800 and 735 Ma based on correlations of $\delta^{13}\text{C}$, $\delta^{18}\text{O}$, and $^{87}\text{Sr}/^{86}\text{Sr}$ characteristics, whereas Avigad et al. (2007) suggest that the deposition started after 740 Ma. Beyth (1972) recognized an unconformable contact between the Tsaliet Group and Tambien Group in the Tsae Anticlinorium and Mai Kenetal areas (Fig. 2.5), whereas Alene et al. (1998) describe a conformable, gradational contact at the Mai Kenetal-Negash area. The contact relationships between the two stratigraphic units in the study area are obscured by the presence of a shear zone and dikes, and field relationships are inconclusive (Figs. 2.8 and 2.12). The Tambien Group does not contain any volcanic material that can be linked to the Tsaliet arc volcanism, and it is not intruded by the ~800 to 735 Ma pre- or syn-tectonic I-type volcanic-arc plutons. Therefore, it is concluded that this magmatism has ceased before Tambien Group deposition. Post-tectonic magmatism in the region commenced at ~620 Ma (Fig. 7.1). Therefore, there seems to be an about 100 Ma lasting lull of magmatism (Avigad et al. 2007; Fig. 7.1).

The complete stratigraphic sequence of the Tambien Group, as described by Alene et al. (2006), is not exposed in the study area (Fig. 2.6). The Tambien Group in this area is characterized by

thick sequence of schists, slates, and phyllites with an apparent thickness of about 4 km (Fig. 2.8). Limestones that could be correlated with the Lower or Upper Limestones are absent. Taking into account the thickness of the schists, slates, and phyllite sequence, these carbonates may not have developed in this part of the basin (see Fig. 2.6). The sericite-chlorite schists and black slate on top of the Tsaliet Group volcanic rocks may correlate with the Lower (Weri) Slate of the Tambien Group, since, according to Beyth (1972), the latter is the base of the Chehmit Inlier (Fig. 2.5). The overlying sequence of alternating slate and phyllite could represent an equivalent of the Upper Slate of the Tambien Group, (Figs. 2.6 and 2.8; Beyth 1972; Alene et al. 2006).

The Negash and Shiraro diamictites lay on top of the Tambien Group. The Negash diamictite forms the core of the Negash Inlier, whereas the Shiraro diamictite lies on top of the Tsaliet Group in the Shiraro area. The Negash and Shiraro diamictites contain clasts of Tambien carbonates, Tsaliet Group volcanic rocks, and pre- or syn-tectonic granites indicating that the region was above sea level and eroded. Uplift and/or a drop of the sea level could have led to the subaerial conditions that enabled erosion. The erosion level reached Tsaliet Group rocks and the crustal level in which pre- or syn-tectonic granite were emplaced. Therefore it must have cut deep into the Tambien Group. The lower contact of the Negash diamictite is described as a gradational contact (Alene et al. 2006) or conformable (Avigad et al. 2007), respectively. Alene et al. (2006) interpreted the diamictite as of glacial origin. However, Avigad et al. (2007) pointed out that the clasts in the diamictite are of local origin and are not derived from distal sources as expected for glacial deposits derived from a continental-scale ice sheet. They suggest that the diamictites were deposited between 720 and 620 Ma. The younger age is based on the fact that post-tectonic granites intruded the diamictites. The lower conformable contact of the diamictite and its deformation suggest that its deposition took place before or at the beginning the major phase of collision (culminating at 630 Ma; Avigad et al. 2007).

The exact age of deformation and metamorphism in the basement rocks of Tigray and the study area is not well constrained. Tadesse et al. (2000) suggested that deformation and metamorphism occurred in the Axum area between 806 to 756 Ma (age range of pre- or syn-tectonic granitoids). However, Alene et al. (2006) disagree with this age estimate because of Tambien Group sedimentation was still ongoing at that time. The fact that the diamictites experienced low grade regional metamorphism and pervasive N-S schistosity (Avigad et al. 2007), and that the 620 Ma

post-tectonic granitoid remained unmetamorphosed suggest that metamorphism is related to deformation at 630 Ma.

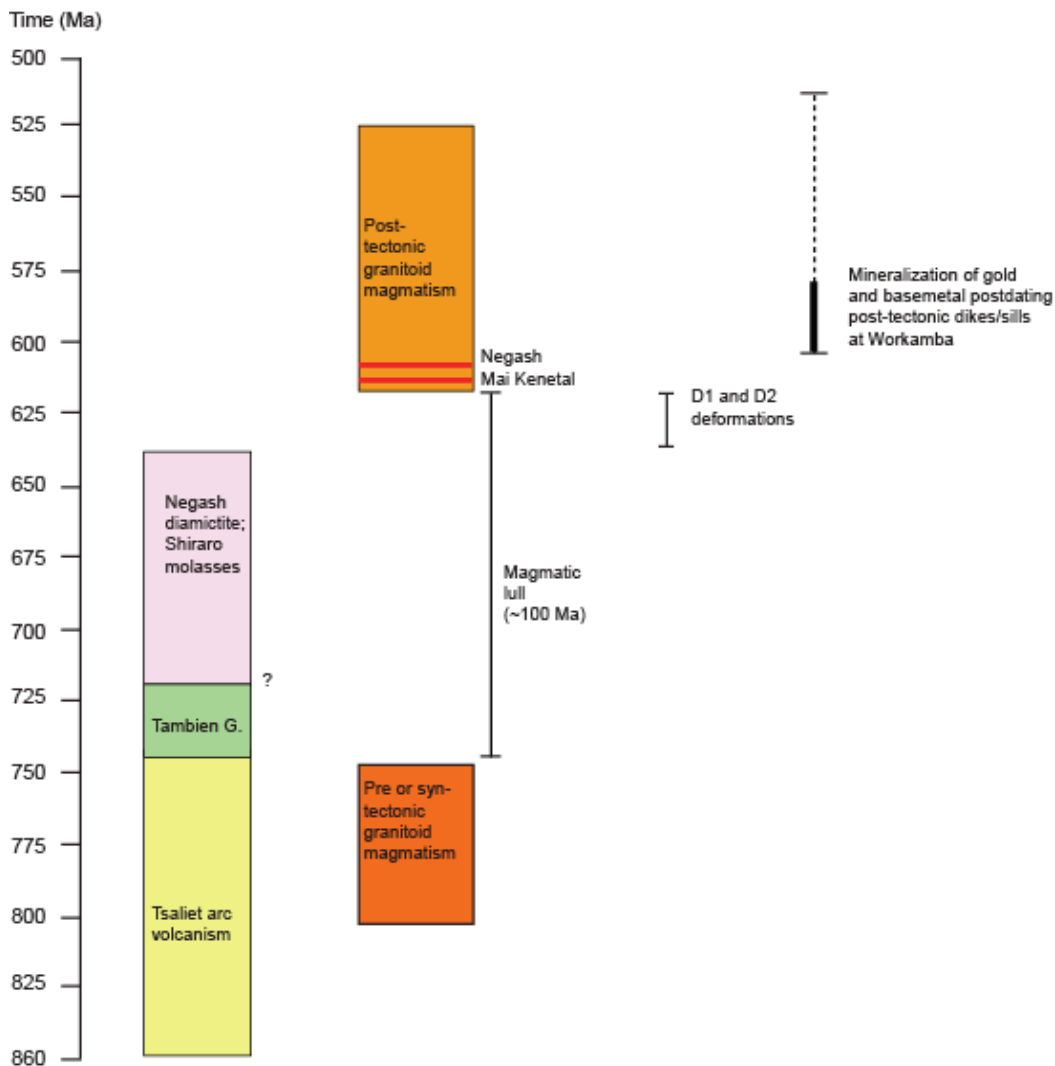


Fig. 7.1. Diagram showing the temporal relationships of Neoproterozoic geologic events in Tigray. The lower age limit for Tsaliyet arc volcanism (~860 Ma) is taken from Teklay et al. (1997), whereas the upper limit (~750 Ma) is from Avigad et al. (2007). The time of Tambien deposition, uplift and erosion of Tambien and Tsaliyet groups, and sedimentation of Negash diamictite and Shiraro molasses are based on the interpretations of Alene et al. (2006) and Avigad et al. (2007). The timing of pre or syn- and post-tectonic granitoid magmatism is constrained from the compiled data in Table 2.1. The 608 Ma Negash and 612 Ma Mai Kenetal plutons are manifestations of post-tectonic magmatism, which are closest to the study area. The monzogranite bodies at Workamba are thought to be related to this post-tectonic magmatism.

According to Alene et al. (2006), pumpellyite-actinolite to lower greenschists metamorphism affecting the Tsaliyet Group rocks was accompanied by D1 deformation (N-S compression), which produced tight minor folds and pervasive regional foliation. D2 deformation is correlated with the end of major collision phase of the East African Orogeny (E-W compression; Alene et

al. 2006) and this major collision has occurred in Tigray at ~630 Ma (Avigad et al. 2007). Similarly, the structures formed by D2 deformation were correlated with the ~650-550 Ma post-accretionary N to NW trending shear zones and strike slip faults that occur elsewhere in the ANS (Alene et al. 2006; Abdelsalam and Stern 1996). In accordance with these interpretations, the NE-trending shear zones, foliations, and fold axis that occur in the study area are part of D1 deformation. More localized NNE-trending shear bands in the study area are assigned to D2 deformation (Fig. 2.12). Like in the regional basement rocks, the grade of metamorphism of the rocks in the Workamba area is of lower greenschist facies. This is consistent with the sericite and chlorite mineral association in the metasedimentary rocks and with the absence of high-grade minerals such as garnet in these rocks.

The structural setting, host rock alteration (silicification, sericitization and carbonatization and the peripheral propylitic alteration), the sulfide (pyrite, sphalerite, galena and chalcopyrite, ± pyrrhotite, and ± arsenopyrite) and gangue (calcite, quartz, and silicates) mineralogy are suggestive for a shear-zone hosted orogenic-gold type deposit at Workamba, though the geological context is permissive for other types of mineralization (e.g. epithermal, skarn or porphyry gold).

The ore-forming fluids of orogenic gold deposits are low salinity aqueous-carbonic fluids of metamorphic origin (Ridley and Diamond 2000). They may contain minor quantities of CH₄ and N₂ (Ridley and Diamond 2000; Roedder 1984). A magmatic-hydrothermal input may have played a role in some orogenic gold systems (Ridley and Diamond 2000). The microthermometric measurements suggest that essentially all fluid inclusions in the study area are of CO₂-poor, low salinity aqueous type. Similar CO₂-poor, low-salinity aqueous fluid inclusions are reported from orogenic gold deposits elsewhere (Racetrack, Western Australia, Gebre-Mariam et al. 1993; Ridley and Diamond 2000). The absence of CO₂ in the fluids has been explained by fluids of modified groundwaters origin or derived from dehydration reactions of essentially CO₂-free source rocks (Roedder 1984). A similar interpretation concerns the absence of CH₄ in the fluid inclusions, which might be due to insufficient quantities of hydrocarbon organic matter at greater depths that could decompose to simpler components (CO₂, H₂O, CH₄, and N₂) or the depth of decomposition is too shallow to convert the organic matter completely to these molecules (Roedder 1984).

The mineralization at Workamba appears to be related to calcite \pm quartz veining events (see paragenetic sequence, Chapter 4). In contrast to the above mentioned concerning CO₂-free source rocks, the carbon isotope data suggest that C is derived from carbonate rock source. Most of the fluid inclusions in calcite and quartz are of secondary (or pseudo-secondary?) origin. Sulfide-bearing quartz-calcite and unmineralized quartz veins in NE trending brittle structures contain the same fluid inclusion types and record similar temperatures suggesting that fluid flow were not restricted to the shear zone but occurred at a larger (regional) scale.

The occurrence of several fluid pulses or phases is compatible with inconsistent behaviour of the fluid inclusion types during heating and freezing suggesting that the coexisting vapor-rich and fluid-rich inclusions did not form from a common process such as boiling. Furthermore, the presence of different generations of sericite (coeval with S1 and post-dating shear deformation; see chapter 4) supports the hypothesis of several episodes of fluid flow. Although none of the fluid inclusion populations can be directly linked with the metallic mineralization, the microthermometric measurements show that fluid temperature are in the range expected for orogenic or intrusion-related gold deposits.

The strongest argument for an orogenic gold type mineralization comes from the Pb isotope data. The different Pb isotope signatures of the sulfides and intrusive rocks preclude the possibility of an intrusion related or porphyry type mineralization. These data suggest that the Pb (and other metals) in the sulfides is derived from the country rocks (i.e. the Tambien and Tsaliet Group) through leaching by hydrothermal fluids. The stable isotope data (S, C, and O) is compatible with a derivation of ore components from the country rocks or involvement of metamorphic fluids as predicted by the orogenic gold model (e.g. Schmidt-Mumm 2000). Also the element distribution of the mineralization in the Workamba area, with anomalous Au, Ag, As, Pb, and Sb values, low Au/Ag ratio (< 10), and low Hg, Bi, and Mo contents, is similar to that of orogenic gold deposits elsewhere (e.g. Racetrack, Western Australia, Gebre-Mariam et al. 1993; McCuaig and Kerrich 1994; Goldfarb et al. 2001; Fig. 7.2).

In summary, the Workamba gold and base metal mineralization is dominantly hosted by the metasedimentary rocks of the Tambien Group. The metallic minerals occurred in a D1 shear-zone though textural characteristics indicate that mineralization post-date shear deformation and occurred under brittle conditions (Chapter 4). A lithological control on the Au mineralization by graphite rich-metasedimentary rocks has been locally observed (National Mining Corporation

2006, personal communication). The shear-zone is intruded by monzogranite and lamprophyre dikes/sills. The monzogranites are related to the post-tectonic granitoids of Tigray region (Chapter 2 and Chapter 3), whereas the nature and provenance of the lamprophyre remain to be investigated. The shear-zone served as a conduit for different pulses of hydrothermal fluid flow. One notable product of these fluid pulses is a strong sericitization (sericite I), with aligned sericite defining D1 foliation. Sericitization is therefore interpreted to have occurred during D1 deformation, i.e. it predates mineralization (Chapter 4). The monzogranite and lamprophyre dikes/sills are affected by post-magmatic hydrothermal alteration, including sericitization (sericite II), chloritization, epidotization, and carbonatization, which by implication also post-date shear deformation (Chapter 4). The fluid inclusion data is consistent with the occurrence of various generations of fluid pulses (see above). The metallic mineralization is roughly coeval with carbonatization and calcite \pm quartz veining. Although most of the fluid inclusions in the quartz-calcite veins are secondary (or pseudo-secondary?) in origin, the recorded minimum trapping temperatures show that fluids that post-date the mineralization still had temperatures of 300°C. The oxygen isotope data of calcite is permissive for a magmatic-hydrothermal contributions to the hydrothermal system. However, overall the isotopic data is consistent with the derivation of metals, sulfur, and other ore components through leaching by metamorphic fluids as it is common for orogenic gold deposits. The mineralization at Workamba most likely was generated by devolatilization and dehydration processes during prograde metamorphism of the Tsaliet and Tambien Group rocks. The major collision orogeny which was culminated in Tigray ~630 Ma (Avigad et al. 2007) might have caused eviction of the mineralizing fluids from deep regions. These mineralizing fluids were then channelized along with the ore components through the shear zone (Fig. 7.3). Gold in orogenic gold deposits is believed to be transported as $\text{Au}(\text{HS})_2^-$ complexes at intermediate oxidation states by near-neutral fluids (pH = ~5.5, Ridley and Diamond 2000; Groves et al. 2003).

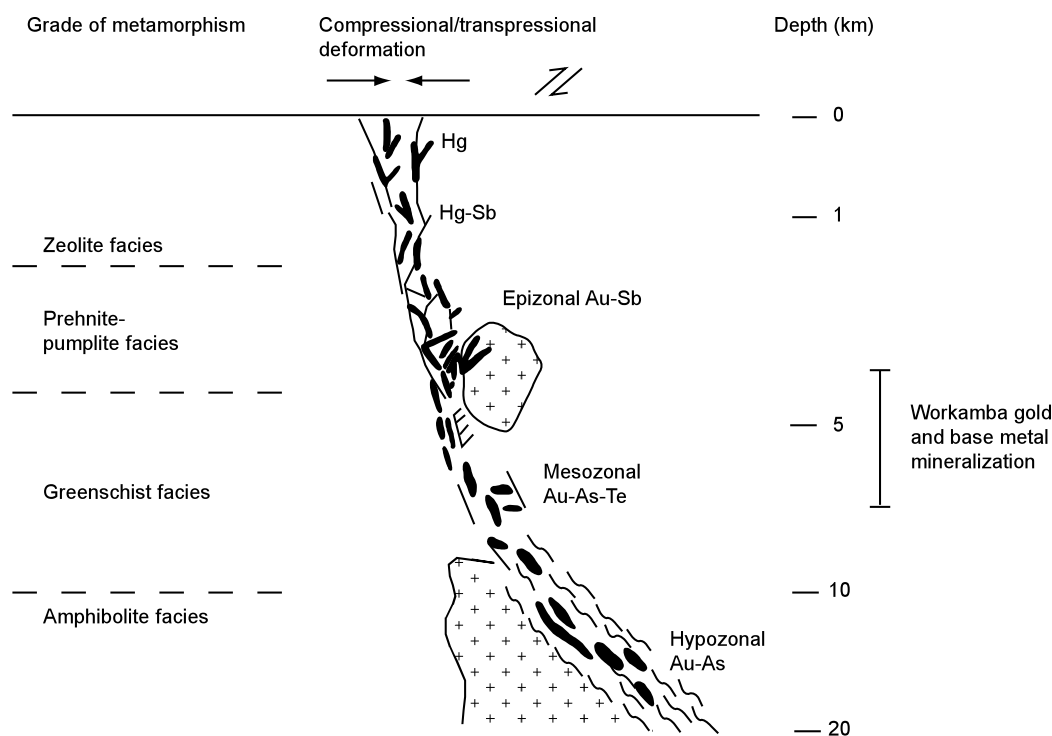


Fig. 7.2. Model of orogenic Au deposits representing depth and structural setting (a convergent plate margin) in which these deposits are formed (after Groves et al. 1998; Gebre-Mariam et al. 1995).

The association of invisible gold and sulfides suggests that destabilization of the $\text{Au}(\text{HS})_2^-$ complex by fluid-wallrock interaction is a likely process for the gold deposition at Workamba (see e.g. Groves and Phillips 1987; Mikucki 1998; Seward and Barnes 1997). Alternatively, simple cooling at a temperature of $<350^\circ\text{C}$ could have played a role in gold deposition. The fact that temperatures of around 300°C remained stable for some time after mineralization could explain the low quantity of gold present at Workamba, because under these conditions gold would be deposited slowly from the solution and dispersed over a wide area without forming economic concentrations (e.g. Seward 1991; Murphy and Roberts 1997). The sub- to greenschist facies metamorphism of the Tambien and Tsaliet Group rocks, geochemical signature of the mineralized rocks (enrichment in Au, Sb, and As and depth relationships, Fig. 7.2 and 7.3), the brittle-ductile shearing experienced by the rocks, and the post-shearing timing of the mineralization puts the range of depth of formation between 4 to 6 km (Fig. 7.2, Miyashiro 1973; Gebre-Mariam et al. 1995; Groves et al. 1998; McClay 1987).

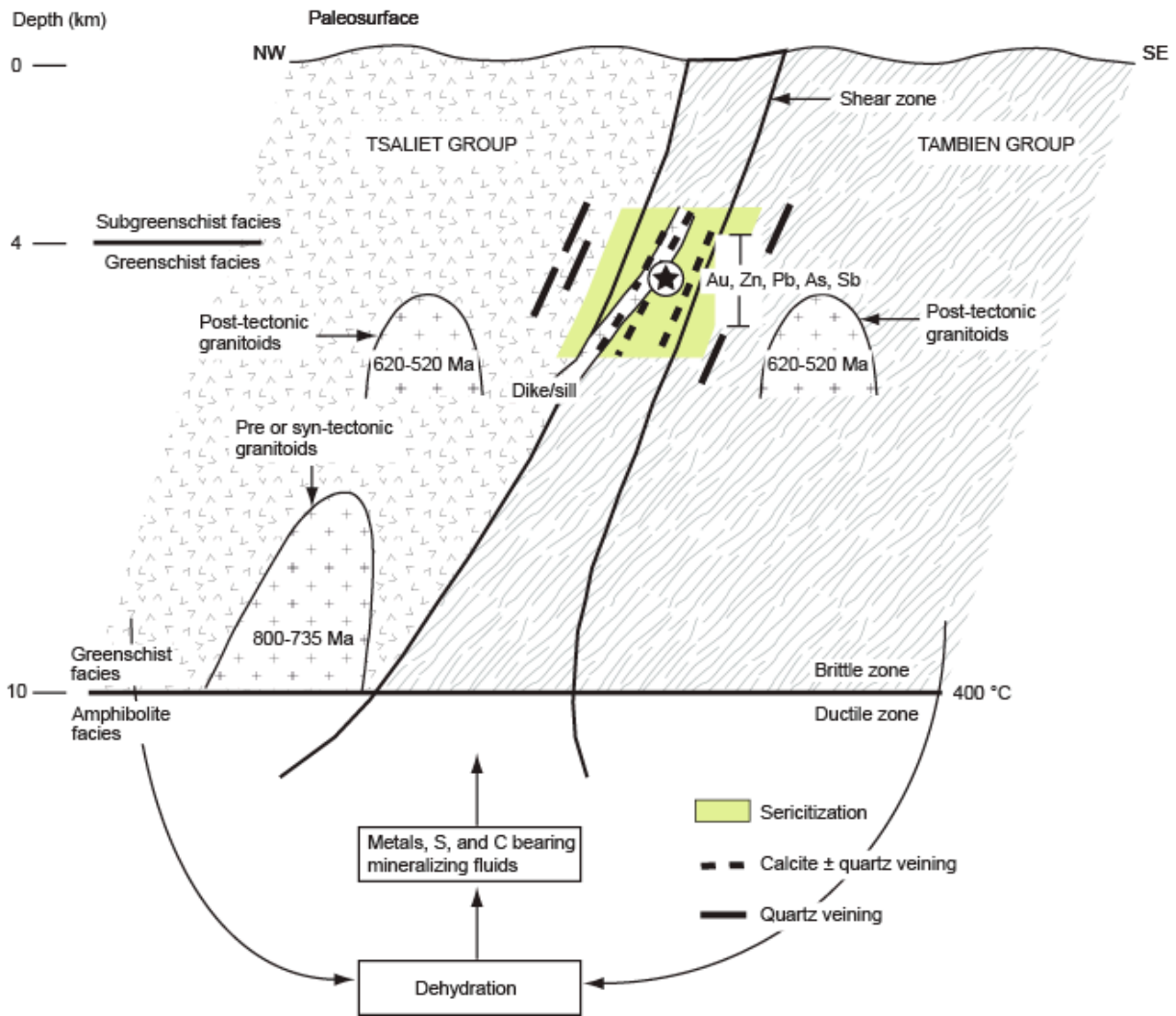


Fig. 7.3. Sketch (not to scale) of the Workamba gold and base metal mineralization based on the geologic, structural, mineralogical, and geochemical interpretations discussed above. Black star in circle denotes the position in which deposition of the mineralization occurs. Level of emplacement inferred from model of Gebre-Mariam et al. (1995) and Groves et al. (1998) is between 4 to 6 kms.

At regional scale, shear-zone controlled orogenic gold deposits, which are similar to that of Workamba are reported in Ethiopia (e.g. Lega Dembi primary gold deposit of southern Ethiopia, Billay et al. 1997; Tadesse 2004), Egypt (Um El Tuyor gold deposit, Zoheir 2004), and elsewhere (Table 7.1; Kerrich and Cassidy 1994; Groves et al 1998; Goldfarb et al. 2001; Klein et al. 2005).

Table 7.1. Comparison of the characteristics of the Workamba gold and base metal mineralization with those of orogenic gold deposit type

Characteristics	Orogenic deposits ^{a, b, c}	Workamba gold and base metal mineralization
Age	Middle Archean to Tertiary; peaks in Late Archean, Paleoproterozoic, Phanerozoic ^{a, b, c}	Late Neoproterozoic
Tectonic setting	Convergent margins (accretionary and collisional orogens) ^b	Accreted intraoceanic arcs
Structural setting	Structural highs during later stages of compressional and transtension stresses ^{a, b}	Shear zones, folds, brittle faults
Host rocks	Mainly mafic volcanic, or intrusive rocks, or greywacke-slate sequences ^a	Mainly metasedimentary rocks
Metamorphic grade	Mainly greenschist facies (can range from subgreenschist to lower-granulite) ^b	Greenschist facies
Of host rocks		
Association with intrusion	Felsic to lamprophyre dykes or continental margin batholiths ^b	Felsic to intermediate intrusive dikes
Ore minerals	Py common then aspy, po, gn, sl, and cp ^a	Py dominant followed by sl, gn, cp ± po ± aspy
Mode of gold occurrence	Native gold, electrum or gold bearing tellurides ^b	Invisible (micron-sized) Au
Timing of mineralization	Late-tectonic, post-metamorphic peak ^{a, b, c}	Post metamorphic and deformation
Mineralization style	Large veins, vein arrays, saddle reefs, replacement of Fe-rich rocks ^a	Quartz-calcite veins, wallrock alteration halo
Hydrothermal alteration	Sericitization, silicification, carbonatization, sulfidization ^c	Sulfidization, carbonatization, sericitization, silicification, and propylitic alteration
T-P conditions	Mainly 350 ± 50 °C; 1.5 ± 0.5 kbar ^a	~300 °C; P 4 to 6 km
Fluid composition	Low salinity (generally ≤ 6 wt. %), H ₂ O-CO ₂ ± CH ₄ ± H ₂ S ± N ₂	Low salinity (1-4 wt. %), H ₂ O-NaCl
Fluid source	Metamorphic and/or magmatic; seldom meteoric ^a	Metamorphic
Carbon and sulfur sources	C: mantle, and/or magmatic and/or metamorphic locally biogenic; S: magmatic ^a	Dominantly metasedimentary and carbonate rocks for carbon; Magmatic or metasedimentary rocks for sulfur
pH	Near neutral	Near neutral (~5.5)
Redox state	Generally reducing ^{a, b}	Intermediate oxidizing
Gold transport	Sulfide ligands ± chloride ligands ^a	Sulfide ligand (Au(HS) ₂)
Gold deposition	wallrock alteration, phase immiscibility, fluid mixing and chemisorption ^a	Fluid-wallrock interaction; cooling

^a = Klein et al. 2005, ^b = Groves et al. 1998, ^c = Goldfarb et al. 2001

However, the absence of CO₂-bearing ore fluids at Workamba deviates from these classic orogenic gold deposits.

On the other hand, the presence of gold mineralization in the host rocks, the proposed deposition model (sulfidization of host rocks), the fine-grained (invisible) nature of gold mineralization, the epigenetic nature of the mineralization, and shallow crustal level of deposition at Workamba match characteristics reported for sediment-hosted disseminated orogenic-gold deposits (e.g. Bierlein and Maher 2001).

The mineralization at Workamba has occurred roughly concomitant with carbonatization and calcite ± quartz veining, after the intrusion of the monzogranite and lamprophyre dikes/sills. The latter are correlated with the post-tectonic granitoids of Tigray region, which were emplaced in the time interval between 620 to 520 Ma. The ~612 Ma Mai Kenetal and ~608 Ma Negash plutons are the manifestation of post-tectonic magmatism closest to the study area, and are taken as a proxy for the maximum mineralization age (Fig 7.1). Avigad et al. (2007) suggested that cooling of the Pan-African orogenic event culminated around 500 Ma, which would represent the youngest possible mineralization age.

8. Conclusions

The lower greenschist facies metavolcanic and low-grade metasedimentary rocks in the study area are correlated to the ~860 to 750 Ma Tsaliet or ~740 Ma Tambien Group of the ANS, respectively. The trace element patterns of the metasedimentary rocks support the hypothesis that they are derived from the island-arc metavolcanic rocks of Tsaliet Group as previously suggested.

The metavolcanic and metasedimentary rocks are affected by at least two phases of ductile deformation (D1 and D2). In the study area, D1 deformation resulted in NE oriented sinistral shear zones and foliations as well as ENE trending folds. D2 deformation caused the local development of NNE oriented shear bands and N-S trending parasitic folds. NW striking brittle faults post-date ductile deformation. Monzogranite and lamprophyre dikes/sills intruded the lower part of Tambien Group, parallel and/or cutting the foliation. The monzogranite is related to the ~620 to 520 Ma post-tectonic magmatism in Tigray, and originated from mantle derived magmas, which are modified by fluid component of the subducted slab or involvement of continental crust. The petrological and geochemical studies on the lamprophyres suggest that they are calc-alkaline type. However, further investigations are required to determine their nature and provenance.

The lead isotope ratios of metasedimentary, metavolcanic, and intrusive rocks, which plot between the mantle and orogene curves suggests a significant mantle component in these rocks. The Pb isotope signature of the intrusive rocks is similar to MORB or primitive arc igneous rocks. The low $^{208}\text{Pb}/^{204}\text{Pb}$ and $^{207}\text{Pb}/^{204}\text{Pb}$ values of the metasedimentary and metavolcanic rock suggest that they are more primitive as the post-tectonic dikes/sills, which is compatible with the geochemical data.

The metavolcanic rocks are locally affected by propylitic alteration and sericitization. The metasedimentary rocks suffered from silicification, sericitization, and carbonatization. Mass balance calculations of the metasedimentary rocks suggest that Na_2O , and Sr are removed from the rocks by hydrothermal fluids. K_2O , MnO, CaO, Ba, and Pb are variably added or removed. Two generations of quartz veins occur in the metavolcanic and metasedimentary rocks, cutting or parallel to D1 foliation. The first generation quartz veins are folded by D2 and less abundant as compared to the unfolded second generations. Both the monzogranite

and lamprophyre dikes/sills are affected by pervasive sericitization, carbonatization, epidotization, and chloritization. However, mass balance calculations indicate that these dikes/sills have retained near original geochemical compositions.

The metallic mineralization at Workamba occurred within a NE oriented D1 sinistral shear zone under brittle conditions, in close spatial proximity to the monzogranite and lamprophyre dikes/sills. The mineralization is characterized by a relatively simple ore mineral assemblage of pyrite, sphalerite, galena, and chalcopyrite and subordinately pyrrhotite, arsenopyrite, and chalcocite. Gold is invisible and only detected in geochemical analysis (micron-sized type gold). Assaying values of the mineralized rocks reveal up to 8 ppm Au contents, which is ~2500 times higher compared to upper continental crust concentrations. Gangue include calcite, sericite, and quartz. The mineralization is anomalous in As and Sb.

The structural setting, host rock alteration, sulfide and gangue mineralogy, and Pb, S, C, and O isotope data are suggestive for an orogenic-gold type mineralization at Workamba. There are many similarities with the Lega Dembi gold deposit in southern Ethiopia, which hosts about 60 t Au (Tadesse et al. 2003). The mineralization was probably formed at temperatures of ~300°C. Metamorphic fluids produced by devolatilization and dehydration processes have leached metals, S, and C from the country rocks. The mineralizing fluids were then transported upwards from deep regions through the shear-zones. Gold is assumed to be transported in thiocomplexes at intermediate oxidation states by near-neutral fluids. Sulfidation of host rocks is supposed to be a likely deposition mechanism for the gold. Simple cooling could have played a role as well. Mineralization is accompanied by carbonatization. The metamorphism grade of host rocks, geochemical signature of mineralized rocks, the nature of host rock deformation suggest that the mineralization at Workamba occurred in a depth interval of 4 to 6 km. Mineralization post-dates dike/sill emplacement and therefore there is no direct genetic relationship to post-orogenic magmatism. The age of mineralization is assumed to be late Neoproterozoic.

Recommendation

The result of this study shows that the basement rocks in this part of Tigray have potential for hosting economic orogenic gold deposits. The geological and structural environment required for the formation of these deposits is present, as well as hydrothermal fluid capable to transport gold. Orogenic gold orebodies commonly occur in clusters, as e.g. shown by the

Chega Tudo gold deposit in the Gurupi Belt (Brazil, Klein et al. 2008). There gold ores occur in bodies at Mina Velha (upper level) and Mandiocal (lower level), in a distance of about 3 km. A similar situation could be present at Workamba. Given the high prices of gold since September 11, 2001, successful discoveries of such gold deposits could contribute its own share in the overall socio-economic improvements of the communities in Tigray. However, the search for economic gold concentrations should be carried out by employing effective and well integrated exploration techniques. The outcomes of this study suggests that the exploration works should focus on areas with sheared and sulfidized metasedimentary rocks. Considerations should be given to sericitized and carbonatized zones with anomalous concentrations of As and Sb. Although not directly genetically related, search for gold in proximity to dikes/sills may also be successful. Graphite-bearing metasediments also have potential for gold mineralization.

In detail, it is suggested to carry out the following investigations for future orogenic gold explorations in Tigray:

1. Detailed geological, structural and alteration mapping at regional scale.
2. Mapping accompanied by stream sediment sampling and chemical analysis. The analysis should focus on path finder elements for orogenic gold deposits, such as As and Sb.
3. Search for shear zones, large-scale faults, second, third, or fourth order structures that may control the mineralization.
4. Geophysical surveys, such as aeromagnetic, electro-magnetic, paleomagnetic and 3-D seismic methods can help to differentiate between the different orders of structures and outline metallic anomalies.
5. Fluid inclusion studies to identify aqueous or aqueous-carbonic fluid types, which are capable of transporting Au.

On future follow-up scientific works

This research shows that the Pb isotope signature of sulfides from the study area represent those of Tsaliyet and Tambien Group rocks and is different from values of post-tectonic granitoids. This hypothesis, however, requires further test by analysing and incorporating more Pb and also Sr isotope data of the rocks and hydrothermal minerals. Therefore, detailed Pb and Sr isotope studies are recommended based on samples from the larger Workamba area

and the district. These studies would improve the petrogenetic interpretation of the rocks. Follow-up field mapping, petrographic, geochemical, and isotope geochemistry studies on the lamprophyres are recommended to determine their nature and origin. Absolute age determinations on biotite using K-Ar or Ar-Ar methods will constrain the age of dikes/sills in the study area and expand the data base on the timing of post-orogenic magmatism in Tigray.

References

- Abdelsalam, M.G., and Stern, R.J., 1996. Sutures and shear zones in the Arabian-Nubian Shield. *Journal of African Earth Sciences* 23, 289-300.
- Alemu, T., 1998. Geochemistry of Neoproterozoic granitoids from Axum Area, northern Ethiopia. *Journal of African Earth Sciences* 27, 437-460.
- Alene, M., 1998. Tectonomagmatic evolution of the Neoproterozoic rocks of the Mai Kenetal-Negash area, Tigray, northern Ethiopia. Unpublished Ph.D. Thesis, University of Turin, Italy.
- Alene, M., Ruffini, R., and Sacchi, R., 2000. Geochemistry and geotectonic setting of Neoproterozoic rocks from northern Ethiopia (Arabian-Nubian Shield). *Gondwana Research* 3, 333-347.
- Alene, M., Jenkin, G. R.T., Leng, M. J., and Darbyshire, F.D.P., 2006. The Tambien Group, Ethiopia: An early Cryogenian (ca. 800-735 Ma) Neoproterozoic sequence in the Arabian-Nubian Schield. *Precambrian Research* 147, 79-99.
- Andersson, U.B., Ghebreab, W., and Teklay, M., 2006. Crustal evolution and metamorphism in east-central Eritrea, south-east Arabian-Nubian Shield. *Journal of African Earth Sciences* 44, 45-65.
- Assefa, G., 1985. The mineral industry of Ethiopia: present conditions and future prospects. *Journal of African Earth Sciences* 3, 331-345.
- Asrat, A., Barbey, P., and Gleizes, G., 2001. The Precambrian Geology of Ethiopia: a review. *Africa Geoscience Review* 8, 271-288.
- Asrat, A., 2002. Etude structurale (ASM), pétrologique et géochimique (Rb-Sr, Sm-Nd, U-Pb) des plutons panafricains de Negash et de Konso (Ethiopie): place des mélanges acides-basiques dans la construction des plutons calco-alcalins. Ph.D. Thesis, Centre de Recherches Pétrologiques & Géochimiques, Vandoeuvre-lés-Nancy, France, 276 pages.
- Avigad, D., Stern, R.J., Beyth, M., Miller, N., McWilliams, M.O., 2007. Detrital zircon U-Pb geochronology of Cryogenian diamictites and Lower Paleozoic sandstone in Ethiopia (Tigray): Age constraints on Neoproterozoic glaciation and crustal evolution of the southern Arabian-Nubian Shield. *Precambrian Research* 154, 88-106.
- Ayalew, T., Bell, K., Moore, J.M., and Parrish, R.R., 1990. U-Pb and Rb-Sr geochronology of the Western Ethiopian Shield. *Geological Society America Bulletin* 102, 1309-1316.
- Belete, K.H., 2000. The Petrology of the mafic-ultramafic rocks and the surrounding basement, western Ethiopia and genesis of platinum-group minerals related to an Alaskan-

- type ultramafic intrusions of Yubdo area. Unpublished Ph.D. Thesis, Institute of Mineralogy and Petrology, University of Graz, Austria.
- Berhe, S. M., 1990. Ophiolites in Northeast and East Africa: implications for Proterozoic crustal growth. *Journal of Geological Society of London* 147, 647-657.
- Beyth, M., 1972. The Geology of Central-Western Tigre. Ph.D. Thesis, Rheinische Friedrich-Wilhelms Universität, Bonn, Germany, 159 pages.
- Beyth, M., Stern, R.J., and Matthews, A., 1997. Significance of high-grade metasediments from the Neoproterozoic basement of Eritrea. *Precambrian research* 86, 45-65.
- Beyth, M., Avigad, D., Wetzel, H.-U., Matthews, A., and Berhe, S.M., 2003. Crustal exhumation and indications for Snowball Earth in the East African Orogen: north Ethiopia and east Eritrea. *Precambrian Research* 123, 187-201.
- Bierlein, F.P., and Maher, S., 2001. Orogenic disseminated gold in Phanerozoic fold belts-examples from Victoria, Australia and elsewhere. *Ore Geology Reviews* 18, 113-148.
- Billay, A.Y., Kisters, A.F.M., Meyer, F.M., and Schneider, J., 1997. The Geology of the Lega Dembi gold deposit, southern Ethiopia: implications for Pan-African Gold exploration. *Mineralium Deposita* 32, 491-504.
- Bhatia, M.R., 1983. Plate tectonics and geochemical composition of sandstone. *The Journal of Geology* 91, 611-627.
- Bhatia, M.R., 1985. Rare earth element geochemistry of Australian Paleozoic graywackes and mudrocks: Provenance and tectonic setting control. *Sedimentary Petrology* 45, 97-113.
- Bhatia, M.R., and Crook, K.A.W., 1986. Trace element characteristics of graywackes and tectonic setting discrimination of sedimentary basins. *Contributions to Mineralogy and Petrology* 92, 181-193.
- Bodnar, R.J., Reynolds, T.J., and Kuehn, C.A., 1985. Fluid-inclusion systematics in epithermal systems, in Berger, B.R., and Bethke, P.M., eds., *Geology and Geochemistry of Epithermal Systems: Society of Economic Geologists, Reviews in Economic Geology* 2, 73-79.
- Bodnar, R.J., 1992a. Revised equation and table for freezing point depressions of H₂O-salt fluid inclusions (Abstract): PACROFI IV, Fourth Biennial Pan-American Conference on Research on Fluid inclusions, Program and Abstracts, Lake Arrowhead, CA, V.14, p. 15.
- Bosellini, A., Russo, A., Fantozzi, P.L., Assefa, G., and Tadesse, S., 1997. The Mesozoic succession of the Mekelle outlier (Tigre Province, Ethiopia). *Memorie DI Scienze Geologiche* 49, 95-116.

- Chang, Z., Large, R.R., Maslennikov, V., 2008. Sulfur isotopes in sediment-hosted orogenic gold deposits: Evidence for an early timing and a sea water sulfur source. *The Geological Society of America* 36, 971-974.
- Chewaka, S., and De Wit, M.J., 1981. Plate tectonics and metallogenesis: some guidelines to Ethiopian Mineral Deposits, *Ethiopian Institute of Geological Surveys Bulletin* 2, 129 pages.
- Clark, A.M.S., 1978. Chemical and mineralogical development of the Sidamo nickeliferous serpentinites (Ethiopia). *Mineralium Deposita* 13, 221-234.
- Condie, K.C., 1993. Chemical composition and evolution of the upper continental crust: contrasting results from surface samples and shales. *Chemical Geology*, 104, 1-37.
- Cooper, J.A., Stacey, J.S., Stoesser, D.B., and Fleck, R.J., 1979. An evaluation of the zircon method of isotopic dating in the southern Arabian craton. *Contributions to Mineralogy and Petrology* 68, 429-439.
- de Wit, M.J., 1981. Precambrian base metals. In: Chewaka, S., and de Wit, M.J. (eds.), *Plate tectonics and metallogenesis: some guidelines to Ethiopian Mineral Deposits*, Ethiopian Institute of Geological Surveys Bulletin 2, 65-82.
- de Wit, M.J., and Berg, R., 1981. Platinum. In: Chewaka, S., and de Wit, M.J. (eds.), *Plate tectonics and metallogenesis: some guidelines to Ethiopian Mineral Deposits*, Ethiopian Institute of Geological Surveys Bulletin 2, 83-96.
- de Wit, M.J., and Chewaka, S., 1981. Plate tectonic evolution of Ethiopia and the origin of its mineral deposits: an overview. In: Chewaka, S., and de Wit, M.J. (eds.), *Plate tectonics and metallogenesis: some guidelines to Ethiopian Mineral Deposits*, Ethiopian Institute of Geological Surveys Bulletin 2, 115-129.
- Faure, G., 1986. *Principles of isotope geology*. John Wiley and Sons eds., New York, 589 pages.
- Friedman, I., and O'Neil, J.R., 1977. Compilation of stable isotope fractionation factors of geochemical interest. In: Fleischer M (eds.) *Data of geochemistry*. US Geological Survey Professional Paper 440-KK, 12 pages.
- Garland, C.R., 1980. *Geology of the Adigrat area*. Memor No. 1. Ministry of Mines and Energy, Addis Ababa, 51 pages.
- Gebre-Mariam, M., Groves, D.I., McNaughton, N.J., Mikucki, E.J., and Vearncombe, J.R., 1993. Archean Au-Ag mineralization at Racetrack, near Kalgoorlie, Western Australia, a high crustal-level expression of the Archean composite lode-gold system. *Mineralium Deposita* 28, 375-387.

- Gebre-Mariam, M., Hagemann, S.G., and Groves, D.I., 1995. A classification scheme for epigenetic Archean lode-gold deposits. *Mineral. Deposita* 30, 408-410.
- Gebresilassie, S., Tadesse, S., and Hailu, K., 2003. Geology, mineralogy, and geochemistry of serpentinites from Kenticha area, southern Ethiopia, and associated Ni-mineralization. In: Eliopoulos et al. (eds.), *Mineral Exploration and Sustainable Development*, Proceedings of 7th Biennial meeting of the Society for Geology Applied to Mineral Deposits, Athens, Greece, V.2, 579-582.
- Goldfarb, R.J., Groves, D.I., and Gardoll, S., 2001. Orogenic gold and geologic time: a global synthesis. *Ore Geology Reviews* 18, 1-75.
- Goldstein, R.H., and Reynolds, T.J., 1994. Systematics of fluid inclusions in diagenetic minerals. *SEPM Short course* 31, 139 pages.
- Grant, J.A., 1986. The Isocon Diagram-A simple solution to Gresens' equation for metasomatic alteration. *Economic Geology* 81, 1976-1982.
- Gresens, L.R., 1967. Composition-volume relationships of metamorphism. *Chemical Geology* 2, 47-65.
- Groves, D.I., and Phillips, G.N., 1987. The genesis and tectonic controls on Archean lode gold deposits of the Western Australia shield: a metamorphic-replacement model, *Ore Geology Reviews* 2, 287-322.
- Groves, D.I., 1993. The crustal continuum model for late-Archean lode-gold deposits of the Yilgarn Block, Western Australia. *Mineralium Deposita* 28, 366-374.
- Groves, D.I., Goldfarb, R.J., Gebre-Mariam, M., Hagemann, S.G., and Robert, F., 1998. Orogenic gold deposits: A proposed classification in the context of their crustal distribution and relationship to other gold deposit types. *Ore Geology Reviews* 13, 7-27.
- Groves, D.I., Goldfarb, R.J., Robert, F., and Hart, C.J.R., 2003. Gold deposits in Metamorphic Belts: Overview of Current Understanding, Outstanding Problems, Future Research, and Exploration Significance. *Economic Geology* 98, 1-29.
- Guilbert, J.M., and Park, Jr., F.P., 1986. *The geology of ore deposits*. W.H. Freeman and Company, USA, 985 pages.
- Guo, F., Fan, W., Wang, Y., and Zhang, M., 2004. Origin of early Cretaceous calc-alkaline lamprophyres from the Sulu orogen in eastern China: implications for enrichment processes beneath continental collisional belt. *Lithos* 78, 291-305.
- Huston, D.L., 2000. Gold in Volcanic-hosted Massive Sulfide Deposits: Distribution, Genesis, and Exploration. *SEG Reviews* 13, 221-244.

- International Monetary Fund 2005a. The Federal Democratic Republic of Ethiopia-Selected issues and statistical appendix: Washington, DC, IMF, January 28, 87 pages.
- Johnson, P.R., and Woldehaimanot, B., 2003. Development of the Arabian-Nubian Shield: perspectives on accretion and deformation in the northern East African Orogen and the assembly of Gondwana. In: Yoshida, M., Windley, B.F., Dasgupta, S. (Eds.), Proterozoic East Gondwana: Supercontinent Assembly and breakup. Geological Society of London, Special Publication 206, 289-325.
- Kazmin, V., 1971. Precambrian of Ethiopia. *Nature* 230, 176-177.
- Kazmin, V., 1975. The Precambrian of Ethiopia and some aspects of the Geology of the Mozambique Belt. *Bulletin Geophysics. Obs., Addis Ababa University* 15, 27-43.
- Kazmin, V., Shiferaw, A., and Balcha, T., 1978. The Ethiopian basement and possible manner of evolution, *Geologische Rundschau* 67, 531-546.
- Kerrich, R., and Cassidy, K.F., 1994. Temporal relationships of lode gold mineralization to accretion, magmatism, metamorphism and deformation: Archean to Present: A Review. *Ore Geology Reviews* 9, 263-310.
- Klein, E. L., Harris, K., Giret, A., Moura, C.A.V., and Angelica, S. R., 2005. Geology and stable isotope (O, H, C, S) constraints on the genesis of the Cachoeria gold deposit, Gurupi Belt, northern Brazil. *Chemical Geology* 221, 188-206.
- Klein, E.L., Ribeiro, J.W.A., Harris, C., Moura, C.A.V., and Giret, A., 2008. Geology and fluid characteristics of the Mina Velha and Mandiocacal orebodies and implications for the genesis of the orogenic Chega Tudo gold deposit, Gurupi Belt, Brazil. *Economic Geology* 103, 957-980.
- Kröner, A., 1985. Ophiolites and the evolution of tectonic boundaries in the late Proterozoic Arabian-Nubian Shield of northeast Africa and Arabia. *Precambrian Research* 27, 277-300.
- Kröner, A., Linnebacher, P., Stern, R.J., Reischmann, T., Manton, W., and Hussein, I.M., 1991. Evolution of Pan-African island arc assemblages in the southern Red Sea Hills, Sudan, and in southwestern Arabia as exemplified by geochemistry and geochronology. *Precambrian Research* 53, 99-118.
- Kröner, A., and Passi, F.P., 1996. Evolution of the northern Somali basement: new constraints from zircon ages. *Journal of African Earth Sciences* 22, 1-15.
- Küster, D., Romer, R.L., Tolessa, D., Zerihun, and Beheemalingeswara, K., 2007. Geochemical evolution and age of the Kenticha Tantalum Pegmatite, southern Ethiopia.

- In: Proceedings of International Symposium, Granitic Pegmatites: The State of the Art, 6th-12th may 2007, Porto, Portugal.
- Lenoir, J.-L., Küster, D., Liégeois, J.-P., Utke, A., Haider, A., and Matheis, G., 1994. Origin and regional significance of late Precambrian and early Palaeozoic granitoids in the Pan-African belt of Somalia. *Geologische Rundschau*, 83, 624-641.
- Loucks, R.R., 2000. Precise geothermometry on fluid inclusion populations that trapped mixtures of immiscible fluids. *American Journal of Science* 300, 23-59.
- McLennan, S. M., Nance, W.B., Taylor, S.R., 1980. Rare earth element-thorium correlations in sedimentary rocks, and the composition of the continental crust. *Geochimica et Cosmochimica Acta* 44, 1833-1839.
- McClay, K., 1987. The mapping of geological structures. John Wiley and Sons, Inc., Chichester, 161 pages.
- McCuaig, T.C., and Kerrich, R., 1994. P-T-t-deformation-fluid characteristics of lode gold deposits: evidence from alteration systematics, in Lentz, D.R., ed., alteration and alteration Processes Associated with Ore-forming systems: Geological Association of Canada, short Course Notes 11, 339-379.
- Mikucki, E.J., 1998. Hydrothermal transport and depositional processes in Archean lode-gold systems: A review. *Ore Geology Reviews* 13, 307-321.
- Miller, J.A., Mohr, P.A., and Rogers, A.S., 1967. Some new K-Ar age determinations of basement rocks from Eritrea. *Bulletin Geophysics* 314, 351-372.
- Miyashiro, A., 1973. Metamorphism and metamorphic belts. George Allen and Unwin LTD., London, 492 pages.
- Mock, C., Arnaud, N.O., Cantagrel, J-M., Yirgu, G., 1999. ³⁹Ar/^{Ar}³⁹ thermochronology of the Ethiopian and Yemeni basements: reheating related to the Afar plume?, *Tectonophysics* 314, 351-372.
- Mogessie, A., Belete, K., and Hoinkes, G., 2000. Yubdo-Tulu Dimtu mafic-ultramafic belt, Alaskan type intrusions in western Ethiopia: its implication to the Arabian-Nubian Shield and tectonics of the Mozambique belt. *Journal of African Earth Sciences* 30, 62.
- Morton, W.H., 1981. Geology and mineralization of the Tsehafi Emba copper prospect, western Tigre. In: Chewaka, S., and de Wit, M.J. (eds.), Plate tectonics and metallogenesis: some guidelines to Ethiopian Mineral Deposits, Ethiopian Institute of Geological Surveys Bulletin 2, 75-88.
- Murphy, P.J., and Roberts, S., 1997. Evolution of a metamorphic fluid and its role in lode gold mineralization in the Central Iberian Zone. *Mineralium Deposita* 32, 459-474.

- Nockolds, S.R., Knox, R.W.O'B., and Chinner, G.A., 1978. *Petrology for students*. Cambridge University Press, Cambridge, 435 pages.
- Ohmoto, H, and Rye, R.O., (1979). Isotopes of sulfur and carbon. In: Barnes, H.L, eds., *Geochemistry of hydrothermal ore deposits*. John Wiley and Sons, New York, 509-567.
- Pearce, J.A., Harris, N.B.W., and Tindel, A.G., 1984. Trace element discrimination diagrams for the tectonic interpretation of granitic rocks. *Journal of Petrology* 25, 956-983.
- Peccerillo, A., and Taylor, S.R., 1976. Geochemistry of Eocene calc-alkaline volcanic rocks from the Kastamonu area, Northern Turkey. *Contributions to Mineralogy and Petrology* 58, 63-81.
- Pouchou, J., L., and Pichor, F., 1991. Quantitative analysis of homogeneous or stratified microvolumes applying the model "PAP. In: Heinrich, K.F.J., Newbury, D.E. (Eds.), *Electron Probe Quantification*. Plenum Press, New York, 31-75.
- Ramdohr, P., 1969. *The ore minerals and their intergrowths*. Pergman Press, Germany.
- Ray, G.E., 1998. Gold skarns: in *Geological Fieldwork 1997*, British Columbia Ministry of Employment and Investment, Paper 1998-1, 24H-1-24H-4.
- Reed, M.H., and Spycher, N.F., 1985. Boiling, cooling, and oxidation in Epithermal systems: a numerical modeling approach: in Berger, B.R., and Bethke, P.M., eds., *Geology and Geochemistry of Epithermal Systems: Society of Economic Geologists, Reviews in Economic Geology* 2, 249-272.
- Révész, K.M., and Landwehr, J.M., 2002. $\delta^{13}\text{C}$ and $\delta^{18}\text{O}$ isotopic composition of CaCO_3 measured by continuous flow isotopic ratio mass spectrometry: statistical evaluation and verification by application to Devils Hole DH-11 calcite. *Rapid Commun. Mass Spectro.* 16, 2102-2114.
- Ribbe, P.H., Phillips, M.W., and Gibbs, G.V., 1972. Tetrahedral bond length variations in feldspars: in Mackenzie and Zussman, eds., *The Feldspars*, Manchester, 25-48.
- Ridley, J.R., and Diamond, L.W., 2000. Fluid Chemistry of Orogenic Lode Gold Deposits and Implications for Genetic Models. *SEG Reviews*, 13, 221-244.
- Rock, N.M.S., 1990. *Lamprophyres*. Blackie, Glasgow and London and Van Nostrand Reinhold, New York, 285 pages.
- Roedder, E., 1984. Fluid inclusions. *Mineralogical Society of America, Revisions in Mineralogy* 12, 646 pages.
- Rollinson, 1993. *Using geochemical data: Evaluation, presentation and interpretation*. Longman publishers, Singapore, 352 pages.
- Rudnick, R.L., and Fountain, D.M., 1995. *Reviews of Geophysics* 33, 267-309.

- Schmidt-Mumm, A., 2000. Regional aktive Fluidsysteme während der Kratonisierung im späten Archaikum Simbabwe und Paläoproterozoikum Ghanas: flüssigkeitseinschlüsse als Bindeglied von Petrogenese, Tektogenese und der Metallogenese von Goldlagerstätten. Mathematisch-Naturwissenschaftlichen-Technischen Fakultät der Martin-Universität Halle Wittenberg, Habilitationsschrift, 148 pages.
- Schröcke, H., and Weiner, K.L., 1981. Mineralogie. Walter de Gruyter, Berlin, New York, 952 pages.
- Seward, T.M., 1991. The hydrothermal geochemistry of gold. In Foster, R.P., (eds.), gold metallogenesis and exploration. Chapman and Hall, London, 37-62.
- Seward, T.M., and Barnes, H.L., 1997. Metal Transport by Hydrothermal Ore Fluids: In Barnes, H.L., (eds.), Geochemistry of hydrothermal ore deposits. John Wiley and Sons, Inc., New York, 435-477.
- Sifeta, K., 2003. Geochemistry, tectonic setting, and provenance of Weri metavolcanic and sedimentary units, northern Ethiopia. M.Sc. Thesis, Shimane University, Japan, 107 pages.
- Stacey, J.S., and Kramers, J.D., 1975. Approximation of terrestrial lead evolution by a two-stage model. *Earth and Planetary Science Letters* 26, 207-221.
- Stacey, J.S., Doe, B.R., Roberts, R.J., Maryse, H.D., and Gramlich, J.W., 1980. A Lead Isotope Study of Mineralization in the Saudi Arabian Shield. *Contributions to Mineralogy and Petrology* 74, 175-188.
- Stacey, J.S., and Stoeser, D.B., 1983. Distribution of oceanic and continental leads in the Arabian-Nubian Shield. *Contributions to Mineralogy and Petrology* 84, 91-105.
- Stacey, J.S., and Hedge, C.E., 1984. Geochronologic and isotopic evidence for early Proterozoic continental crust in eastern Arabian Shield. *Geology* 12, 310-313.
- Stacey, J.S., Stoeser, D.B., Greenwood, W.R., and Fischer, L.B., 1984. U-Pb zircon geochronology and geological evolution of the Halaban-Al Amar region of the Eastern Arabian Shield, Kingdom of Saudi Arabia. *Journal of Geological Society of London* 141, 1043-1055.
- Stern, R.J., and Kröner, A., 1993. Late Precambrian crustal evolution in NE Sudan: isotopic and geochronologic constraints. *The Journal of Geology* 101, 555-574.
- Stern, R.J., 1994. Arc assembly and continental collision in the Neoproterozoic East African Orogen: implications for consolidation of Gondwana land. *Annual Reviews Earth Planetary Sciences* 22, 319-351.

- Stern, R.J., and Abdelsalam, M.G., 1998. Formation of juvenile continental crust in the Arabian-Nubian Shield: Evidence from granitic rocks of the Nakasib suture, NE Sudan. *Geologische Rundschau* 87, 150-160.
- Stern, R.J., 2002. Crustal evolution in the East African Orogen: a neodymium isotope perspective. *Journal of African Earth Sciences* 34, 109-117.
- Stern, R.J., Avigad, D., Miller, N.R., and Beyth, M., 2006. Evidence for the Snowball Earth hypothesis in the Arabian-Nubian Shield and the east African Orogen. *Journal of African Earth Sciences* 44, 1-20.
- Streckeisen, A., 1976. To each plutonic rock its proper name. *Earth Science Reviews* 12, 1-33.
- Sultan, M., Tucker, R.D., El Alfy, Z., Attia, R., and Ragab, A.G. 1994. U-Pb (zircon) ages for the gneissic terrane west of Nile, southern Egypt. *Geologische Rundschau* 83, 514-522.
- Sun, S., and McDonough, W.F., 1989. Chemical and isotopic systematics of oceanic basalts: implications for mantle composition and processes: In Sunders, A.D., and Norry, M.J. (eds), *Magmatism in ocean basins*, Geological Society Special Publication No. 42, 313-345.
- Tadesse, T., 1996. Structure across a possible intra-oceanic suture zone in low-grade Pan-African rocks of northern Ethiopia. *Journal of African Earth Sciences* 23, 575-381.
- Tadesse, T., Suzuki, K., Hoshino, M., 1997. Chemical Th-U-total Pb isochron age of zircon from the Mereb granite in northern Ethiopia. *Journal Earth Planetary Science Nagaya University* 44, 21-27.
- Tadesse, T., Hoshino, M., and Sawada, Y., 1999. Geochemistry of low-grade metavolcanic rocks from the Pan African of the Axum area, northern Ethiopia. *Precambrian Research*, 99, 101-124.
- Tadesse, T., Hoshino, M., Suzuki, K., and Iisumi, S., 2000. Sm-Nd, Rb-Sr, and Th-U-Pb zircon ages of syn- and post-tectonic granitoids from the Axum area of northern Ethiopia. *Journal of African Earth Sciences* 30, 313-327.
- Tadesse, S., Milesi, J.P., and Deschamps, Y., 2003. Geology and mineral potential of Ethiopia: a note on Geology and mineral map of Ethiopia. *Journal of African Earth Sciences* 36, 273-313.
- Tadesse, S., 2004. Genesis of the shear-zone related gold vein mineralization of the Lega Dembi gold deposit, Adola Gold Field, southern Ethiopia. *Gondwana Research* 7, 481-488.

- Taylor, S.R., and McLennan, S.M., 1985. *The Continental Crust: its composition and evolution*. Blackwell scientific publishers, Oxford, 312 pages.
- Teklay, M., 1997. *Petrology, Geochemistry, and Geochronology of Neoproterozoic Magmatic Arc Rocks from Eritrea: Implications for Crustal Evolution in the southern Nubian Shield*. V. 1. Eritrea Department of Mines Memoir, 125 pages.
- Teklay, M., Kröner, A., Mezger, K., and Oberhansli, R., 1998. Geochemistry, Pb-Pb single Zircon ages and Nd-Sr isotope composition of Precambrian rocks from southern and Eastern Ethiopia: implications for crustal evolution in East Africa. *Journal of African Earth Sciences*, 26, 207-227.
- Teklay, M., Kröner, A., and Mezger, K., 2002. Enrichment from plume interaction in the generation of Neoproterozoic arc rocks in northern Eritrea: implications for crustal accretion in the southern Arabian-Nubian Shield. *Chemical Geology* 184, 167-184.
- Thompson, R.N., 1982. British Tertiary Volcanic Province. *Scottish Journal of Geology* 18, 49-107.
- Thompson, J.F.H., and Newberry, R.J., 2000. Gold deposits related to reduced granitic intrusions. *Society of Economic Geology Reviews* 13, 221-244.
- Tosdal, R.M., Wooden, J.L., Bouse, R.M., 1999. Pb isotopes, ore deposits, and metallogenic terranes. In: Lambert, D.D., Ruiz, J., (eds.), *application of radiogenic isotopes to ore deposit research and exploration*. *Reviews in Economic Geology* 12, 1-28.
- Twiss, R.J., and Moores, E.M., 1973. *Structural Geology*. W.H. Freeman and Company, New York. 532 pages.
- Vail, J.R., and Hughes, D.J., 1977. Tholeiite derivative dyke swarms near Erkowit, Red Sea Hills, Sudan. *Geologische Rundschau* 66, 228-237.
- Vail, R.V., 1983. Pan-African crustal accretion in north-east Africa. *Journal of African Earth Sciences* 1, 285-294.
- Vail, J.R., 1985. Pan-African (late Precambrian) tectonic terranes and the reconstruction of the Arabian-Nubian Shield. *Geology* 13, 839-842.
- Walsh, J., 1981. Ethiopian Mineral Deposits, introduction. In: Chewaka, S., and de Wit, M.J. (eds.), *Plate tectonics and metallogenesis: some guidelines to Ethiopian Mineral Deposits*, Ethiopian Institute of Geological Surveys Bulletin 2, 36-37.
- Whalen, J.B., Currie, L.K., and Chappell, W.B., 1987. A-type granites: geochemical characteristics, discrimination and petrogenesis. *Contributions to Mineralogy and Petrology* 95, 407-419

- Wilson, M., 1989. *Igneous petrogenesis: a global tectonic approach*. Unwin Hyman, London, 466 pages.
- Yanagisawa, F., and Saki, H., 1983. Preparation of SO₂ for sulfur isotope ratio measurements by the thermal decomposition of BaSO₄-V₂O₅-SiO₂ mixtures. *Anal Chem* 55, 985-987.
- Yang, P., and Rivers, T., 2000. Trace element partitioning between coexisting biotite and muscovite from metamorphic rocks, Western Labrador: Structural, compositional and thermal controls. *Geochimica et Cosmochimica Acta* 64, 1451-1472.
- Zartman, R.E., and Doe, B.R., 1981. Plumbotectonics-the Model. *Tectonophysics* 75, 135-162.
- Zoheir, A.B., 2004. Gold Mineralization in the Um El Tuyor area, South Eastern Desert, Egypt: Geologic context, characteristics and genesis. Ph.D. Thesis, Ludwig-Maximilians University of Munich, Germany, 159 pages.

Annexes

Annex 1. Lithological and mineralogical data

Annex 2. Whole-rock geochemical data

Annex 3. Electronmicroprobe data

Annex 4. Microthermometric data

Annex 5. Isotope geochemistry data

Annex 1. Lithological and mineralogical data

Annex 1.1. List and description of samples collected from the Workamba area.

Sample	Location (UTM) Latitude/Longitude	Elevation (m)	Lithology	Description
TG06001	1535883; 565371	2275	Negash granite	Pink, rich of feldspars, mica, and quartz quartz monzonite/monzogranite
TG06002	1538076; 0490402	1760	Mai Kenetal Granitoid	Circular, coarse-grained, rich of feldspar phenocrysts, biotite, muscovite, and quartz
TG06003	1538239; 0490650	1843	Graywacke	Dark volcanic or graywacke material
TG06004	1520799; 0507021	1814	Early quartz veins	2-3 cm thick, gold bearing, and hematized
TG06005	1517904; 0500365	1886	Metavolcanic rock	Greenish, foliated, containing 1-5 cm thick clasts
TG06006	1517307; 0500912	1880	Metavolcanic rock	Greenish, foliated, and shows epidote alteration
TG06007	1517307; 0500914	1885	Metavolcanic rock	Greenish, mafic, and strongly foliated
TG06008	1517212; 0501657		Aplitic dike	Pinkish and fine-grained
TG06009	1517235; 0501019	1909	Quartz vein	Second generation, 10 cm thick
TG06010	1517001; 0501978	1876	Phyllite	white pinkish, foliated
TG06011	1516029; 0503002	1891	Phyllite	Pinkish, intercalated with graphite schist
TG06012	1516116; 0503347	1826	Phyllite	Whitish pink, fractured, locally silicified
TG06013			Slate/phyllite	Hard and silicified
TG06014	1516259; 0503361	1836	Sericite-chlorite schist	Greenish, fine-grained, and foliated
TG06015	1516501; 0503305	1817	Sericite-chlorite schist	Greenish, fine- to medium-grained, foliated and crenulated
TG06016	1516501; 0503307		Quartz vein	Second generation; parallel to the foliation
TG06017	1516882; 0503240	1817	Silicified rock	Less foliated, pinkish, composed of quartz and feldspar
TG06018	1517221; 0503200	1852	Metavolcanic rock	Greenish and medium-grained
TG06019	1517372; 0503233	1858	Sericite-chlorite schist	Greenish, fine-grained, and foliated
TG06020	1517372; 0503233	1858	Quartz vein	Second generation; parallel to the foliation
TG06021	1517613; 0503350		Metavolcanic rock	Silicified, composed of quartz, chlorite, and feldspar
TG06022	1517690; 0503328	1865	Metavolcanic rock	Greenish without clasts
TG06023	1518970; 0504271	1798	Slate	Grayish black
TG06024	1518970; 0504271	1798	Quartz vein	Second generation, normal to foliation
TG06025	1517714; 0505637		Slate/phyllite	Foliated, grayish black, and fractured
TG06026	1517857; 0505607	1734	Slate/phyllite	Foliated, grayish black, and fractured
TG06027	1517992; 0505592	1748	Sericite-chlorite schist	Foliated, whitish green, and foliated
TG06028	1518067; 0505523	1748	Quartz vein	Second generation, perpendicular to foliation, ~2 m thick, and boudinaged
TG06029	1518142; 0505508		Quartz vein	Second generation; parallel to foliation
TG06030	1518356; 0505547	1729	Sericite-chlorite schist	Whitish pink and crenulated
TG06031	1518491; 0505358	1741	Slate	Black and foliated
TG06032	1518491; 0505358	1741	Metavolcanic rock	Whitish and silicified
TG06033	1518491; 0505358	1741	Aplitic dike	Pinkish, fine-grained, and 50 cm thick
TG06034	1518589; 0505392	1750	Slate	Black, and foliated

Annex I.1. Continued.....

Sample	Location (UTM) Latitude/Longitude	Elevation (m)	Lithology	Description
TG06035	1518632; 0505268	1758	Sericite-chlorite schist	Greenish, medium-grained, and strongly foliated
TG06036	1518870; 0505195	1762	Quartz-sericite rock	Whitish grey, highly silicified
TG06037	1518715; 0505167		Monzogranite dike	Coarse-grained, composed of quartz, feldspar, and biotite
TG06038	1518852; 0505111	1781	Sericite-chlorite schist	Whitish pink; intercalated with metavolcanic rocks
TG06039	1519341; 0505091	1813	Metavolcanic rock	Greenish, highly foliated and locally epidotized
TG06040	1519198; 0505525	1829	Quartz-sericite rock	Pinkish grey, massive, and fine- to medium-grained
TG06041	1519081; 0505535	1839	Quartz-sericite rock	Pinkish-grey, massive, and fine- to medium-grained
TG06042	1519074; 0505648		Quartz-sericite rock	Pinkish-grey, massive, and fine- to medium-grained
TG06043	1519055; 0505660	1804	Monzogranite dike/sill	Pinkish grey, massive, and coarse-grained medium to coarse-grained
TG06044	1519038; 0505697	1801	Sericite-chlorite schist	Greenish, sheared, and rich in oxidized pyrite
TG06045	1519013; 0505715	1794	Sericite-chlorite schist	Greenish, sheared/ crenulated, and rich of oxidized pyrites
TG06046	1519029; 0505702		Marble lens	Intercalated within the mineralized Sericite-chlorite schist
TG06047	1519029; 0505702		Aplitic dike	Fine-grained, located just beneath the marble Lens (sample TG06046) and ~ 50 cm thick
TG06048	1519160; 0505760		Sericite-chlorite schist	Whitish green; silicified
TG06049	1519160; 0505760		Monzogranite dike/sill	Pinkish, ~ 100 m thick
TG06050	1519322; 0505929	1813	Monzogranite dike/sill	Northern part of the dike/sill, similar characteristics as TG06050
TG06051	1518997; 0505620	1805	Monzogranite dike/sill	Southern part of the dike/sill, contains mafic minerals (e.g. biotite)
TG06052	1518909; 0505476	1811	Monzogranite dike/sill	Same monzogranite dike as sample TG06051
TG06053	1519043; 0505395	1787	Quartz-sericite rock	Whitish pinkish and slightly foliated
TG06054	1519827; 0505962	1782	Quartz-sericite rock	Affected by brittle-ductile shear zone
TG06055	1519519; 0506394	1760	Phyllite	Fine-grained; shows lustrous sheen
TG06056	1520920; 0506962	1796	Metavolcanic rock	From Au-copper zone; characterized by malachite staining
TG06057	1520895; 0506983	1785	Metavolcanic rock	From copper-bearing zone; characterized by malachite staining
TG06058	1520799; 0507021	1786	Early quartz veins	Gold-bearing, folded and 1-2 cm thick
TG06059			Early quartz veins	Gold-bearing, folded and 1-2 cm thick
TG06060			Quartz vein	Second generation; parallel to the foliation
TG06061	1521529; 0506975	1756	Metavolcanic rock	At the Au-copper zone; characterized by malachite staining
TG06062	1519856; 0504742		Metavolcanic rock	Greenish; affected by epidote alteration
TG06063	1519963; 0504625	1807	Sericite-chlorite schist	Sheared and strongly foliated

Annex 1.1. Continued.....

Sample	Location (UTM) Latitude/Longitude	Elevation (m)	Lithology	Description
TG06064	1520319; 0504512	1808	Metavolcanic rock	Characterized by 1-5 cm thick clasts
TG06065	1520516; 0504379		Quartz vein	Second generation; parallel to foliation
TG06066	1520804; 0504015	1814	Quartz-sericite rock	Whitish-pink; slightly foliated
TG06067	1520802; 0503824	1820	Metavolcanic rock	Rich of round to angular clasts
TG06068	1520169; 0502529	1826	Metavolcanic rock	Greenish, epidotized, and foliated
TG06069	1519062; 0499148	1898	Metavolcanic rock	Greenish and less foliated
TG06070	1519533; 0498699	1938	Metavolcanic rock	Fine- to medium-grained, whitish green, more of intermediate in nature

Annex 1.2. Orientation of representative geological structures present in the study area

No.	Location (UTM) Latitude/Longitude	Lithology	Types of measured structures	Strike/dip or Trend/plunge
1	1517904; 0500365	Metavolcanic rock	Foliation	N40°E/62°NW
2	1517307; 0500914	Metavolcanic rock	Foliation	N35°E/55°NW
3	1517307; 0500914	Metavolcanic rock	Foliation	N60°E/80°NW
4	1517212; 0501657	Aplitic dike	Dike orientation	N45°E/80°NW
5	1517235; 0501019	Quartz vein	Vein orientation	N60°E/70°SE
6	1517001; 0501978	Phyllite	Foliation	N50°E/63°NW
7	1516029; 0503002	Phyllite	Foliation	N55°E/45°NW
8	1516116; 0503347	Phyllite	Foliation	N45°E/40°NW
9	1516116; 0503347	Phyllite	Orientation of joints	N70°W/60°SE
10	1516259; 0503361	Sericite-chlorite schist	Foliation	N45°E/25°NW
11	1516501; 0503305	Sericite-chlorite schist	Foliation	N40°E/60°NW
12	1517221; 0503050	Metavolcanic rock	Foliation	N55°E/45°NW
13	1517601; 0503100	Metavolcanic rock	Foliation	N45°E/55°NW
14	1517320; 0503200	Metavolcanic rock	Foliation	N55°E/55°NW
15	1517372; 0503233	Quartz vein	Vein orientation	N55°E/40°NW
16	1517714; 0505637	Slate/phyllite	Foliation	N50°E/70°NW
17	1517700; 050501	Sericite-chlorite schist	Foliation	N40°E/65°NW
18	1518820; 050487	Sericite-chlorite schist	Foliation	N35°E/65°NW
19	1518392; 0505592	Sericite-chlorite schist	Foliation	N45°E/68°NW
20	1518142; 0505508	Sericite-chlorite schist	D2 fold axis	N10°E/35°NE
21	1518491; 0505358	Aplitic dike	Dike orientation	N45°E; with subvertical dip
22	1518589; 0505392	Slate	Foliation	N80°E/80°NW
23	1518632; 0505268	Sericite-chlorite schist	Foliation	N50°E/60°NW
24	1518500; 0505697	Sericite-chlorite schist	Foliation	N50°E/52°NW
25	1517519; 0505905	Phyllite	Foliation	N50°E/70°NW
26	1521529; 0506975	Slickenside	lineation	N50°E/70°
27	1518100; 0507057	Slate/phyllite	Foliation	N40°E/65°NW
28	1519856; 0504742	Metavolcanic rock	Foliation	N55°E/65°NW
29	1520516; 0504379	Quartz vein	Vein orientation	N20°E/70°NW
30	1521350; 0507000	D2 parasitic fold	D2 fold axis	N-S; 75°N
31	1517050; 0504978	D1 fold	D1 fold axis	N80°W/50°ENE
32	1521000; 0503850	Metavolcanic rock	Foliation	N45°E/52°NW
33	1520900; 0504200	Metavolcanic rock	Foliation	N40°E/45°NW
34	1520000; 0504880	Metavolcanic rock	Foliation	N35°E/70°NW
35	1520600; 0505500	Metavolcanic rock	Foliation	N40°E/45°NW
36	1519200; 0505600	Silicified rock	Foliation	N35°E/40°NW
37	1521500; 0506780	Metavolcanic rock	Foliation	N45°E/52°NW

Annex. 1.3. Geological logging data of the drilled boreholes from the mineralized zone. The left column represents depth interval in meters. Boreholes J2, J4, J5, J6, J7, and J9 were drilled during the detailed exploration program of the company in April 2006, whereas GBH10 and 18 were developed during the reconnaissance exploratory survey in 2004 (next page).

Hole J2; X = 505795; Y = 1519053; elevation = 1816 m, azimuth = 140°, inclination = 55°, total depth = 95 m	
0-1.46	Soil and silicified rock (sample J2-1)
1.46-30.90	Fine-grained, whitish-pink silicified rock; foliated; locally intercalated with chlorite-rich schist (e.g. samples J2-05 to 07, J2-13); locally overprinted by hematite stain (e.g. samples J2-11 to 13)
30.90-31.90	Lamprophyre characterized by biotite phenocrysts in fine-grained ground mass (sample J2-14)
31.90-70	Fine-grained, greenish chlorite-rich schist; foliated; locally crenulated and sulfidized (samples J2-19 to 23), and cut by lamprophyre (sample J2-18)
70-79.76	Aplitic dikes/sills and lamprophyre cutting the chlorite-rich schist (samples J2-28 to 31)
79.76-95	Fine- to medium-grained, greenish chlorite-rich schist; strongly foliated; sulfidized and carbonatized; samples J2-32 to 36
Hole J4; X = 505719; Y = 1518999; elevation = 1820 m, azimuth = 140°, inclination = 53°, total depth = 86 m	
0-16.52	Medium to coarse-grained, pinkish monzogranite dike/sill (samples J4-1 to 5)
16.52-37.52	Fine-grained, whitish-pink silicified rock (samples J4-6 to 9 and J4-11 to 12); locally showing lustrous sheen and cut by aplitic dike/sill (sample J4-10)
37.52-70.38	Fine-grained, greenish to light-greenish chlorite-rich schist; foliated; commonly crenulated and silicified; samples (J4-13 to 23)
70.38-85.38	Aplitic dikes commonly cut by calcite veinlets
Hole J5; X = 505674; Y = 1518927; elevation = 1797 m, azimuth = 140°, inclination = 50°; total depth = 65 m	
0-3.60	Soil and weathered pinkish silicified rock (sample J5-01)
3.60-31	Fine-grained, pinkish silicified rock; locally crenulated and overprinted by hematite dust; samples J5-02 to 07
31-72.58	Fine-grained, greenish chlorite rich-rock; cut by aplitic dike/sills and lamprophyre (samples J5-09, 11, and 13); foliated; locally sulfidized and carbonatized (samples J5-10, 12, 14, and 15)
Hole J6; X = 505630; Y = 15118871; elevation = 1803 m, azimuth = 140°, inclination = 65°, total depth = 56 m	
0-8	Soil and weathered silica-rich rock (sample J6-01)
8-21.58	Fine-grained, whitish-pink silica-rich rock; locally overprinted by hematite dusts; samples J6-02 to 03
21.58-25.30	Aplitic dike/sill (samples J6-04 to 05)
25.30-55.44	Fine-grained, greenish, chlorite-rich schist, cut by calcite veinlets; samples J6-07 to 12
J7; X = 505583; Y = 1518854; elevation = 1765 m, azimuth = 140°, inclination = 65°, total depth = 81 m	
0-24	Medium to coarse-grained; pinkish monzogranite dike/sill; samples J7-01 to 02
24-45	Medium-grained, pinkish silicified sericite-chlorite schist; samples J7-03 to 05
45-80.6	Fine-grained, greenish, chlorite-rich schist cut by aplitic dikes and calcite veinlets; locally sulfidized; samples J7-06 to 12
Hole J9; X = 505542; Y = 1518827; elevation = 1765 m, azimuth = 140°, inclination = 80°, total depth = 91 m	
Data for upper part of the section not available; lower part is dominated by chlorite-rich schist cut by aplitic dike/sill (J9-13)	
Hole GBH10; X = 505442; Y = 1518874; elevation = 1796 m, azimuth = 140°, inclination = 65°, total depth = 200 m	
0-0.63	Soil
0.63-57.2	Fine-grained, pinkish, silicified rock (samples GBH10-02 to 39), locally intercalated by cherty layer (GBH10-16) and cut by aplitic dike/sill (GBH10-35)
57.2-79.15	Fine- to medium-grained, light greenish pink, sericite-quartz-chlorite schist samples (GBH10-40 to 58); locally sulfidized and cut by calcite veinlets
79.15-119.65	Fine- to medium-grained, greenish, chlorite-rich schist (cores from GBH10-59 to 94, sulfidized and carbonatized, commonly cut by lamprophyre (GBH10-67) and aplitic dike/sill (GBH10-89)
119.65-157.6	Pinkish monzogranite dike/sill (cores from GBH10-95 to 97)
157.6-200.1	Greenish, chlorite-rich schist; sulfidized and carbonatized, locally silicified; samples GBH10-98 to 120
Hole GBH18; X = 505676; Y = 1518927; elevation = 1797 m, azimuth = 140°, inclination = 50°, total depth = 69 m	
0-8.2	Pinkish monzogranite dike (cores from GBH18-1 to 5)
8.2-22.10	Whitish pink silicified sericite-rich schist (cores from GBH18-6 to 15), locally cut by aplitic dikes/sills (GBH18-08; GBH18-14)
22.10-68.8	Fine-grained, greenish chlorite-rich schist (cores from GBH18-16 to 59); sulfidized and carbonatized; locally cut by lamprophyre (e.g. sample GBH18-19)

Annex. 1.4. Summary of the petrographic description of studied rocks. Abbreviations: qz = quartz, ser = sericite, chl = chlorite, bt = biotite, pl = plagioclase, and cal = calcite.

Thin section no.	Description	Rock name
GBH10-01; GBH10-16; GBH10-33; GBH10-118; GBH18-12; GBH18-58; J7-06; TG-06-054	Mineralogical composition: qz = ~50%, ser = ~45%, chl 4% and hematite = 1%; sericite not/or slightly foliated; quartz occurs as veinlets cutting sericite or as clustered grains. Quartz shows undulose extinction (e.g. in sample GBH10-01)	Quartz-sericite rock
GBH10-50; GBH10-55; GBH10-59; GBH10-63; GBH10-115; GBH10-120; GBH18-06; GBH18-16; GBH18-25; GBH18-40; GBH18-44; GBH18-45; GBH18-59; J2-03; J2-04; J2-05; J2-08; J2-10; J2-13; J2-13'; J2-24; J2-24'; J2-25; J5-14; J6-02; J6-03; J6-10	Mineralogical composition: ser = ~20 to 60%, commonly ~40%, qz = ~20 to 45%, mostly ~30%; chl = ~5 to 15%, commonly ~10%; accessories include feldspar, biotite (e.g. GBH18-44), calcite, pyrite, and hematite. Sericite is strongly foliated (e.g. J2-04; J2-13'); quartz occurs as clustered grains (e.g. GBH18-06) and veinlets (e.g. GBH10-59; GBH10-115; GBH10-120); Calcite veinlet locally cuts sericite (e.g. GBH10-50; GBH10-59; GBH18-59)	Sericite-quartz-chlorite schist
GBH10-84; GBH10-66; GBH10-102; GBH10-103; GBH18-26; GBH18-31; GBH18-51; GBH18-54; GBH18-57; J2-32; J2-34; J2-34'; J2-35; J2-36; J7-10	Mineralogical composition: cal = ~25 to 90%, chl = 2 to ~30%, commonly ~20%; qz = ~3 to 45%; sulfides (dominantly sphalerite) = ~5 to 25%; ser = ~5%. Calcite veinlet cutting sericite or quartz (e.g. GBH10-84). Calcite also replaces chlorite/sericite (e.g. GBH18-51; J2-34)	Carbonatized chlorite-quartz schist
GBH10-70; GBH18-28; GBH18-34; J2-15; J2-17; J2-19; J7-10	Mineralogical composition: chl = ~20 to 70%, qz = 35 to 50%; accessories include cal, ser, sulfides, and hematite. Calcite veinlet cuts chlorite (e.g. GBH18-28)	Chlorite-quartz schist
GBH10-95; GBH10-96; GBH10-97; GBH18-01; GBH18-05; TG-06-049; TG-06-052	Mineralogical composition: qz = ~25 to 40%; K-feldspar = ~30%, pl = ~20%; bt = ~5-10%; accessories include calcite and hematite. Quartz occurs interstitial to feldspars or as clustered grains. Alteration: sericitization of feldspars; pervasive carbonatization, which is usually expressed by calcite disseminations	Medium to coarse-grained monzogranite dike/sill
GBH10-35; GBH10-89; GBH18-08; GBH18-14; J2-14; J2-16; J2-23; J2-28; J2-29; J2-32'; J5-02; J6-04, 05; J7-08	Mineralogical composition: feldspar = ~20 to 40%, qz = ~15 to 35%; bt = ~5-10%; ser = 20%); accessories include chl, ep, and sulfides. Alteration: sericitization of feldspars, epidotization, chloritization, and carbonatization. The aplitic dikes/sills are severely altered than the monzogranite dikes/sills	Aplitic dike/sill or fine-grained monzogranite
GBH10-67; GBH18-19; J2-18; J2-30; J2-30'; J4-04; J4-28; J5-13	Mineralogical composition: bt = ~ 55%; feldspar = ~20 to 40%; qz = up to 5%; cal = up to 15%; accessories include chl and ep. Biotite occurs as phenocrysts in a feldspar dominated ground mass. Quartz shows undulose extinction (e.g. GBH10-67). Alteration: carbonatization characterized by calcite veinlet cutting biotite, feldspar, and sericite; chloritization of biotite and epidotization.	Lamprophyre

Annex 1.5. Type and characteristics of recognized sulfides in studied polished sections

Polished section no	Types of sulfides	Description
GBH18-58; GBH10-89, GBH10-120; J2-25; J2-27; J2-35; J2-36; J2-36'; J4-29, J5-10; J6-09; J7-12; J9-11; J9-21; J9-29; J9-31	Major: pyrite Minor: chalcopyrite, pyrrhotite, sphalerite, and galena	Pyrite occurs as continuous to discontinuous veinlets, and disseminations; chalcopyrite as inclusions or veinlets cutting pyrite; galena as inclusions in pyrite; sphalerite overgrowths in pyrite
GBH18-25	Major: galena Minor: sphalerite, chalcopyrite, pyrite	Galena veinlet cuts sphalerite; chalcopyrite occurs as inclusions in sphalerite; pyrite occurs as disseminated grains
GBH10-59; GBH10-70; GBH10-84; GBH18-28; GBH18-31 and 34; J2-26	Major: sphalerite Minor: galena, pyrite, chalcopyrite	Sphalerite occurs as discontinuous to continuous veinlets; galena occur as inclusions in sphalerite; chalcopyrite exsolutions in sphalerite (chalcopyrite disease)

Annex 2. Whole rock geochemical data

Annex 2.1. Major (wt. %), trace and rare earth element (ppm) compositions of the Negash granitoid of Asrat (2002) used in this work for comparison.

Rock	Monzogabbros			Monzodiorites						Hybrid monzodiorites			
Samples	N9-25	N9-21	N9-29	N9-42	N9-3	N9-47	N9-4	N9-43	N9-2	N9-24	N9-19	N9-13	N9-41
SiO ₂	46.66	48.11	48.30	49.67	49.76	51.48	53.26	53.74	53.87	55.74	50.99	53.12	53.74
Al ₂ O ₃	13.00	10.01	14.61	16.13	15.48	13.15	16.17	16.32	13.49	15.64	17.35	18.09	18.40
FeOt	12.61	14.17	11.74	11.47	11.53	11.46	10.37	9.40	10.72	9.06	9.48	8.21	7.57
MnO	0.14	0.16	0.13	0.13	0.13	0.14	0.12	0.10	0.13	0.1	0.10	0.09	0.09
MgO	7.03	8.97	6.76	4.41	4.83	6.35	3.58	3.71	5.97	3.84	5.50	4.52	4.19
CaO	8.91	9.15	7.91	7.85	7.94	7.26	6.49	6.32	5.68	5.73	5.77	6.01	5.65
Na ₂ O	2.86	2.23	3.08	3.84	3.64	3.11	4.10	4.24	2.92	4.07	4.56	4.75	4.85
K ₂ O	0.91	0.93	1.31	1.37	1.05	1.30	1.95	1.98	2.08	1.99	2.87	2.09	2.63
TiO ₂	4.86	4.76	4.48	3.09	3.32	4.06	2.68	2.49	2.76	2.27	2.08	1.48	1.58
P ₂ O ₅	1.13	0.70	0.38	1.26	1.22	0.52	1.01	0.87	0.68	0.72	0.43	0.54	0.46
LOI ^b	0.62	0.76	1.66	1.21	1.48	0.68	0.46	0.82	1.72	0.83	0.87	1.14	0.87
Total	98.73	99.95	100.36	100.43	100.38	99.51	100.17	99.99	100	99.99	100	100	100
Ba	440	373	535	535	6.36	557	738	884	775	859	726	963	833
Cs	0.34	0.54	0.32	0.54	0.34	0.45	0.68	0.62	0.85	0.96	1.11	0.67	0.72
Rb	16.60	13.50	20	22.30	15.90	21.20	35.20	37.50	37.30	39.40	61.50	40.10	49.50
Sr	961	656	906	1318	1443	874	1077	1171	791	1085	1067	1391	1326
Y	18.20	17.60	11.10	22	22.70	16.40	23.40	21.50	19.20	20.10	22.20	21.80	21.40
Zr	146	127	97.70	99.10	120	163	171	219	202	197	275	251	191
Nb	12.70	12.70	10.60	15.30	13.10	11.20	17.20	13.10	12.30	11.90	20	8.85	14.40
Th	0.95	1.14	0.76	1.18	1.03	1.24	2.20	2.37	1.15	1.43	4.20	2.73	2.33
U	0.39	0.49	0.30	0.59	0.45	0.53	0.72	0.85	0.58	0.74	1.68	0.65	0.91
V	224	246	198	198	189	199	142	138	146	136	178	165	150
Ni	124	187	167	31.60	48.90	131	17.80	31.70	103	47.20	85.30	66.40	74.20
Cr	278	561	448	53.40	63.20	358	19.30	45.30	303	88.40	140	86.60	129
Pb	3.05	3.37	3.41	5.26	4.67	4.86	6.39	7.96	5.85	7.03	7.77	7.50	7.26
La	23.30	17.4	13.30	26.90	26.40	18.70	37.60	34.60	23.20	26.90	36.50	48.30	28.50
Ce	54.70	44.30	30.90	66.30	64.80	42.40	81.80	77.80	56.20	62.40	83	102	68.20
Pr	7.67	6.15	4.36	9.46	9.07	5.88	10.60	10.40	7.28	8.18	10.30	11.80	8.64
Nd	34.20	28.60	19	40.40	41.50	24.80	45.50	42.90	32.60	34.10	42.60	43.60	34.50
Sm	7.33	6.60	3.96	9.08	8.79	5.50	9.23	8.61	6.86	7.12	7.88	7.50	6.84
Eu	2.59	2.14	1.74	3.11	3.19	1.90	3.26	2.80	2.31	2.57	2.31	2.42	1.89
Gd	6.34	5.72	3.63	7.39	7.77	5.35	7.54	6.82	6	6.03	6.28	5.65	5.12
Tb	0.75	0.70	0.50	0.91	0.96	0.59	0.99	0.90	0.78	0.78	0.87	0.80	0.70
Dy	3.90	3.64	2.51	4.53	5.18	3.30	4.90	4.67	3.81	3.93	4.62	4.14	3.94
Ho	0.60	0.60	0.43	0.81	0.80	0.59	0.77	0.81	0.71	0.74	0.80	0.80	0.74
Er	1.45	1.54	1.06	1.93	1.94	1.51	1.96	2.06	1.71	1.73	2.06	2.03	1.93
Tm	0.20	0.19	0.14	0.22	0.25	0.20	0.25	0.28	0.23	0.25	0.30	0.31	0.27
Yb	1.08	1.12	0.823	1.53	1.46	1.26	1.42	1.70	1.49	1.53	1.68	1.84	1.77
Lu	0.16	0.17	0.11	0.20	0.22	0.16	0.21	0.21	0.24	0.22	0.29	0.29	0.28
ΣREE	144	119	82	173	172	112	206	195	143	156	199	231	163
Eu/Eu*	1.14	1.04	1.38	1.13	1.16	1.06	1.16	1.08	1.08	1.17	0.97	1.09	0.94
(La/Yb) _N	14.40	10.40	10.8	11.80	12.10	9.90	17.70	13.60	10.40	11.80	14.50	17.60	10.80
(Ce/Yb) _N	2	1.60	2.10	1.80	1.90	2.10	2.50	2.50	2.10	2.30	2.90	4	2.60
XFe ^b	0.64	0.61	0.63	0.72	0.70	0.64	0.74	0.72	0.64	0.70	0.63	0.64	0.64

Annex 2.1. Continued.....

Samples	Granodiorite-tonalite									Monzogranite		Aplite
	N9-16	N9-44	N9-39	N9-17	N9-36	N9-45	N9-23	N9-37	N9-15	N9-30	N9-14	N9-1
SiO ₂	55.18	58.31	59.60	61.89	62.05	64.58	65.64	66.14	68.28	64.66	66.46	71.65
Al ₂ O ₃	14.59	16.07	18.21	16.75	17.25	16.83	17.10	16.09	15.28	16.73	15.70	13.63
FeOt	7.57	6.04	5.40	5.17	4.64	3.76	3.39	3.45	3.16	3.74	3.70	0.98
MnO	0.09	0.09	0.05	0.06	0.05	0.04	0.03	0.03	0.04	0.04	0.05	— ^a
MgO	6.98	5.37	3.33	3.04	2.75	2.12	1.74	2.03	1.73	2.25	2.02	—
CaO	5.69	5.33	4	4.05	3.30	3.37	3.03	3.04	2.55	3.06	2.85	0.85
Na ₂ O	3.32	4.48	5.16	4.75	4.82	4.98	5.20	4.77	4.33	4.77	4.52	4.81
K ₂ O	2.90	2.44	2.67	2.60	3.43	2.85	2.68	3.15	3.52	3.23	3.31	3.81
TiO ₂	1.10	1.02	0.82	0.91	0.66	0.61	0.55	0.54	0.51	0.52	0.57	—
P ₂ O ₅	0.28	0.48	0.23	0.25	0.17	0.18	0.15	0.16	0.14	0.14	0.16	—
LOI ^b	1.87	0.78	0.54	0.55	0.87	0.68	0.49	0.54	0.41	0.85	0.63	0.31
Total	99.58	100.41	100	100	99.99	100	100	99.94	99.95	99.99	99.97	96.04
Ba	779	883	947	1049	953	1120	1053	779	774	952	809	30.80
Cs	1.16	0.58	0.62	0.85	0.96	0.40	1.26	0.69	1.37	1.15	1.50	13.70
Rb	60.40	49.20	55.50	48.40	65.10	38.90	54.80	53.60	69.50	62.60	66.20	337
Sr	871	1581	1381	1261	1119	1125	1075	978	908	1120	978	12.40
Y	14	15	8.44	15.90	7.81	9.13	9.89	8.43	10.50	7.81	9.87	3.48
Zr	164	201	133	192	133	162	158	125	154	119	162	109
Nb	6.51	6.86	3.39	6.78	3.66	4.12	4.11	3.78	4.81	3.41	5.11	3.96
Th	2.91	1.79	0.96	2.11	1.74	0.92	1.70	1.61	5.11	2.71	4.40	30.90
U	1.09	0.75	0.39	0.90	0.65	0.45	0.83	0.73	1.41	1.04	1.41	9.98
V	148	115	99.50	99.10	80.70	66	65.60	61.60	53	65.30	64	2.40
Ni	196	146	61.80	52.20	50.90	34.10	25.90	36	27.30	39.70	34.30	0
Cr	389	238	104	93.20	79.70	55.70	41.50	62.60	49.50	65.80	59.30	6.60
Pb	5.37	7.12	6.97	9.25	8.17	8.90	9.92	8.30	13.80	11.70	15.30	68.40
La	24.90	34	13.80	22.60	15.50	14.90	12.80	15.20	23.40	16.60	22.70	4.55
Ce	54.10	73.70	29.70	54.60	29.40	33	28.20	30.60	44	32	45.60	4.35
Pr	6.36	9.13	3.64	6.90	3.41	3.99	3.55	3.53	4.94	3.76	5.31	0.368
Nd	23.90	36.80	14.70	26.90	13.20	15.40	14	13.60	18.70	14.20	19.10	0.934
Sm	4.31	6.22	2.73	5.04	2.12	2.54	2.81	2.43	3.25	2.47	3.45	0.156
Eu	1.35	1.66	0.91	1.46	0.83	0.88	0.91	0.85	0.97	0.74	0.93	0.04
Gd	3.31	4.26	1.97	3.83	1.78	2.31	2.16	1.92	2.32	2.04	2.40	0.21
Tb	0.50	0.58	0.28	0.56	0.25	0.32	0.33	0.27	0.36	0.29	0.34	0.03
Dy	2.80	3.24	1.81	3.06	1.44	1.65	1.77	1.53	1.82	1.60	1.74	0.23
Ho	0.48	0.54	0.32	0.54	0.25	0.34	0.35	0.30	0.37	0.28	0.34	0.06
Er	1.27	1.47	0.85	1.46	0.77	1.01	0.78	0.83	0.97	0.76	0.92	0.24
Tm	0.18	0.19	0.13	0.21	0.11	0.14	0.13	0.11	0.14	0.14	0.14	0.06
Yb	1.19	1.26	0.84	1.34	0.75	0.86	0.85	0.73	0.97	0.76	0.86	0.62
Lu	0.19	0.20	0.13	0.20	0.13	0.14	0.13	0.12	0.14	0.12	0.15	0.19
ΣREE	125	173	72	129	70	77	69	72	102	76	104	12
Eu/Eu*	1.06	0.94	1.15	0.98	1.27	1.10	1.09	1.16	1.03	0.98	0.94	0.61
(La/Yb) _N	14	18	11	11.30	13.80	11.50	10.10	14	16.20	14.70	17.60	4.9
(Ce/Yb) _N	3.60	3.40	3.10	2.80	4.50	3.60	2.80	3.90	4.40	4.10	4.10	18
XFe ^b	0.52	0.53	0.62	0.63	0.63	0.64	0.66	0.63	0.65	0.62	0.65	1

Annex 2.2. Major (wt. %), trace and REE (ppm) compositions of the Rama, Sibta, Mereb, and Shire post-tectonic granitoids used to compare with the geochemical characteristics of the Workamba intrusive rocks, after Tadesse et al. (2000). Abbreviations: na = not analyzed.

Location	Rama	Sibta		Mereb	Shire	
Sample	TT900	TT950	TT788	TT428	AG1117	AG1101
SiO ₂	63.03	71.38	68.31	69.06	70.5	71.06
Al ₂ O ₃	16.66	13.58	15.94	15.58	15.64	15.3
Fe ₂ O ₃	0.40	1.09	0.79	0.8	0.52	0.18
FeO	3.95	1.15	1.65	1.79	1.29	1.01
MnO	0.08	0.05	0.03	0.04	0.03	0.02
MgO	3.18	0.62	1.01	0.91	0.92	0.33
CaO	4.75	1.13	1.96	1.98	2.11	1.43
Na ₂ O	3.83	3.44	4.41	4	4.64	4.29
K ₂ O	2.86	5.13	4.34	4.75	3.57	4.76
TiO ₂	0.59	0.43	0.46	0.43	0.3	0.22
P ₂ O ₅	0.12	0.11	0.2	0.14	0.11	0.07
LOI ^b	0.48	0.46	0.57	0.4	0.45	0.71
Total	99.91	98.57	99.66	99.89	100.08	99.37
Ba	859	726	1571	932	1212	978
Ce	28	114	54	56	23	35
Cr	90	8	13	3	14	6
Ga	19	16	19	20	19	22
Nb	9	24	Na	7	6	3
Ni	16	6	10	5	13	4
Pb	na	na	146	115	na	194
Rb	76	164	77	139	75	175
Sr	406	292	1141	401	864	478
Th	4	18	6	12	2	18
V	50	8	Na	43	22	na
Y	20	21	9	13	4	6
Zr	194	244	198	191	140	148

Annex 2.3. Major (wt. %) and trace element (ppm) concentrations of the Mai Kenetal-Hawzen area mafic/intermediate metavolcanic rocks (Alene et al. 2000) plotted together with trace element values of Workamba metasedimentary rocks for comparison.

Mafic/intermediate metavolcanic rocks																			
Sample	NW3	NW35	NW41b	NW79	NW80	NW82	HM24c	MK4	MK13	MK16	MK19	MK26	MK27	MK31b	MK33b	MK48b	MK49	MK58b	MK62
SiO ₂	47.49	50.26	57.96	52.26	53.92	48.75	53.25	48.71	49.55	55.31	51.75	51.92	51.79	46.64	52.22	48.25	51.50	51.75	44.96
TiO ₂	0.71	0.71	0.71	1.87	1.65	1.53	2.05	1.37	0.94	1.29	1.08	1.10	0.89	1.25	0.98	1.39	0.90	1.13	1.76
Al ₂ O ₃	18.37	17.60	15.94	14.80	16.38	16.05	14.14	15.70	16.10	16.02	17.32	16.93	20.33	18.04	17.15	19.68	17.07	17.27	17.31
FeO	7.11	1.89	2.40	5.32	2.57	8.82	3.16	7.32	2.38	4.74	5.75	3.73	5.40	6.77	4.47	6.31	5.77	4.04	9.86
Fe ₂ O ₃	3.02	6.04	3.39	4.23	6.73	4.53	8.31	6.43	8.29	6.19	5.07	7.35	5.40	6.11	6.02	5.20	5.12	6.74	5.53
MnO	0.14	0.17	0.09	0.23	0.14	0.32	0.34	0.21	0.17	0.20	0.19	0.18	0.18	0.23	0.16	0.19	0.17	0.18	0.23
MgO	14.43	17.85	7.22	7.72	6.79	10.06	4.24	6.75	11.13	4.75	6.91	7.58	5.53	5.88	4.10	4.20	5.96	5.33	6.78
CaO	4.86	0.39	7.18	8.22	4.86	5.93	6.62	9.43	6.30	6.82	7.10	7.16	5.14	10.30	11.52	9.98	8.24	8.16	9.76
Na ₂ O	3.53	4.88	3.19	4.65	6.34	3.53	5.78	2.22	4.09	3.84	2.75	3.72	3.35	3.48	3.02	3.06	3.62	4.27	2.71
K ₂ O	0.11	0.07	1.77	0.35	0.36	0.02	1.05	1.04	0.78	0.34	1.49	0.15	1.73	0.85	0.10	1.01	1.17	0.52	0.11
P ₂ O ₅	0.23	0.14	0.15	0.35	0.26	0.46	1.07	0.82	0.28	0.49	0.59	0.19	0.27	0.45	0.26	0.72	0.48	0.62	0.98
Total	100.00	100.00	100.00	100.00	100.00	100.00	100.00	100.00	100.00	100.00	100.00	100.00	100.00	100.00	100.00	100.00	100.00	100.00	100.00
Sc	38	36	21	31	30	42	38	26	50	32	29	41	23	33	30	22	30	36	37
V	194	190	130	188	188	469	118	272	273	233	215	379	222	463	258	309	256	282	391
Cr	233	276	239	224	105	41	30	155	223	48	126	48	15	34	53	21	83	15	34
Co	37	45	43	45	38	43	20	38	48	26	28	40	34	38	34	25	34	30	42
Ni	68	127	146	85	30	22	12	39	54	84	46	27	17	22	15	17	35	10	28
Ga	12	14	20	14	15	17	18	21	16	18	24	16	23	18	17	19	20	20	17
Rb	1	1	19	4	5	1	15	13	10	4	15	2	17	10	1	10	15	6	2
Y	7	10	17	41	33	41	77	29	21	35	31	23	20	22	23	28	24	30	45
Zr	21	11	38	47	46	42	84	54	21	38	57	16	22	23	45	65	39	28	108
Nb	1	1	3	8	7	6	6	5	2	5	5	2	3	2	4	5	4	3	9
Hf	1.2	0.4	1.1	1.5	2.8	2.8	2.5	2.4	2.6	2.2	2.6	0.6	0.7	0.9	1.5	2.7	1.6	2.4	2.9
Th	1.2	0.3	1.7	1.5	2.5	2.7	1.8	2.4	2.7	2.2	2.7	0.7	0.9	1	1.6	2.9	2.5	2.3	3.5
U	1.1	0.1	0.9	0.8	2.5	2.7	0.9	1.8	2.8	1.9	2.1	0.5	0.5	0.7	1.1	2.3	1.6	2.2	1.4
La	3.7	2.2	10.1	15.2	9.4	12.4	12.8	14.3	7.4	13.7	14.3	6.9	8	7.5	9.6	14.8	12.6	10.6	26.6
Ce	7.2	5.1	21.4	35	24.8	30.1	34.4	32.8	17.2	30.8	32.2	15	17.4	17.3	20.3	33.1	26.4	24.7	57.1
Pr	1.4	0.8	2.9	4.9	3.9	4.7	5.4	4.9	2.9	4.7	4.7	2.2	2.5	2.6	2.8	4.8	3.5	3.9	7.6
Nd	6.2	4.2	12.2	22.8	18.4	22.3	27.1	21.4	14.1	20.9	20.9	10	11.1	12.4	12.5	20.9	15.4	17.9	31.7

Annex 2.3. Continued.....

Mafic/intermediate metavolcanic rocks																			
Sample	NW3	NW35	NW41b	NW79	NW80	NW82	HM24c	MK4	MK13	MK16	MK19	MK26	MK27	MK31b	MK33b	MK48b	MK49	MK58b	MK62
Sm	1.8	1.1	2.8	5.6	5	5.9	8.1	4.8	4.1	5.1	5	2.7	3.1	3.2	3	4.8	3.7	4.7	6.9
Eu	0.7	0.4	1	1.7	1.9	2.3	2.7	1.7	1.8	1.8	1.8	1.1	1.2	1.3	1	1.6	1.3	1.8	2.1
Gd	1.9	1.4	3.1	6.8	5.9	7.1	10.9	5.1	4.7	6	5.4	3.4	3.5	3.6	3.6	5.1	4.2	5.3	8.2
Tb	0.3	0.2	0.4	1	1	1.2	1.7	0.8	0.9	1	0.9	0.5	0.5	0.5	0.5	0.8	0.6	0.9	1.1
Dy	1.5	1.2	2.1	5.4	5.3	6.2	9.6	4.3	4.1	5.1	4.5	2.8	2.6	2.9	2.8	4.2	3.2	4.7	5.7
Ho	0.3	0.3	0.4	1.1	1.1	1.3	2	0.9	0.9	1.1	1	0.6	0.5	0.6	0.6	0.9	0.7	1	1.2
Er	0.9	0.8	1.2	2.8	3	3.8	5.6	2.7	2.6	3	2.8	1.7	1.5	1.7	1.8	2.6	2	2.9	3.4
Tm	0.2	0.1	0.1	0.3	0.6	0.7	0.6	0.5	0.6	0.5	0.5	0.2	0.2	0.2	0.2	0.5	0.6	0.6	0.4
Yb	1	0.7	0.9	2.1	2.7	3.3	4.5	2.5	2.5	2.7	2.7	1.5	1.4	1.5	1.6	2.5	1.8	2.7	3
Lu	0.3	0.1	0.2	0.3	0.6	0.8	0.7	0.6	0.7	0.6	0.6	0.2	0.2	0.3	0.3	0.6	0.4	0.7	0.5
REE total	27.4	18.5	58.7	105	83.7	102.1	126.2	97.4	64.4	96.8	97.3	48.7	53.6	55.5	60.7	97.2	76.4	82.3	155.5
La/Lu (N)	1.3	2.4	6.8	5.1	1.5	1.7	1.9	2.6	1.1	2.5	2.4	2.9	3.6	3	3.1	2.6	3.7	1.6	5.5

Annex 2.4. Major (wt. %) and trace element (ppm) values of the Mai Kenetal-Hawzen area felsic metavolcanic/volcanoclastic rocks (Alene et al. 2000) used in this work for comparison.

Felsic metavolcanic/volcanoclastic rocks										
Sample	MKNB8	WG6a	NW25	NW33c	NW34	NW81	HM41c	MK15b	MK38	NW28
SiO ₂	51.76	56.37	71.85	62.43	65.64	55.22	73.98	68.82	64.11	49.36
TiO ₂	1.18	1.19	0.67	0.73	0.46	0.86	0.35	0.61	0.73	4.40
Al ₂ O ₃	18.07	15.33	12.30	16.70	16.47	15.74	12.79	14.58	14.55	12.72
FeO	3.92	4.41	2.82	2.80	2.82	2.31	0.29	0.76	5.54	6.26
Fe ₂ O ₃	6.16	5.60	2.36	3.59	2.02	5.57	2.55	3.87	1.39	4.29
MnO	0.18	0.23	0.11	0.12	0.10	0.16	0.05	0.05	0.23	0.12
MgO	2.53	4.85	4.46	4.75	4.06	7.59	0.35	0.80	4.44	9.06
CaO	10.75	6.37	0.41	1.16	0.37	2.34	1.66	1.90	3.66	9.19
Na ₂ O	4.20	3.21	4.28	6.78	7.88	6.68	5.73	3.63	4.64	2.63
K ₂ O	0.65	1.74	0.56	0.73	0.03	1.97	2.17	4.77	0.18	1.00
P ₂ O ₅	0.60	0.70	0.17	0.21	0.14	1.55	0.07	0.22	0.52	0.97
Total	100.00	100.00	100.00	100.00	100.00	100.00	100.00	100.00	100.00	100.00
Sc	26	30	14	20	13	24	7	14	17	24
V	259	246	101	131	90	275	15	53	121	230
Cr	30	45	161	53	19	54	9	74	18	233
Co	32	29	12	28	22	30	15	11	21	46
Ni	25	63	36	19	14	32	6	10	11	91
Ga	20	29	11	14	10	14	15	36	16	18
Rb	8	17	5	5	0	1	26	50	3	9
Y	33	31	21	24	15	27	54	40	30	17
Zr	53	51	57	43	46	48	180	137	76	34
Nb	7	7	4	3	3	3	6	9	6	15
Hf	1.5	1.4	2.1	1.5	1.7	1.4	5.3	5.5	2.1	1.5
Th	2.4	2.7	2.5	2.1	2.6	1.3	4.4	6.7	2.6	1.3
U	1.1	1	1.6	1	1.2	0.6	2.1	4.5	1.2	1
La	19.2	23.1	16.8	10	4.6	11	14	22.8	21.8	14.1
Ce	41.6	47.9	34.3	20.3	11	24.2	34.5	49.3	46	33.3
Pr	5.6	6.6	5.4	2.8	1.4	3.4	4.9	6.7	6.1	5
Nd	23.9	28.2	21.6	12.1	5.7	15.4	21.1	27.2	25.9	22.8
Sm	5.2	6.3	4.2	2.9	1.5	3.5	5.2	6.7	5.4	5
Eu	1.6	2	1.3	1	0.5	1.1	0.8	2.1	1.6	2.1
Gd	6.4	7	2.3	3.3	1.8	4.3	6.1	6.8	6.1	5
Tb	0.8	0.8	0.6	0.5	0.3	0.6	0.9	1.2	0.7	0.6
Dy	4.1	4	3.3	2.8	1.8	3.3	5.2	6	3.6	2.9
Ho	0.8	0.8	0.7	0.6	0.4	0.7	1.3	1.3	0.7	0.5
Er	2.4	2.3	2.1	1.9	1.4	2.1	4.3	4	2.2	1.4
Tm	0.3	0.2	0.4	0.2	0.2	0.2	0.5	0.9	0.2	0.2
Yb	2	1.9	2.3	1.8	1.5	1.8	4.5	4.2	1.9	1.1
Lu	0.3	0.3	0.5	0.3	0.3	0.3	0.8	1	0.3	0.2
REE total	114.1	131.4	95.7	60.6	32.2	71.8	104	140.3	122.5	94.3
La/Lu (N)	6.2	7.8	3.6	3.1	1.6	4	1.8	2.3	7.2	5.8

Annex 2.5. Major (wt. %) and trace element (ppm) concentrations of Weri metavolcanic rocks (Sifeta 2003) used in this work for comparison.

Pyroclastic metavolcanic rocks																		Porphyritic metavolcanic rocks									
Sample	WV 141	WV 142	WV 143	WV 144	WV 145	WV 146	WV 147	WV 148	WV 150	WV 151	WV 152	WV 168	WV 169	WV 170	WV 181	WV 182	WV 183	WV 184	WV 153	WV 154	WV 163	WV 164	WV 165	WV 175	WV 176	WV 177	
SiO ₂	52.16	46.99	53.77	51.93	46.30	50.72	50.50	69.42	61.19	52.48	54.37	51.01	50.42	55.37	49.42	50.92	54.11	48.97	63.17	50.89	65.44	52.45	51.10	51.15	49.59	52.09	
TiO ₂	1.01	1.06	0.95	1.14	0.91	0.84	0.97	0.25	0.28	0.89	0.84	0.96	0.99	0.88	0.89	0.97	0.90	0.91	0.66	0.88	0.63	1.25	1.33	1.58	1.59	1.48	
Al ₂ O ₃	16.85	16.78	17.34	18.31	18.10	19.35	17.57	14.03	17.33	18	16.63	17.12	17.79	18.73	15.72	17.60	17.57	17.69	16	18.38	15.16	15.32	15.43	14.92	15.92	16.73	
Fe ₂ O ₃	10.37	11.38	9.36	8.57	9.36	9.26	9.95	1.51	2.92	8.79	8.09	10.33	9.93	8.15	9.73	10.07	7.48	9.37	5.96	9.87	5.71	8.50	9.22	11.62	12.52	11.42	
MnO	0.16	0.16	0.12	0.16	0.17	0.17	0.14	0.01	0.02	0.11	0.11	0.14	0.14	0.17	0.15	0.11	0.16	0.18	0.09	0.24	0.09	0.13	0.14	0.17	0.14	0.12	
MgO	4.97	5.69	4.19	4.58	4.48	4.07	5	0.18	0.24	4.24	3.77	4.61	5	3.54	3.38	4.11	3.07	3.2	1.32	4.46	1.52	1.27	1.48	4.09	1.90	2.73	
CaO	6.76	6.78	5.60	6.09	11.91	5.37	7.20	0.08	0.19	5.45	5.98	7.06	4.80	2.31	8.52	5.23	7.35	11.67	5.14	6.35	3.65	9.68	10.11	8.76	10.06	4.15	
Na ₂ O	4.36	5.69	5.03	5.02	1.38	0.10	3.84	0.20	0.27	2.97	4.08	3.93	5.82	7.56	4.86	5.35	5.16	2.13	2.33	5.04	2.68	4.25	4.19	2.64	2.13	6.19	
K ₂ O	0.17	0.22	0.64	0.64	1.42	5.07	1.66	12.81	16.64	2.09	1.18	0	0.03	0.01	0.70	1.09	0.38	0.89	2.83	0.69	2.73	0.36	0.26	1.86	1.30	0.25	
P ₂ O ₅	0.44	0.39	0.43	0.54	0.31	0.27	0.25	0.03	0.03	0.31	0.41	0.26	0.28	0.26	0.31	0.31	0.36	0.40	0.21	0.30	0.20	0.59	0.62	0.77	0.68	0.80	
LOI	2.66	4.93	2.51	2.71	5.13	4.78	2.78	0.49	0.59	4.61	4.47	4.70	4.92	3.30	6	4.31	3.14	3.82	1.94	2.75	1.92	4.86	4.98	2.07	3.37	3.26	
Total	99.90	100	99.90	99.70	99.50	100	99.90	98.50	99.10	99.90	100	100	100	100	99.70	100	99.70	99.30	99.70	99.90	99.70	98.70	98.90	99.70	99.20	99.20	
Ba	129	133	455	357	1117	2437	959	2330	2413	769	468	61.8	98	126	306	445	194	440	1021	424	1004	256	219	1384	599	95.8	
Ce	42	27	46	38	9	n.d.	16	22	80	34	34	28	28	27	34	32	34	32	24	41	23	56	52	47	57	77	
Cr	48	39	11	16	54	28	38	n.d.	n.d.	3	13	37	39	33	8	6	1	154	14	23	15	13	15	29	20	15	
Ga	21	18	20	19	21	22	19	11	16	20	17	18	16	16	17	19	16	20	18	20	17	15	16	18	19	20	
Nb	9	2	14	9	6	6	5	12	15	8	6	6	8	6	8	8	9	6	8	7	8	11	10	12	11	13	
Ni	23	22	12	15	23	21	22	2	3	9	6	8	10	12	10	10	7	10	7	21	7	15	16	18	20	19	
Pb	8	3	7	6	11	10	6	10	22	7	5	8	2	2	9	8	8	16	10	13	9	11	11	11	12	9	
Rb	5	5	13	16	16	115	31	165	196	41	25	3	4	4	15	22	8	17	70	14	72	10	8	26	27	10	
Sc	28.3	33.3	20.3	27	24.2	26.6	30.2	4.7	6.6	21.9	22.4	30.4	31.9	27.1	24.3	23.5	23.8	20.5	17.3	21.6	15.7	25.1	24.5	29.7	28.5	24.3	
Sr	836	496	713	627	315	154	2360	241	167	435	405	136	177	274	964	711	699	1787	701	255	808	591	615	1293	793	325	
Th	0.7	1.2	1.8	3	1.6	0.4	0.4	6.9	7.8	1	0.6	1	1.2	0.4	3.3	2.7	2.6	1	1.7	2	1.1	3.5	4.3	3	2.3	4.3	
V	244	299	220	219	182	233	233	6	12	208	184	190	238	190	188	215	173	221	77	205	91	257	262	294	345	220	
Y	15	16	15	19	17	14	14	31	40	17	16	19	20	18	18	16	17	15	19	23	19	28	30	34	33	37	
Zr	59	36	79	65	59	23	23	274	310	72	64	71	74	72	63	70	84	35	106	96	102	136	140	147	141	183	

Abbreviations: n.d. = not determined.

Annex 2.6. Major (wt. %) and trace element (ppm) concentrations of Weri metasedimentary rocks of Sifeta (2003) used in this work for comparison.

Sample	MS 121	MS 122	MS 123	MS 124	MS 125	MS 126	MSB 126	MS 127	MS 128	MS 129	MS 130	MS 131	MS 132	MS 133	MS 171	MS 172	MS 173	MS 174	MS 178	WS 134	WS 135	WS 136	WS 137	WS 138	WS 139	TS 155	TS 156	TS 158	TS 159	TS 160	TS 162
SiO ₂	80.07	83.97	81.42	79.99	72.58	77.48	77.59	63.64	70.96	68.37	63.11	37.73	68.67	59.09	62.29	60.13	54.12	65.25	63.12	81.25	63.04	73.07	61.02	72.18	70.93	55.60	52.30	62.30	59.20	61.10	88.90
TiO ₂	0.31	0.29	0.30	0.54	0.31	0.44	0.48	1.08	0.43	0.78	0.96	0.27	0.83	1.09	0.95	1.17	0.63	0.57	0.90	0.44	0.92	0.51	0.85	0.59	0.72	1.40	0.70	0.80	0.90	0.40	0.30
Al ₂ O ₃	11.58	8.96	7.17	12.04	11.02	10.07	9.72	17.62	8.82	15.83	18.35	14.92	15.99	21.19	18.45	19.57	16.52	12.62	16.59	11.51	15.03	12.95	17.56	13.80	13.67	20.30	16.80	16.20	15.20	14.40	5.10
Fe ₂ O ₃	1.74	0.93	5.96	1.62	9.02	6.25	6.26	8.83	5.68	6.28	7.93	12.14	5.82	9.43	8.71	9.58	15.85	11.39	8.28	0.67	7.04	4.46	8.52	4.54	4.71	11.10	17.10	8.30	13.80	3.70	0.20
MnO	0.02	0.01	0.04	0.01	0.07	0.03	0.03	0.11	0.03	0.10	0.09	0.40	0.10	0.09	0.10	0.09	0.07	0.07	0.04	0.01	0.10	0.08	0.12	0.08	0.08	0.10	0.10	0.20	0.10	0.02	0.01
MgO	0.78	0.43	1.81	0.25	2.78	1.58	1.96	1.80	1.80	1.78	1.52	4.77	1.75	2.13	2.08	1.87	5.83	4.43	2.78	0.45	5.04	1.72	3.63	1.58	1.86	2.20	5.40	4.10	4.10	4.80	0.20
CaO	0.19	0.15	0.14	0.09	0.16	0.20	0.24	0.61	0.21	0.99	1.16	13.10	0.91	0.55	0.60	0.40	0.61	0.77	0.30	0.13	1.27	0.49	0.63	0.34	0.72	0.70	0.30	0.50	0.40	3.40	0.10
Na ₂ O	0.47	1.10	1.55	0.91	0.13	0.27	0.09	1.54	0.15	1.29	1.56	0.80	1.28	1.38	0.94	0.91	0.33	0.22	n.d.	0.30	0.15	4.37	1.04	5.06	4.56	0.90	0.60	2	0.80	0.50	0.60
K ₂ O	1.97	1.02	0.03	1.67	1.03	0.82	0.71	1.44	0.64	1.34	1.81	0.46	1.34	1.76	1.89	2.3	0.66	0.57	3.42	2.43	2.23	0.51	2.82	0.30	0.62	2.40	1	2.10	1	4.2	0.80
P ₂ O ₅	0.02	0.01	0.06	0.01	0.05	0.01	0.02	0.26	0.02	0.43	0.37	0.05	0.28	0.19	0.09	0.19	0.18	0.36	0.16	0.01	0.26	0.13	0.19	0.16	0.19	0.30	0.10	0.20	0.20	0.10	0.01
LOI	2.32	1.78	1.67	2.59	3.25	3.01	3	3.26	11.34	2.94	3.20	14.26	3.05	4.12	3.93	3.86	5.09	3.97	4.50	2.10	4.85	1.94	3.82	1.72	2.03	5.10	5.10	3.70	4.40	6.60	2.60
Total	99.50	98.70	100	99.70	100	100	100	100	100	100	100	98.9	100	101	100	100	99.90	100	100	99.30	99.90	100	100	100	100	100	99.40	100	100	99.20	98.90
CIA	78.4	74	72.7	77.9	88.1	85.7	88.2	79.4	87.3	78.5	76.2	36.9	77.9	81.9	80.5	82.2	89.4	89.4	81.3	77.6	77.6	60.9	76.4	60.8	60.2	81.8	87.9	72.9	84.9	56	71.8
PIA	89.6	79.2	72.1	86.2	95.5	91.9	94	82.3	92.9	79.9	78.8	36.5	80.3	86.1	86.5	89.1	88.9	88.9	97	92.5	92.5	60.8	84.2	60.4	60	87.6	91.7	77.6	87.9	58.6	78.6
Ba	844	466	54	791	535	299	272	848	248	804	1019	247	786	855	939	1065	283	283	658	740	686	259	670	111	211	791	248	604	310	1613	342
Ce	22	12	15	n.d.	n.d.	n.d.	12	12	3	14	65	26	9	60	14	37	17	17	67	18	19	38	50	41	43	25	22	42	17	10	21
Cr	14	50	12	24	9	30	28	43	22	23	34	11	22	25	26	48	31	31	79	107	200	72	91	104	163	115	69	98	72	50	19
Ga	16	11	8	14	11	13	13	20	12	20	23	19	19	25	22	23	16	16	21	17	18	9	22	11	11	23	19	20	19	18	7
Nb	8	6	6	9	5	8	7	8	8	8	10	6	10	10	9	9	9	9	17	14	13	7	11	8	10	9	8	11	10	8	10
Ni	6	9	5	2	3	14	10	12	9	10	12	13	9	14	13	20	14	14	58	4	80	21	54	27	29	49	43	59	39	54	1
Pb	4	5	2	9	5	2	1	10	0	8	12	4	8	9	9	6	2	2	3	3	3	3	7	8	6	2	3	8	4	7	27
Rb	52	33	5	43	25	28	25	38	23	39	49	12	38	45	50	59	17	17	95	90	60	17	71	12	19	54	27	53	28	109	34
Sc	11.2	9.8	8.8	19.9	13.8	14.1	8.9	21.5	11.3	18.4	23.8	9.7	21.6	26.3	23	27.8	12.7	12.7	20	7.5	16.8	9.7	24.4	13.6	11	32.9	17	19.7	17.3	9.3	6.1
Sr	123	116	57	89	48	71	62	410	57	349	440	229	349	485	347	304	66	66	26	109	69	196	129	185	154	303	62	97	109	73	59
Th	1.2	2.5	1	1.5	0.4	2.5	1.7	2.9	2.2	1.2	3	2.6	3.7	3.9	4.5	3.1	2.9	2.9	5.1	4.1	5.5	1.3	4.1	2.2	1.8	1.2	3.9	3.1	2.5	4.1	0.1
V	43	190	39	68	28	65	67	206	61	134	143	100	131	141	159	150	69	69	96	195	150	71	158	84	103	215	125	147	134	319	67
Y	16	15	8	8	3	9	12	17	11	15	37	12	21	26	18	20	20	20	31	7	22	14	21	18	18	25	17	27	22	15	23
Zr	129	112	56	107	68.1	76.9	84.9	138	76.4	102	139	94.7	135	149	131	135	94.2	94.2	200	126	191	103	157	126	160	109	106	166	129	123	110
Th/Sc	0.1	0.25	0.11	0.07	0.31	0.18	0.2	0.14	0.2	0.06	0.13	0.27	0.17	0.15	0.2	0.11	0.23	0.23	0.25	0.55	0.33	0.13	0.17	0.16	0.16	0.04	0.23	0.16	0.14	0.44	0.02

Abbreviations: n.d = not determined

Annex 2.7. REE (ppm) values of Weri metavolcanic and metasedimentary rocks (Sifeta 2003) used in this work for comparison.

Metavolcanic rocks															Metasedimentary rocks																
Sample	WV 141	WV 142	WV 143	WV 144	WV 151	WV 152	WV 168	WV 169	WV 182	WV 183	WV 154	WV 165	WV 176	WV 177	MS 121	MS 122	MS 124	MS 126	MS 127	MS 132	MS 133	MS 171	MS 174	WS 134	WS 136	WS 138	WS 139	TS 156	TS 158	TS 159	TS 162
La	17.90	9.44	20.40	18.60	16.6	15.80	9.20	9.60	15.20	15.80	15.80	21	26.90	26.30	8.52	13.94	0.98	2.42	4.96	2.99	35.3	8.53	8.23	7.37	11.84	13.18	7.40	6.93	17.39	5.78	2.72
Ce	35.40	22.70	45.50	43	36.9	34.50	22.70	23.80	34.40	32.50	37.90	58.20	55.30	56.70	9.39	23.35	2	3.68	10.84	10.02	79.53	21.70	17.93	9.83	23.62	28.58	35.34	18.69	39.25	14.16	3.71
Pr	4.79	3.30	5.25	5.54	5.03	4.45	2.99	3.13	4.43	4.63	4.50	6.89	7.04	8.01	2.35	4	0.38	0.45	1.98	2.10	7.68	3.07	2.73	1.44	2.96	3.75	2.45	2.41	5.10	2.20	0.84
Nd	20.30	15.80	21.50	24.10	22	17.3	13.90	14	19.60	18.80	19.40	31.80	31.80	34.50	10.32	17.98	2.12	1.97	9.40	10.39	34.73	12.90	12	6.39	12.04	15.19	10.46	10.94	21.58	10.96	4.37
Sm	4.26	3.57	4.15	5.06	4.58	4.20	3.43	3.50	3.98	3.95	4.30	7.31	7.31	7.64	2.22	3.14	0.84	0.66	2.49	2.87	6.30	3.17	2.98	1.71	2.58	3.48	2.67	2.92	4.86	3.15	1.41
Eu	1.56	1.37	1.54	1.66	1.84	1.58	1.21	1.16	1.47	1.30	1.54	2.43	2.43	2	0.79	0.83	0.55	0.33	0.85	1.11	1.97	1.27	0.83	0.51	0.92	0.96	0.84	0.76	1.47	0.92	0.46
Gd	4.22	3.49	4.56	5.02	4.64	4.11	3.41	3.46	3.97	4.06	4.46	7.27	7.27	7.58	2.23	3.36	0.62	0.82	2.28	2.73	6.34	3.20	3.16	1.44	2.72	3.51	2.70	2.89	4.88	3.17	1.57
Tb	0.73	0.65	0.69	0.83	0.77	0.73	0.68	0.66	0.66	0.69	0.82	1.28	1.28	1.32	0.38	0.48	0.14	0.19	0.47	0.63	0.95	0.56	0.55	0.21	0.44	0.58	0.54	0.55	0.86	0.64	0.34
Dy	3.71	3.69	3.75	4.44	4.20	3.85	3.97	3.86	3.62	3.79	4.67	7.14	7.14	7.48	2.06	2.75	0.89	1.31	2.95	4.05	5.33	3.40	3.18	1.09	2.66	3.43	3.32	3.46	5.22	4.01	2.22
Ho	0.58	0.61	0.56	0.73	0.65	0.60	0.70	0.71	0.59	0.60	0.79	1.27	1.27	1.29	0.36	0.51	0.24	0.31	0.64	0.81	0.90	0.68	0.64	0.21	0.48	0.63	0.66	0.64	0.99	0.81	0.51
Er	1.67	1.77	1.71	2.08	1.89	1.83	2	2.09	1.71	1.69	2.39	3.49	3.49	3.79	1.14	1.79	0.83	0.99	1.94	2.36	2.66	2.09	1.86	0.69	1.40	1.85	1.88	1.83	2.78	2.28	1.36
Tm	0.22	0.25	0.22	0.27	0.24	0.24	0.28	0.30	0.23	0.22	0.32	0.49	0.49	0.55	0.18	0.27	0.15	0.17	0.32	0.38	0.39	0.32	0.29	0.13	0.20	0.28	0.29	0.28	0.43	0.36	0.19
Yb	1.48	1.60	1.54	1.86	1.61	1.57	1.98	2	1.61	1.50	2.33	3.20	3.20	3.61	1.35	2.06	1.30	1.25	2.19	2.58	2.68	2.27	1.96	1.03	1.36	1.88	2.04	1.89	2.85	2.46	1.22
Lu	0.22	0.25	0.24	0.27	0.25	0.22	0.29	0.30	0.24	0.23	0.33	0.49	0.49	0.54	0.23	0.34	0.23	0.2	0.34	0.39	0.41	0.35	0.32	0.20	0.21	0.29	0.31	0.28	0.45	0.38	0.20
ΣREE	97	68.50	111.60	113.50	101.10	90.90	66.80	68.5	91.70	89.70	99.50	155.50	155.50	161.30	41.35	74.80	11.28	14.74	41.63	43.42	185	63.10	56.70	32.20	63.40	77.60	70.90	54.50	108	51.30	21.10
LREE/HREE	6.44	4.45	7.29	6.21	5.97	5.79	3.93	4.03	6.15	5.92	5.08	5.21	5.21	5.09	4.14	5.40	1.43	1.75	2.67	2.04	8.32	3.80	3.67	5.36	5.60	5.16	4.97	3.54	4.78	2.57	1.72
Eu/Eu*	1.12	1.19	1.08	1.01	1.22	1.16	1.08	1.02	1.13	0.99	1.07	1.02	1.02	0.80	1.09	0.78	2.33	1.37	1.09	1.21	0.95	1.22	0.82	1	1.06	0.84	0.95	0.81	0.92	0.89	0.94
(La/Yb)N	8.16	3.99	8.95	6.75	6.95	6.80	3.15	3.23	6.38	7.12	4.58	5.69	5.69	4.92	4.27	4.58	0.51	1.31	1.53	0.78	8.90	2.54	2.84	4.84	5.88	4.75	2.45	2.47	4.12	1.59	1.50
(Gd/Yb)N	2.31	1.77	2.40	2.19	2.34	2.12	1.40	1.40	2	2.19	1.55	1.84	1.84	1.70	1.34	1.32	0.39	0.53	0.84	0.86	1.92	1.14	1.31	1.13	1.62	1.52	1.07	1.24	1.39	1.04	1.04

Annex 3. Electronprobe microanalysis data

The microanalysis was done on a Cameca SX100 electronprobe with an acceleration voltage of 15 kV, and a beam current of 20 nA. Calibrations were performed on standards from sulfide minerals and native metals. ZAF correction was made based on the Cameca PAP procedure (Pouchou and Pichoir 1991). Energy Dispersive Spectrometer (EDS) scanning was also accomplished to generate more qualitative data of the ore and gangue minerals (Annex 3.2). The EDS spectrometer was run using an acceleration voltage of 20 V and current of 3.6 A. All values are presented in weight percent.

Annex 3.1. Electronprobe analysis result of sulfides from the Workamba area

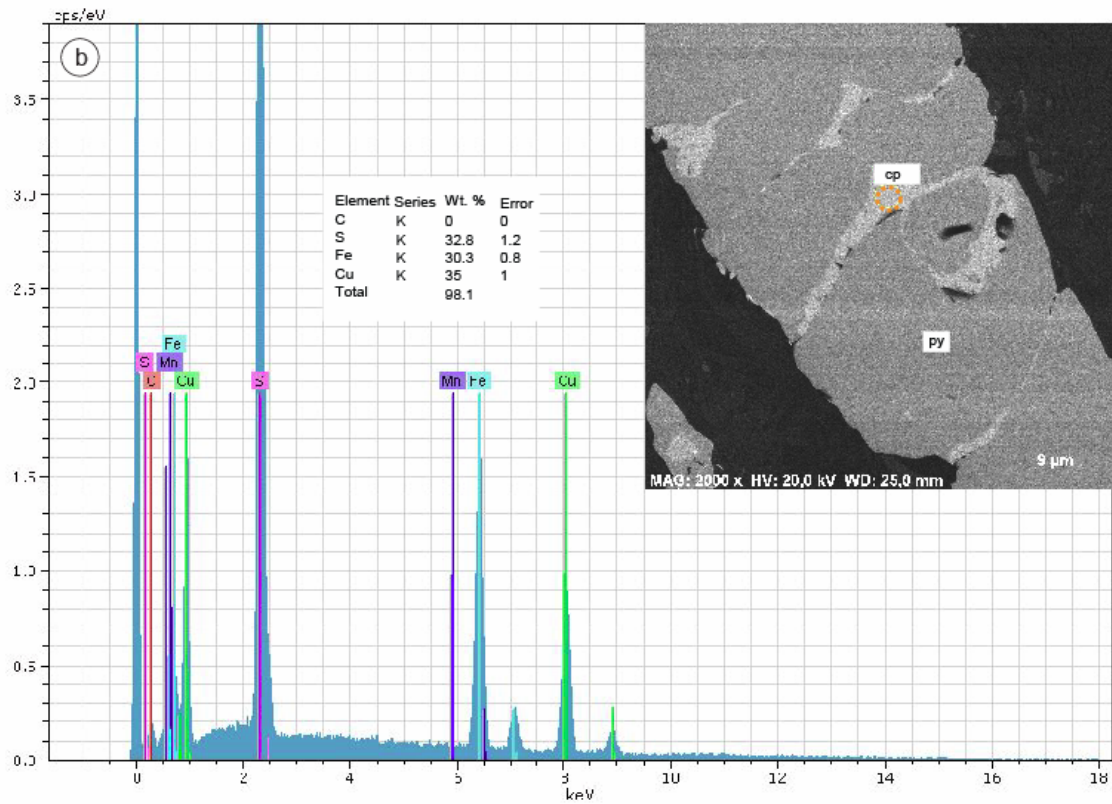
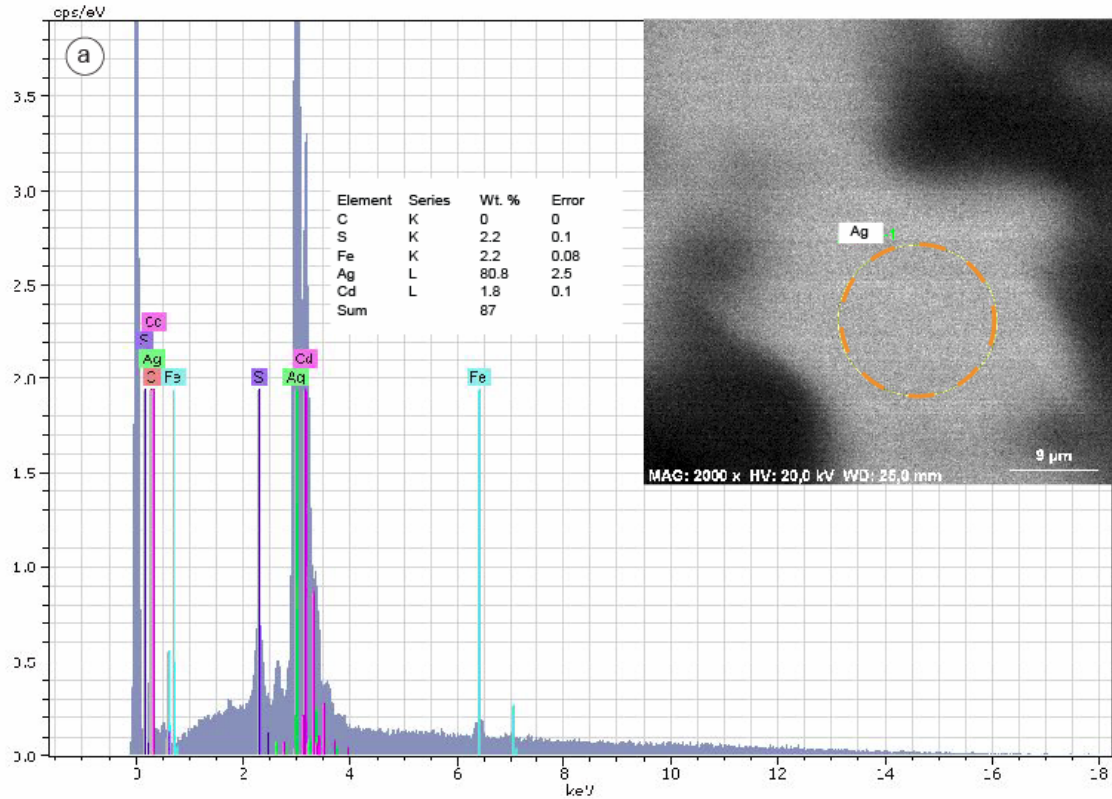
Pyrite									Sphalerite							Galena									
Dataset /Point	S	Fe	Co	Cu	Zn	As	Ni	Total	Dataset /Point	S	Fe	Cu	Zn	As	Pb	Total	Dataset /Point	S	Mn	Fe	Cu	Zn	Ag	Pb	Cd
2 / 1	54.95	42.09	0.00	0.00	0.00	0.07	0.00	97.11	14 / 1	32.78	1.20	0.00	64.34	0.02	0.00	98.34	1 / 1	13.31	0.01	0.03	0.00	0.00	0.01	85.24	0.04
2 / 2	55.13	42.64	0.00	0.00	0.00	0.06	0.00	97.83	14 / 2	33.25	1.14	0.07	64.05	0.03	0.00	98.54	2 / 1	13.37	0.00	0.00	0.00	0.05	0.14	84.76	0.06
2 / 3	54.95	42.57	0.00	0.00	0.00	0.07	0.05	97.64	14 / 3	33.47	1.10	0.02	64.05	0.00	0.00	98.65	3 / 1	13.25	0.01	0.02	0.02	0.01	0.07	86.64	0.05
2 / 4	54.95	42.52	0.00	0.00	0.00	0.08	0.02	97.57	14 / 4	32.92	1.06	0.00	63.26	0.00	0.00	97.24	4 / 1	13.12	0.02	0.00	0.00	0.07	0.00	86.61	0.09
3 / 1	54.58	42.21	0.00	0.00	0.00	0.20	0.00	97.01	14 / 5	32.23	1.16	0.02	63.20	0.03	0.00	96.64	6 / 1	13.36	0.00	0.09	0.02	0.02	0.03	86.03	0.09
3 / 2	54.48	42.42	0.00	0.00	0.00	0.19	0.00	97.09	14 / 6	32.32	1.14	0.08	62.40	0.05	0.00	96.01	7 / 1	13.47	0.00	0.00	0.03	0.00	0.01	85.96	0.07
4 / 1	55.03	42.67	0.00	0.00	0.00	0.05	0.01	97.78	14 / 7	32.49	1.13	0.05	63.04	0.03	0.00	96.74	8 / 1	13.37	0.00	0.03	0.01	0.00	0.00	86.38	0.00
4 / 2	54.38	42.76	0.00	0.00	0.01	0.12	0.03	97.30	14 / 8	33	1.11	0.04	62.60	0.00	0.00	96.48	9 / 1	13.62	0.04	0.00	0.08	0.00	0.17	84.74	0.03
4 / 3	54.90	42.95	0.00	0.01	0.00	0.06	0.03	97.95	14 / 9	32.64	1.11	0.04	63.04	0.01	0.00	96.85	10 / 1	13.27	0.02	0.01	0.00	0.02	0.00	86.43	0.00
4 / 4	54.55	43.12	0.00	0.06	0.20	0.09	0.09	98.10	14 / 10	32.88	1.07	0.02	62.84	0.02	0.00	96.83	11 / 1	13.64	0.00	0.00	0.04	0.05	0.08	85.43	0.06
4 / 5	54.88	42.69	0.00	0.01	0.03	0.12	0.04	97.76	14 / 11	32.7	1.09	0.02	63.09	0.00	0.00	96.9	2 / 1	13.37	0.00	0.00	0.04	0.05	0.14	84.76	0.06
6 / 1	54.15	43.17	0.00	0.00	0.06	0.31	0.01	97.69	15 / 1	27.96	1.04	0.03	61.97	0.01	0.00	91.01	3 / 1	13.25	0.01	0.02	0.02	0.01	0.07	86.64	0.05
6 / 2	54.55	43.01	0.00	0.00	0.02	0.19	0.01	97.79	15 / 2	27.63	1.07	0.05	62.07	0.00	0.00	90.82	4 / 1	13.12	0.02	0.00	0.00	0.07	0.00	86.61	0.09
6 / 3	54.23	43.31	0.00	0.02	0.03	0.28	0.08	97.95	15 / 3	27.84	1.09	0.00	62.33	0.00	0.00	91.23	6 / 1	13.36	0.00	0.09	0.02	0.02	0.03	86.03	0.09
6 / 4	53.65	43.01	0.00	0.00	0.00	0.25	0.00	96.91	15 / 4	27.7	1.06	0.00	62.72	0.00	0.00	91.48	7 / 1	13.47	0.00	0.00	0.03	0.00	0.01	85.96	0.07
6 / 5	54.24	43.16	0.00	0.00	0.10	0.26	0.01	97.77	15 / 5	27.49	1.01	0.00	61.60	0.00	0.00	90.10	8 / 1	13.37	0.00	0.03	0.01	0.00	0.00	86.38	0.00
6 / 6	54.49	42.84	0.00	0.00	0.05	0.22	0.00	97.6	15 / 6	27.35	1.07	0.10	62.52	0.00	0.00	91.05	9 / 1	13.62	0.04	0.00	0.08	0.00	0.17	84.74	0.03
6 / 7	53.88	42.80	0.00	0.00	0.06	0.19	0.00	96.93	15 / 7	26.91	1.04	0.06	62.40	0.00	0.00	90.44	10 / 1	13.27	0.02	0.01	0.00	0.02	0.0	86.43	0.00
6 / 8	53.55	42.95	0.00	0.04	0.00	0.28	0.00	96.82	15 / 8	26.7	1.04	0.03	61.90	0.00	0.00	89.68	11 / 1	13.64	0.00	0.00	0.04	0.05	0.08	85.43	0.06
6 / 9	54.04	42.86	0.00	0.04	0.00	0.25	0.00	97.19	15 / 9	27.57	1.07	0.08	61.95	0.00	0.00	90.67	13 / 1	13.76	0.00	0.06	0.03	0.83	0.08	83.49	0.06
7 / 1	54.36	43.26	0.00	0.03	0.07	0.04	0.00	97.76	16 / 1	32.99	2.06	0.00	63.09	0.00	0.00	98.15	46 / 1	13.81	0.00	0.08	0.35	2.02	0.00	85.47	0.03
7 / 2	54.28	43.48	0.00	0.00	0.00	0.03	0.02	97.81	16 / 2	32.88	2.07	0.02	62.65	0.00	0.00	97.62	47 / 1	14.07	0.00	0.12	0.28	3.45	0.01	85.42	0.01
7 / 3	54.42	43.12	0.00	0.00	0.01	0.01	0.01	97.57	16 / 3	32.86	2.03	0.09	62.52	0.02	0.00	97.53	49 / 1	13.74	0.00	0.18	0.05	0.03	0.00	85.29	0.03
7 / 4	54.26	42.89	0.00	0.10	0.00	0.00	0.02	97.27	16 / 4	32.78	2.02	0.00	62	0.00	0.00	96.80	67 / 1	12.86	0.00	1.77	2.09	0.00	0.14	79.68	0.05

Table 3.1. Continued.....

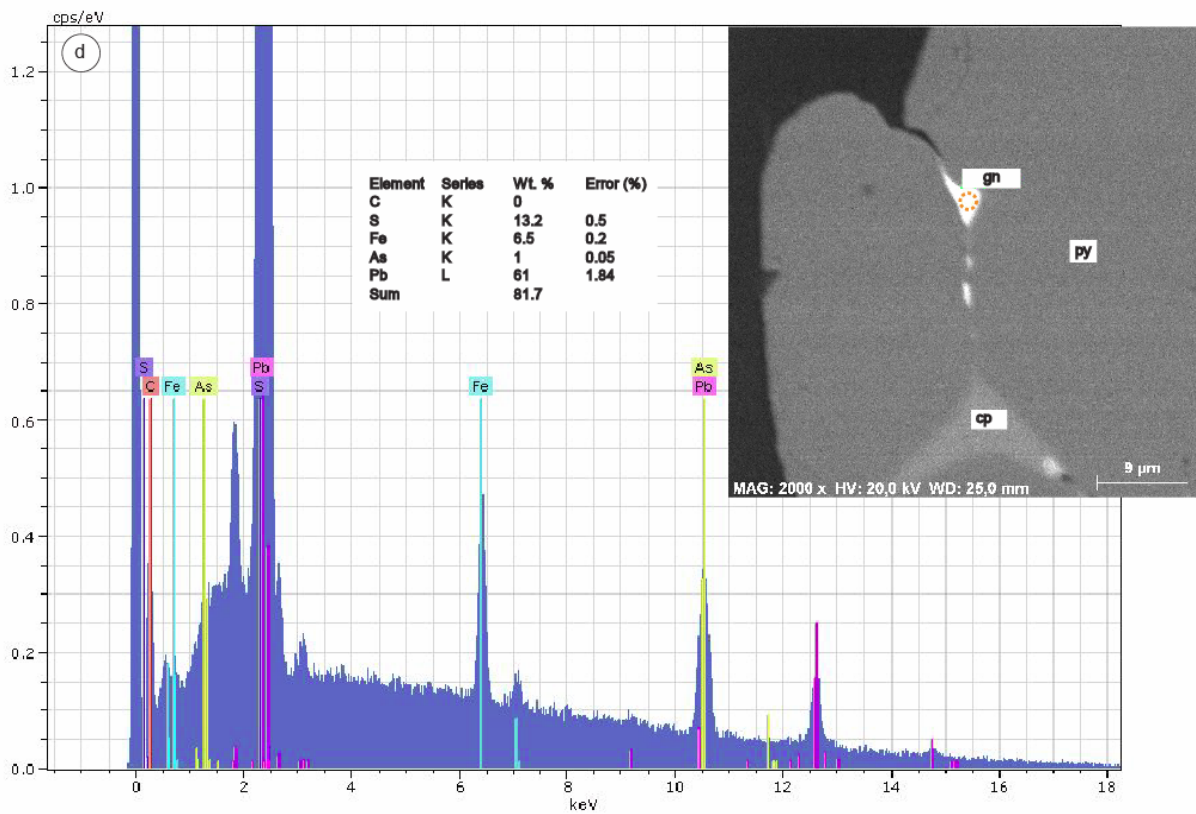
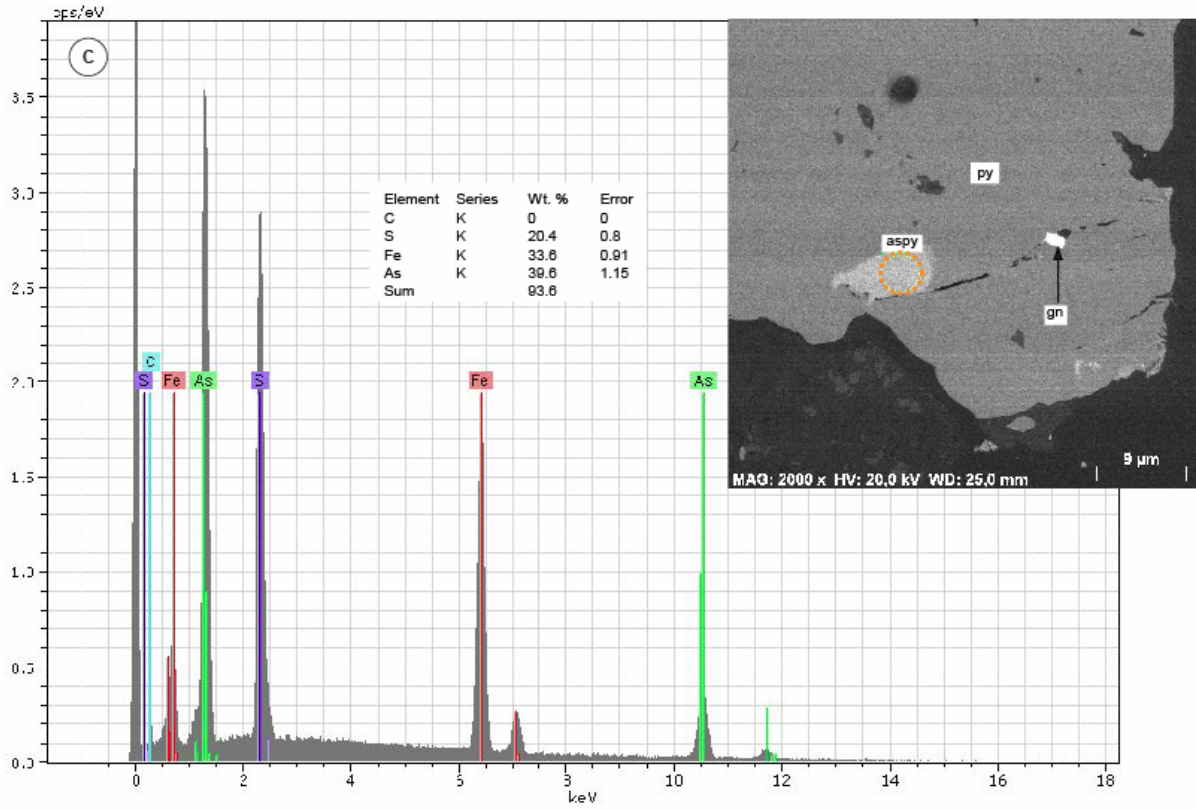
Pyrite									Sphalerite								Galena								
Dataset /Point	S	Fe	Co	Cu	Zn	As	Ni	Total	Dataset /Point	S	Fe	Cu	Zn	As	Pb	Total	Dataset /Point	S	Mn	Fe	Cu	Zn	Ag	Pb	Cd
7 / 5	54.05	43.41	0.00	0.01	0.00	0.03	0.00	97.51	16 / 5	33	2.17	0.06	62.28	0.01	0.00	97.52	68 / 1	13.81	0.00	2.33	0.00	0.01	0.00	84.53	0.00
9 / 1	54.51	43.31	0.00	0.00	0.03	0.10	0.00	97.94	18 / 1	32.42	2.65	0.28	59.47	0.07	0.00	94.91	69 / 1	13.96	0.00	2.07	0.00	0.00	0.04	82.32	0.05
9 / 2	54.20	43.03	0.00	0.00	0.00	0.11	0.00	97.34	18 / 2	33.10	2.82	0.21	60.97	0.05	0.00	97.15	77 / 1	13.74	0.01	1.86	0.00	0.02	0.14	84.29	0.00
9 / 3	54.50	43.49	0.00	0.00	0.00	0.12	0.00	98.10	18 / 3	32.87	2.64	0.18	60.36	0.06	0.00	96.11	79 / 1	13.96	0.05	2.20	0.01	0.00	0.00	83.05	0.00
9 / 4	54.06	43.40	0.00	0.08	0.00	0.13	0.00	97.67	18 / 4	33.05	2.68	0.18	60.67	0.00	0.00	96.58	86 / 1	15.78	0.01	7.65	0.20	0.06	0.00	78.48	0.02
9 / 5	54.31	43.49	0.00	0.00	0.00	0.08	0.00	97.89	18 / 5	32.82	2.69	0.19	60.08	0.02	0.00	95.79	87 / 1	13.53	0.04	1.85	0.16	0.00	0.00	85.38	0.04
9 / 6	53.81	43.31	0.00	0.05	0.04	0.15	0.04	97.40	18 / 6	32.91	2.72	0.28	60.41	0.00	0.00	96.33	88 / 1	13.44	0.00	1.81	0.01	0.00	0.12	85.05	0.05
9 / 7	54.12	42.78	0.00	0.00	0.10	0.11	0.00	97.12	18 / 7	32.94	2.70	0.20	59.84	0.00	0.00	95.66	95 / 1	15.5	0.02	4.95	0.42	0.00	0.03	81.26	0.00
10 / 1	54.39	43.57	0.00	0.00	0.00	0.03	0.02	98.01	18 / 8	33.12	2.62	0.26	59.48	0.00	0.00	95.48	96 / 1	13.95	0.05	2.55	0.07	0.00	0.10	82.62	0.07
10 / 2	54.89	42.98	0.00	0.03	0.00	0.02	0.00	97.92	19 / 1	32.77	1.69	0.06	62.42	0.00	0.00	96.94	97 / 1	13.95	0.01	4.98	0.90	0.00	0.04	78.21	0.04
10 / 3	54.65	43.41	0.00	0.07	0.07	0.02	0.03	98.26	19 / 2	33.63	1.70	0.05	61.85	0.01	0.00	97.24	110 / 1	13.57	0.00	3.52	0.00	0.03	0.28	84.04	0.08
10 / 4	54.57	43.38	0.00	0.00	0.09	0.00	0.00	98.04	19 / 3	32.87	1.78	0.04	62.36	0.00	0.00	97.05	112 / 1	13.63	0.02	2.29	0.05	0.02	0.01	83.25	0.04
10 / 5	54.59	43.31	0.00	0.00	0.01	0.03	0.00	97.94	19 / 4	32.41	1.66	0.04	61.69	0.01	0.00	95.82	115 / 1	13.87	0.02	0.08	0.07	0.09	0.08	83.79	0.00
11 / 1	54.49	43.25	0.00	0.00	0.00	0.11	0.00	97.85	19 / 5	33.04	1.64	0.06	62.04	0.01	0.00	96.79	119 / 1	13.87	0.00	0.84	0.12	0.00	0.11	83.37	0.16
11 / 2	54.35	43.19	0.00	0.04	0.02	0.08	0.00	97.68	19 / 6	32.48	1.72	0.00	61.63	0.02	0.00	95.86	120 / 1	13.90	0.03	0.01	0.00	0.06	0.06	82.94	0.04
11 / 3	54.32	44.02	0.00	0.03	0.00	0.14	0.00	98.52	19 / 7	33.07	1.76	0.00	61.21	0.00	0.00	96.04	132 / 1	13.50	0.00	0.02	0.00	0.69	0.13	82.43	0.07
11 / 4	54.83	43.36	0.00	0.00	0.01	0.11	0.04	98.34	19 / 8	32.75	1.74	0.04	62.39	0.00	0.0	96.92	134 / 1	13.73	0.01	0.05	0.00	0.59	0.02	83.86	0.00
11 / 5	54.07	43.77	0.00	0.00	0.03	0.09	0.00	97.96	20 / 1	33.44	1.22	0.06	63.70	0.04	0.00	98.46									
11 / 6	53.93	43.22	0.00	0.00	0.01	0.11	0.00	97.28	20 / 2	33.23	1.24	0.02	63.22	0.05	0.00	97.85									
11 / 7	54.64	43.06	0.00	0.00	0.00	0.10	0.02	97.82	20 / 3	33.07	1.16	0.05	64.06	0.01	0.00	98.35									
11 / 8	53.86	43.24	0.00	0.00	0.00	0.10	0.04	97.24	20 / 4	32.80	1.19	0.02	63.58	0.02	0.00	97.61									
11 / 9	54.17	42.72	0.00	0.00	0.00	0.10	0.06	97.05	20 / 5	33.46	1.11	0.08	63.25	0.03	0.00	97.93									
12 / 1	53.79	43.40	0.00	0.00	0.00	0.07	0.03	97.30	20 / 6	32.98	1.25	0.00	63.29	0.00	0.00	97.52									
12 / 2	54.47	43.47	0.00	0.07	0.02	0.00	0.05	98.07																	
12 / 3	54.26	43.31	0.00	0.00	0.00	0.04	0.01	97.62																	
12 / 4	54.66	43.77	0.00	0.16	0.00	0.02	0.02	98.64																	
12 / 5	54.10	43.32	0.00	0.00	0.06	0.00	0.06	97.55																	
12 / 6	54.51	43.34	0.00	0.00	0.00	0.05	0.09	97.98																	
12 / 7	54.43	43.40	0.00	0.01	0.10	0.04	0.00	97.99																	

Table 3.1. Continued.....

Sphalerite										
Dataset /Point	S	Mn	Fe	Cu	Zn	As	Ag	Pb	Cd	Total
12 / 1	32.84	0.47	5.28	0.07	63.05	0.01	0.00	0.00	0.15	101.87
14 / 1	32.92	0.31	2.87	0.27	66.30	0.00	0.00	0.00	0.12	102.79
26 / 1	36.42	0.15	10.16	0.46	53.26	0.00	0.00	0.00	0.17	100.62
27 / 1	35.03	0.23	5.31	0.38	58.52	0.00	0.00	0.00	0.22	99.69
29 / 1	39.57	0.21	7.21	0.08	50.93	0.00	0.00	0.00	0.13	98.13
39 / 1	33.24	0.00	3.11	0.13	66.46	0.03	0.00	0.00	0.16	103.13
41 / 1	32.87	0.33	3.11	0.26	66.15	0.02	0.00	0.00	0.19	102.93
42 / 1	33.15	0.31	3.44	0.37	65.62	0.00	0.00	0.00	0.13	103.02
43 / 1	33.01	0.40	3.56	0.33	65.62	0.00	0.00	0.00	0.19	103.11
48 / 1	32.67	0.12	4.75	2.33	63.28	0.00	0.05	0.00	0.18	103.38
50 / 1	32.09	0.06	1.92	0.08	60.14	0.01	0.00	5.94	0.23	100.47
52 / 1	29.16	0.05	1.99	0.00	53.50	0.00	0.00	11.90	0.21	96.90
114 / 1	33.05	0.08	2.47	0.00	66.44	0.00	0.00	0.00	0.08	102.12
116 / 1	32.83	0.04	2.59	0.00	66.63	0.01	0.07	0.00	0.12	102.29
121 / 1	33.93	0.12	2.83	0.06	66.31	0.00	0.03	0.00	0.00	103.28
122 / 1	32.71	0.15	2.88	0.03	66.32	0.00	0.01	0.00	0.12	102.22
123 / 1	32.82	0.09	2.13	0.09	66.53	0.00	0.00	0.00	0.16	101.82
128 / 1	32.92	0.03	2.56	0.00	65.79	0.02	0.00	0.00	0.19	101.51
129 / 1	32.44	0.06	1.69	0.00	66.36	0.05	0.03	0.00	0.11	100.74
131 / 1	32.71	0.07	1.41	0.00	67.06	0.01	0.05	0.00	0.19	101.50
133 / 1	33.36	0.15	2.92	0.00	66.13	0.02	0.00	0.00	0.14	102.72



Annex 3.2. Representative results of energy dispersive spectrometry (EDS) showing the composition of a) silver inclusion in pyrite; b) chalcopyrite veinlet cutting pyrite;



Annex 3.2. c) arsenopyrite inclusion in pyrite; d) galena inclusion in pyrite. Dashed circle represents analysed part of the image.

Annex 4. Microthermometric data

Annex 4.1. List of the degree of fill, ice melting temperature, salinity, size and homogenization temperature of the fluid inclusions identified in the quartz and quartz-calcite veins of the study area.

Inclusion number	L /V proportion	Tm ice	Salinity (%)	Size (µm)	Th (°C)	Comment
TG06016 ^b						
1	80/20	-1	1.74	8	189.1	(L-V)->L
2	80/20	-1.5	2.57	8	163.5	(L-V)->L
3	70/30	-0.5	0.88	10	296.9	(L-V)->L
4	80/20	-1	1.74	3	124	(L-V)->L
5	80/20	-1.5	2.57	4	136.4	(L-V)->L
6	80/20	-1.5	2.57	4	203.3	(L-V)->L
7	80/20	-1.5	2.57	3	235	(L-V)->L
8	40/60	-1.5	1.74	12	260.3	(L-V)->L
9	40/60	n.d.	n.d.	8	289.6	(L-V)->L
10	10/90	n.d.	n.d.	8	311.8	(L-V)->L
11	40/60	-1.5	2.57	8	366.4	(L-V)->L
12	60/40	-2.5	4.18	12	341.7	(L-V)->L
13	70/30	-1.5	2.57	2	362.1	(L-V)->L
14	80/20	-1	1.74	2	256.8	(L-V)->L
15	80/20	-1	1.74	2	281	(L-V)->L
16	80/20	-1	1.74	2	281	(L-V)->L
17	80/20	-1	1.74	2	309	(L-V)->L
18	80/20	-1	1.74	n.d.	321	(L-V)->L
19	80/20	-1	1.74	n.d.	333.2	(L-V)->L
20	20/80	n.d.	n.d.	n.d.	370	(L-V)->L
21	20/80	n.d.	n.d.	n.d.	380	(L-V)->L
22	20/80	n.d.	n.d.	n.d.	385.9	(L-V)->L
23	80/20	n.d.	n.d.	n.d.	210	(L-V)->L
24	30/70	n.d.	n.d.	n.d.	370	(V-L)->V
25	60/40	n.d.	n.d.	n.d.	350	(L-V)->L
26	30/70	n.d.	n.d.	n.d.	310	(V-L)->V
27	30/70	n.d.	n.d.	n.d.	405	(V-L)->V
28	20/80	n.d.	n.d.	n.d.	380	(V-L)->V
29	20/80	n.d.	n.d.	n.d.	250	(V-L)->V
30	20/80	n.d.	n.d.	n.d.	296.5	(V-L)->V
31	80/20	n.d.	n.d.	n.d.	320	(L-V)->L
32	80/20	n.d.	n.d.	n.d.	349	(L-V)->L
34	90/10	n.d.	n.d.	n.d.	217	(L-V)->L
35	20/80	n.d.	n.d.	n.d.	385.9	(V-L)->V
36	80/20	n.d.	n.d.	n.d.	252.6	(L-V)->L
37	80/20	n.d.	n.d.	n.d.	256	(L-V)->L
38	80/20	n.d.	n.d.	n.d.	294	(L-V)->L
39	40/60	-1.5	2.57	n.d.	305	(L-V)->L

Abbreviations:

L = liquid phase; V = vapor phase

^a mineralized quartz-calcite vein samples

^b unmineralized quartz vein samples

n.d. = not determined

Th = Homogenization temperature

Tm = melting temperature

(L-V)->L = liquid-rich two-phase fluid inclusion homogenizing to a liquid phase

(V-L)->V = Vapour-rich two-phase fluid inclusion homogenizing to a vapour phase

Annex 4.1. Continued.....

Inclusion number	L /V proportion	Tm ice	Salinity (%)	Size (µm)	Th (°C)	Comment
TG06059 ^b						
1	80/20	-2	3.39	<3	153	(L-V)->L
2	80/20	-3	4.96	<3	165	(L-V)->L
3	80/20	-1.5	2.57	<3	152.4	(L-V)->L
4	80/20	-2.5	4.18	<3	163	(L-V)->L
5	80/20	-3	4.96	n.d.	145	(L-V)->L
6	80/20	-3	4.96	<2	152.3	(L-V)->L
7	80/20	-3	4.96	2	152.3	(L-V)->L
8	40/60	-3	4.96	2	281.8	(L-V)->L
9	70/30	-0.5	0.88	<2	266.4	(L-V)->L
10	80/20	-1.5	2.57	<2	150.1	(L-V)->L
11	80/20	-1.5	2.57	<2	242.8	(L-V)->L
12	10/90	n.d.	n.d.	n.d.	350	(V-L)->V
13	10/90	n.d.	n.d.	n.d.	405	(V-L)->V
14	10/90	n.d.	n.d.	n.d.	358	(V-L)->V
15	10/90	n.d.	n.d.	n.d.	405	(V-L)->V
16	80/20	n.d.	n.d.	n.d.	160	(L-V)->L
17	90/10	n.d.	n.d.	n.d.	158	(L-V)->L
18	90/10	n.d.	n.d.	n.d.	142	(L-V)->L
19	80/20	n.d.	n.d.	n.d.	240	(L-V)->L
20	80/20	n.d.	n.d.	n.d.	290	(L-V)->L
21	60/40	n.d.	n.d.	n.d.	329	(L-V)->L
22	80/20	n.d.	n.d.	n.d.	235	(L-V)->L
23	80/20	n.d.	n.d.	n.d.	280	(L-V)->L
24	80/20	n.d.	n.d.	n.d.	310	(L-V)->L
25	60/40	n.d.	n.d.	n.d.	327	(L-V)->L
26	80/20	n.d.	n.d.	n.d.	310	(L-V)->L
27	80/20	n.d.	n.d.	n.d.	272	(L-V)->L
28	90/10	n.d.	n.d.	n.d.	310	(L-V)->L
29	70/30	n.d.	n.d.	n.d.	327	(L-V)->L
30	80/20	n.d.	n.d.	n.d.	252	(L-V)->L
31	70/30	n.d.	n.d.	n.d.	328	(L-V)->L
32	90/10	n.d.	n.d.	n.d.	212	(L-V)->L
33	90/10	n.d.	n.d.	n.d.	228	(L-V)->L
34	10/90	n.d.	n.d.	n.d.	350	(V-L)->V
35	20/80	n.d.	n.d.	n.d.	405	(V-L)->V
36	10/90	n.d.	n.d.	n.d.	358	(L-V)->V
37	10/90	n.d.	n.d.	n.d.	405	(V-L)->V
38	90/10	n.d.	n.d.	n.d.	250	(L-V)->L
39	30/70	-1.5	2.57	n.d.	327	(V-L)->V
GBH10-33 ^b						
1	80/20	-2	3.39	10	159.3	(L-V)->L
2	80/20	-2	3.34	6	205.6	(L-V)->L

Abbreviations see page 122

Annex 4.1. Continued.....

Inclusion number	L /V proportion	Tm ice	Salinity (%)	Size (µm)	Th (°C)	Comment
3	80/20	-1	1.74	n.d.	226.7	(L-V)->L
4	80/20	-2	3.39	12	218.4	(L-V)->L
5	80/20	-3	4.96	2	190	(L-V)->L
6	80/20	-2	3.39	3	232.1	(L-V)->L
7	80/20	-2	3.39	7	173.7	(L-V)->L
8	80/20	-2.5	4.18	4	194.2	(L-V)->L
9	80/20	-1	1.74	2	227.4	(L-V)->L
10	80/20	-2.5	4.18	2	200.5	(L-V)->L
11	80/20	-3	4.96	n.d.	237	(L-V)->L
12	80/20	-2.5	4.18	n.d.	184.7	(L-V)->L
13	20/80	n.d.	n.d.	4	397	(V-L)->V
14	20/80	n.d.	n.d.	4	397	(V-L)->V
15	60/40	-3	4.96	10	269.5	(L-V)->L
16	80/20	-0.5	0.88	4	145	(L-V)->L
17	80/20	-0.5	0.88	4	186.5	(L-V)->L
18	80/20	-0.5	0.88	4	149.7	(L-V)->L
19	20/80	n.d.	n.d.	6	385	(V-L)->V
20	90/10	n.d.	n.d.	n.d.	165	(L-V)->L
21	80/20	n.d.	n.d.	n.d.	150	(L-V)->L
22	80/20	n.d.	n.d.	n.d.	170	(L-V)->L
23	80/20	n.d.	n.d.	n.d.	165	(L-V)->L
24	90/10	n.d.	n.d.	n.d.	167	(L-V)->L
25	80/20	n.d.	n.d.	n.d.	178	(L-V)->L
26	80/20	n.d.	n.d.	n.d.	188	(L-V)->L
27	20/80	n.d.	n.d.	4	389	(V-L)->V
J2-036 ^a						
1	80/20	-0.5	0.88	4	294.4	(L-V)->L
2	80/20	-0.5	0.88	2	258.2	(L-V)->L
3	80/20	-0.5	0.88	10	<100	(L-V)->L
4	59/50	-0.5	0.88	4	342.9	(L-V)->L
5	80/20	-0.5	0.88	2	330	(L-V)->L
6	80/20	-0.5	0.88	4	265.8	(L-V)->L
7	70/30	-0.5	0.88	12	321.7	(L-V)->L
8	20/80	n.d.	n.d.	4	400	(L-V)->L
9	80/20	-0.5	0.88	4	307.5	(L-V)->L
10	70/30	n.d.	n.d.	10	359.5	(L-V)->L
11	10/90	n.d.	n.d.	n.d.	405	(V-L)->V
12	10/90	n.d.	n.d.	3	385	(V-L)->V
13	40/60	-1.5	2.57	4	387	(L-V)->L
14	30/70	-0.5	0.88	10	378.6	(L-V)->L
15	40/60	n.d.	n.d.	n.d.	310	(L-V)->L
16	90/10	-0.5	0.88	n.d.	180.5	(L-V)->L
17	20/80	n.d.	n.d.	n.d.	370	(L-V)->L
18	40/60	n.d.	n.d.	n.d.	324.2	(L-V)->L

Abbreviations see page 122

Annex 4.1. Continued.....

Inclusion number	L /V proportion	Tm ice	Salinity (%)	Size (µm)	Th (°C)	Comment
19	40/60	-1	1.74	n.d.	256	(L-V)->L
20	40/60	-1.5	2.57	n.d.	356.7	(L-V)->L
21	40/60	-1	1.74	n.d.	368.6	(L-V)->L
22	40/60	-1	1.74	n.d.	368	(L-V)->L
23	90/10	n.d.	n.d.	n.d.	210	(L-V)->L
24	80/20	n.d.	n.d.	n.d.	330	(L-V)->L
25	60/40	n.d.	n.d.	n.d.	310	(L-V)->L
26	80/20	n.d.	n.d.	n.d.	350	(L-V)->L
27	80/20	n.d.	n.d.	n.d.	378	(L-V)->L
28	40/60	n.d.	n.d.	n.d.	324.2	(L-V)->L
29	40/60	-1.5	2.57	n.d.	380	(L-V)->L
J6-07 ^a						
1	60/40	-0.5	0.88	6	311.3	(L-V)->L
2	80/20	-1.5	2.57	4	277	(L-V)->L
3	60/40	n.d.	n.d.	n.d.	315	(L-V)->L
4	80/20	n.d.	n.d.	n.d.	283	(L-V)->L
5	80/20	n.d.	n.d.	n.d.	340.5	(L-V)->L
6	30/70	n.d.	n.d.	n.d.	305	(V-L)->V
7	60/40	n.d.	n.d.	n.d.	315	(L-V)->L
8	90/10	n.d.	n.d.	n.d.	290	(L-V)->L
9	80/20	n.d.	n.d.	n.d.	258	(L-V)->L
10	40/60	n.d.	n.d.	n.d.	320	(L-V)->L
J4-29-1 ^b						
1	80/20	-1	1.74	2	133.5	(L-V)->L
2	80/20	-1	1.74	2	135	(L-V)->L
3	80/20	-1.5	2.57	3	137.2	(L-V)->L
4	80/20	-1.5	2.57	4	133.5	(L-V)->L
5	80/20	-1.5	2.57	4	139.7	(L-V)->L
6	80/20	-1.5	2.57	3	187	(L-V)->L
7	80/20	-1.5	2.57	7	220	(L-V)->L
8	80/20	-1.5	2.57	8	205	(L-V)->L
9	70/30	-1.5	2.57	12	188	(L-V)->L
10	80/20	n.d.	n.d.	n.d.	175	(L-V)->L
11	80/20	n.d.	n.d.	n.d.	150	(L-V)->L
12	90/10	n.d.	n.d.	n.d.	274	(L-V)->L
13	90/10	n.d.	n.d.	n.d.	240.5	(L-V)->L
14	80/20	n.d.	n.d.	n.d.	391.7	(L-V)->L
15	60/40	n.d.	n.d.	n.d.	340	(L-V)->L
16	30/70	n.d.	n.d.	n.d.	405	(V-L)->V
17	80/20	-2.5	4.18	n.d.	175	(L-V)->L
J6-12 ^a						
1	90/10	-2	3.39	n.d.	156	(L-V)->L
2	80/20	-2	3.39	n.d.	175	(L-V)->L
3	70/30	-0.5	0.88	n.d.	290	(L-V)->L

Abbreviations see page 122

Annex 4.1. Continued.....

Inclusion number	L /V proportion	Tm ice	Salinity (%)	Size (µm)	Th (°C)	Comment
4	80/20	-2.5	4.18	n.d.	300	(L-V)->L
5	60/40	n.d.	n.d.	n.d.	250	(L-V)->L
6	80/20	n.d.	n.d.	n.d.	230	(L-V)->L
7	20/80	n.d.	n.d.	n.d.	220	(V-L)->V
8	20/80	n.d.	n.d.	n.d.	200	(V-L)->V
9	20/80	n.d.	n.d.	n.d.	300	(V-L)->V
10	60/40	n.d.	n.d.	n.d.	280	(L-V)->L
11	80/20	-1.5	2.57	n.d.	150	(L-V)->L
TG06-024 ^b						
1	80/20	-0.5	0.88	n.d.	199.5	(L-V)->L
2	60/40	-1	1.74	n.d.	190	(L-V)->L
3	60/40	-1.5	2.57	n.d.	298.4	(L-V)->L
4	20/80	n.d.	n.d.	n.d.	378.3	(L-V)->L
5	40/60	n.d.	n.d.	n.d.	378.1	(L-V)->L
6	80/20	n.d.	n.d.	n.d.	199.5	(L-V)->L
7	80/20	n.d.	n.d.	n.d.	277.2	(L-V)->L
8	60/40	n.d.	n.d.	n.d.	240	(L-V)->L
9	60/40	n.d.	n.d.	n.d.	315	(L-V)->L
10	60/40	n.d.	n.d.	n.d.	298.4	(L-V)->L
11	40/60	n.d.	n.d.	n.d.	352	(L-V)->L
12	40/60	n.d.	n.d.	n.d.	353.1	(L-V)->L
13	40/60	-0.5	0.88	n.d.	352	(L-V)->L
14	40/60	-1	1.74	n.d.	353.1	(L-V)->L

Abbreviations see page 122

Annex 5. Isotope geochemistry data

Annex 5.1. Sulfur isotope analytical method

Sulfides selected for sulfur isotope analysis were hand-picked or extracted with a diamond drill. About 100 mg of powder from each sample were prepared. The analysis was performed in the stable isotope laboratory of the Institute of Mineralogy at the TU Bergakademie Freiberg, Germany, using a Finnigan MAT Delta E mass spectrometer. The sulfides were converted in to SO₂ in the presence of V₂O₅ and SiO₂ using the technique of Yanagisawa and Saki (1983). After that $\delta^{34}\text{S}$ analyses were accomplished. SO₂ was used as internal standard and calibrated against the International Atomic Energy Agency (IAEA) standard NBS 127. The analytical error was $\leq \pm 0.3\%$. The $\delta^{34}\text{S}$ values are reported relative to the Vienna Canyon Diablo Troilite standard (VCDT).

Annex 5.2. Carbon and oxygen isotope analytical method

Five samples of calcite were obtained from hydrothermal calcite veinlets that cut the metasedimentary rocks or dikes/sills. About 0.5 mg of powder of each sample was analysed for its carbon and oxygen isotope composition. The analysis was performed in the stable isotope laboratory of the GeoBioCenter, Munich, Germany with a Thermo/Finnigan Delta Plus Isotope Ratio Mass Spectrometer (IRMS) connected to an automated Thermo/Finnigan online preparation device “Gas Bench II” that uses continuous flow mode (Révész and Landwehr 2002). Samples reacted with phosphoric acid at 72°C under helium (>99.996 vol. %) atmosphere in individual reaction tubes sealed with a septum. The released CO₂ from the calcite powders was collected, purified, and transported in a Helium flow via capillaries into the IRMS. The $\delta^{13}\text{C}$ and $\delta^{18}\text{O}$ values are reported in ‰ relative to Vienna Peedee Belemnite (VPDB) and Vienna Standard Mean Ocean Water (VSMOW). The standard deviation for the repeated analyses of carbonate standards for both $\delta^{13}\text{C}$ and $\delta^{18}\text{O}$ typically was $\leq 0.1\%$. $\delta^{18}\text{O}_{(\text{VPDB})}$ results of the analysed samples vary from -19.1 and -15.5‰ and that of $\delta^{13}\text{C}_{(\text{VPDB})}$ values range from -5.6 to +1.8‰ (Annex 4.3).

Annex 5.3. Carbon and oxygen data of hydrothermal calcites from the study area together with published data from the carbonates and metasedimentary rocks located near to the study area. All results are given in ‰.

Sample	Unit	Description	$\delta^{13}\text{C}$ VPDB	$\delta^{18}\text{O}$ VPDB	$\delta^{13}\text{C}$ VPDB	Source
J4-28-1		Hydrothermal calcite vein	-2.9	-16.9	-2.9	a
J4-29-1		Hydrothermal calcite vein	-3.2	-18.9	-3.2	a
J5-14		Hydrothermal calcite vein	-5.6	-15.5	-5.6	a
J6-07		Hydrothermal calcite vein	1.8	-19.1	1.8	a
J6-12		Hydrothermal calcite vein	1.1	-19.1	1.1	a
Mai Kenetal area						
MK77	Upper Limestone	Whole-rock black limestone	5.8	-8.5	5.8	b
MK76v	Upper Limestone	Vein containing calcite and rock	6	-7.9	6	b
MK78v	Upper Limestone	Vein containing calcite and rock	5	-8.7	5	b
MK79ev	Upper Limestone	Earlier calcite vein in sample MK79	4.5	-14.1	4.5	b
MK98g	Lower Limestone	Black lamina in sample MK98	-4.5	-11.7	-4.5	b
MK77	Upper Limestone	Whole-rock black limestone	5.8	-8.5	5.8	b
MK76r	Upper Limestone	Whole-rock black limestone	5.8	-9.6	5.8	b
MK78r	Upper Limestone	Whole-rock black limestone	5.2	-9.4	5.2	b
MK80	Upper Limestone	Whole-rock brecciated black limestone	5.3	-11.4	5.3	b
MK79vl	Upper Limestone	Later calcite vein in sample MK79	4.8	-14.4	4.8	b
MK79r	Upper Limestone	Whole-rock black limestone	5.7	-13.9	5.7	b
MK75gl	Lower Limestone	Whole-rock light-grey limestone	-0.8	-9.2	-0.8	b
MK75b	Lower Limestone	Black lamina in sample MK75	-1	-9.7	-1	b
MK74	Lower Limestone	Whole-rock grey limestone	-1	-9.5	-1	b
MK73	Lower Limestone	Whole-rock grey limestone	-0.9	-8.1	-0.9	b
MK72v	Lower Limestone	Calcite vein in sample MK72	-1.9	-20.6	-1.9	b
MK72r	Lower Limestone	Whole-rock grey limestone	-1	-11.5	-1	b
MK71	Lower Limestone	Whole-rock black limestone	-2	-8.9	-2	b
Tsedia area						
MK97	Lower Limestone	Whole-rock black limestone	-3	-11.3	-3	b
MK98b	Lower Limestone	Black lamina in sample MK98	-4.3	-11.9	-4.3	b
MK98g	Lower Limestone	Grey lamina in sample MK98	-4.5	-11.7	-4.5	b
MK99	Lower Limestone	Whole-rock grey limestone	-2.9	-8.1	-2.9	b
MK96	Lower Limestone	Whole-rock black limestone	-3.9	-11.1	-3.9	b
MK100	Lower Limestone	Whole-rock black limestone	-0.7	-12.2	-0.7	b
Negash area						
NW121	N. limestone	Whole-rock black limestone	4	-10	4	b
NW122	N. Limestone	Whole-rock black limestone	6.8	-4.7	6.8	b
NW123v	N. Limestone	Calcite vein	3.7	-9.7	3.7	b
NW123r	N. Limestone	Whole-rock black limestone	5.3	-7.5	5.3	b
NW124f	N. Limestone	Whole-rock black limestone	4.9	-8.8	4.9	b
NW124c	N. Limestone	Coarse-grained black limestone	6.6	-6.8	6.6	b
NW125	N. Limestone	Whole-rock black limestone	6.3	-6.6	6.3	b
NW98		Black limestone/marble	6.98	-5.48	6.98	c
NW84	Lower slate		-2.3	-13.51	-2.3	c
NW85	Lower slate		-1.19	-9.96	-1.19	c
NW86		Dolomite	1.71	-4.2	1.71	c
NW87		Dolomite	1.46	-0.63	1.46	c
NW97		Black limestone/marble	6.42	-4.81	6.42	c
NW96		Black limestone/marble	6.55	-5.56	6.55	c
NW88		Black limestone/marble	6.59	-5.14	6.59	c

Sample	Unit	Description	$\delta^{13}\text{C}$	$\delta^{18}\text{O}$	$\delta^{13}\text{C}$	Source
			VPDB	VPDB	VPDB	
Negash area						
NW89	Upper Slate	Black Limestone	-2.05	-8.38	-2.05	c
NW102	Lower Diamictite	Pebbly slate	-2.71	-5.42	-2.71	c
NW100	Lower Diamictite	Pebbly slate	-1.95	-7.64	-1.95	c
NW99	Lower Diamictite	Pebbly slate	-6.51	-8.29	-6.51	c
NW93	Lower Diamictite	Pebbly slate	-1.68	-4.03	-1.68	c
NW104	Middle Diamictite	Pebbly slate	-3.49	-7.89	-3.49	c
NW103	Middle Diamictite	Pebbly slate	-0.54	-6.39	-0.54	c
NW90	Middle Diamictite	Pebbly slate	-3.11	-11.35	-3.11	c
NW101	Upper Diamictite	Pebbly slate	-0.86	-6.06	-0.86	c
NW94	Upper Diamictite	Pebbly slate	-2.36	-7.68	-2.36	c
NW92	Upper Diamictite	Pebbly slate	-1.75	-8.09	-1.75	c
NW91	Upper Diamictite	Pebbly slate	-1.09	-7.08	-1.09	c

Abbreviations:

a = this study

b = Alene et al. 2006

c = Miller et al. 2003

N. = Negash

Annex 5.4 Lead isotope analytical method

Eleven sulfide (pyrite, galena, and sphalerite), five whole-rock samples, and three feldspar separates were prepared for lead isotope analysis (Annex 5.5). Feldspars were hand-picked after crushing of monzogranite dike/sill samples in to smaller pieces. They were then pulverized into powder using agate mortar. Powders of the whole-rock samples were prepared by grinding from relatively unaltered and representative whole-rock samples. Lead isotope analysis was carried out at the Laboratory for Radiogenic Isotopes of Bayerische Staatssammlung für Paläontologie und Geologie, Munich. Around 50 mg of the feldspar separates and whole-rock samples were placed in cleaned and sealed Teflon beakers and dissolved by a combination of 1.5 and 0.5 ml hydrofluoric acid (HF) and nitric acid (HNO_3), respectively, for 36 hours at 120°C . The samples were then cooled down and centrifuged. The leach solutions were dried and the elements were transformed into chlorides by adding 1ml 6n HCl and heating for another 24 hours at 120°C in closed vessels. Finally, the samples were dried down and converted in to bromide form by the addition of 0.5 ml of hydrobromic acid (HBr) and subsequent drying.

Sulfide samples were dissolved over night at a temperature of 109°C using 1 ml 6n hydrochloric acid (HCl) in sealed Teflon beakers. Then the samples were cooled down and

centrifuged. The leach solutions were then dried. 1 ml 6n HCl was added and the solution was heated for another 24 hours at 120°C in closed vessels. Finally, the samples were dried down and converted into bromide form by the addition of 0.5 ml of concentrated hydrobromide acid (HBr) and subsequent drying. Lead separation for all samples was performed in columns using 0.05 ml Dowex 1x8. The resin has been previously cleaned and conditioned by adding H₂O, 6n HCl, 1n HNO₃, and 0.5n HBr to the columns. The samples were dissolved in 0.5 n HBr and then added to the columns. After stepwise rinsing with 0.5n HBr, Pb was transferred into chlorides by adding 2n HCl and then washed out with 6n HCl. After drying the samples, the separated Pb was cleaned in the same columns by a second cycle using 2n HCl as cleaning agent instead of HBr. After washing out with 6n HCl, the samples were then ready for mass spectrometry. For that, 0.2 to 2 µl (respectively around 100 ng of Pb) of the sample was loaded on to precleaned rhenium filaments using the silica gel technique and lead isotope ratios were measured on a MAT Finnigan 261.5 mass spectrometer in a static mode. Lead isotope ratios were corrected for fractionation with $-0.1\% \pm 0.05\%$ per amu, a factor based on repeated analyses of the NBS981 international standard. Galena, and other base metal sulfides commonly contain common lead (Faure 1986) and their lead ratios are used without recalculating initial lead ratios. Initial lead ratios were determined for the feldspars and whole-rock samples to remove radiogenic Pb based on the measured lead isotope ratios, current concentrations of U and Th, and assumed ages of the intrusive, metavolcanic, and metasedimentary rocks. The age of the intrusive rocks was assumed to be similar as that of the nearby Negash late- to post-tectonic granitoid (608 ± 7 Ma, Asrat 2002). The age of the metasedimentary rocks is taken from the estimated age of the Tambien Group (735 Ma, Alene et al. 2006; see Fig. 2.8), whereas that of metavolcanic rock is from the approximate age of Tsaliet Group (800 Ma, Teklay 1997; see Fig. 2.8). In case of element concentrations were below detection limit, half of the concentration of the detection limit was used for calculation of initial lead isotope ratios (e.g. U of sample TG06007). The detailed information on sample location, description and analytical errors (2σ) are provided in Annex 5.5.

Annex 5.5. Lead isotope data of sulfides, feldspars of monzogranite dike/sill, aplitic dike/sill, metasedimentary and metavolcanic rocks.

Samples	Location (UTM)	Elevation (meter)	Description	Type of sample	$^{208}\text{Pb}/^{204}\text{Pb}_m$	$^{208}\text{Pb}/^{204}\text{Pb}_{em}$	$^{207}\text{Pb}/^{204}\text{Pb}_m$	$^{207}\text{Pb}/^{204}\text{Pb}_{em}$	$^{206}\text{Pb}/^{204}\text{Pb}_m$	$^{206}\text{Pb}/^{204}\text{Pb}_{em}$	$^{208}\text{Pb}/^{207}\text{Pb}_m$
J2-26	0505795E, 1519053N	1816	Gn with minor sl	core sample	36.7907	0.0164	15.4236	0.0109	17.3290	0.0086	2.3853
J2-36	0505795E, 1519053N	1816	Py with minor gn, sl, po, and cp	core sample	36.8009	0.0087	15.4248	0.0059	17.3763	0.0053	2.3858
J9-24	0505542E, 1518827N	1765	Py and cp with minor gn inclusion	core sample	36.8297	0.0600	15.4270	0.0053	17.4306	0.0044	2.3874
J9-31	0505542E, 1518827N	1765	Py and cp with minor gn inclusion	core sample	36.8190	0.0079	15.4333	0.0043	17.4477	0.0040	2.3857
18-25	0505676E, 1518927N	1797	Gn with minor sl	core sample	36.7951	0.0247	15.4240	0.0182	17.3320	0.0155	2.3856
18-28	0505676E, 1518927N	1797	Sl with minor gn, py, and cp	core sample	36.8259	0.0066	15.4346	0.0042	17.3377	0.0043	2.3859
18-31	0505676E, 1518927N	1797	Sl with minor gn, py and cp	core sample	36.8406	0.0159	15.4377	0.0107	17.3450	0.0089	2.3865
18-34	0505676E, 1518927N	1797	Sl with minor gn, py and cp	core sample	36.7835	0.0107	15.4225	0.0068	17.3278	0.0066	2.385
18-58	0505676E, 1518927N	1797	Py, cp with minor gn	core sample	36.8006	0.0071	15.4264	0.0049	17.3456	0.0049	2.3855
10-59	0505442E, 1518874N	1796	Sl with minor gn, py, and cp	core sample	36.8373	0.0161	15.4352	0.0113	17.3457	0.0094	2.3866
10-84	0505442E, 1518874N	1796	Sl with minor gn, py and cp	core sample	36.8061	0.0167	15.4262	0.0112	17.3308	0.0081	2.3859
TG06037	0505167, 1518718N	1774	Feldspar from monzogranite dike/sill	surface sample	37.6012	0.0067	15.4937	0.0050	18.5483	0.0038	2.4269
TG06049	0505760E, 151910N	1813	Feldspar from monzogranite dike/sill	surface sample	37.3254	0.0027	15.4652	0.0024	18.1779	0.0025	2.4135
TG06052	0505476E, 1518909N	1811	Feldspar from monzogranite dike/sill	surface sample	37.4124	0.0038	15.4727	0.0039	18.2273	0.0038	2.4180
TG06034	0505392E, 1518569N	1750	Black slate	surface sample	41.2185	0.0318	15.6982	0.0320	21.0834	0.0306	2.6257
J2-015	0505795E, 1519053N	1816	Sericite-chlorite schist	core sample	38.0404	0.0099	15.4899	0.0068	18.4240	0.0059	2.4558
TG06007	0500914E, 1517307N	1885	Mafic metavolcanic rock	surface sample	37.1609	0.0105	15.4407	0.0095	17.6949	0.0089	2.4068
TG06015	0503305E, 1516501N	1817	Sericite-chlorite schist	surface sample	39.9789	0.0177	15.6733	0.0111	21.4004	0.0109	2.5506
J4-010	0505719E, 1519076N	1843	Aplitic dike/sill	core sample	37.4591	0.0056	15.4875	0.0046	18.2063	0.0039	2.4187

Abbreviations:

m and em = measured value and measured error in percent, respectively

c and ec = corrected value and measured error in percent, respectively

UTM = Universal Traverse Mercator

Py = pyrite

Sl = sphalerite

Gn = galena

Cp = chalcopyrite

Po = pyrrhotite

Annex 5.5. Continued.....

Samples	Location (UTM)	Elevation (meter)	Description	Type of sample	$^{208}\text{Pb}/^{207}\text{Pb}_{em}$	$^{206}\text{Pb}/^{207}\text{Pb}_m$	$^{206}\text{Pb}/^{207}\text{Pb}_{em}$	$^{208}\text{Pb}/^{204}\text{Pb}_c$	$^{208}\text{Pb}/^{204}\text{Pb}_{ec}$	$^{207}\text{Pb}/^{204}\text{Pb}_c$	$^{207}\text{Pb}/^{204}\text{Pb}_{ec}$
J2-26	0505795E, 1519053N	1816	Gn with minor sl	core sample	0.0065	1.1235	0.0032	36.9427	0.2007	15.4714	0.1504
J2-36	0505795E, 1519053N	1816	Py with minor gn, sl, po, and cp	core sample	0.0038	1.1265	0.0015	36.9530	0.2002	15.4726	0.1501
J9-24	0505542E, 1518827N	1765	Py and cp with minor gn inclusion	core sample	0.0033	1.1299	0.0024	36.9819	0.2088	15.4748	0.1501
J9-31	0505542E, 1518827N	1765	Py and cp with minor gn inclusion	core sample	0.0043	1.1305	0.0010	36.9711	0.2002	15.4811	0.1501
18-25	0505676E, 1518927N	1797	Gn with minor sl	core sample	0.0076	1.1237	0.0035	36.9471	0.2015	15.4718	0.1511
18-28	0505676E, 1518927N	1797	Sl with minor gn, py, and cp	core sample	0.0040	1.1233	0.0011	36.9781	0.2001	15.4824	0.1501
18-31	0505676E, 1518927N	1797	Sl with minor gn, py and cp	core sample	0.0053	1.1235	0.0026	36.9928	0.2006	15.4855	0.1504
18-34	0505676E, 1518927N	1797	Sl with minor gn, py and cp	core sample	0.0048	1.1235	0.0018	36.9355	0.2003	15.4703	0.1502
18-58	0505676E, 1518927N	1797	Py, cp with minor gn	core sample	0.0047	1.1244	0.0018	36.9527	0.2001	15.4742	0.1501
10-59	0505442E, 1518874N	1796	Sl with minor gn, py, and cp	core sample	0.0055	1.1238	0.0021	36.9895	0.2006	15.4830	0.1504
10-84	0505442E, 1518874N	1796	Sl with minor gn, py and cp	core sample	0.0069	1.1235	0.0030	36.9582	0.2007	15.4740	0.1504
TG06037	0505167, 1518718N	1774	Feldspar from monzogranite dike/sill	surface sample	0.0020	1.1972	0.0017	37.7569	0.2001	15.5417	0.1501
TG06049	0505760E, 151910N	1813	Feldspar from monzogranite dike/sill	surface sample	0.0008	1.1754	0.0009	37.4796	0.2000	15.5131	0.1500
TG06052	0505476E, 1518909N	1811	Feldspar from monzogranite dike/sill	surface sample	0.0019	1.1780	0.0010	37.5670	0.2000	15.5207	0.1501
TG06034	0505392E, 1518569N	1750	Black slate	surface sample	0.0028	1.3430	0.0039	41.3888	0.2025	15.7468	0.1534
J2-015	0505795E, 1519053N	1816	Sericite-chlorite schist	core sample	0.0036	1.1894	0.0017	38.1976	0.2002	15.5379	0.1502
TG06007	0500914E, 1517307N	1885	Mafic metavolcanic rock	surface sample	0.0035	1.1460	0.0017	37.3145	0.2003	15.4886	0.1503
TG06015	0503305E, 1516501N	1817	Sericite-chlorite schist	surface sample	0.0059	1.3654	0.0031	40.1441	0.2008	15.7219	0.1504
J4-010	0505719E, 1519076N	1843	Aplitic dike/sill	core sample	0.0015	1.1756	0.0013	37.6139	0.2001	15.5355	0.1501

Abbreviations see page 131

Annex 5.5. Continued.....

Samples	Location (UTM)	Elevation (meter)	Description	Type of sample	$^{206}\text{Pb}/^{204}\text{Pb}_c$	$^{206}\text{Pb}/^{204}\text{Pb}_{ec}$	$^{208}\text{Pb}/^{207}\text{Pb}_c$	$^{208}\text{Pb}/^{207}\text{Pb}_{ec}$	$^{206}\text{Pb}/^{207}\text{Pb}_c$	$^{206}\text{Pb}/^{207}\text{Pb}_{ec}$
J2-26	0505795E, 1519053N	1816	Gn with minor sl	core sample	17.3648	0.1004	2.3878	0.0504	1.1223	0.0501
J2-36	0505795E, 1519053N	1816	Py with minor gn, sl, po, and cp	core sample	17.4122	0.1001	2.3883	0.0501	1.1253	0.0500
J9-24	0505542E, 1518827N	1765	Py and cp with minor gn inclusion	core sample	17.4666	0.1001	2.3899	0.0501	1.1287	0.0501
J9-31	0505542E, 1518827N	1765	Py and cp with minor gn inclusion	core sample	17.4837	0.1001	2.3882	0.0502	1.1293	0.0500
18-25	0505676E, 1518927N	1797	Gn with minor sl	core sample	17.3678	0.1012	2.3881	0.0506	1.1225	0.0501
18-28	0505676E, 1518927N	1797	Sl with minor gn, py, and cp	core sample	17.3735	0.1001	2.3884	0.0502	1.1221	0.0500
18-31	0505676E, 1518927N	1797	Sl with minor gn, py and cp	core sample	17.3808	0.1004	2.3890	0.0503	1.1223	0.0501
18-34	0505676E, 1518927N	1797	Sl with minor gn, py and cp	core sample	17.3636	0.1002	2.3875	0.0502	1.1223	0.0500
18-58	0505676E, 1518927N	1797	Py, cp with minor gn	core sample	17.3814	0.1001	2.3880	0.0502	1.1232	0.0500
10-59	0505442E, 1518874N	1796	Sl with minor gn, py, and cp	core sample	17.3815	0.1004	2.3891	0.0503	1.1226	0.0500
10-84	0505442E, 1518874N	1796	Sl with minor gn, py and cp	core sample	17.3666	0.1003	2.3884	0.0505	1.1223	0.0501
TG06037	0505167, 1518718N	1774	Feldspar from monzogranite dike/sill	surface sample	18.5867	0.1001	2.4294	0.0500	1.1959	0.0500
TG06049	0505760E, 151910N	1813	Feldspar from monzogranite dike/sill	surface sample	18.2155	0.1000	2.4160	0.0500	1.1742	0.0500
TG06052	0505476E, 1518909N	1811	Feldspar from monzogranite dike/sill	surface sample	18.2650	0.1001	2.4205	0.0500	1.1768	0.0500
TG06034	0505392E, 1518569N	1750	Black slate	surface sample	21.1270	0.1046	2.6284	0.0501	1.3417	0.0502
J2-015	0505795E, 1519053N	1816	Sericite-chlorite schist	core sample	18.4621	0.1002	2.4583	0.0501	1.1882	0.0500
TG06007	0500914E, 1517307N	1885	Mafic metavolcanic rock	surface sample	17.7314	0.1004	2.4092	0.0501	1.1448	0.0500
TG06015	0503305E, 1516501N	1817	Sericite-chlorite schist	surface sample	21.4445	0.1006	2.5532	0.0503	1.3640	0.0501
J4-010	0505719E, 1519076N	1843	Aplitic dike/sill	core sample	18.2439	0.1001	2.4212	0.0500	1.1743	0.0500

Abbreviations see page 131

Lebenslauf

I. Persönliche Daten

Name: Solomon Gebresilassie Gebremariam
Nationalität: Äthiopien
Geburtsdatum: 05.01.1977
Familienstand: verheiratet, zwei Kinder

II. Schulbildung und Studium

2005-2009: Doktorand an der Department für Geologie und Umwelt Wissenschaften, LMU-München
2000-2002: Studium mit Erlangung des M.Sc. im Fachbereich Geologie, Addis Ababa Universität, Äthiopien
1995-1999: Studium der Geologie mit dem Abschluss Bachelor, Addis Ababa Universität, Addis Ababa, Äthiopien
1995: Allgemeine Hochschulreife

III. Berufstätigkeit

2002-2004: Dozent für Wirtschaftsgeologie, Department für Geologie, Mekelle Universität, Äthiopien
1999-2000: Wissenschaftlicher Mitarbeiter, Department für Geologie, Mekelle Universität, Äthiopien

IV. Publikationen

- Gebresilassie, S., Marschik, R., Hölzl, S., and Sifeta, K. 2008. Metasedimentary-rock hosted Au-base metal mineralization in the Workamba area, central Tigray, northern Ethiopia. 33 International Geological Congress, Oslo, Norwegen, August 6-14., Compact Disk, 1307673.
- Gebresilassie, S., Marschik, R., Sifeta K., and Chewaka S. 2007. Geology and base metal-gold occurrences of Workamba area, central Tigray, northern Ethiopia. Proceedings of the 9th SGA Biennial Meeting, Dublin Ireland, 1027-1030.
- Gebresilassie, S., and Marschik, R., 2007. Geology and geochemistry of intrusive dikes and metasedimentary rocks of Workamba area, Tigray province, northern Ethiopia. 23th International Applied Geochemistry Symposium (IAGS), Oviedo, Spanien, Juni 14-19, Zusammenfassung, S. 32-43.
- Gebresilassie, S., Tadesse, S., and Hailu, K., 2003. Geology, mineralogy, and geochemistry of serpentinites from Kenticha area, southern Ethiopia, and associated Ni-mineralization. In: Eliopoulos et al. (eds.), Mineral Exploration and Sustainable Development, Proceedings of 7th Biennial meeting of the Society for Geology Applied to Mineral Deposits, Athen, Griechenland, V.2, 579-582.
- Gebresilassie, S., 2002. Geology, mineralogy, and geochemistry of Ni-Cr-Co- bearing ultramafic bodies of Kenticha area, southern Ethiopia. M.Sc. Thesis (unveröffentlicht), Addis Ababa Universität, Addis Ababa, Äthiopien, 97 S.